Systematic Azimuth Quadrupole and Minijet Trends from Two-Particle Correlations in Heavy-Ion Collisions

David Kettler

A dissertation
submitted in partial fulfillment of the
requirements for the degree of

Doctor of Philosophy

University of Washington

2013

Reading Committee:

Thomas Trainor, Chair

Gordon Watts

Gerald Miller

Program Authorized to Offer Degree:
UW Department of Physics

University of Washington

Abstract

Systematic Azimuth Quadrupole and Minijet Trends from Two-Particle Correlations in Heavy-Ion Collisions

David Kettler

Chair of the Supervisory Committee:
Professor Thomas Trainor
Physics

Heavy-ion collisions at the Relativistic Heavy Ion Collider (RHIC) produce a tremendous amount of data but new techniques are necessary for a comprehensive understanding of the physics behind these collisions. We present measurements from the STAR detector of both p_t-integral and p_t-differential azimuth two-particle correlations on azimuth (ϕ) and pseudorapidity (η) for unidentified hadrons in Au-Au collisions at $\sqrt{s_{NN}} = 62$ and 200 GeV. The azimuth correlations can be fit to extract a quadrupole component—related to conventional v_2 measures—and a same-side peak. Both p_t-integral and p_t-differential results are presented as functions of Au-Au centrality. We observe simple universal energy and centrality trends for the p_t-integral quadrupole component. p_t-differential results can be transformed to reveal quadrupole p_t spectra that are nearly independent of centrality. A parametrization of the p_t-differential quadrupole shows a simple p_t dependence that can be factorized from the centrality and collision energy dependence above 0.75 GeV/c. Observed trends seem to be in conflict with standard hydrodynamic theories.

Angular correlations contain jet-like structure with most-probable hadron momentum ~ 1 GeV/c. For better comparison to RHIC data we analyze the energy scale dependence of fragmentation functions from e^+-e^- collisions on rapidity y. The results in a parameterization of fragmentation functions that enables extrapolation to low Q in order to describe fragment distributions at low transverse momentum p_t in heavy ion collisions. We convert

measured minimum-bias jet-like angular correlations to single-particle hadron yields and compare them with parton fragment yields inferred from spectrum hard components. We find that jet-like correlations in central 200 GeV Au-Au collisions correspond quantitatively to pQCD predictions, and the jet-correlated hadron yield comprises one third of the Au-Au final state in central collisions. These observations conflict with claims of "jet quenching" at RHIC.

TABLE OF CONTENTS

Page

LIST OF FIGURES

ACKNOWLEDGMENTS

Completing a Ph.D is not an acheivement I can claim to have accomplished on my own. First I would like to thank the DOE Office of Science for funding this research. None of this would have been possible without the RHIC facility and STAR detector. Of course I need to thank my advisor Tom Trainor who has been instrumental in providing insight into the problems encountered in this analysis. His unconventional approach may often conflict with colleagues in the field but that's precisely what has made these results so exciting. I would also like to thank Duncan Prindle and Lanny Ray for their valuable wisdom and assistance. I would like to thank the rest of my committee for their interest and enthusiasm. And I would like to thank Hamish Robertson for giving me the push I needed to bring all of this work together.

Throughout this endeavor I have received less direct but no less valuable support from friends and colleagues at the University of Washington and in the STAR collaboration. There are probably more names than I can list here but in particular I would like to thank Charlie Hagedorn and Tracy Lovejoy for being wonderful and supportive friends. I would also like to thank members of the SDF Public Access UNIX System for their encouragement. Last but certainly not least I have thank my parents for always being there to inspire me. It is unthinkable that I could have made it this far without their guidance.

Chapter 1

INTRODUCTION

1.1 Nuclear Collisions

The study of high-energy heavy-ion collisions involves colliding large nuclei at energy scales typically encountered in high-energy elementary particle physics. The development of accelerators able to achieve increasingly large energies in the center-of-mass frame of a collision of leptons or hadrons has been the driving force behind developments in high-energy physics. High center-of-mass energy allows new particles to be created and new physical regimes to be studied. For example, if an electron and a positron collide at high energy they produce a system with a large amount of available energy but no net quantum numbers—conserved quantities which restrict allowed particle production. This permits new heavier particles to be created. In a proton-proton collider such as the Large Hadron Collider (LHC) at CERN, the collisions occur in the substructure of the proton, but the ultimate goal is the same. Protons are not fundamental particles, and in this energy regime most of the hard scatterings are dominated by gluons found within the protons.

While the physics goals of the heavy-ion program at the Relativistic Heavy Ion Collider (RHIC) differ from elementary particle physics, the accelerator and detectors have much in common. Originally, the primary goal of the relativistic heavy-ion physics program was the creation of a quark gluon plasma (QGP), a deconfined state of matter consisting of free quarks and gluons. But even if no QGP were formed at RHIC there is still much to be learned by studying heavy-ion collisions. In the most general sense what we study in heavy-ion collisions is collective effects in nuclear matter under extreme conditions. In this dissertation we summarize statistical methods to analyze RHIC data with as little bias as possible in order to avoid imposing preconceived physical models. Many conventional analysis techniques at RHIC are based on physical assumptions which can produce biased conclusions.

1.1.1 The Quark Gluon Plasma

Quantum Chromodynamics (QCD) is the theory that describes the strong nuclear force holding nuclei together. One of the essential properties of QCD is confinement: quarks and gluons cannot exist as free particles and are instead confined in particles known as hadrons. In QCD—unlike the similar theory of quantum electrodynamics (QED) which describes electromagnetism—the force-carrying gluons themselves carry the "charge" of the strong nuclear force: color. This means that the QCD field is strongly self-interacting. A pair of electrically charged particles in a bound state can be pulled apart, and the strength of the force between the particles diminishes with distance. But the QCD field between a pair of particles with color is confined within narrow tubes and does not become weaker with distance. In fact as one does work on the system in an attempt to separate a pair of bound quarks eventually there will be enough energy to create a new quark-antiquark pair. This new quark-antiquark pair may bind with existing quarks to form new hadrons. The quarks can only exist in a colorless bound state with other colored particles. This is the property of confinement.

This phenomenon is the principle behind jets, which are prevalent in all hadronic collisions above a center of mass energy of about 13 GeV [159] and will be explained further in Sec. 1.3. Under the extreme temperatures and pressures present in heavy-ion collisions it has been proposed that the quarks and gluons within hadronic matter might exist as a plasma rather than in hadronic bound states. This quark-gluon plasma would be a fundamentally new state of strongly-interacting matter[130]. Creating this state has been one of the principle goals of the RHIC program.

Because the search for the QGP has been the driving goal behind the development of the RHIC physics program many of the observables that have been studied at RHIC were chosen according to models which claimed they should be signatures of a QGP. However, while pure QCD calculations of QGP properties under ideal conditions have been performed using lattice QCD, it is impossible to calculate all possible dynamics in a heavy-ion collision with current techniques. QCD is a difficult theory to work with even in ideal circumstances because the self-interactions of the QCD field make it highly nonlinear. In a heavy-ion

collision the QGP, if produced at all, is an extremely short-lived state existing in a violent and dynamic environment. Because QCD calculations of QGP properties under these circumstances are nearly impossible to make, much of the theory discussed in the field relies on simplified models based on hydrodynamics.

An expected consequence of the formation of a QGP is rapid collective expansion, typically called "flow" [101]. It should be noted, however, that the existence of flow does not require a QGP. Hydrodynamics is the standard framework for analyzing flow and we will spend much of this paper exploring the implications of flow for experimental observables. However, we wish to avoid imposing preconceptions on the data and will attempt to analyze the collective behavior of nuclear matter in a model-independent way.

1.1.2 History of Heavy-Ion Physics

High energy heavy-ion collisions have been studied since the Bevalac; the name given to the union of the 6 GeV Bevatron accelerator at Lawrence Berkeley National Laboratory and the SuperHILAC linear accelerator. The Bevatron was built as a weak-focusing proton synchroton which began operating in 1954, and SuperHILAC was a flexible linear accelerator that originally functioned independently but was linked to the Bevatron in 1974. The Bevalac was the only machine in the world capable of accelerating any element on the periodic table. A wide variety of fixed-target heavy ion collisions were carried out there.

Physics at Bevalac energies is very different from what we study today at RHIC, but many of the measurement techniques used today have their origins at the Bevalac. Hydrodynamic models were developed at the Bevalac, but they described different underlying physics. Since there wasn't enough energy at the Bevalac to produce a QGP, or even significant additional particle production, these models described compression-expansion cycle of projectile nucleons involved in the collision [152]. Observations from the Bevalac were largely consistent with these hydro models, including sideways deflection of the momentum flux and complete nucleon stopping at near-zero impact parameters [144].

The next major facility for studying heavy ion collisions at the time was the 33 GeV Alternating Gradient Synchrotron (AGS) built at Brookhaven lab which began operating

in 1960. This facility is actually still in use today as the booster for RHIC.

Prior to the RHIC program the highest-energy heavy-ion accelerator was the Super Proton Synchrotron (SPS) at CERN. Housed in a 6.9 km circumference tunnel, the SPS has been operating since 1976 and is capable of accelerating protons to 450 GeV and Pb ions to 158 GeV per nucleon (fixed target). It is still in use today as the booster for the Large Hadron Collider. Heavy-ion physics at SPS energies is qualitatively different from that at the Bevalac. At the SPS production of new hadrons from jets became possible, while at much lower energies the observed particles are dominated by the protons and neutrons already present in the nuclei of the colliding ions.

The Bevalac, AGS and SPS accelerators all drove fixed-target programs. A fixed target means that the center-of-mass energy available in collisions is considerably less than the beam energy, and the gap between the energy of the accelerator and the center-of-mass energy only gets larger at higher energies. For instance the 158 GeV per nucleon Pb beam used at the SPS only corresponds to about 17 GeV per nucleon in the center-of-mass frame.

Moving to a collider allows access to the beam full energy. When two projectiles collide with equal but opposite momenta, the lab frame *is* the center-of-mass frame and the available energy is the sum of the energy in the two beams. The world's first hadron collider was the Intersecting Storage Rings (ISR) at CERN which began running in 1971, but heavy-ion experiments were not performed with a collider prior to RHIC.

After the success of the ISR at CERN there were plans to build a proton-proton collider at Brookhaven National Lab called ISABELLE, after "Intersecting Storage Accelerator" plus "Belle" for beauty—a reference to the original name of the bottom quark. But that project ran into many problems, in particular with the superconducting magnets that were necessary for the desired energies. After many setbacks the project was canceled in 1983.

With the growing importance of heavy-ion physics an alternative use of the ISABELLE facility was proposed. It was found that a Relativistic Heavy Ion Collider could be built on the site of the ISABELLE project [129]. Construction of RHIC was completed in 1999 and physics data taking began with the first collisions occurring in Run 1 on June 12, 2000 at 56 GeV per nucleon center-of-mass. Subsequent operations achieved 130 GeV per nucleon later in 2000. The design energy of 200 GeV per nucleon was achieved during Run 2 in

2001.

The Large Hadron Collider (LHC) heavy-ion physics program is now running at a much higher energy than RHIC, capable of colliding heavy ions at 2.76 TeV per nucleon. Some might question the value of continuing RHIC in the LHC era, but there is still much to learn at RHIC energies. A number of observables—some of which will be discussed in this paper—have hinted at a fundamental shift in physics between SPS and RHIC energies. If there is a phase transition in that region then it makes sense to study observables near the transition point rather than well past it at LHC energies. A recent beam energy scan program at RHIC intentionally lowered the machine's energy well below design energy in order to probe for this transition. And this paper will demonstrate that there is still much we don't completely understand even at full RHIC energy.

1.2 Hydrodynamics

The QGP phase of matter is conventionally described theoretically in terms of relativistic hydrodynamics. In a hydrodynamic description of A-A collisions a large pressure is assumed to arise early in the initial state and drives collective motion or flows. Flows manifest both as radial expansion of the the system—known as radial flow—and an anisotropy in the azimuth particle distribution due to an initial-state overlap anisotropy in non-central collision, which can be described as either directed flow or elliptic flow. These types of flow will be discussed throughout this paper.

1.2.1 Assumptions of Hydrodynamics

For hydrodynamics to be applicable there must first be a locally thermalized system [154]. The exact mechanism of thermalization is unknown, and the requirement for thermalization is one of the most difficult aspects of hydrodynamic theory. The timescale required for thermalization is actually less than the size of the system divided by the speed of light, which means that complete thermalization is not even possible in principle. But many models assume only local thermalization.

There are actually three components to a hydrodynamic calculation. The first is the relativistic hydrodynamics calculation, followed by freezeout (hadron production), and hadron

rescattering. Furthermore, since a hydrodynamic calculation starts with the assumption of a locally-equilibrated system it cannot describe anything about the system prior to equilibration. Initial conditions have to be provided from some other source, and different initial conditions can affect the final outcome significantly.

Momentum anisotropies in the final state (produced particles that can be measured in a detector) require the existence of an initial spatial anisotropy. In standard hydrodynamic theory final-state anisotropy requires rescattering within the produced matter [101]. In any collision that is not perfectly central there is a natural spatial anisotropy defined by the reaction plane, the plane defined by the impact parameter between two nuclei and the beam direction.

The emergence of hadrons from a QGP system is typically described as "freezeout". In theoretical models hadrons are generated at freezeout with procedures such as the Cooper-Fry formula. The hadrons are subsequently rescattered with a model such as Relativistic Quantum Molecular Dynamics (RQMD) [154]. There are actually two different freezeouts in hydrodynamic theory, a chemical freezeout which fixes the abundance of hadron species and a kinetic freezeout after which the hadrons are no longer rescattering enough to act as a thermal system.

Unfortunately, there is no comprehensive theoretical model that can address all of the complexities in heavy-ion physics. Instead we have a patchwork of several theories and models applied to specific aspects of the collision system, each with its own assumptions, tunable parameters, and uncertainties [26]. Conceptual advancement must be driven by experiment rather than theory.

1.2.2 Predictions of Hydrodynamics

While many observations from RHIC have been attributed to hydrodynamics, after the first few years of RHIC running it is clear that there is no "smoking gun" evidence that a QGP has been formed [26]. The QGP has even been predicted to exist at SPS energies but should "live" longer at RHIC [154]. The size of the system can also affect QGP properties, and this has been explored to some degree at RHIC with collisions of smaller copper nuclei in

place of gold nuclei.

One class of hydrodynamic predictions is global event variables: statistical measures based on integrals of particle yields over momentum space (kinetically accessible) inspired by thermodynamic quantities. Examples of analogs to temperature include spectrum inverse slope parameter T and ensemble-mean p_t, $\hat{p}_t$. Analogs to chemistry include hadron yields and their ratios, for instance the K/π meson ratio [64, 77]. There are also several measures related to critical point fluctuations [151].

One of the most widely-discussed global features is the large-scale angular structure of the event-wise particle distribution. This is commonly expressed using low-order spherical or cylindrical harmonics on azimuth and described as "flow". Flow may manifest itself in several ways. Radial flow is inferred from the transverse momentum spectra of measured hadrons. The hydrodynamic expansion of the medium is said to drive a collective velocity of produced hadrons. It is measured with phenomenological fits to the p_t spectra assuming some (ad hoc) velocity profile and a common decoupling temperature [106].

In addition to radial expansion, flow might produce an anisotropy in the momentum distribution of particles produced in a non-central nucleus-nucleus collision. In non-central collisions it may be possible for hydrodynamics to convert the initial spatial anisotropy into a momentum anisotropy, described as elliptic flow. Elliptic flow is said to be measured at RHIC by observing the azimuth anisotropy of the measured hadron spectrum $dN/(dyp_\perp dp_\perp d\phi_p)$ [101]. Anisotropic flow is also claimed to have been observed at the AGS [63] and SPS [140].

The conventional measure of elliptic flow is v_2, which is defined theoretically by the second component of the Fourier decomposition of the particle azimuth distribution relative to the plane of the collision. This reaction plane is not a directly observable quantity however, and there are a number of systematic biases that make estimating it difficult. Techniques for measuring v_2 will be explored in Chapters 4 and 5. In hydrodynamics the maximum v_2 occurs in the limit of perfect local thermal equilibrium at every space-time point [101].

Some authors refer to the measured quantity v_2 directly as "elliptic flow" but this is a confusing practice. Elliptic flow is a physical mechanism and v_2 is a measured anisotropy

in the particle distribution. While the theory of elliptic flow certainly does produce a v_2 coefficient, other physical processes can as well. It is dangerous to assume that any observed v_2 is the result of elliptic flow.

It is generally assumed that large-scale angular structure represents collective motion of the thermalized medium. Therefore, large v_2 values are interpreted by many as direct evidence for event-wise thermalization in heavy ion collisions [74]. This leads to fitting event-wise angular distributions with model functions conventionally associated with collective dynamics, that are then interpreted physically as thermodynamic in nature.

The hydrodynamic description of heavy-ion collisions is far from complete, however. Hydrodynamic predictions are expected to fail for very peripheral collisions as well as at sufficiently high p_t. There is still a conflict between continuum hydrodynamics and discrete multiparticle systems. Furthermore, hydrodynamic models are classical models and do not include quantum mechanical effects. Quantum effects may still play a major role in heavy-ion collisions.

1.2.3 The "Nonflow" Problem

Thus far we have been describing hydrodynamics and its predictions as if flow were the only mechanism responsible for particle dynamics at RHIC. In real data other processes can affect bulk measurements, such as Hanbury Brown Twiss (HBT) correlations, resonance decays, and jets. In the context of v_2 measurements such effects are often collectively referred to as "nonflow". While several factors may contribute to nonflow, there is evidence that a large number of minijets—fragments from low-energy partons, mainly gluons—are produced at RHIC [28, 29], and this is likely the dominant source of nonflow.

Hydrodynamics cannot describe jets, so it is typically assumed that jets are either not produced until the freeze-out stage or must come from very high-energy partons that have to force their way through the QGP medium. Jets produced under these conditions would therefore have very different scaling properties from jets produced from fragmentation in vacuum. For instance, the number of observed jets would be suppressed in heavy-ion collisions compared to a linear superposition of nucleon-nucleon collisions. We will discuss jets

in more detail in the next section.

In a conventional flow analysis all azimuth correlation structures not attributable to hydrodynamic flow are labeled "nonflow" and treated as a systematic bias. While nonflow has a relatively small contribution to correlation structures at SPS energies and below, at RHIC there is evidence of copious minijet production that's actually in excess of what would be predicted from a superposition of nucleon-nucleon collisions [29, 28, 138, 139, 30]. This means that the nonflow contribution may be as large or even larger than the flow contribution. If that is the case then it is necessary to reassess this analysis strategy and treat "flow" and "nonflow" more equally.

1.3 pQCD in HEP and Nuclear Collisions

QCD describes the strong interaction, but it is a difficult theory to work with. In [87] it was said about QCD, "Perhaps it is for the first time in the history of physics that a theory which is neither precisely defined nor proved to have the right to exist as a consistent theory has become so popular." The non-abelian nature of the QCD field means it is self-interacting. As a result there are very few conditions in which analytic calculations can be made within the theory. Even numerical techniques like lattice QCD are inefficient and difficult to apply.

Despite the difficulties of working with QCD it has been a successful theory within certain limits. One of these is the high-energy perturbative QCD (or pQCD) limit, the principle prediction of which is fragmentation. Fragmentation is a fractal-like splitting process in which an initial high-energy parton turns into a shower of correlated hadrons we call a jet. Since hadrons are massive particles there is a minimum amount of energy needed to create them so unlike a true fractal the QCD splitting process cannot continue indefinitely. The end result is a shower of correlated final-state hadrons. Perturbative QCD does a good job of describing these jets over a large range of energies.

Feynman rules in the QCD Yang-Mills theory made it possible to perform calculations with perturbation theory by expanding amplitudes in the dimensionless coupling α_s, analogous to the fine structure constant in QED [87]. But the color coupling constant $\alpha_s = g^2/4\pi$ is not small as in QED. This makes the perturbative expansion difficult, and it is typically limited to high energies.

1.3.1 Descriptions of Jets

The field of high-energy heavy-ion collisions is unique because of the convergence of the disciplines of nuclear physics and high energy physics. So far we have discussed the hydrodynamic description of nuclear collisions and bulk properties which are usually only studied in nuclear physics. However, jets have been observed experimentally in high-energy collisions since 1975 with the SPEAR e^+e^- storage ring at the Stanford Linear Accelerator Center [99]. They remain an important contribution at RHIC.

Jets can be produced in any collision with sufficient energy. Jets in hadronic collisions are common, but they are simpler to analyze in e^+-e^- collisions. In the most common e^+-e^- jet event, a back-to-back quark-antiquark pair is produced initially and each quark fragments into a jet. In the simplest jet events in e^+-e^- the back-to-back jet pairs (dijet) is all that is produced in the collision. Not only is it a very clean signal, but we know the precise energy of the initial partons because momentum conservation dictates that each must have exactly half of the center-of-mass collision energy.

Hadronic collisions are more complicated, since hadrons are not elementary particles. There can be a hard scattering between a pair of quarks or gluons within a hadron, but the remaining components of the hadron must also react in some way which produces backgrounds. Furthermore, the initial energy of the partons produced in a hard scattering can't be known exactly because the momenta of quarks and gluons within a hadron will fluctuate. But jets are an important process and have been observed in some form or other by every modern hadronic collider.

In heavy-ion collisions it is possible that the jet structure is actually modified compared to what we observe in proton-proton collisions [28, 168]. There has even been some debate over what the term "jet" means. Some would claim that true jets are only produced by a vacuum pQCD fragmentation process. Meaning that if the parton interacts with a medium before or during fragmentation then whatever is produced isn't actually a jet. The fragmentation process of a jet in a strongly-interacting medium is altered. In this dissertation we will use the most basic definition: a jet is a cluster of correlated particles produced from a single parton (a quark or gluon). But in this context we must be explicit about what we

are measuring or calculating as a jet.

At high energies in elementary collisions jets have been well described by perturbative QCD calculations. However, these calculations start in the limit of asymptotic freedom and cannot describe jets fragments at very low energies [165]. Experimental techniques has also relied on large-energy hadron clusters to identify jets and were therefore not effective at measuring low-energy jets. Low-energy jets are a problem for both theory and experiment. But we must remember that pQCD is, by nature, nothing more than an approximation to the true QCD physics. If a pQCD approximation at an energy outside of its range of validity does not accurately describe an observation it is not necessarily a failure of QCD as a theory of nature. It is a failure of our ability to *calculate* quantities using QCD.

1.3.2 Minijets at RHIC

Throughout this dissertation we will use the term "minijet" for low-energy jets observed without a jet trigger. A number of observations at RHIC have indicated that the non-sinusoidal components of angular correlations are dominated by fragments from low-energy partons [29, 138, 28, 165]. These have been studied using both fluctuation techniques [29] and two-particle correlations [138, 28]. This document emphasizes correlation techniques. We identify certain correlations of small numbers of hadrons—sometimes only two or three in a cluster—as minijets.

High-energy jets are an important part of QCD theory and experiment, being one of the few observable processes that can be accurately calculated in QCD theory using perturbation techniques. Due to the asymptotic freedom at high energies in QCD theory, the pQCD expansion starts at high energies and then works towards lower energies. Since the initial discover of jets many measurements have been made with a wide variety of collision systems and detectors. As pQCD theory has continued to develop, adding next-to-leading order (NLO) and next-to-next-to-leading order (NNLO) terms, the boundary of what can be described theoretically has been pushed lower and lower. At the same time more-sensitive experimental techniques have led to jet measurements at lower and lower energies.

The term "minijet" was first used by the UA1 collaboration [43] and referred to jet-like

structure that pushes the boundary of what is typically classified as a jet. It is very difficult to calculate pQCD terms beyond NNLO, so minijets may occur at energies below what can be described theoretically. Even so, pQCD is ultimately an approximation and minijet observations appear to be on a continuum with higher-energy jet measurements. It is not unreasonable to label them as jets.

While certain angular correlation structure is one of the defining properties of jets, an angular correlation alone does not imply that the correlation was the product of fragmentation of a parton. Jet-like angular structure is a necessary but not sufficient condition. With detailed analysis of the momentum dependence, centrality evolution, and the relationship to jet observations in other collisions systems it is possible to link the angular correlation measurements done at RHIC to fragmentation processes as will be discussed in Chapter 9.

Minijet observations are important theoretically as well as experimentally. QCD theory predicts that an abundance of soft gluons (minijets) should be produced in collisions at RHIC. [114] Furthermore, minijets may dominate the production mechanism for the QCD medium (QGP) [132, 62]. Minijets may also serve as a probe of medium properties, including the extent of thermalization. It's possible that minijet effects can even offer alternative explanations for certain hydrodynamic observables. Minijets may relate medium properties and collective motion to a theoretical QCD context. Minijets can be regarded as Brownian probe particles for the QCD medium. Their systematics provide strong constraints on "nonflow" in the conventional flow context.

1.4 Correlations

In much of high-energy physics there is an emphasis on quantities that can be extracted from a single event. A large event sample is desired for statistical purposes, of course, but many fundamental techniques such as jet reconstruction have to be done effectively on an event-by-event basis. In the extremely noisy environment of heavy-ion collisions this isn't always a practical approach. Throughout much of this document we discuss techniques which determine correlations averaged over ensembles of many events. We find that this is a powerful tool for the analysis of heavy-ion data.

There is a large volume of data collected in heavy-ion collisions, not simply in terms of

the number of events but also the number of particle tracks observed in each event. This can lead to novel analysis approaches. A typical analysis may address millions of events, each of which can include over a thousand observed particles in each event. Fig. 1.1 gives an example of a single central Au-Au collision in the STAR time projection chamber (TPC) [15]. The details of how this detector works will be explained in Chapter 2, but for now it is enough to understand that each line represents a track made by one particle in the TPC. When dealing with so much data a statistical approach must be taken. Many of the techniques presented in this dissertation were developed from information-theory principles and then applied to particle data for heavy-ion collisions.

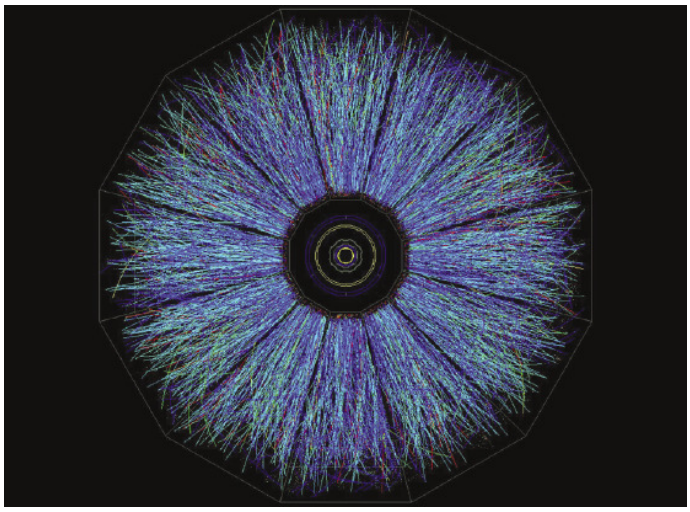

Figure 1.1: Example of tracks in a reconstructed event in the STAR TPC [15].

Correlation techniques are not new to particle physics. The most general methods for studying any sort of anisotropy in particle production require measuring correlations between particles. An early example is measurements of two-particle angular correlations in p-p collisions at the CERN ISR on momentum subspace (η, ϕ) [113] which were described in terms of longitudinal (string) fragmentation [53].

Correlation measurements are sensitive to a range of physical processes. The benefit is that they can be sensitive even to very small effects which may be difficult to observe any

other way. But since so many different physical processes can contribute to a correlation, at times it can be difficult to properly interpret the results. Correlations are also very sensitive to systematic issues in data taking and track reconstruction. Some of these issues can be reduced with the proper choice of statistical reference—see Chapter 5—but even so interpreting correlation data physically should be done with caution.

Nuclear collisions may exhibit complex correlation structures that depend on the geometry of the parton collisions, nucleon collisions, and nucleus collisions corresponding to minijets, N-N collision dynamics, and collective behavior. All three sources are important. Hydrodynamic flow is not isolated from these other mechanisms, but instead exists on a continuum with them. We therefore require analysis methods that treat the jet and flow contributions on equal footing in order to provide distinction and comparisons. We also do not wish to impose the hypothesis being tested onto the measurements. For these goals correlation analysis is the best available tool. Correlations can be measured and modeled in p-p and Au-Au collisions without imposing a physical hypothesis, and they provide access to fragments from minimum-bias partons as well as even softer physics.

In Chapter 5 we will present analysis methods and statistical measures that can be used to distinguish *geometrically* the azimuth quadrupole moment attributed to elliptic flow from "nonflow" effects, primarily minijet correlations. Quadrupole amplitudes are obtained from fits to 2D angular autocorrelations on azimuth and pseudorapidity. Jet structures are also isolated and can be related to known fragmentation processes.

1.5 Structure of this Dissertation

This Introduction gives a broad overview of the points that will be discussed over the course of this document. Chapter 2 will discuss the experimental setup, variables, and data sets of the RHIC facility and STAR experiment. Chapter 3 will discuss the conflict between hard and soft physics in heavy-ion collisions. Chapter 4 will give an overview of the standard flow analysis techniques and measurements in use today. Chapter 5 will describe the correlation methods unique to this analysis. Chapter 6 will apply those methods to p_t-integral data. Chapter 7 will apply those methods to p_t-differential data. Chapter 8 will discuss an analysis of fragmentation functions in e^+e^- collisions and how it relates to

heavy-ion collisions. Chapter 9 will return to our correlation data and discuss what we can learn from the observed same-side peak structure in the context of minijets. Finally, we will discuss what all of these results mean for the field of heavy-ion physics in Chapter 10

Chapter 2

THE STAR EXPERIMENT

2.1 Overview of RHIC

The Relativistic Heavy Ion Collider was constructed to investigate strongly interacting matter at high energy density. This is accomplished by colliding heavy ions at per-nucleon center-of-mass energies ($\sqrt{s_{NN}}$) up to 200 GeV. Typically, gold ions are collided but p-p collisions are an important reference system. d-Au and Cu-Cu collisions have been used to study the properties of different collision systems. There is also a spin physics program at RHIC using polarized proton beams, but the spin program will not be discussed in this document.

RHIC was designed to be an extremely flexible machine. As mentioned in Chapter 1 it was built in the 3.8 km circumference tunnel originally intended for the ISABELLE accelerator. During the design of RHIC some of its parameters were constrained by the desire to reuse existing ISABELLE facilities, but many of its features were brand new.

RHIC was designed to be able to collide proton beams as well as beams of different ion species with the same center of mass energy per nucleon. This requires beam rigidities—which correspond to the strength of the magnets necessary to steer the beam—to be able to vary by as much as a factor of 2.5. Asymmetric collisions are also possible, with the most the extreme case being colliding gold ions with a deuteron beam. This requires separate rings that can operate with different magnetic fields as the rigidities of the two beams will be different. Unfortunately while the beam rigidities at RHIC can accommodate both protons and gold ions it is not possible to operate the two beam lines with such a large rigidity difference simultaneously so proton-gold collisions are not possible.

One of the principal design features of RHIC is the use of superconducting magnets. Cryogenically cooled to 4 Kelvin the dipole bending magnets generate the 3.458 T field necessary for 100 GeV per nucleon beams to make their trip around the RHIC tunnel. In

addition to the bending magnets a number of additional magnets are needed for focusing, primarily quadrupoles and sextupoles. Gold ions experience a much stronger intrabeam scattering from Coulomb repulsion than protons do, as the force is proportional to Z^2/A^2 [100]. Therefore, a heavy-ion accelerator needs much stronger focusing than a typical proton machine.

RHIC was also designed for a spin physics program that collides polarized proton beams. It is the highest energy polarized proton facility in the world. The spin vector precession frequency is proportional to $G\gamma$, where G is the anomalous magnetic moment of the proton and γ is the usual Lorentz factor [100]. The number and strength of potentially depolarizing resonances increase along with this frequency, so the higher the beam energy the more difficult it is to maintain beam polarization, which was a significant factor in the design of RHIC.

2.1.1 The Acceleration Process

The RHIC rings are the final stage of the acceleration process, but there are several additional systems required to create the beam and bring it to injection energy. Fig. 2.1 shows the complete BNL accelerator complex. For heavy-ion physics the important facilities are the tandem Van de Graaf accelerators, the AGS booster, the AGS, and RHIC itself.

For 40 years the ion source of the AGS and RHIC complex was a pair of tandem Van de Graaf accelerators, though that has now been replaced by the Electron Beam Ion Source (EBIS) facility. The data used in this dissertation were taken with the older Van de Graaf facility in place. The purpose of both facilities was to function as an ion source and handle the initial acceleration of these ions. Ions would enter the booster accelerator with energies as high as 2 MeV per nucleon and $Q = +32$. There is also a 200 MeV linear accelerator which functions as the first stage for protons.

The booster accelerates the ions up to 95 MeV per nucleon and bunches the beam with a two-cavity RF system. The bunching process operates on the eighth harmonic of the revolution frequency to produce one bunch per harmonic and reaches a frequency of 5 MHz. When it is time to extract the beam the eight bunches are merged into four and the ions are

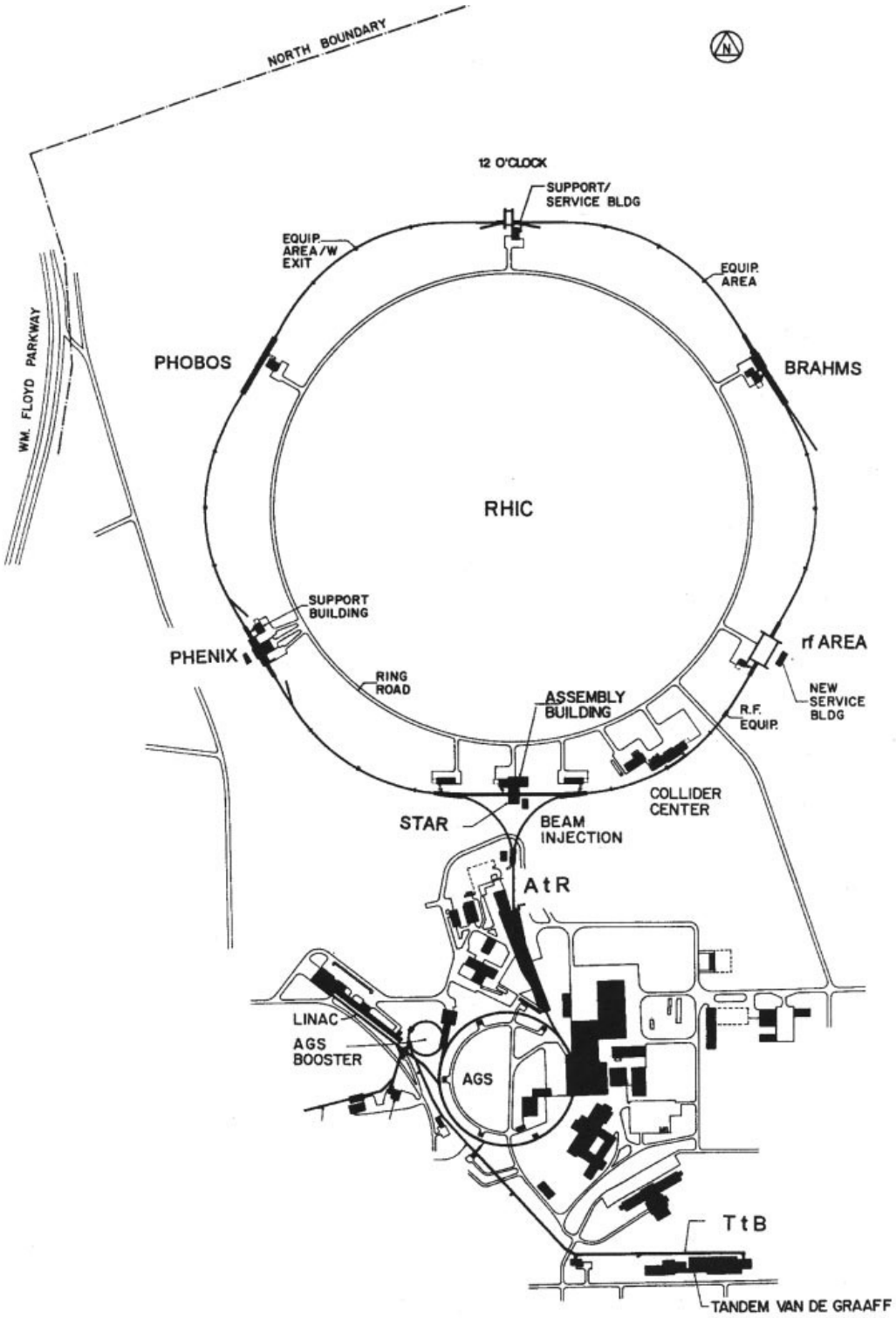

Figure 2.1: An overview of the BNL accelerator complex containing RHIC, its boosters, and sources [100].

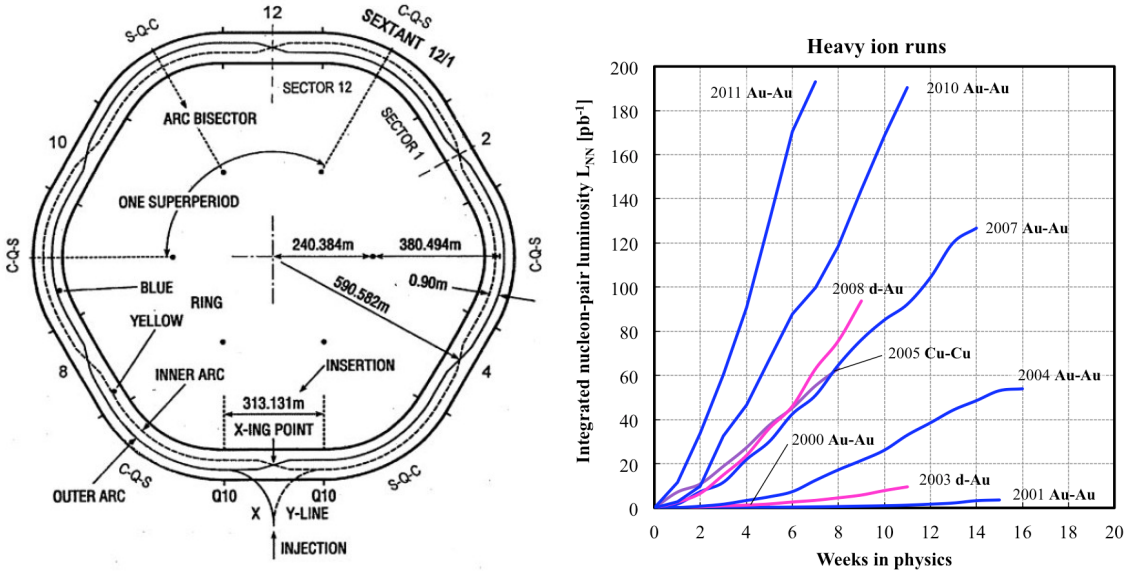

Figure 2.2: Left: RHIC geometric layout and beam lines [100]. Right: A summary of integrated luminosities for RHIC heavy-ion runs gathered from [59].

stripped to $Q = +77$ and delivered to the AGS. The tandem-booster cycle itself operated at a rate of 5 Hz, producing 16 bunches in the AGS. The AGS merged these bunches and accelerates the single bunch to 10.8 GeV per nucleon. The final two electrons are then stripped on the way to RHIC.

Each ring of RHIC consists of three inner and three outer arcs and six interaction regions joining them. Figure 2.2 (left panel) shows a more detailed diagram of the accelerator. Arcs are divided into 11 cells, with each cell consisting of a single dipole and a spool-piece assembly each containing a quadrupole and a sextupole, plus concentric correction elements. In total the arc system consists of 288 dipoles, 276 quadrupoles, 288 sextupoles, and 492 corrector magnets.

Each RHIC ring is typically filled with 60 bunches from the AGS, with each bunch containing approximately 10^9 ions. The insertion system consists of 108 dipoles and 216 quadrupoles. In addition there are 72 trim quadrupoles. These systems allow RHIC to reach up to 100 GeV per nucleon per beam.

RHIC reached its design goal of 200 GeV center-of-mass energy in Au-Au collisions in Run 2 (2001). Since then RHIC has surpassed its luminosity goals. Figure 2.2 (right panel) shows integrated luminosity numbers for all heavy-ion physics runs to date. In this paper we will be using Au-Au collision data from runs 1 and 4.

2.2 Overview of STAR

The Solenoidal Tracker at RHIC (STAR) experiment is one of four experiments located at the Relativistic Heavy Ion Collider (RHIC) at Brookhaven National Laboratory. STAR and PHENIX—the two large detector systems—are still operational. The other two experiments, PHOBOS and BRAHMS, were smaller more-specialized experiments which are no longer running.

While PHENIX was developed as a collection of specialized subsystems designed to be sensitive to specific physics signals and emphasized non-hadronic physics, STAR was designed to track as many particles as possible to obtain more general information about each event. STAR's design emphasizes hadronic physics. STAR has much in common with detectors used in high energy particle physics, being built around a large solenoid and tracking chamber with full azimuth coverage.

2.2.1 STAR detector subsystems

STAR was designed to measure many observables simultaneously with the intent of looking for signatures of a QGP phase transition. The primary design feature of STAR is measurement of hadron production over a large solid angle with high precision tracking. This is primarily achieved in STAR's large-volume time projection chamber (TPC). In addition a Silicon Vertex Tracker (SVT) for charge particle tracking close to the interaction region was part of the initial design for STAR, but it has been removed in the most recent runs. The SVT consisted of 216 silicon drift detectors (or about 13 million pixels) arranged in three cylindrical layers at approximately 7, 11, and 15 cm from the beam axis [15]. This was supplemented with a layer of Silicon Strip Detectors (SSD) which are still in place.

There is a basic diagram of the STAR detector subsystems in Fig. 2.3. The heart of STAR is the 4 m long TPC with complete 2π azimuth coverage and a pseudorapidity range

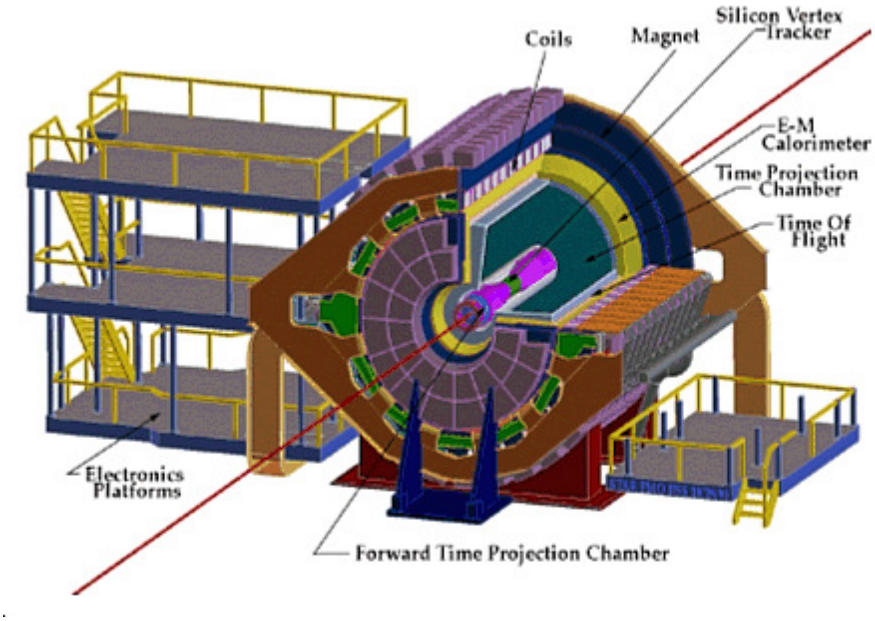

Figure 2.3: A Perspective view of the various detector subsystems in STAR [15].

$|\eta| \leq 1.8$. It provides the equivalent of 70 million voxels (3D space bins) via 136,608 channels of front-end electronics (FEE) [15]. The momentum of tracked particles is determined by the curvature of particle tracks in the 0.5 Tesla magnetic field. Another important feature of the STAR detector is particle identification by ionization energy loss (dE/dx) in the TPC. A recent upgrade to STAR has added a time of flight (TOF) system based on multigap resistive plate chambers (RPC) which greatly enhances its particle identification capabilities [128]. The TOF system extends the momentum range at which particles can be identified but was not available for the present analysis.

Additional tracking is provided in the forward region with a pair of radial-drift forward TPCs (FTPC) covering 2π azimuth and $2.5 < |\eta| < 4$. There is also an electromagnetic calorimeter (EMC) and endcap electromagnetic calorimeter (EEMC) that feature shower-maximum detectors to distinguish high momentum single photons from photon pairs produced by meson decays (not shown on the diagram).

The Zero Degree Calorimeters (ZDC) measure neutral particles produced in the direction

of the beampipe and are important for triggering as will be discussed in Section 2.3.2. The ZDCs consist of tungsten absorber plates with optical fiber connections to a PMT. Since the ZDCs are outside of the dipole magnets charged particles are deflected and can't reach them. However, neutrons produced from the breakup of the heavy-ion nuclei in a non-central collision continue along the original beam direction and reach the ZDCs. The ZDCs are unique detectors in that they measure a larger signal in peripheral collisions than in central collisions. In a central collision most of the nucleons participate in the collision and do not maintain their initial forward momentum. However an extremely peripheral collision may fail to completely break up the collision nuclei, producing fewer neutrons than a slightly more central collision. The ZDC will then measure a smaller signal for the most peripheral collisions.

The first major subsystem for triggering was the Central Trigger Barrel (CTB). That has now been replaced by the TOF system. The CTB consisted of 240 slats surrounding the TPC which measured charged particle multiplicities in 2π azimuth and $|\eta| \leq 1$. Unlike the TPC the CTB didn't do any detailed tracking, but it was a much faster detector so it could be used for triggering. Like most mid-rapidity detectors the CTB provided a stronger signal for more-central collisions, since more particles are produced.

The kinematic quantities describing the particles we measure are the particle's azimuth angle ϕ, pseudorapidity η, and transverse momentum p_t. Pseudorapidity is a spatial coordinate describing the polar angle of a particle relative to the beam axis, defined by $\eta \equiv -\ln[\tan(\theta/2)]$ where θ is the polar angle. Transverse momentum p_t is measured by the curvature of tracks in the TPC. The majority of data in used in the analysis presented in this document are based entirely on the TPC for consistency, reliability, and quantity.

2.2.2 Kinematics

The precise location of a collision event in the detector is called the event vertex. Particles produced in the event travel outwards from this vertex through the various detector subsystems. The vertex position is tightly constrained in two dimensions by the geometry of the beampipe but it can vary significantly along the beam axis.

Because of the cylindrical symmetry of the detector it is natural to separate kinematic variables into longitudinal (typically referred to as the z coordinate in a Cartesian coordinate system) and transverse quantities (the x-y plane). This is particularly important for momentum since it is measured by observing the curve of a particle track in the detector magnetic field. Due to the orientation of the magnetic field we can only measure momentum in the transverse plane. The magnitude of the momentum in the transverse plane is the transverse momentum p_t, with $p_t^2 = p_x^2 + p_y^2$. We also refer to other transverse variables that defined in a similar manner.

It is conventional in particle physics to use a rapidity y_z for the longitudinal momentum p_z. Rapidity is a relativistic measure of speed constructed such that rapidities in parallel directions are simply additive. The small-rapidity limit is equivalent to non-relativistic speed. The formal definition of rapidity is a hyperbolic angle

$$y \equiv \tanh^{-1} \frac{v}{c}. \tag{2.1}$$

In particle physics the following definition is commonly used for longitudinal rapidity

$$\begin{aligned} y_z &= \frac{1}{2} \ln \left(\frac{E + p_z}{E - p_z} \right) \\ &= \ln \left(\frac{E + p_z}{m_t} \right), \end{aligned} \tag{2.2}$$

where E is the total energy and $m_t^2 = m^2 + p_t^2$. This variable is so common in high-energy physics it is often simply referred to as "rapidity" and represented with just y. However we use rapidity y_t in the transverse direction as well so the distinction is important. Transverse rapidity y_t is calculated from

$$y_t = \frac{1}{2} \ln \left(\frac{E_t + p_t}{E_t - p_t} \right). \tag{2.3}$$

In the case of longitudinal rapidity, if $E \gg m$—meaning a highly relativistic particle—then we can make the approximation $E \approx |\mathbf{p}|$, which leads to the definition of pseudorapidity η,

$$\eta = \frac{1}{2} \ln \left(\frac{|\mathbf{p}| + p_z}{|\mathbf{p}| - p_z} \right). \tag{2.4}$$

However it is much more common to see pseudorapidity written in the form:

$$\eta \;=\; -\ln\left[\tan\left(\frac{\theta}{2}\right)\right], \tag{2.5}$$

where θ is the polar angle. In this equation we see that while pseudorapidity is derived from a measurement of momentum it actually doesn't depend on the momentum magnitude at all. Instead it is a measure of the polar angle that the particle was emitted with respect to the beam axis. This is because for large-momentum particles their speed in the lab frame is always approximately c. What is relevant is simply the direction of the momentum vector which depends only on the particle's relative momentum in the transverse and longitudinal directions, not the total momentum of the particle.

If particles are emitted perpendicular to the beam ($\theta = \pi/2$) then $\eta = 0$, while in the limit of particles emitted near the beam axis η approaches $\pm\infty$. It is common to use η as an angular coordinate along with azimuth angle ϕ for describing the particles produced in a collision. Since longitudinal momentum cannot be measured directly in experiments like STAR it can be tempting to make the approximation $y_z \approx \eta$. However, this relationship only holds if the total momentum of the particle is sufficiently large and the total momentum of large-η particles is often poorly known. Large η does *not* imply large y_z in the absence of knowledge of p_t.

2.2.3 Centrality

Collisions of heavy-ions are different from collisions of elementary particles because heavy-ions are large complex objects, and it is not necessary for all of the atomic nucleus to be involved in the collision. If we think about the collisions in terms of an impact parameter b, then a completely central $b = 0$ collision is an infinitesimally unlikely event. In most collisions not all of the particles that make up the nucleus will actually participate in the collision. If we model a nucleus as a solid sphere of radius R then b should range from 0 for the most central collisions to $2R$ for the most peripheral collisions.

When we describe collision energies of heavy-ions we use center-of-mass per nucleon-nucleon collision, or $\sqrt{s_{NN}}$. The full center-of-mass energy of a nucleus-nucleus collision would actually be that number times half the number of participant nucleons. Thus the

total energy of a RHIC collision depends directly on the centrality of that collision. But total energy is not the relevant quantity for most RHIC physics, as that energy is spread over many particles and distinct binary collisions. But one quantity which varies with total energy is the observed multiplicity of particles produced in an event. Because the total energy of a collision varies dramatically with centrality so does the multiplicity. This makes multiplicity a useful proxy for centrality.

Impact parameter b is an easy to understand description of heavy-ion centrality from a theoretical standpoint but is not actually observed directly in a collision. As a result there are several other centrality measures in use. The least model-dependent approach is to simply observe the multiplicity distribution over many events and then divide the distribution into bins corresponding to fractions of the total cross section. For instance, if 10% of events have a multiplicity greater than 800 and 20% have a multiplicity greater than 700, then events with a multiplicity larger than 800 are in the 0-10% bin, events with a multiplicity between 700 and 800 are in the 10-20% bin, etc. For this centrality measure 0% corresponds to the most central events and 100% corresponds to the most peripheral events.

Other centrality measures in use are model-dependent, such as the number of nucleons that participate in the collision, n_{part}, and the number of N-N binary collisions (individual nucleon-nucleon collisions), n_{bin} (also sometimes denoted n_{coll}). These parameters are estimated using a Monte Carlo Glauber model [131]. Nucleons are randomly positioned within the two spherical nuclei based on their nuclear density profiles, and the nuclei are overlapped for a given impact parameter. If any two nucleons are within the minimum distance for their inelastic scattering cross section they are assumed to interact.

n_{part} and n_{bin} scale differently because a given nucleon can actually experience multiple binary collisions if the part of the nucleus it passes through is multiple nucleons thick. Thus, the ratio of n_{bin} to $n_{part}/2$ can actually be interpreted as the average path length through the colliding nuclei. We define this ratio as ν and show in Chapter 6 that is a useful centrality measure with convenient scaling properties.

2.3 Data Acquisition

2.3.1 DAQ system

The STAR data acquisition system (DAQ) must receive data from multiple detectors with a wide range of readout rates. The raw data size of a single even can be as high as about 200 MB and the original DAQ system processed input event rates of up to 100 Hz [15]. Subsequent upgrades to the DAQ system now allow for rates of up to 1000 Hz.

RHIC beams are optimized so that a collision is likely to occur in each bunch crossing. Since RHIC began operations the rate of bunch crossings has increased significantly as improvements have been made to the accelerator. Bunch crossing rates can now approach up to 10 MHz. This is a much higher rate than STAR is capable of recording, so triggers are necessary to reduce the rate of *recorded* data.

The TPC, FTPC, and SVT (for those runs when it was present) together produce about 80 MB of information per event. Even after the triggers DAQ event rates in the hundreds of hertz mean that this is too large an amount of information to write to tape for permanent storage. The DAQ system can optimize the raw data the detectors produce and dramatically reduce this data volume to around 30 MB/s [124]. This is a more manageable quantity.

2.3.2 Triggers

The purpose of a trigger system is to use low-level hardware and software on the actual detector to reduce the data volume to a level that can be processed by the DAQ system. Events can be thrown out at random but there would then be no reason to have an accelerator event rate higher than what the DAQ can record. Triggers are used to select characteristic signatures of rare events, boosting their contribution to the number of recorded events beyond their normal likelihood. In this document we only discuss minimum-bias data, produced from a simple trigger designed only to determine whether or not an event has occurred. Minimum bias events do occur with a greater frequency than the DAQ can process so the number is reduced with a prescaler.

Triggers work in stages, with initially very fast detectors and trigger systems that can reduce the data volume to the point where more time can be spent to make a decision

about each event. Level-0 triggers use fast detectors and issue an event trigger immediately. Following that there is a period of several milliseconds required for detectors to read out and digitize data. Level-1 triggers operate during this time period and spend 100 μs to analyze the event with more finely-grained criteria. Level-2 triggers spend 5 ms. If an event passes all of these triggers it proceeds to Level 3, which is a higher level analysis that involves complete online reconstruction of the event [33]. This is done with a rack of CPUs integrated within the DAQ system.

The fastest detectors are the Zero Degree Calorimeters (ZDCs) and Central Trigger Barrel (CTB), the latter having been upgraded to the TOF system in more recent runs. The data used in the present analysis was taken using the CTB system. Even for minimum-bias data we wish to ascertain that there was an actual event recorded in the detector, so the basis for a minimum-bias trigger is coincidence of neutrons in the two ZDCs and a minimum threshold in the CTB. As mentioned in Section 2.2.1, the ZDC and CTB signals tend to have opposite dependence on centrality. This dependence is shown in Fig. 2.4. The minimum-bias event rate should be nearly as high as the bunch-crossing rate which can be much higher than what the STAR DAQ can process. In any given data-taking run a portion of the events will be minimum-bias, reduced by a prescaler, while triggers for less common events are run in parallel.

2.3.3 Data Sets

Data collected with the STAR detector is organized into different data sets based on the type of collisions, year of the run, and trigger conditions. While there are many trigger types—typically searching for rare events like very high-p_t jets—this analysis focuses exclusively on minimum-bias data.

Minimum-bias data are useful for correlation analysis and studies of collective behavior. By nature collective behavior should occur in most events so there is no need to trigger for special event characteristics. In fact, using such a trigger could introduce biases that make the analysis more difficult. STAR has triggers for central collisions as well, but we wish to understand the entire centrality evolution of the system from the most peripheral to the

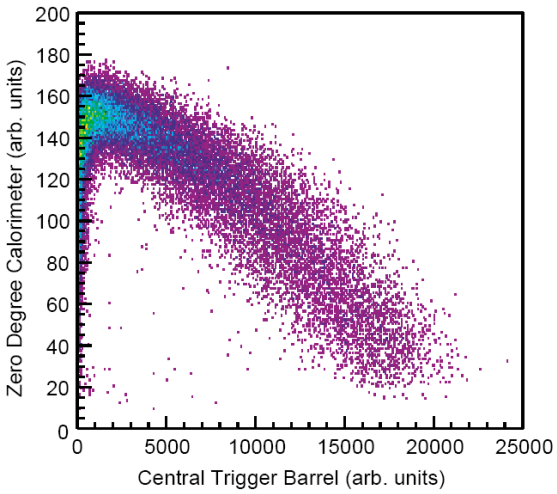

Figure 2.4: Summed pulse heights for events in the ZDC and CTB [15].

most central events. For this analysis it makes more sense to use a trigger that keeps all centralities and then divide events into centrality classes in the analysis itself.

In this analysis we discuss certain cuts (conditions), including event cuts. But cuts are distinct from triggers because they are performed in a high-level analysis after the data have been processed. Given the strict time limits imposed by a triggering scenario the types of analysis that can be performed are limited.

2.4 The STAR TPC

Since the STAR time projection chamber (TPC) is the most important detector subsystem in STAR and the system primarily responsible for all of the data that will be used in this analysis it is necessary to describe the TPC technology in more detail. The first major application of a TPC was the PEP-4 detector at SLAC. Prior to the STAR experiment large volume TPCs were used with great success in heavy-ion physics as part of the NA49 detector at the SPS.

The STAR TPC was the largest TPC in the world when constructed, though it has now been surpassed by the ALICE experiment at the LHC. TPCs are useful in particle

and nuclear physics because they can accurately track many particles simultaneously with minimal material budget. As they are entirely gas-filled there is a much lower likelihood that particles being measured undergo hard scatterings within the detector material when compared to most competing technologies.

2.4.1 About TPCs

TPC operation is based on digitizing tracks deposited in the TPC chamber as fast charged particles pass through it. These particles ionize the gas in the TPC. The secondary electrons released in the ionization process then drift along a uniform electric field to readouts (in STAR these readouts are on the end caps). The location where a drift electron hits the end cap provides information about its position in two dimensions (x, y). The third coordinate (z) comes from the drift time.

It is much more economical to fill a large volume with gas to make a TPC than to build a similar sized solid state detector, such as a silicon detector. This has practical applications for physics as well. Standard tracking detectors all measure a particle's scalar momentum by the amount its track curves in a magnetic field. For higher momentum resolution it is necessary to have either a stronger magnetic field (which can cause low-momentum particles to spiral) or a larger physical detector volume so the curvature in the track is more discernible. The TPC excels at covering large volumes, and with a low material budget can also track very low-momentum particles that might not make it through other detectors.

The major limitation of TPCs is the drift time; they are inherently slow detectors. Not only are they unsuitable for triggering but with the collision rates of modern particle physics experiments it is normal for tracks from several distinct events to be drifting in a TPC simultaneously. This "pileup" complicates the data analysis because it is necessary to figure out which tracks belong to which events.

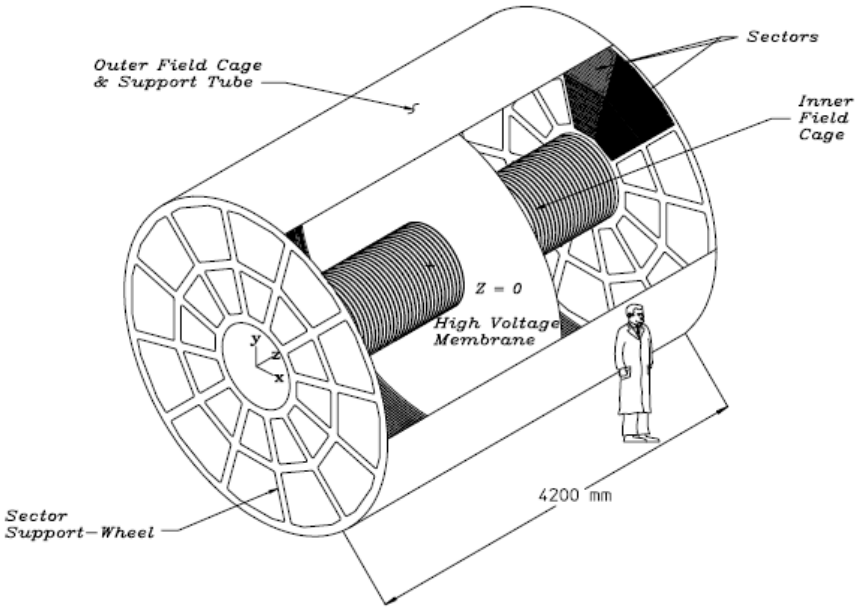

Figure 2.5: Diagram of the STAR TPC [52].

2.4.2 STAR TPC design

Details about the STAR TPC design can be found in [52]. The STAR TPC is a 4.2 m long cylindrical volume with the cross section of an annulus with inner radius 50 cm and outer radius 200 cm. It is separated into east and west halves by a central membrane. Each half is further divided into 12 wedge-shaped sectors and each sector is split into inner and an outer subsectors. See Fig. 2.5.

Electrons produced in the TPC gas volume drift in a uniform electric field of 135 V/cm. The central membrane operated at 28 kV and the end caps at ground. This means electrons always drift away from the central membrane to the anodes at the endcaps.

The TPC volume is bounded by the Inner Field Cage (IFC) and Outer Field Cage (OFC). The field cage cylinders consist of a series of equipotential rings, constructed from 183 2 MOhm resistors. The inner field cage is constructed out of aluminum to reduce the chance of multiple scattering at the inner radius. The outer field cage was constructed out of copper for simpler electrical connections and construction. Scattering in the detector is

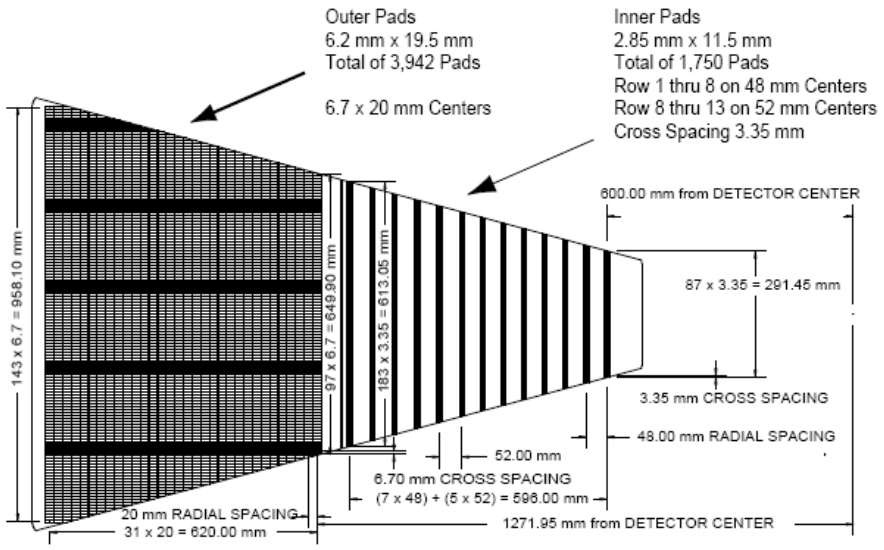

Figure 2.6: Diagram of a single sector of the STAR TPC [52].

minimal. The inner field cage is only 0.5% of a radiation length. The outer cage is 1.3% of a radiation length, which is comparable to the gas in the detector.

The TPC is filled with P10 gas, which is a mixture of 90% argon and 10% methane. It is a common gas for TPCs and has a fast drift velocity that peaks with a relatively low electric field. The gas is held 2 mbar above atmospheric pressure which prevents contamination from electron absorbers which can interfere with the drift electrons. Common electron absorbers are water, which is kept at less than 10 ppm, and oxygen which is kept at less than 100 ppm.

Drifting electrons are measured in the endcap readout which uses Multi-Wire Proportional Chambers (MWPC) with readout pads. There are 136,608 such pads in the detector. A diagram of a single TPC sector is given in in Fig. 2.6. Drifting electrons induce an avalanche when they approach the thin anode wires. The avalanche provides an amplification factor of 1000-3000. Image charge is spread over several adjacent pads, allowing for accurate reconstruction of the original track position to within a small fraction of a pad width.

The anode field wires are complemented by a ground grid plane in order to terminate

the field in the avalanche region and provide additional shielding for the pads. This ground grid is located 2mm from the inner subsector and 4mm from the outer subsector. There is also a gating grid, 6mm from the ground grid, which acts as a shutter to control the entry of electrons from the TPC drift volume to the anode planes. It can be made transparent to electrons while events are being recorded and block them otherwise.

The TPC magnet coils carry up to 4500 A of current and consume 3.5 MW of power to produce a maximum field strength of 0.5 T. A detailed description of the TPC magnet is given in [65]. It consists of 30 flux return bars, four end rings, and two poletips. Ten 5.3 m inner diameter coils create the magnetic field with two space trim and two poletrip trim coils to help maintain field uniformity. The magnet weighs 1100 tons with 272 tons of supporting structure

2.4.3 STAR TPC Performance

The TPC's theoretical maximum acceptance of high momentum particles perpendicular to the beam axis is 96%, with some tracks lost in sector boundaries, but a fiducial volume cut excludes hits on the outermost pads which reduces the acceptance to 94%. Though exact running conditions vary, bad pads and dead channels as well as software issues like track merging can further reduce the acceptance to 80-90% depending on the run [52].

Since the z-coordinate of a particle's position is determined by drift time the drift velocity of electrons in the TPC must be known to within 0.1%. Variations in the drift velocity can be caused by the gas mixture, temperature, pressure, and electric field variations. For calibration purposes a narrow ultraviolet laser beam is split with many small mirrors made from glass rods with a 45 degree cut and covered in a 100% reflective dielectric coating in order to produce 252 laser beams that sample each half of the TPC [5]. These laser beams imitate charged particle tracks. Since the position of the lasers is known they make an effective calibration tool. Any errors affects track curvature and therefore particle scalar momentum. The relative error between a track model fit and a point is 50 μm. The absolute error for any single point is 500 μm.

It is possible to estimate a primary vertex from the global average of all event tracks to

within 0.3 mm for central collisions [52]. This can help to improve momentum resolution and isolate secondary vertices. Transverse momentum is determined by projecting a track to the (x, y)-plane and then fitting a circle through both the hit points within the TPC and the primary vertex. An example of a reconstructed event for a central collision in the TPC was shown in Fig 1.1.

The TPC is the heart of the STAR experiment and is a very powerful and versatile detector. It is capable of measuring positions and momentum from a handful of tracks in an extremely peripheral collision to over a thousand tracks in a central Au-Au collision with great accuracy. TPC data will be the basis of the analysis discussed throughout this dissertation.

Chapter 3

THE RHIC CONFLICT

3.1 Two Components

Heavy-ion collisions are complex and there are many different physical processes that contribute to the final-state properties we observe in our detectors. The most common classification we see in heavy-ion physics is the division of certain event properties into distinct "hard" and "'soft" components. Different theoretical calculations and measurement techniques have been developed to analyze these different regimes. The interplay of these two components is the source of much conflict and misunderstandings in the field of heavy-ion physics. This will be a recurring theme throughout this dissertation.

3.1.1 Motivation

Hard processes are processes with a large momentum transfer to the hadron system in which distances small in comparison to the dimensions of hadrons are important. Hard processes have been extensively studied outside of the field of heavy-ion physics as well. Examples include—but are not limited to—deep inelastic scattering of leptons on hadrons, e^+-e^- annihilation into hadron jets, and the production of large p_t partons in proton-proton collisions which fragment to produce jets. The last example is the hard process that is most closely resembles heavy-ion physics. Fragmentation in e^+-e^- is also quite important and its relationship to hadronic collisions will be discussed in Chapter 8.

Soft processes in nuclear collisions are typically collective or statistical properties of low-p_t particles. But that is a broad category. We will find that exactly what constitutes "high" and what constitute "low" p_t varies significantly depending on the specific physical process and historical context. In heavy-ion physics "soft" processes is something of a catch-all term for any particles that were *not* produced from a hard scattering of two partons that underwent fragmentation. In most RHIC theories soft physics is the domain of hydrodynamic

calculations, though there are other low-p_t effects as well such as HBT correlations.

It was conjectured some time ago [70] that particle production in high-energy nucleus-nucleus collisions would be dominated by hard processes. But measurements at the SPS [112] remained approximately consistent with scaling based on the number of participant nucleons n_{part} (typically associated with soft physics) and the "wounded nucleon" model [68]. There are deviations from perfect n_{part} scaling even at the SPS, as the WA98 Collaboration observed scaling of $n_{part}^{1.08}$ in 158 GeV (fixed target) Pb-Pb collisions [38]. RHIC physics is at high enough center-of-mass energy to see completely new types of energy scaling come into play.

There is a vested interest in the separation of hard and soft components because many authors believe (i.e., [146]) that properties of the soft particles are properties of the QGP matter produced in the collision while the hard component exists outside of this theory. From this perspective hard particles are just a background produced from jets that exists on top of the properties we do wish to study at RHIC. In this document we will find that both components are essential parts of RHIC collisions and the separation of the two components is difficult but possible with appropriate methods.

3.1.2 Heavy-Ion Multiplicities

If we start with the simple model that a heavy-ion collision is composed of several independent nucleon-nucleon collisions then each collision can produce some combination of soft particles and hard particles in the final state. The Kharzeev-Nardi description of heavy-ion multiplicities starts with the assumption that soft processes scale with the number of participant nucleons n_{part} and hard processes scale with the number of binary collisions n_{bin} to give us two distinct components [120]

$$\frac{dn}{d\eta} = (1-x)n_{pp}\frac{\langle n_{part}\rangle}{2} + xn_{pp}\langle n_{bin}\rangle\,, \tag{3.1}$$

where x is the fraction of the multiplicity measured in p-p collision n_{pp} due to hard processes and $(1-x)$ is the remaining fraction from soft processes. The value of x must be determined phenomenologically. The simplest assumption we can make is that x is a constant value, however it is also possible for it to vary with centrality or other conditions.

This two component model is found throughout the field of heavy-ion physics. It is referenced in much of the theory in the field as well as event generators such as HIJING [175]. It is a convenient model because the hard component can be simulated based on well-studied pQCD processes with a sound theoretical basis while the soft component—which is more difficult to predict from QCD calculations—can be based on simpler phenomenological models.

3.1.3 Two Components of Proton-Proton Collisions

While this distinction between soft and hard physics is often discussed in heavy-ion collisions, it should be noted that even protons are composite objects as they are made of quarks and gluons and get most of their mass from binding energy. Even in proton-proton collisions there is a distinction between hard scattering of partons and the breakup of the rest of the proton ("the underlying event"). This means that proton-proton collisions can also exhibit separate hard and soft components.

This was clearly shown in a detailed analysis that STAR conducted in [24] of the multiplicity dependence of spectra data in proton-proton collisions. Data are classified according to the observed charged multiplicity in one event $\hat{n}_{ch}$, as see in the first two panels of in Fig. 3.1, on p_t and transverse rapidity y_t. While p_t is a more conventional variable, by nature it forces the majority of the data to the low-p_t edge of the plot. y_t presents a more balanced picture since $y_t \sim \ln p_t$ as p_t gets large. We make the assumption that events with hard scatterings should tend to produce more particles than events without. The solid lines show a soft component reference that will be explained below. In the last panel the spectra data on y_t are all given the same normalization and we see a common underlying shape.

Under the assumption that the average multiplicity variation between events is due to the hard component we can define the soft component as the limiting case where the where the observed event multiplicity goes to zero. A Lévy distribution is a good choice for the soft component shape [180] and appears to match the data well [24]:

$$S_0(m_t;\beta_0,n) = A_s/(1+\beta_0(m_t-m_\pi)/n)^n. \tag{3.2}$$

The pion mass m_π is being assumed for all unidentified particles. Parameters β_0 and n

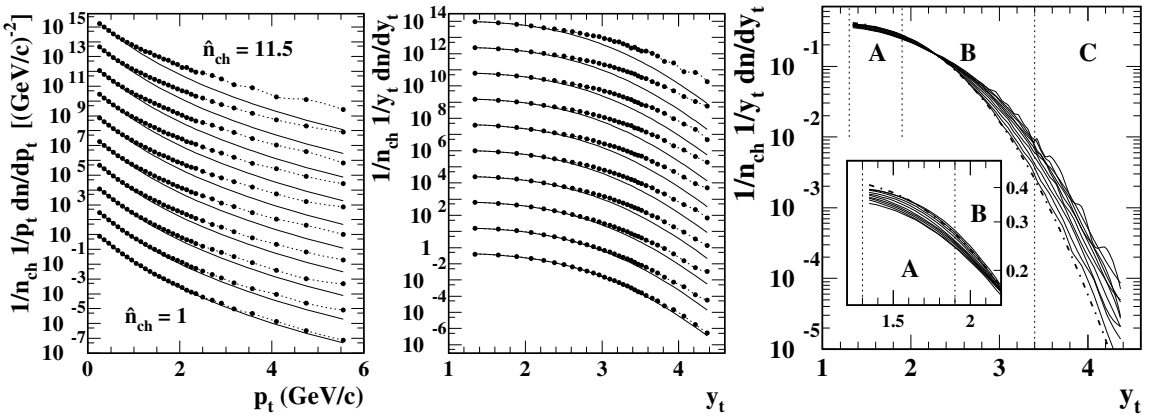

Figure 3.1: First panel: Measured spectra in proton-proton collisions on p_t organized into ten different multiplicity classes. The solid curve is a soft component reference. Second panel: The same data plotted on y_t. Third panel: The different multiplicity classes are normalized and a common underlying spectrum shape is revealed [24].

are fit to the data while the amplitude A_s is fixed by normalization. The next step of the analysis is to subtract out the common soft component shape, as seen in Fig. 3.2 (left panel).

Once the soft component has been subtracted there is what appears to be a Gaussian of varying amplitude in the remaining spectra. There is some deviation for low-p_t in the low-multiplicity classes, but there are also significant uncertainties there. In Fig. 3.2 (right panel) the hard components of the different multiplicity classes have been given a common normalization.

What this demonstrates is that hard the proton-proton spectrum can be reasonably described by a simple formula. The functional form of the hard component does not very with multiplicity, only its amplitude. So if we describe the hard component by

$$H_0(y_t; \bar{y}_t, \sigma_{y_t}) = A_h \exp\left(-\frac{1}{2}\left[\frac{y_t - \bar{y}_t}{\sigma_{y_t}}\right]^2\right), \tag{3.3}$$

then all of the proton-proton spectra can be described by

$$\frac{1}{y_t}\frac{dn}{dy_t} = n_s(\hat{n}_{ch})S_0(y_t) + n_h(\hat{n}_{ch})H_0(y_t), \tag{3.4}$$

where n_s and n_h are the soft and hard component multiplicities. The components S_0 and

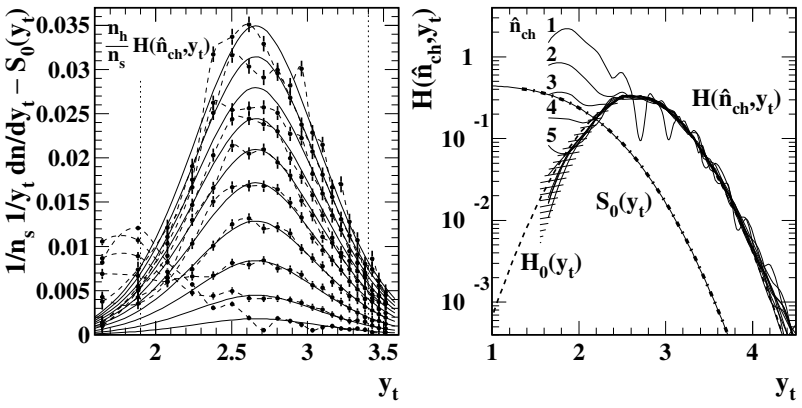

Figure 3.2: Left panel: Spectra data with the soft component subtracted. Right panel: The hard components of the spectrum [24].

H_0 have only two parameters each and yet this simple model is a better fit to the data than the standard 30-parameter power-law model [24].

There is additional evidence in favor of a two-component interpretation of proton-proton data in the form of two-particle correlations. The two-particle analogue of spectra would be a correlation in (p_{t1}, p_{t2}) space. These types of correlations will be explained in more detail in Chapter 5, but for now just consider the density of particle *pairs* to be the two-particle analogue of a single-particle density. Similar to how a spectrum can be constructed from a histogram of observed particle p_t values, a correlation can be constructed from a histogram of pairs of particle (p_{t1}, p_{t2}) values. It is more convenient to work in (y_{t1}, y_{t2}) space for reasons discussed in Sec. 2.2.2, which yields the two-particle $y_t \times y_t$ correlation from [139] shown in Fig. 3.3 (left panel).

The existence of two distinct components in the two-particle space is visually obvious. There are two distinct peaks that are separated well enough that we can isolate them with a simple diagonal cut in (y_{t1}, y_{t2}). The second and third panels of Fig. 3.3 give the corresponding *angular* correlations for the two regions defined by this cut. The angular correlation is constructed by projecting the four dimensional angular space $(\eta_1, \eta_2, \phi_1, \phi_2)$ to the difference variables (η_Δ and ϕ_Δ). A more detailed analysis of correlations will have to wait until after we have introduced the complete methodology in Chapter 5. But even

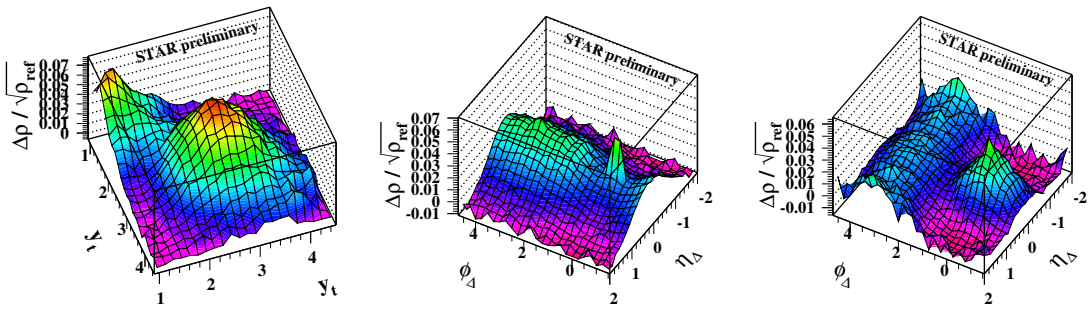

Figure 3.3: First panel: Longitudinal (soft) and transverse (hard) fragment correlations on (y_{t1}, y_{t2}). Second panel: Soft fragment angular correlations on difference axes $(\eta_\Delta, \phi_\Delta)$ Third panel: Hard fragment angular correlations [139].

on a qualitative level it should be clear that the angular correlations in the two different $y_t \times y_t$ regions have very different properties. The "high-y_t" region exhibits exactly the sort of angular correlation structure we expect from jets—a narrow jet peak and an away-side ridge from momentum conservation—while the low-y_t region appears to have contributions from a variety of sources, including longitudinal fragmentation, HBT correlations and e^+-e^- pair production. While we are primarily concerned with the study of hadrons the effect of e^+-e^- pair production from photons can't be completely eliminated by cuts.

This clean separation of the two physical regimes is only possible in the two-particle space. The cut we made is diagonal in (y_{t1}, y_{t2}), along the difference axis. The single-particle spectrum is related to a projection of the two-particle correlation to y_{t1} or y_{t2} which implies that there should be considerable overlap between the two components. Of course it is possible to make a single-particle p_t cut above the soft component but in order to eliminate soft contributions it would also have to be above the mode of the "hard" peak. Meaning that in order to completely avoid soft contributions with a cut in the one-dimensional space it would be necessary to cut out the majority of the particles produced in hard processes as well. This is consistent with the spectra data see in Fig. 3.1 and Fig. 3.2. The separation into hard and soft components was based on the *shape* of the spectra but there was still considerable overlap between the components.

Actually, there is no fundamental reason why such a clean separation should be possible

even in the two-particle space. We will see in heavy ions that the "hard" component softens and there is considerable overlap with the "soft" particles even in the two-particle space. There may well be distinct physical processes contributing to the final correlations we observe in heavy-ion collisions, but there is no basis for believing that the p_t distributions of these processes won't overlap. To really understand heavy-ion collisions a more systematic approach is necessary. We will introduce such an approach in Chapter 7.

3.2 The Soft Component

The previous section established the importance of hard and soft components in heavy-ion collisions so now we will explore some of the existing theory and observations describing each component. Most theories describing the soft component fall into the category of hydrodynamics. The interpretation of heavy-ion collisions in terms of hydrodynamic flow is a major part of heavy-ion physics theory and it has also influenced the development of experimental observation techniques.

3.2.1 Theory

Hydrodynamic theories—in which a thermalized parton flux leads to large energy and pressure gradients which drive hydrodynamic flows [107]—dominate discussions of soft physics at RHIC. The basic theory behind hydrodynamics was presented in Sec. 1.2. There are additional physics present in the soft regime as well, for example Hanbury Brown Twiss (HBT) correlations but these are outside the scope of this work.

Hydrodynamic flows—elliptic flow in particular—are the most important physical observables predicted by hydrodynamic theory. Anisotropic flow is considered by many to be a fundamental part of hydrodynamic theory since it is unique to systems with rescattering. According to hydrodynamic theory if a system does not produce some sort of medium with rescattering it should be impossible to have an elliptic flow term. Large anisotropic flow is not observed in proton-proton collisions, consistent with this expectation.

The hydrodynamic limit is where complete thermalization is assumed. In this case the mean free path is much smaller than the geometric size of the system. This implies that the centrality dependence of hydrodynamic processes in this regime should be completely

governed by the initial geometry of the system [172]. This geometry is typically described in terms of the number of participating nucleons and the eccentricity of the overlap region of the two colliding nuclei. These factors change drastically with centrality.

The other extreme is the low density limit (LDL) where dynamic thermalization is not expected and it produces different predictions for the centrality dependence of physics such as elliptic flow. In LDL the mean free path is comparable or larger than the system size. In the extreme limit of infinite mean free path there should be no azimuth anisotropy [172]. LDL can be thought of as the first correction to the collisionless limit, with only small changes in particle momenta from rescattering during the evolution of the system. This results in a value of v_2 proportional to the eccentricity of overlap between the colliding nuclei as well as the initial particle space density (which determines the probability of rescattering) [103].

The QGP phase transition was expected to be accompanied by critical fluctuations [151]. The idea is that a system evolving near the boundary of a phase transition should develop significant dynamical fluctuations away from its mean thermodynamic properties. However, the RHIC program has failed to produce any compelling evidence for critical fluctuations.

The introduction of finite viscosity to hydrodynamic models complicates the calculations but it has been done. It has been found that any viscosity will reduce v_2 and make it difficult to explain the large values that have been experimentally observed. The conclusion that can be drawn from this is that there is very little viscosity in the QGP produced at RHIC—it must be at or near the theoretical lower limit—and thus RHIC creates a "perfect liquid" [105, 82]. Of course this is predicated on the validity of hydrodynamic models to the data they are attempting to describe.

3.2.2 Observables

One method proposed to demonstrate the existence of QCD matter is to measure trends of *global event variables*, statistical measures formulated by analogy with macroscopic thermodynamic quantities and based on integrals of particle yields over kinematically accessible momentum space. Corresponding fluctuation measures have been formulated for the event-wise

mean p_t, $\hat{p}_t$ ("temperature" fluctuations), the K/π ratio (chemical or flavor fluctuations), and the baryon to meson ratio (another type of chemical fluctuation) [153, 102, 97, 156, 7].

Large-scale angular structure of the event-wise particle distribution is another global feature. The components of angular structure can be described by low-order spherical or cylindrical harmonics or "flows." The basic assumption is that such structure represents *collective* motion of a thermalized medium, and hydrodynamics is therefore an appropriate description. Observation of larger flow amplitudes is therefore interpreted by many to provide direct evidence for event-wise thermalization in heavy ion collisions [74]. Given those assumptions each collision event is treated separately. Event-wise angular distributions are fitted with model functions associated with collective dynamics. The model parameters are interpreted physically in a thermodynamic (i.e., collective, thermalized) context.

At Bevalac energies there is a large observed sideways flow [143], but the mechanism is very different from what we see at RHIC energies. For these low-energy collisions we are seeing "squeeze-out" of the constituent nucleons rather than forming new particles from some sort of QGP. One qualitative difference between this kind of flow and what we observe at RHIC is that the direction of the flow relative to the reaction plane is different.

One of the initial analysis tools used at the Bevalac was the directivity vector in the transverse plane

$$[83]\tilde{\vec{Q}}_1 \equiv \sum_i^n w_i \vec{p}_{ti} = \sum_i^n w_i p_{ti} \vec{u}(\phi_i) = \tilde{Q}_1 \vec{u}(\Psi_1), \tag{3.5}$$

for individual partile momenta $\vec{p}_{ti}$, a weight w_i, unit vectors $\vec{u}$, and where Ψ_1 is an estimate of the true reaction-plane angle. The weights w_i are set to ± 1 corresponding to whether the particles are in the forward or backward halves of the detector. Particles in a mid-rapidity region are often excluded.

This quantity is most closely related to what is now called directed flow, or v_1. Unlike v_2—which was introduced in Chapter 1 and is related to elliptic flow—v_1 is expected to be zero when measuring particles at the same pseudorapidity. Nonzero values are obtained by comparing particles in forward and backward regions of the detector. The response of the medium is expected to be proportional to the driving force so the ratio v_2/ϵ is

another quantity of interest. Here ϵ is the eccentricity which will be defined in Sec. 4.3 and describes the initial collision geometry. In the LDL limit of ideal hydrodynamics $v_2 \propto \epsilon$ [134]. Chapter 4 will go into detail about the various methods used for estimating flows with a focus on v_2. Elliptic flow observations will be discussed extensively in Chapters 6 and 7 and are a major focus of this dissertation so we will not go into more detail about them them here.

Predictions of critical point fluctuations have been difficult to verify in part because of significant non-critical fluctuations in processes unrelated to a thermodynamic phase transition [151]. The challenge is to devise a method for measuring fluctuations that minimizes experimental artifacts and can discriminate between statistical and non-statistical effects. While global fluctuation measures have failed to provide compelling evidence for critical point fluctuations the development of fluctuation theory did lay the groundwork for correlation analysis due to the relationship between correlations and fluctuations that will be discussed in Chapter 5.

Another common field of study in heavy-ion physics is quantum correlations or HBT. HBT is named for astronomers R. Hanbury Brown and R. Q. Twiss who measured the size of stars with interferometry. HBT correlations are seen between identical particle types at small momentum values and this is to infer space-time dimensions of the particle emission source [126]. While HBT correlations are certainly a real effect, we will see in Chapters 6 and 7 that they are dwarfed by other correlation sources.

3.3 The Hard Component

There is little dispute that at RHIC energies QCD plays a role in heavy-ion collisions. It is, after all, the fundamental theory for strong interactions. But QCD theory is non-abelian and it is difficult to calculate observable quantities within the theory outside of very specific limiting cases. Most QCD calculations are therefore either high-energy perturbative cases, effective field theories, or lattice QCD approximations. Hard scatterings are one type of QCD process that has a long history of being well-described by perturbative QCD theory. But are vacuum QCD calculations applicable to RHIC collisions?

3.3.1 Theory

At higher multiplicities, particle production from a pair of protons colliding at RHIC energies is dominated by jets. Even in heavy-ion collisions jets should play some role, though there is debate over how extensive that role is. There is ample evidence for high-energy triggered jets even in nuclear collisions but it has been suggested that the bulk of particle production at RHIC could from recombination of quarks in the QGP medium rather than fragmentation [96]. Hadron production in a QGP-dominated system can differ significantly from in vacuum. If there really is a plasma of quarks and gluons created then partons can form hadrons by combining with quarks present in the plasma. This effect is expected to be most significant for intermediate momentum hadrons and since this recombination process favors the production of baryons such as protons it can affect the proton to pion ratio [98].

On the other hand QCD theory calculations have predicted that an abundance of soft gluons (minijets) should be produced in relativistic collisions at RHIC [114]. Copious gluon production may drive formation of the colored medium in heavy ion collisions and global hydrodynamic phenomena [132, 133]. However, the degree of equilibration of minijets in heavy ion collisions remains uncertain theoretically and experimentally. We should therefore search for and study remnants of *low-*Q^2 (energy scale $Q \sim$ 1 - 5 GeV) partons in single-particle and two-particle distributions of final-state hadrons. As we will see in Chapter 8, low-Q^2 fragmentation is related to local parton-hadron duality (LPHD).

Flow and QCD need not be irreconcilable since copious gluon production could drive formation of the colored medium in heavy ion collisions and global hydrodynamic phenomena [132, 133]. But the degree of equilibration of minijets in heavy ion collisions remains uncertain both theoretically and experimentally. A non-equilibrated system can produce very different results from the flow-centric hypothesis. With so many disparate theories advancement needs to come from experimental observables. The next two sections will make a case for the importance of jets—especially minijets—at RHIC.

3.3.2 Observables

The phenomenon of jets is unusual in QCD in that it can be calculated accurately theoretically but is also relatively easy to measure experimentally. Jets are therefore one of the most important observables in QCD. Initial measurements of two-particle angular correlations in p-p collisions at Fermilab (fixed target) and the CERN ISR on momentum subspace (η, ϕ) (pseudorapidity and azimuth) [179] were described in terms of longitudinal (string) fragmentation [53]. Jets—correlated fragments from hard-scattered partons—were first observed at larger p_t and $\sqrt{s}$, establishing the nature of hard parton scattering and the validity of perturbative QCD (pQCD) [55]. A pioneering study of two-particle fragmentation functions in LEP e^+-e^- collisions is described in [19] (*cf.* a related theoretical treatment in [93]).

Of course the most unambiguous way to study jets is with full jet reconstruction. Complete jet reconstruction in heavy-ion collisions poses many problems but it is an ongoing field of research. But the studies that have been done are inconclusive and are outside the scope of this document .

One jet-related phenomenon which is frequently claimed to be observed at RHIC is so-called "jet quenching", which refers to a body of evidence that suggests that jet production is reduced in central A-A collisions compared to more peripheral or p-p collisions. Studies of high-p_t physics at RHIC have been dominated by claims of jet quenching. Jet quenching is typically presented in one of two forms: the nuclear modification factor R_{AA} and correlation measurements. R_{AA} is defined as the ratio of the p_t-spectra produced in A-A collisions to the spectra of proton-proton collisions. In the context of jet quenching, correlations studies are typically done using high-p_t trigger particles and modification of the away-side ridge is observed.

An example of R_{AA} for charged hadrons at STAR is shown in Fig. 3.4 [31]. This example is for all charged hadrons but R_{AA} can be—and typically is—calculated for specific hadron or even lepton species. In the most central 0-5% collisions R_{AA} is said to be suppressed at higher p_t when compared to more peripheral collisions and this is interpreted to mean that high-p_t jet production is reduced or quenched in central collisions.

However when just taking the ratio between A-A and p-p spectra the result will be

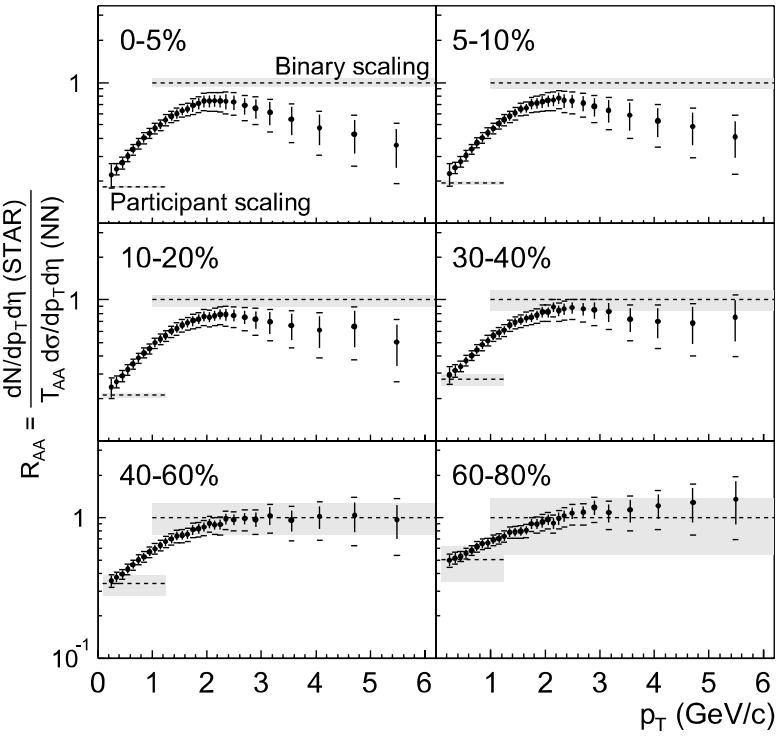

Figure 3.4: R_{AA} for charged hadrons at STAR for different centralities [31].

completely dominated by the fact that there are simply more particles produced in A-A collisions. This is a trivial result of the fact that there are both more participating nucleons and binary collisions between nucleons in A-A collisions. It is therefore necessary to scale the p-p spectra by some factor to make a reasonable comparison. But what should that factor be? R_{AA} studies make the assumption that above a certain momentum value the spectra are dominated by hard physics and therefore the spectra should be scaled by the number of binary collisions. In this view R_{AA} is only relevant for higher momenta particles but it is thought to be a reasonable approximation in that regime.

But we saw in Sec. 3.1.3 that the p-p spectra have distinct hard and soft components which scale differently. Furthermore, the soft component is relevant at much higher p_t than is typically assumed. Because the soft and hard components scale differently it is impossible to construct a meaningful spectrum ratio by scaling the entire spectrum by a

single number. However if the soft and hard components are isolated *before* making the ratio then it is possible to create the equivalent of R_{AA} for just the hard component. In that case scaling by the number of binary collisions is valid. Such an analysis was done in [159] and it presents a different interpretation. It is true that at high-p_t the hard component is reduced in central Au-Au compared to peripheral or p-p collisions, but at low-p_t it is actually *enhanced*. This is impossible to discern from a normal R_{AA} analysis where the low-p_t part of the hard component is overwhelmed by a soft component that has been scaled by the wrong factor. The enhancement of the low-p_t part of the hard component suggests that jets are being modified by the medium but not quenched. In fact jets in central Au-Au collisions appear to produce *more* total particles with less energy per particle.

Jet quenching is also claimed to be observed in two-particle correlations such as is seen in the bottom two panels of Fig. 3.5 [23]. These correlation studies are done both with a high-p_t trigger particle and a p_t cut for the "associated" particles that are correlated with that trigger. The claim is that the away-side ridge at $\Delta\phi = \pi$ vanishes in central Au-Au collisions when compared to p-p collisions.

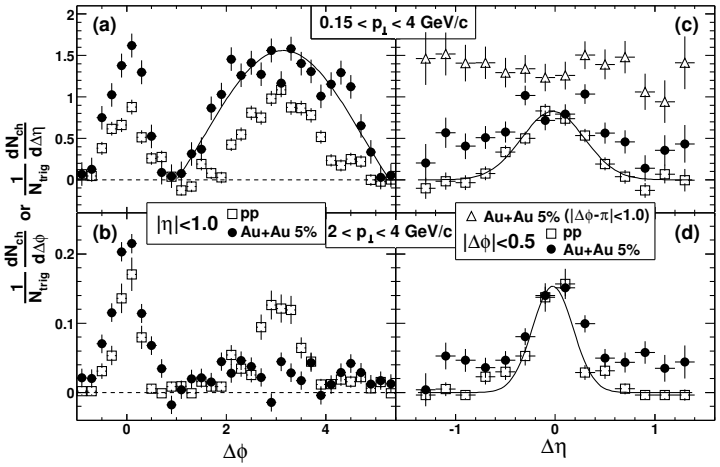

Figure 3.5: Background subtracted $\Delta\eta$ and $\Delta\phi$ distributions for p-p and 0-5% central Au-Au collisions with a trigger particle $4 < p_t^{trig} < 6$ GeV/c and two different associated particle p_t ranges [23].

In Chapter 6 and 7 we conduct extensive correlation studies of both p_t-integral correlations and correlations with marginal p_t cuts—cuts where only the p_t of one of the particles in the two-particle correlation is restricted. We see absolutely no evidence for any sort of quenching in these correlations. In order to see this effect it is necessary to impose significant p_t cuts on both particles. The example in Fig. 3.5 has a trigger particle p_t of at least 4 GeV and an associated particle p_t of at least 2 GeV. This ignores the vast majority of the particles in an event and again is completely consistent with the *modification* of jets in central Au-Au rather than quenching. The particles from those jets still exist just at a lower p_t but have been excluded with these cuts.

The quantitative correspondence between spectrum hard components [24, 159] and pQCD fragment distributions established in Ref. [161] strongly suggests that the parton fragment interpretation for hard components is valid. However, no such correspondence has been established for minimum-bias angular correlations (without p_t "trigger/associated" cuts). Interpretation of low-p_t jet-like features as true jet structure [138, 139, 28, 84] is questioned by some as outside the scope of high-p_t hard processes nominally described by pQCD (e.g. [96, 7]). Coupling spectrum hard components *and* minimum-bias jet-like correlations to pQCD predictions within a single quantitative system would provide compelling support for a comprehensive interpretation in terms of parton fragmentation to minijets. This will be explored more in Chapter 9.

3.3.3 Minijets in Nuclear Collisions

The UA1 collaboration at the CERN SPS measured jets from minimum bias trigger data for $\sqrt{s} = 200$ GeV to 900 GeV proton-antiproton collisions [43] using their standard jet-finding algorithm [58]. In typical jet studies a high-p_t trigger is used to look for rare events with large-energy jets but in this UA1 analysis they analyzed all of their data looking for energy clusters in their calorimeter. They found that clusters with E_t as low as 5 GeV met all of their jet criteria and coined them "minijets".

Early predictions for minijets at RHIC energies estimated an average of 100 jets with $p_t > 3$ GeV/c in central U-U collisions [114]. Subsequent analyses of high-p_t spectra and

correlations at RHIC led to the conclusion that there was significant jet quenching and such low-p_t minijets, even if they existed, would not make it through the medium in any meaningful form. Furthermore, precise pQCD predictions were not available for these low-momentum minijets.

We mentioned in Chapter 1 the existence of low-Q^2 (energy scale $Q \sim 1-5$ GeV) parton fragments we call minijets which are observable using correlation techniques. We will go into more detail about them in Chapter 8 and Chapter 9. These types of jets are very difficult to observe with conventional jet-finding algorithms even in clean collision environments, and with the large number of particles produced in heavy-ion collisions that becomes even more difficult. Thus it is necessary to use statistical analysis methods. Measurements of two-particle correlations at RHIC have revealed substantial unequilibrated low-Q^2 parton fragmentation structure in p-p and Au-Au collisions [157, 29, 30, 142, 170, 138, 28, 136, 137]

Fragment correlations have been measured in p-p collisions on transverse rapidity y_t (defined below) and complementary angular subspace (η, ϕ) with *no jet hypothesis* (no high-p_t trigger particle), providing access to fragments from minimum-bias partons (no analysis constraint on parton momentum) dominated by minijets. Jet correlations have been observed in p-p collisions for hadron p_t down to 0.35 GeV/c (parton $Q \sim 1-2$ GeV) [137, 157]. Similar measurements in heavy ion collisions have revealed unexpected complexity.

In p-p and A-A collisions at RHIC we encounter copious parton fragmentation in an energy regime where pQCD is not applicable but where trends from pQCD may provide semi-quantitative guidance for analysis and interpretation. We therefore distinguish between conditional pQCD fragmentation functions and unconditional fragment distributions measured in nuclear collisions. Given that distinction we can attempt to connect low-Q^2 phenomena in nuclear collisions to QCD through the close connection between FFs and fragment distributions as a limiting case. This is a new aspect of fragmentation which lies outside the scope of conventional pQCD fragmentation analysis.

Minijet-related correlations observed in p-p collisions are strongly modified with increasing centrality in Au-Au collisions. While low-Q^2 partons play an important role in forming the colored medium and driving large-scale hydrodynamic phenomena according to theory, they may also function as sensitive probes of that medium. However, theoret-

ical descriptions of low-Q^2 scattering and fragmentation are limited. Factorization is not applicable since low-Q^2 parton scattering and fragmentation remain intimately connected. However, new aspects of fragmentation observed *via* correlations in nuclear collisions (including strong dependence of fragment angular correlations on Q^2 [138]) suggest a complex but understandable low-Q^2 process. See Chapter 9 for more details.

To facilitate theoretical descriptions of low-Q^2 phenomena we have attempted to extrapolate a phenomenological representation of measured FFs in e^+-e^- collisions to low Q^2 as will be seen in Chapter 8. We want to connect two-particle fragment correlations in p-p and heavy ion collisions to pQCD and conventional jet phenomenology through single-particle fragmentation functions. The extrapolation imposes special demands on the fragment representation (particularly for small particle momenta) which have led us to employ rapidity y and normalized rapidity u as our basic kinematic variables. That decision led to the discovery that the beta distribution on u is a good model of light-quark and gluon fragmentation functions.

Demonstrating the existence and properties of collective flows and of jets using correlation techniques is actually formally equivalent. Both phenomena manifest as correlations between particles produced in the collision and many of the analysis methods overlap. Therefore it makes sense to study both simultaneously and on equal footing. We will present a method for doing so in Chapter 5.

Chapter 4

CONVENTIONAL ANALYSIS METHODS

4.1 Reaction Kinematics

This chapter describes conventional methods for analyzing azimuth anisotropy in nuclear collisions. Azimuth anisotropy can refer to any correlation signal on the azimuth coordinate but is most commonly attributed to correlations related to the initial-state geometry of the heavy-ion collision. Such correlations are believed to play an insignificant role in proton-proton collisions but dominate heavy-ion physics. The conversion of the initial collision-system geometry to azimuth correlations of final-state particles is typically attributed to a flowing medium formed early in the event.

In Chapter 2 we introduced the primary measurement variables we will be concerned with in this analysis: transverse momentum p_t, azimuth angle ϕ, and pseudorapidity η for each particle we observe in the STAR TPC. This chapter explains how we go from those variables to v_2, a conventional measure of "azimuth anisotropy."

4.1.1 Collision Planes

When two ions collide with a non-zero impact parameter the A-A overlap defines a natural set of variables. The reaction plane is the name given to the plane defined by the impact parameter between the two colliding ions and the direction they travel in the beampipe, defining the z axis in this coordinate system. The reaction plane is a theoretical concept since it is not something we can measure directly in an experiment. The reaction-plane angle Ψ_r is the azimuth angle of this plane with respect to the detector. The orientation of the detector with respect to the overlap of the colliding ions is arbitrary, so most analyses are concerned with momentum angles relative to the reaction plane or an estimate of that direction.

The event plane (EP) is an estimation of the reaction plane using particles measured in

a collision event. It will be described in more detail in Sec. 4.2.1. The EP is the basis for the most common v_2 calculation methods. Given a finite number of particles in an event the event plane can never be a perfect estimation of the reaction plane. Certain methods are said to compensate for the event-plane uncertainty. In addition to statistical issues the estimation of the event plane can by biased by sources of correlation unrelated to the reaction plane, which leads to the so-called "nonflow" problem discussed throughout this document.

There is one more collision plane discussed in heavy-ion physics known as the participant plane. The participant plane was introduced because if there are significant fluctuations in the positions of nucleons within a nucleus then the plane of the nucleons participating in a collision does not perfectly correspond to the ideal plane defined by the impact parameter of the nuclei [71]. If point-like nucleons randomly populate a symmetric volume that defines the nucleus then in any given collision it is possible to define a distinct plane by the distribution of the nucleons rather than the nuclei modeled as spheres. The participant model of eccentricity discussed in Sec. 4.3 is closely related to this concept and has been proposed as a means of describing so-called "flow fluctuations".

4.1.2 Nonflow

The catch-all term "nonflow" is used to refer to correlations that can potentially contribute to the measured values of v_2 but are not directly correlated with the initial geometry of the collision system. If an observed azimuth anisotropy measured by v_2 is driven by hydrodynamic flows in response to pressure gradients then it is usually referred to as "flow". Historically, it was generally assumed that the only major source of correlations is flow, but that assumption is not valid at SPS energies and above [72]. Since azimuth correlations are the only way to measure flow methods must be adopted that can distinguish between "flow" and "nonflow" correlations.

Several physical processes can contribute "nonflow" correlations. Development of new v_2 estimation methods has been driven primarily by a desire to eliminate these contributions. Examples of nonflow sources include jets, resonance decays, and quantum HBT correlations.

We will provide ample evidence in Chapters 6, 7, and 9 that the dominant source of nonflow correlations at RHIC is the production of a large number of minijets. Understanding the relationship between "nonflow" and minijets is thus essential.

Conventional methods sometimes refer erroneously to self-pair contributions to angular correlations as "autocorrelations" in the sense of a bias or systematic error. The autocorrelation function is a well-defined mathematical concept which we will use extensively in this dissertation. The autocorrelation concept is described in detail in Chapter 5. The self-pair contribution can be entirely eliminated with appropriate methods and is not considered here as part of the nonflow term.

4.1.3 Flow Fluctuations

With two-particle analysis methods we cannot measure linear v_2 directly. Instead we calculate v_2^2 for each event, and then take the ensemble average over many events. Even though $\overline{v_2}$ may not be a measurable quantity, the fundamental inequality $\overline{v_2^2} \geq \overline{v_2}^2$ still holds. The "extra" term can be referred to as v_2 fluctuations σ_2^2 since it arises from event-by-event variations in v_2: $\overline{v_2^2} = \overline{v_2}^2 + \sigma_2^2$

However in multiparticle analyses—which were originally introduced to reduce nonflow correlations, see Sec. 4.2.3—the fluctuation term can actually appear with the opposite sign. For instance for Gaussian-random fluctuations in a four-particle cumulant v_2, $\overline{v_2^2\{4\}} \approx \overline{v_2}^2 - \sigma_2^2$ [174]. But this contradicts the naive expectation that the difference between v_2 in a two-particle correlation and v_2 in a multiparticle correlations is entirely due to the nonflow term. Instead we find that this difference is due to some combination of v_2 fluctuations and nonflow effects. There have even been suggestions that this difference is dominated the fluctuation term and that nonflow is a relatively small contribution to the two-particle correlation. But actually isolating the two terms is difficult without a two-particle method that isn't sensitive to nonflow. We will present exactly such a method in Chapter 5.

The participant model of nucleons mentioned in Sec. 4.1.1 is closely related to the concept of flow fluctuations because it provides a possible mechanism for significant event-by-event fluctuations in v_2. This will come up again in Sec. 4.3 when we discuss eccentricity.

4.2 v_2 Methods

It is simple to define v_m theoretically, but it is difficult to obtain unbiased measurements of it. We can define a Fourier decomposition of the distribution of particle emission azimuth angles with respect to the true reaction plane:

$$E\frac{d^3n}{d^3p} = \frac{1}{2\pi}\frac{d^2n}{p_t dp_t dy_z}\left(1 + \sum_{m=1}^{\infty} 2v_m \cos(m(\phi - \Psi_r))\right). \tag{4.1}$$

The sine terms vanish due to reflection symmetry with respect to the reaction plane. This is a nominal definition of v_m but not a useful measurement technique since Ψ_r isn't observable. Therefore, many conventional measurement techniques first attempt to estimate the reaction plane. But other techniques that use angular correlations directly are closely related to these methods.

4.2.1 Event Plane Method

The standard event-plane (EP) method of calculating v_2—typically represented by $v_2\{EP\}$—involves estimating the reaction plane of the collision using the particles measured in the TPC. This estimate of the reaction plane is called the event plane. v_2 is then calculated as the second Fourier component of the distribution of tracks within the TPC relative to the event-plane estimate rather than the true reaction plane. In the absence of systematic bias the value of v_2 calculated this way will always be too small because in a system with finite multiplicity there will always be random fluctuations in the reaction plane estimation. It therefore must be corrected by a factor known as the "event-plane resolution".

The method of calculating v_m coefficients from estimates of the reaction plane was initially proposed by Danielewicz and Odyniec [83] and was further developed in [141] to the form presented here. The first step is to define the components of the event flow vector $\mathbf{Q}_m$ using the sum over measured tracks:

$$\begin{aligned} Q_m \cos(m\Psi_m) &= X_m = \sum_i w_i \cos(m\phi_i), \\ Q_m \sin(m\Psi_m) &= Y_m = \sum_i w_i \sin(m\phi_i), \end{aligned} \tag{4.2}$$

which leads to

$$\Psi_m = \frac{1}{m}\left(\tan^{-1}\frac{\sum_i w_i \sin(m\phi_i)}{\sum_i w_i \cos(m\phi_i)}\right), \tag{4.3}$$

where the sums are over all particles used in the event-plane determination and the w_i are weight factors defined below. Ψ_m is the event-plane and there is an event plane defined for each harmonic m. Because of the importance of the v_2 coefficient to flow theories the term "event plane" is often used synonymously with Ψ_2, which will be a focus of this analysis.

For real experimental data biases from the finite detector acceptance affect the measured event plane. Since there is no physical correlation between the collision orientation and the detector we expect that the event-plane distribution with respect to the detector should be isotropic. That is not necessarily the case if there are gaps in the detector acceptance. Several methods exist to correct for this problem (called "flattening"), but the most common involves using the distribution of measured particles over many events as a measure of the detector acceptance. The inverse of this distribution is used to determine weights w_i in the above event-plane calculation.

Other flattening methods include re-centering the (X_m, Y_m) distributions by subtracting their average over all events, using mixed events as a reference, and fitting the unweighted event-plane distribution with a Fourier expansion to devise an event-by-event shifting of event planes. These methods are described in more detail in [141] but none of them are without complications. It is always necessary to check that the corrected event plane distribution is indeed isotropic (uniform on ϕ).

Once the event-plane angle has been calculated it is possible to study particle distributions with respect to it. Recall the definition of the v_m coefficients in terms of the azimuth distribution of particles with respect to the reaction plane from Eq. (4.1). We now write this in terms of the event-plane angle [141]:

$$\frac{d(wn)}{d(\phi - \Psi_m)} = \frac{\overline{wn}}{2\pi}\left(1 + \sum_{k=1}^{\infty} 2v_{km}^{obs}\cos(km(\phi - \Psi_m))\right) \tag{4.4}$$

We use km in this equation because the Fourier coefficient v_m can be for any harmonic that is a *multiple* of m. For instance, when $m = 2$ all even terms are used. w is a weight value set to 1 for the standard study of particle number flow. But it is also possible to study other

quantities. For instance, w could be set to p_t to study transverse momentum flow. The coefficients are referred to as v_m^{obs} to distinguish them from the true v_m values in Eq. (4.1).

We can evaluate the v_m^{obs} coefficients directly by

$$v_m^{obs} = \langle \cos(m(\phi - \Psi_m)) \rangle \,, \tag{4.5}$$

where the brackets represent an average over the particles in an event. In practice v_2 is measured using many events so there is an average over events not shown here. So long as the even plane is being estimated with a finite number of particles it will always have some random variation around the true reaction plane even in the absence of any systematic biases. These random variations will reduce the value of v_m^{obs} so it is necessary to correct it by a quantity known as the event-plane resolution [141] to get:

$$v_m\{EP\} = \frac{v_m^{obs}}{\langle \cos(m(\psi_m - \psi_r)) \rangle}, \tag{4.6}$$

The label $v_m\{EP\}$ represents the standard event-plane method of estimating v_m. Several such methods will be discussed so it is necessary to distinguish them symbolically.

There is a self-pair bias—sometimes erroneously referred to as an "autocorrelation"—introduced when calculating the contribution to v_m of a particle that was used in the estimation of the event plane. One possible method to deal with this is to use sub-events, where half the particles in an event are used to estimate the event plane and the other half are used to estimate v_m. This will be discussed more in the next section, but in practice the standard event plane method actually involves calculating a separate event plane for each particle using all the particles in the event *except* that particle. So in the average in Eq. (4.5) we actually replace Ψ_n with a slightly different angle for each particle.

There are both analytic and data-based ways to determine the event-plane resolution. An analytic expression is derived in [141, 171]:

$$\langle \cos[km(\psi_n - \psi_r)] \rangle = \frac{\sqrt{\pi}}{2\sqrt{2}} \chi_m e^{-\chi_m^2/4} \left[I_{\frac{k-1}{2}}(\chi_m^2/4) + I_{\frac{k+1}{2}}(\chi_m^2/4) \right], \tag{4.7}$$

where I_x is the modified Bessel function of order x and $\chi_m \equiv v_m/\sigma$ where $\sigma^2 = \langle w^2 \rangle / (2n\langle w \rangle)$, n being the number of particles used to determine the event plane. This is an unwieldy

expression but we found in [166] that it can be well-approximated with the much simpler expression

$$\langle \cos[m(\psi_m - \psi_r)] \rangle \approx \sqrt{\frac{n-1}{n}} \frac{V_m}{Q_m}, \tag{4.8}$$

where $V_m^2 = n^2 v_m^2$ is a quantity that will be discussed in Chapter 5. While it may seem circular to define the event-plane resolution in terms of v_m, this is actually an essential property of the event-plane resolution which relates the event-plane method to direct angular correlation methods.

This "standard" (event plane) method of measuring v_2 depends on shifting the single-particle densities according to the estimate of the reaction plane and averaging the shifted single-particle densities. If the reaction plane were known perfectly this would be immune to any correlations that are not with respect to the reaction plane. When averaged over many events they would contribute as a flat background. However, when the reaction plane is estimated using particles in the event there are correlations between the particles used to estimate the reaction plane and the particles used to measure the azimuth anisotropy, making the event-plane technique effectively another type of two-particle correlation. This is also the origin of the nonflow problem in the event-plane method.

A detailed analysis of the relationship between the even-plane method and two-particle correlations is presented in Chapter 5, but to a close approximation the event-plane method is not different from taking the second Fourier coefficient of a straightforward two-particle correlation calculation. The language used when discussing event-plane v_2 tends to confuse this relationship, but with some simple approximations the mathematics can be made unambiguous [166]. For this reason we assume $v_2\{EP\} \approx v_2\{2\}$, where $v_2\{2\}$ is obtained from 1D sinusoid fits to a basic two-particle correlation.

4.2.2 Event Plane Variations

There is actually a whole class of methods based on the basic event-plane method described above, introducing only small variations. Usually these variations take the form of limiting the particles used in the event-plane estimation. The most basic type uses subevents to separate the particles used to estimate the reaction planes from the particles used to measure

v_2. Using random subevents selected from all available particles reduces the statistical power of the v_2 measurement, but it can potentially eliminate certain systematic issues. However subevents are most commonly chosen using specific criteria rather than randomly. For instance, the event plane is estimated using particles with pseudorapidities larger than some value and v_2 is measured with particles that have pseudorapidities smaller than that value. It is generally believed that having a pseudorapidity gap between the particles used to estimate the event plane and the particles used to measure v_2 should reduce nonflow contributions. This reduces the statistical power of the analysis in exchange for possibly reducing systematic effects.

The event-plane estimation is not necessarily restricted to particles measured in the TPC. One version of this method used by the STAR collaboration actually estimates the event plane using particles from the FTPC detector system at large η while calculating v_2 with particles in the TPC at smaller η. This method is typically referred to as $v_2\{\text{FTPC}\}$. Using the FTPC allows for a much larger pseudorapidity separation between the two sets of particles.

Other phase-space cuts besides pseudorapidity can be used to distinguish the particles used to determine the event plane from the particles that are correlated with it to determine v_2. In a p_t-differential v_2 analysis the event plane is still typically determined with the full range of measured p_t values while the particles correlated with it are divided into p_t bins to observe the p_t dependence. p_t cuts can also be made in an effort to reduce the impact of nonflow (jet) correlations. But as we saw for the two-component model in Chapter 3 the overlap between the hard (jet) and soft (nonjet) components of heavy-ion collisions is significant, so this approach is not actually effective.

4.2.3 Multiparticle Methods

Correlations of four or more particles are typically referred to as multiparticle correlations. Several multiparticle v_2 methods are commonly in use today. They are favored as a way to reduce or eliminate contributions from nonflow. Multiparticle v_2 is based on the idea that there is only one reaction plane per event so all particles contributing to a flow correlation

should be correlated with that plane. Nonflow correlations on the other hand tend to come from many distinct processes producing a smaller number of highly-correlated particles. For instance, if minijets produce clusters of only a few particles that are correlated with each other and not with other minijets in the event their contribution to a multiparticle correlation should be much smaller than in a two-particle correlation.

By looking at correlations of four or more particles, contributions to the correlation from isolated groups of particles should be significantly reduced. The impact of this reduction is even stronger than one might naively estimate thanks to combinatorics. Even if a minijet or other isolated group of particles *does* contain more than four particles it only contributes to a four-particle correlation if all four particles sampled are from the same minijet. When a single minijet only represents a small fraction of the number of particles in the collision this becomes statistically unlikely. More precisely, if an event has n total particles and N uncorrelated physical processes that each produce k particles, then the magnitude of a two-particle correlation is proportional to $kN(N-1)/n^2$ while a four-particle correlation is proportional to $kN(N-1)(N-2)(N-3)/n^4$. If $N \ll n$ then the second quantity will be significantly smaller.

The multiparticle cumulant analysis [73] is a popular type of multiparticle v_2 measurement method. The idea of cumulants is to develop an expansion where lower-order contributions are subtracted from the higher-order terms. In complex notation the standard two-particle azimuth correlation can be expressed as

$$v_m\{2\} \equiv \left\langle e^{im(\phi_1-\phi_2)} \right\rangle = \langle e^{im\phi_1}\rangle\langle e^{-im\phi_2}\rangle + \left\langle \left\langle e^{im(\phi_1-\phi_2)} \right\rangle \right\rangle, \tag{4.9}$$

where $\langle\langle e^{im(\phi_1-\phi_2)}\rangle\rangle$ is the second-order cumulant. In this case the first-order terms should vanish by symmetry in a perfect detector. They are nonzero if the detector has limits in its acceptance, so the second-order cumulant is nothing more than a simple two-particle correlation that has been corrected for detector artifacts. It is therefore directly comparable to the two-particle correlations that we will describe in Chapter 5.

Now consider the four-particle case. Construct the average of all possible combinations of four particles [73]

$$\left\langle e^{im(\phi_1+\phi_2-\phi_3-\phi_4)} \right\rangle = \langle e^{im(\phi_1-\phi_3)}\rangle\langle e^{im(\phi_2-\phi_4)}\rangle + \langle e^{im(\phi_1-\phi_4)}\rangle\langle e^{im(\phi_2-\phi_3)}\rangle \tag{4.10}$$

$$+ \quad \left\langle\left\langle e^{im(\phi_1+\phi_2-\phi_3-\phi_4)}\right\rangle\right\rangle,$$

where $\langle\langle e^{im(\phi_1+\phi_2-\phi_3-\phi_4)}\rangle\rangle$ is then the four-particle cumulant. The other terms on the right-hand side are two-particle correlations. Due to the symmetry between the ϕ_i variables this can be rewritten as

$$\left\langle e^{im(\phi_1+\phi_2-\phi_3-\phi_4)}\right\rangle = 2\langle e^{im(\phi_1-\phi_3)}\rangle^2 \left\langle\left\langle e^{im(\phi_1+\phi_2-\phi_3-\phi_4)}\right\rangle\right\rangle. \tag{4.11}$$

This procedure can be generalized to higher orders, but in practice there is not much difference seen between four-particle cumulants and cumulants of six or more particles [22].

While it is possible to compute these correlations directly it is extremely difficult computationally since the calculation scales as $O(n^k)$ for multiplicity n and cumulant order k. For heavy-ion collisions n can be over 1000 so a complete computation would take dramatically longer than the two-particle case. In practice it is more common to use a generating function to calculate higher-order cumulants [73] . A related multiparticle method is the Lee-Yang zeroes (LYZ) method which obtains v_2 from zeroes in the complex plane of a generating function of azimuth correlations [67]. LYZ is in some sense analogous to an infinite-order cumulant, but we will not discuss it further here.

Multiparticle methods can considerably reduce the effect of nonflow correlations but there are limitations. "Multiplicity distortions" associated with small even multiplicities are a significant systematic issue that can be minimized to some degree by analysis strategies. But they remain an issue in conventional flow measurements. For this reason flow measurements using many-particle methods are often omitted for the most peripheral collisions. For the generating-function and similar methods to work at all it is necessary that $v_m \gg 1/n$ [73]. These methods will fail if v_2 is too small or in very-peripheral collisions where n is too small. Statistical errors in many-particle analyses depend on the resolution parameter $\chi \approx v_m\sqrt{n}$ [67]. For usable results it is necessary that $\chi > 1$. These issues can also explain the difficulty of measuring v_2 with many-particle methods in the most central collisions at STAR because while n is certainly not small in this regime we will show in Chapter 6 that v_2 can be unexpectedly small.

4.3 Eccentricity

Some interpretations of the final-state Au-Au azimuth asymmetry require understanding the geometry of the initial collision system as characterized by the eccentricity [150] defined by

$$\epsilon = \frac{\langle y \rangle^2 - \langle x \rangle^2}{\langle y \rangle^2 + \langle x \rangle^2}, \tag{4.12}$$

where x and y are coordinates in the plane perpendicular to the beam axis and x refers to the direction along the reaction plane. This is basically the initial-state position-space analogue to v_2 but is not an experimentally observable quantity and must be estimated from models. There are major disagreements concerning the correct way to calculate eccentricities for nuclear collisions.

One of the simplest approaches is the optical model, in which the colliding nuclei are approximated by continuous transverse density profiles, typically modeled by a Woods-Saxon distribution. We shall refer to the resulting ϵ estimates as ϵ_{opt}. In this model the density of participants per nuclear collision is [110]

$$\frac{d^2 n_{part}}{ds^2} = T_A(b_A) \cdot \left(1 - e^{-T_B(b_B)\sigma_{NN}}\right) + T_B(b_B) \cdot \left(1 - e^{-T_A(b_A)\sigma_{NN}}\right), \tag{4.13}$$

where σ_{NN} is the nucleon-nucleon cross section, T_A and T_B are the nuclear thickness functions

$$T_A(|\vec{s}|) = \int d_z \rho_A(z, \vec{s}), \tag{4.14}$$

and ρ_A and ρ_B are the Woods-Saxon distributions

$$\rho_A(r) = \rho_0 \cdot \frac{1}{1 + e^{(r - R_A)/a}}, \tag{4.15}$$

with $r = \sqrt{s^2 + z^2}$, $R_A = 1.12 \cdot A^{1/3}$, $\rho_0 = 0.159\,\text{GeV/fm}^3$, and $a = 0.535$ fm for Au [110].

The calculation in [110] was done for the SPS energy $\sqrt{s_{NN}} = 17$ GeV assuming a nucleon-nucleon cross section of 30 mb and then parametrized with a 5th order polynomial. At RHIC energies (200 GeV) a cross section of 42 mb is more appropriate. Furthermore, as can be seen in the left panel of Fig 4.1, the given parametrization does not describe the

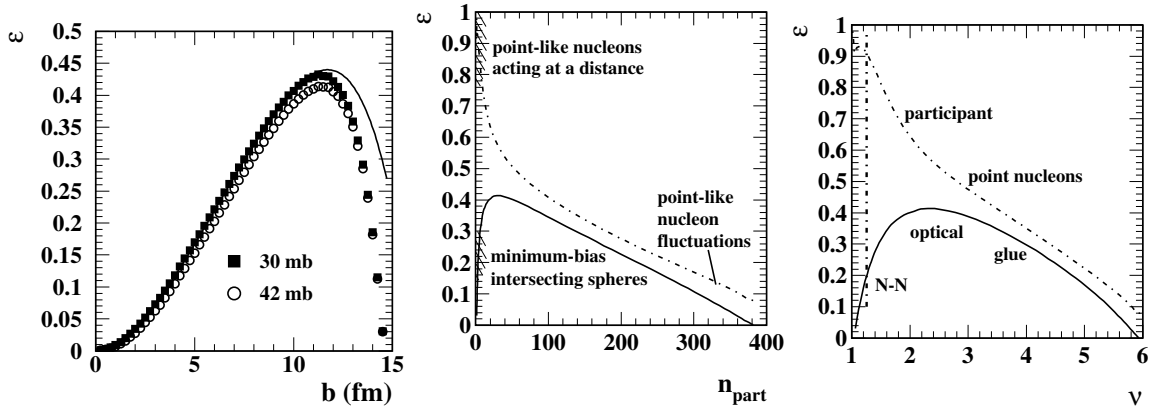

Figure 4.1: Left panel: Calculations from the wounded nucleon optical eccentricity model. The solid curve is the parametrization for a 30 mb nucleon-nucleon cross section given in [110]. Middle panel: Optical eccentricity $\epsilon_{\rm opt}$ and participant eccentricity $\epsilon_{\rm part}$ [158] *vs* participant nucleon number $n_{\rm part}$. Right panel: The same curves *vs* mean participant path length ν. The vertical dash-dot line denotes the mean value of ν for N-N collisions [169]

most peripheral collisions. We seek a complete description of eccentricity and so repeated the calculation with the appropriate 42 mb cross section (open circles). A polynomial parametrization was attempted, but to get reasonable agreement with the simulation out to the most peripheral data required significantly more terms. We then found an alternate and much simpler parametrization using a beta distribution on n_{bin}:

$$\epsilon_{\rm opt}(n_{\rm bin}) = \frac{1}{5.68}\log_{10}\left(\frac{3n_{\rm bin}}{2}\right)^{0.96}\log_{10}\left(\frac{1136}{n_{\rm bin}}\right)^{0.81}, \tag{4.16}$$

which describes the calculation with great accuracy. This parametrization of the eccentricity is also shown in the second and third panels of Fig. 4.1 on both n_{part} and ν.

The other major approach to eccentricity calculations is the participant-nucleon model of eccentricity. A Monte Carlo toy model builds nuclei by randomly placing nucleons according to a Woods-Saxon density distribution [66]. This model is used as a mechanism to introduce significant event-by-event fluctuations even for a fixed impact parameter. We shall refer to this estimate as $\epsilon_{\rm part}$. This model is favored because of the apparent scaling the ratio $v_2/\epsilon_{\rm part}$ exhibits between Cu-Cu and Au-Au collision systems [49]. However, in [49] v_2 was measured with the event-plane method which does not account adequately for nonflow (jet) biases which are large in central collisions. Any apparent scaling based on measurements

with large uncorrected systematic biases should be questioned. The second and third panels of Fig. 4.1 show the large differences between the participant and optical eccentricities.

By construction $\epsilon_{\rm part}$ is made to produce significant eccentricity (and therefore v_2) fluctuations in the most central collisions, meaning that unlike the optical eccentricity it does not approach zero. But $\epsilon_{\rm part}$ also behaves pathologically for peripheral collisions, actually approaching unity for the most peripheral collisions. This would imply that the nucleons behave as point-like objects. This flaw is not considered important in many v_2 studies since they focus primarily on the mid-central to central collision region and do not consider very peripheral collisions. But if we desire a complete description of v_2 for all centralities then the behavior of the participant model in peripheral collisions is a serious limitation.

We will see in Chapter 6 that the v_2 measurements from this study approach zero for central collisions, consistent with $\epsilon_{\rm opt}$. There is simply no need to invoke a participant eccentricity model to explain this data. Given the possibility that elliptic flow is a "long-wavelength" probe [158]—which would actually reduce any dependence on the initial positions or transverse structure of individual nucleons—we believe that $\epsilon_{\rm opt}$ is a more realistic approximation.

4.4 Monte Carlo Studies

Due to the number and complexity of the different v_2 measurement methods, it is useful to test them with a simple Monte Carlo model. Our goal is neither to produce an accurate physics simulation nor to model detector effects, but rather to compare the effectiveness of different methods on a variety of input signals with different but known amounts of azimuth correlations, clusters (jet production), and fluctuations.

We explore three types of correlation signals with Monte Carlo simulations. First are minijets described by two or more particles distributed according to a two-dimensional Gaussian probability function about the jet center. The number of particles in a minijet is determined according to a Poisson distribution. The second source of correlation comes from flow terms. Both v_1 and v_2 terms can be described, but v_1 is typically set to zero. These terms are implemented by first randomly selecting a true reaction plane and then biasing the distribution of single particles and minijet centers by sinusoids.

The third source of correlations is momentum conservation. Momentum conservation is difficult to treat properly in a simple simulation since there are many ways to conserve momentum. For instance, momentum conservation in hard scatterings should to be dominated by the products of back-to-back parton pairs. On the other hand, in a thermal system momentum is conserved among all particles in the event but that is difficult to simulate.

We will not attempt to model the full details of nuclear collisions. Instead it is necessary to explore several different algorithms and compare them to in the data. For instance, if we assume that most events are dominated by back-to-back scattering of partons we could generate single particles and minijets in roughly back-to-back pairs. Rather than making them perfectly back-to-back the second minijet in the pair can be determined by a Gaussian on azimuth centered away from the first minijet (acoplanarity).

A different approach to momentum conservation is to assign each particle a momentum value and keep a running total of the momentum of the system as more particles are added. The magnitude and direction of that momentum can then be used to bias the probability distribution for the next particle added so that it is less likely to be in the direction of the current total momentum vector. This produces a rough approximation to thermal momentum conservation.

Neither approach strictly conserves momentum, although the momentum of observed particles in a real collision is also not strictly conserved since there exist particles that are produced but not observed in the detector. These methods do produce a rough approximation to the effect of momentum conservation in real collisions. The back-to-back scattering approach produces an away-side Gaussian on ϕ, not necessarily a cosine. But since ϕ is periodic this away-side Gaussian is actually repeated every 2π and in the limit of large Gaussian width it approaches a simple cosine. A large width is not unusual for the momentum scales encountered in minimum-bias collisions at RHIC due to k_t broadening—the transverse component of the initial parton momentum—so either approach can produce results similar to the observed data.

We can then calculate v_2 from these simple simulations with different methods to understand their sensitivity to these signals to under controlled conditions. In the first panel of Fig. 4.2 we have adjusted the parameters of the Monte Carlo to roughly follow expected

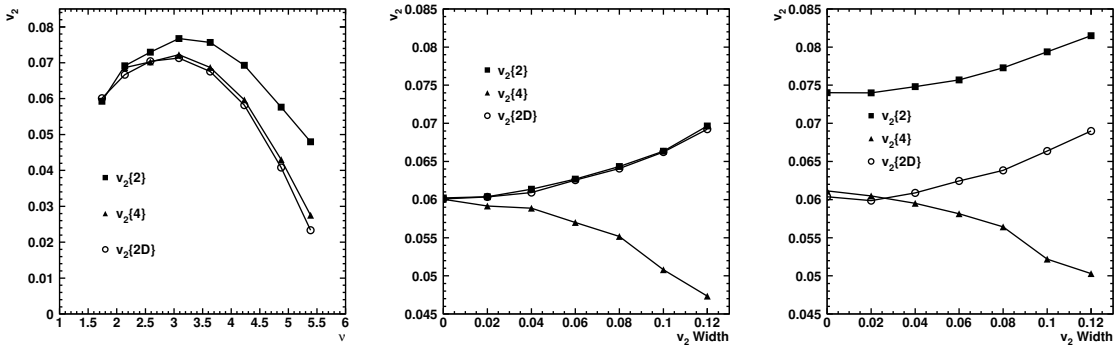

Figure 4.2: First Panel: Simulated centrality evolution of $v_2\{2\}$, $v_2\{4\}$, and $v_2\{2D\}$. Second Panel: Effect on simulated $v_2\{2\}$, $v_2\{4\}$, and $v_2\{2D\}$ as a function of increasing v_2 fluctuation width in the absence of the minijet term. Third Panel: Effect on simulated $v_2\{2\}$, $v_2\{4\}$, and $v_2\{2D\}$ as a function of increasing v_2 fluctuation width in presence of a minijet term.

centrality trends and display three v_2 methods: Two-particle cumulant $v_2\{2\}$, four-particle cumulant $v_2\{4\}$, and v_2 from two-dimensional fits to two-particle correlations $v_2\{2D\}$—which is the method introduced in Chapter 5 and the major focus of this work. We see that both $v_2\{4\}$ and $v_2\{2D\}$ effectively handle the minijet component of the simulation with very different approaches while $v_2\{2\}$ gives a significantly higher value because of the "nonflow" (jet) contribution.

Since v_2 fluctuations are another area of interest we can also model fluctuations simply by randomly varying v_2 parameters event-to-event. For simplicity this is done with a uniform random distribution of v_2 values with some width. While that may not seem like a physically realistic situation, v_2 is always measured within a centrality bin, not at a specific centrality value. For our purposes a uniform distribution works well enough. The second panel of Fig. 4.2 shows the effect of v_2 fluctuations in the absence of any other terms in the simulation. In this case $v_2\{2\}$ and $v_2\{2D\}$ behave identically while $v_2\{4\}$ has the opposite behavior. In the third panel we re-introduce the minijet term which again contributes to a larger $v_2\{2\}$ value. When just comparing the different between $v_2\{2\}$ and $v_2\{4\}$ it is ambiguous whether the source is nonflow or fluctuations. This is the fluctuation puzzle introduced

early in this chapter. $v_2\{2D\}$, on the other hand, is still a two-particle correlation which is affected by fluctuations the same way v_2^2 is. Since $v_2\{2D\}$ can also handle the minijet contribution it offers a potential solution to the fluctuation problem. In the next chapter we will explain generalized angular correlations and the $v_2\{2D\}$ method in greater detail and then in Chapter 6 and Chapter 7 we will apply this method to real data.

Chapter 5

CORRELATIONS

5.1 Overview

Correlation analysis is a flexible and reliable tool for studying the distribution of particles produced in a heavy-ion collision. The correlation method we will present in this chapter is based on the standard autocorrelation technique commonly used in signal analysis but adapted to the particular needs of this analysis.

Autocorrelations are fundamental in many fields including time-series analysis, the Brownian motion problem and its generalizations, and astrophysics. They serve as a powerful tool for separating "flow" and "nonflow". They do not suffer from "finite multiplicity biases" and permit the study of A-A centralities from central collisions to N-N collisions.

5.1.1 Motivation

Cross-correlations are used to measure the similarity of two waveforms with a lag (time shift) applied to one of them. Though often applied to functions on time the formalism is more general. An autocorrelation is defined as the cross-correlation of a signal with itself. On a continuous variable x this is written

$$\rho_A(x_\Delta) = \int_{-\infty}^{\infty} \rho(x')\rho(x' - x_\Delta)dx'. \tag{5.1}$$

In signal processing the quantity x_Δ is often referred to as the lag.

Norbert Wiener first applied autocorrelations to the study of Brownian motion. The autocorrelation concept was developed in response to the Brownian motion problem and the Langevin equation which contains a stochastic term. In the Brownian motion problem there was a need to separate large-scale, possibly-deterministic probe-particle motion from small-scale random motion due to collisions with water molecules.

There is a formal similarity between event-wise particle distributions on angle and the

time series of displacements of a particle in Brownian motion. Both cases involve a discrete distribution which combines a large random component with a smaller deterministic component and the correlation analysis is used to distinguish the two. In heavy-ion collisions at STAR we want to extract the azimuth correlation structure which persists over an event ensemble from event-wise random variations.

The key advantage of autocorrelations is that all of the structure (information) in an event is preserved, which for heavy-ion collisions includes both "flow" and "nonflow" effects. Understanding how to separate the distinct correlation components is the focus of much of this analysis. We apply this correlation method to multiple variables simultaneously and use the joint correlation—a correlation on multiple variables—structure to distinguish different physical features.

The autocorrelation method has many useful properties. Of note for this analysis is the fact that the autocorrelation of the sum of two or more uncorrelated functions is the sum of the autocorrelations of the functions. This will be important for interpreting correlation data since several distinct physical processes may contribute to the total correlation structure. The autocorrelation of a system with multiple uncorrelated sources of correlation—meaning there are correlations within one source but not correlations between different sources—do not depend on the overall positions of these sources. This means many different sources of correlations can overlap and contribute to a common structure. For instance, a single minijet may be difficult to detect at RHIC but so long as minijets are produced with similar characteristics many distinct minijets will contribute to one peak.

5.1.2 Fluctuations

Historically, global fluctuation measures have been popular tools to study heavy-ion collisions. But fluctuation measures can be calculated for different scales and yield different results than a global analysis. For instance, the fluctuations within a small bin can be different from the global fluctuations over an entire detector. Furthermore, it has been shown that fluctuation measures are nothing more than integrals of correlations [155]. There is no information contained in a global fluctuation measure that is not present in the corre-

sponding differential correlation measure and it is always possible to obtain the fluctuation measure by integrating the correlation. If the scale-dependent fluctuations have been calculated then it is possible to invert these fluctuations to obtain differential correlations [155, 142]. A correlation cannot be calculated from a single fluctuation scale, but if fluctuations are calculated as a function of a scale variable then it is possible to solve an integral equation to derive the correlations from the fluctuations.

The relationship between correlations and fluctuations is interesting in its own right, but in practice if the data to calculate fluctuations as a function of a scale parameter are available it is possible to simply calculate the correlations directly. In terms of computation time it is possible for the fluctuation method to be more efficient with proper optimizations, though both methods are still of the same order. But it is easier to use the direct correlation method when performing more involved analyses with sub-binning of particles within an event. That is the method employed in this analysis.

From the beginning of the field of heavy-ion collisions there was major emphasis placed on fluctuation measurements which persists even today. Experiments often report global fluctuation values—not scale dependent—to compare with theoretical calculations. Such quantities may be easy to calculate in theoretical models, but real heavy-ion collisions often contain additional physics not present in these models. Correlations analyses contain more information than global fluctuation measures. So much information that many of the details observed in correlations are not well modeled theoretically. This can make direct comparison to theory difficult, but the goal of this analysis is to present the most comprehensive and accurate representation of phenomenology in heavy-ion collisions possible.

5.1.3 Application of Correlations to RHIC

As discussed in Chapter 3, hard and soft processes play significant roles in heavy-ion collisions at RHIC. We strive to treat all contributions to correlations on equal footing. To avoid imposing the hypothesis being tested on the measurement scheme we develop a consistent set of neutral symbols, manipulate random variables with minimal approximations, introduce proper statistical references so that systematic correlations of any origin can be isolated

unambiguously, and treat azimuth structure *ab initio* in a model-independent manner using standard mathematical methods [166].

We make no approximations in the statistical analysis and invoke proper correlation references to obtain a minimally-biased, self-consistent analysis system in which "flow" and "nonflow" terms are both represented. These terms are then distinguished by applying fits to the correlation data with different physically-motivated components deduced from the structure of the data itself. The physical interpretation of these components is not unique but is well-motivated by numerous observations at RHIC. This methodology will then be applied to data in Chapter 6 and Chapter 7.

5.2 The Two-particle Correlation Method

We now present in detail the two-particle correlation analysis method that is used throughout this document.

5.2.1 Pair Counting

We wish to analyze the continuum parent density (particle source) but it is not directly observable. Instead we will construct correlations of observed particles in an event to infer properties of the parent density. In practice an autocorrelation can be derived from a pair density $\rho(x_1, x_2)$ by projecting it along diagonals in space (x_1, x_2) parallel to the sum axis $x_1 + x_2$. We do this via pair counting: we loop through all possible pairs of particles in an event (with the exception of self pairs) to construct the pair density. By filling histograms on the difference variables, $x_1 - x_2$, we are averaging over the sum axis.

The event-wise azimuth density can be represented as a sum over Dirac delta functions

$$\rho(x) = \sum_{i=1}^{n} r_i \delta(x - x_i), \tag{5.2}$$

where n is the number of particles and the r_i are weights determined by the physical context. For number correlations $r_i = 1$ but they could also represent the p_t or E_t of a particle. The two-particle density in one event is then the Cartesian product $\rho(x_1, x_2) = \rho(x_1)\rho(x_2)$

$$\rho(x_1, x_2) \quad = \quad \sum_{i=1}^{n} r_i^2 \, \delta(x_1 - x_i)\delta(x_2 - x_i) \tag{5.3}$$

$$+ \quad \sum_{i \neq j}^{n,n-1} r_i r_j \, \delta(x_1 - x_i)\delta(x_2 - x_j),$$

with the first term representing self pairs which we will ignore. In practice this event-wise density is histogrammed and then averaged over an event ensemble as explained in in Sec. 5.2.3.

Rather than describing this space in terms of x_1 and x_2 we can convert it to sum and difference variables $x_\Sigma = x_1 + x_2$ and $x_\Delta = x_1 - x_2$. The projection by averaging of the two-particle density onto x_Δ is mathematically equivalent to the standard autocorrelation. Consider a binned space x with bin width δ. The autocorrelation on a periodic variable x with period 2π is then

$$\begin{aligned} \rho_A(x_\Delta) &= \frac{1}{2\pi\delta} \int_{-\pi}^{\pi} dx'_\Sigma \int_{x_\Delta - \delta/2}^{x_\Delta + \delta/2} dx'_\Delta \, \rho(x'_1)\rho(x'_2) \\ &= \frac{1}{\pi\delta} \int_{x_\Delta - \delta/2}^{x_\Delta + \delta/2} dx'_\Delta \int_{\frac{-\pi + x'_\Delta}{2}}^{\frac{\pi + x'_\Delta}{2}} dx'_1 \, \rho(x'_1)\rho(x'_1 - x'_\Delta). \end{aligned} \tag{5.4}$$

If we take advantage of the periodicity of x then in the limit where the bin width goes to zero we get

$$\rho_A(x_\Delta) = \frac{1}{2\pi} \int_{-\pi}^{\pi} \rho(x')\rho(x' - x_\Delta)dx', \tag{5.5}$$

which is the standard definition of an autocorrelation for a periodic variable.

In Fig. 5.1 we illustrate two different averaging schemes for the case where the single-particle space has been pre-binned and for the case where the binning occurs on the difference variable directly [155]. In the first panel the autocorrelation is constructed as an average of diagonal combinations of microbins of a 2D histogram on (x_1, x_2) An autocorrelation can be constructed on an already binned space in this manner, but we will only be dealing with autocorrelations made directly from pair counting as illustrated the right panel.

The same pair counting procedure can be applied even if x is not periodic, however there are some additional complications. The autocorrelation of a periodic function always has the same period as the original function, but when we apply this method to a finite non-periodic space the range of x_Δ will be twice that of x. In addition, simple combinatorics tells us that pair counting will produce a triangular distribution peaked at the mean value

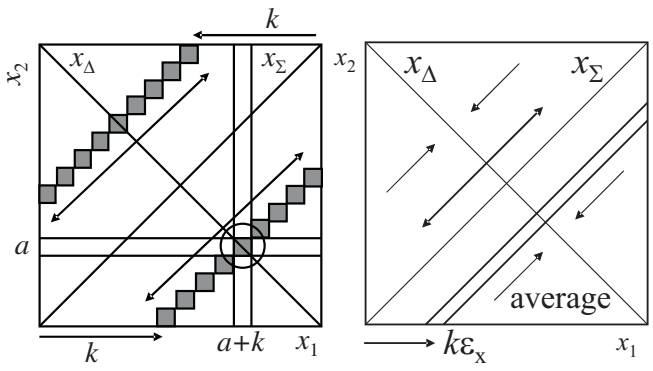

Figure 5.1: Autocorrelation averaging schemes on $x_\Sigma = x_1 + x_2$ for a prebinned single-particle space (left panel) and for pairs accumulated directly into bins on the two-particle difference axis (right panel) [155].

of x_Δ. It is a simple procedure to correct for this triangular bias, but it does mean that the statistical significance of bins at the extreme values of x_Δ will be significantly less than those in the center.

5.2.2 Correlation Spaces

Up to this point we have only discussed correlations on a generic variable x. Now let us consider the variables used in the analysis of heavy-ion collisions. The relevant variables we measure for tracks in the STAR TPC are azimuth angle ϕ, pseudorapidity η, and transverse momentum p_t. In a two-particle analysis we are therefore analyzing a six dimensional space, $(\eta_1, \eta_2, \phi_1, \phi_2, p_{t1}, p_{t2})$

It is possible to construct correlations on any pair of these variables, but for this analysis we will be focusing on η and ϕ while making cuts on p_t. The variables η and ϕ are treated equally in this analysis because they are both angular variables indicating the momenta of particles produced in the collision and it is natural to consider them simultaneously. One major distinction is that ϕ is periodic while η is not, but the correlation can still be constructed. The autocorrelation concept is not restricted to periodic boundary distributions or discrete Fourier transforms [57].

A 2D—or joint—autocorrelation is made by applying the pair-counting procedure to

two pairs of variables simultaneously. In this analysis it is typically a projection from the $(\eta_1, \eta_2, \phi_1, \phi_2)$ space onto the $(\eta_\Delta, \phi_\Delta)$ space. Although the details of the averaging schemes on η and ϕ differ because only ϕ is periodic the resulting autocorrelations are formally equivalent. The projection onto the difference variables is nominally exact on ϕ with an ideal detector but only approximate on η, depending on the validity of the "boost invariance" (stationarity) over the relevant pseudorapidity interval [155]. p_t can either be integrated to produce p_t-integrated correlations or we can define a set of p_t cut bins to do a p_t-dependent analysis.

Events are typically divided into bins on collision centrality, so we will study the evolution of correlation structures with centrality. We develop a complete description of correlations from the most peripheral to the most central collisions. p_t cuts serve as another tool which can be utilized to study correlation systematics. Since the two-particle p_t space is two-dimensional there are actually many ways to define p_t cuts. Chapter 6 will focus on p_t-integrated (inclusive p_t) correlations while Chapter 7 discusses a particular class of p_t cuts.

Centrality determination is done at the event level. The same analysis procedure is applied to different classes of events and the details of the analysis do not change. p_t cuts are a bit different in this respect since they are applied to particle *pairs* within an event. We need to construct sub-bins within an event for different pairs of particles based on the pair momentum in the two-dimensional (p_{t1}, p_{t2}) space. Pair density histograms are constructed for the angular variables as normal within the momentum sub-bins.

5.2.3 Event Ensembles

While the autocorrelation procedure is mathematically well-defined for a single event, in practice the number of particles in an event is far too small—even in central Au-Au collisions—to measure two-particle densities with any statistical accuracy. It is therefore essential to construct an average of the autocorrelations over many events. Even within a single event there can be many different physical processes which contribute to the correlation, but we know that the autocorrelation of a sum of uncorrelated distributions is the

sum of the corresponding autocorrelations. This doesn't change when averaging over many events. Assuming that the events being summed are similar enough to be dominated by the same physical processes—it is best not to sum events with drastically different properties—then in effect we are doing nothing more than increasing the number of terms being summed and therefore the statistical power of the final correlation.

It is interesting to note that for the full two-particle density on $(\phi_\Sigma, \phi_\Delta, \eta_\Sigma, \eta_\Delta)$ we should not expect there to be a lack of information on $(\phi_\Sigma, \eta_\Sigma)$ within a single event. This is because the overall position with respect to the detector *is* relevant for a single event. In particular, in an event with a reaction plane and particles correlated with respect to it there should be significant structure on ϕ_Σ within one event. But in practice there are not enough particles in one event to construct useful correlations of this form.

When we average over many events the information on $(\phi_\Sigma, \eta_\Sigma)$—which is not part of the autocorrelation—is lost while the information on $(\phi_\Delta, \eta_\Delta)$—the autocorrelation—is successfully averaged. The differences between particle positions do not depend on absolute position or orientation of the overall event. They are relative variables. This way we can access information in the two-particle correlations no matter how small the event-wise multiplicities are, so long as there is a sufficient number of collision events.

All of the quantities referred to so far in this chapter have been event-wise quantities. The ensemble average over events comes into play in Sec. 5.4.1. In order to avoid confusion in the following sections, we will refer to event-wise quantities with a tilde and quantities that are ensemble-averaged without a tilde.

5.2.4 Correlation Measures

A proper statistical measure can help us understand how these correlations scale with centrality, momentum, and other variables. In general the single-particle ensemble-averaged distribution $\rho(\eta, \phi)$ can have arbitrary structure. We wish to subtract a statistical reference structure from the two-particle distribution $\rho(\eta_1, \phi_1, \eta_2, \phi_2)$ to isolate "true" two-particle correlations. In this section we will only be considering weight $r_i = 1$ (from Eq. 5.2), or number correlations.

We construct correlation histograms both for pairs of particles taken from the same event (sibling pairs) and pairs of particles taken from different events (mixed pairs). The latter provides a reference $\rho_{\rm ref}$ that only contains information about the single-particle distribution. It is still affected by overall multiplicities and imperfections in the detector's acceptance. We use it to both eliminate detector artifacts and to create a measure with desirable scaling properties. Correlation amplitudes are extracted from pair ratio $\Delta\rho/\rho_{\rm ref} \equiv (\rho_{\rm sib} - \rho_{\rm mix})/\rho_{\rm mix} = \rho_{\rm sib}/\rho_{\rm mix} - 1$. This quantity has the advantage of only containing the ratio of $\rho_{\rm sib}$ and $\rho_{\rm mix}$. Detector artifacts can then be canceled out in the ratio when these quantities are properly normalized. $\Delta\rho/\rho_{\rm ref}$ is a per-pair measure.

Alternatively we may use $\Delta\rho/\sqrt{\rho_{\rm ref}}$, a per-particle measure that has useful scaling properties when the total number of charged particles—denoted n or n_{ch}—is varied. This measure is inspired by Pearson's normalized covariance converted to a density ratio [166]. We will see the advantages of this approach in Chapter 6. But in practice this is not a "safe" way to construct our correlation measure because detector artifacts will not be eliminated in this ratio. For this reason we sometimes use the expression $\Delta\rho/\sqrt{\rho_{\rm ref}}$ as a shorthand for $\sqrt{\rho_s}\Delta\rho/\rho_{\rm ref}$ where ρ_s is an ideal version of $\rho_{\rm ref}$ that is free from detector effects. In the case of angular correlations this is nothing more than a constant value (ρ_0) since within the STAR acceptance particles are emitted isotropically and the *only* structure in $\rho_{\rm ref}$ is detector artifacts. But that is not true for $y_t \times y_t$ correlations as the overall multiplicity is highly y_t-dependent. When comparing correlations in different multiplicity bins—such as when analyzing them as a function of centrality—a per-particle measure is preferred because a per-pair measure can be dominated by the change in multiplicity alone.

Given N events there are $N(N-1)$ possible mixed events. We are limited statistically by the number of sibling pairs, so there is no reason to calculate the correlations for all possible mixed events. Furthermore it is desirable to mix only "similar" events (similar properties) in order to avoid creating artifacts in the data. For this reason we typically bin events into multiplicity and z-vertex position classes and only match events with such properties for creating the mixed-pair reference.

This approach can be contrasted with the widely-used ZYAM (zero yield at minimum) method which should really only be applicable for narrow, well-separated peaks on azimuth.

The primary difference is in the normalization of mixed pairs to sibling pairs. The ZYAM method imposes the criterion that the minimum of the correlation histogram $\Delta\rho$ should have value zero and adjusts the background or $\rho_{\rm ref}$ normalization in order to achieve that. But if the physics signal contains distinct but overlapping peaks then it is possible that the true correlation value of the minimum of the histogram should be nonzero. The ZYAM normalization also affects the amplitudes of the peaks and can lead to questionable conclusions [164].

5.3 Reaction Plane-Dependent Correlations

The original goal of this research was to study minijet correlations relative to the reaction plane. This was thought to be achievable with methods similar to those used in three-particle correlations [9]. However, instead of describing the correlations with respect to a trigger particle, we would use the estimated event plane as the third "particle". As mentioned in Sec. 5.2.3 there is still information on the ϕ_Σ axis of the two-particle correlation if the correlations are shifted with respect to a well-defined event plane for each event.

This would be done by estimating the event plane for each event with the standard methods described in Chapter 4. Then a correlation similar to the standard (ϕ_1, ϕ_2) two-particle correlation can be constructed but with the reaction plane angle subtracted to make a $(\phi_1 - \psi_r, \phi_2 - \psi_r)$ correlation. We tested this on the same basic Monte Carlo model introduced in Sec. 4.4. The first panel of Fig. 5.2 is an example of what a standard (ϕ_1, ϕ_2) correlation looks like without subtracting the reaction-plane angle. Since we average over many events and the events are all randomly oriented with respect to our detector there is only information on the difference angle $\phi_\Delta = \phi_1 - \phi_2$.

In the second panel of Fig. 5.2 we use the true reaction-plane angle—known from the simulation—to do the subtraction. This is the ideal case, and does not reflect real experimental data. With each event shifted by this angle there is significant structure on the sum axis in addition to the difference axis. Even though there is a significant minijet term present in the simulation—though it is not necessarily correlated with the reaction plane—the data in this format is still dominated by v_2. To study minijet properties it would be necessary to subtract the large v_2 contribution.

In simulations we have access to the true reaction-plane angle, but that isn't an observable quantity in real data. So we wish to estimate the event-plane using the standard EP method. As described in Sec. 4.2.1, in order to eliminate self-pair biases it is standard practice to estimate a slightly different event plane for each particle using all particles in the event *except* that particle. When we attempted to use this approach with simulated data it differed dramatically from the ideal case with the true reaction-plane angle. A necessary but not sufficient criterion for any good reaction-plane estimation algorithm is that for uncorrelated data the $(\phi_1 - \psi_2, \phi_2 - \psi_2)$ plot should have no correlations induced by the reaction-plane estimation algorithm itself. In the third panel of Fig. 5.2 we apply this procedure to uniform random data and find that is not the case for the standard event-plane method. There is a significant correlation structure created by the algorithm for estimating the event plane.

The only way to avoid such artificial correlations is to completely exclude tracks that were used in the estimation of the reaction plane from the two-particle correlation. This is essentially the sub-event method. We select half of the particles in an event at random to estimate the event plane and use the other half to create the correlation. We find that this method does not introduce any correlations in uniform random data, though it does reduce the statistical significance of our measurement since we are only using half the particles. It also reduces the event-plane resolution. The fourth panel of Fig. 5.2 shows the result of applying this method to the Monte Carlo data. In this simplified case it compares favorably with the true reaction-plane method.

But this is still a rather idealized situation. The simulation was done with a perfect detector which requires no ϕ-weighting to estimate the event plane. The only non-flow effects came from small Gaussian clusters of particles and a simplified momentum-conservation algorithm. Real data would require more thorough analysis.

v_2 dominates these correlations, and if we wish to study the minijet structure with respect to the reaction plane v_2 must first be subtracted. There are complications, however. In the standard event-plane v_2 method imperfect estimation of the event plane necessitates the introduction of a quantity known as the event-plane resolution to "correct" v_2^{obs} (or really to make it equivalent to a two-particle correlation as we will see in Sec. 5.4.2). There is a

very similar problem here but imperfect estimation of the event plane doesn't only reduce the amplitude of v_2, it actually smears out the correlation along the sum axis. This alters the *shape* of the v_2 term, and the magnitude of that effect is dependent on the event-plane resolution. Furthermore, existing measurements of v_2 were significantly affected by nonflow effects and/or fluctuations and it is very difficult to apply them under these circumstances.

The original goal of this study was to compute a two-particle jet correlation relative to the event plane (effectively a three-particle correlation) in order to study minijets with respect to the Au-Au reaction plane. To really understand this however required a precise understanding of the v_2 background. The available methods gave a wide range of values that were not adequately understood. While the original goal seemed to have achieved limited success in simulations, this was not the case with real data. We needed to develop better methods for measuring v_2 accurately and directly using two-particle correlations.

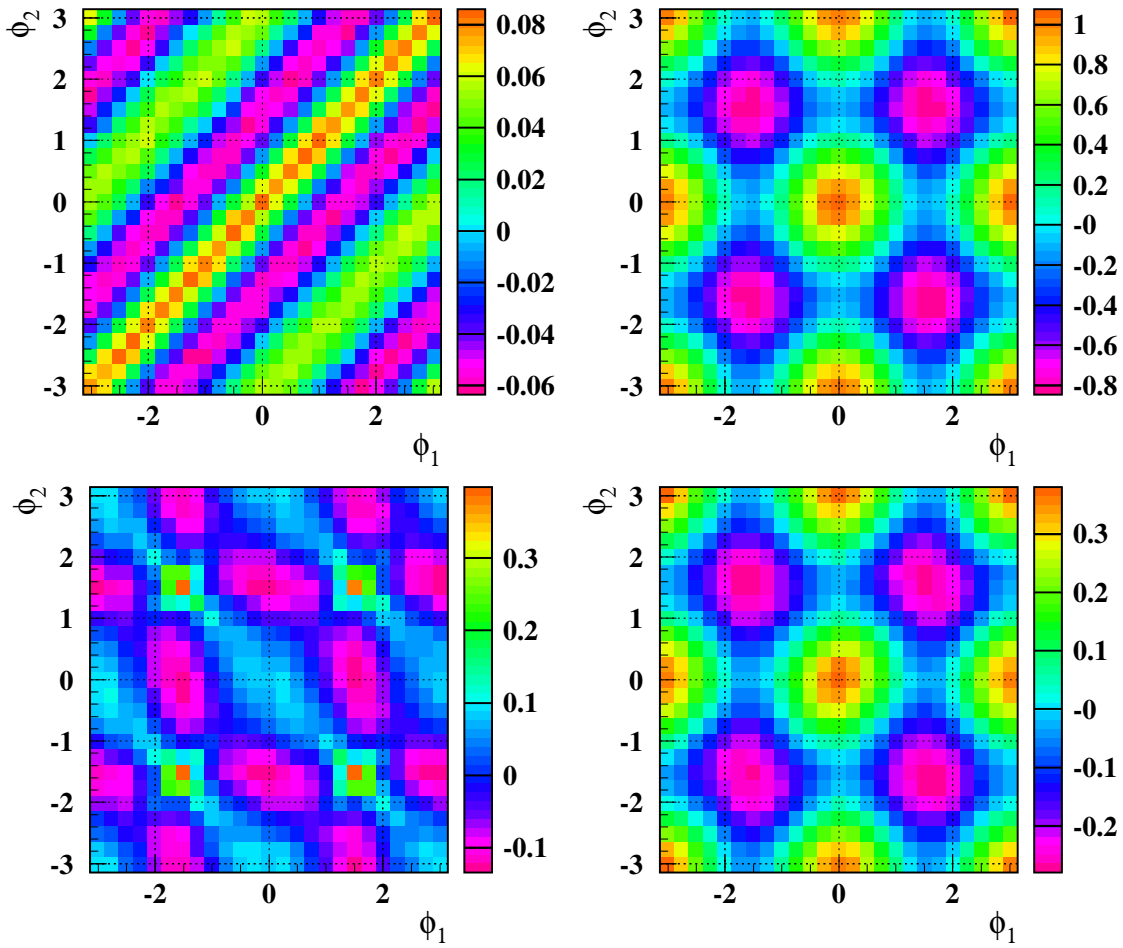

Figure 5.2: First Panel: A Monte Carlo calculation of a (ϕ_1, ϕ_2) correlation without any reaction-plane subtraction. Second Panel: The $(\phi_1 - \Psi_r, \phi_2 - \Psi_r)$ correlation of the same data using the true reaction plane from the Monte Carlo simulation. Third Panel: The $(\phi_1 - \Psi_2, \phi_2 - \Psi_2)$ correlation of uniform random data using an event plane estimated with the standard event-plane method. Fourth Panel: The $(\phi_1 - \Psi_2, \phi_2 - \Psi_2)$ correlation of the simulated data using a sub-event method.

5.4 Autocorrelation Algebra

We will now describe the detailed algebraic structure of azimuth autocorrelations, their relationship to standard v_2 measurements, and how we can interpret our results.

5.4.1 Fourier Transforms of Autocorrelations

We first consider correlations on azimuth alone. The Fourier transform of the event-wise single particle density on azimuth is

$$\begin{aligned} \tilde{\rho}(\phi) &= \sum_{m=-\infty}^{\infty} \frac{\tilde{\mathbf{Q}}_m}{2\pi} \exp(i\, m\phi) \\ &= \frac{Q_0}{2\pi} + 2\sum_{m=1}^{\infty} \frac{\tilde{Q}_m}{2\pi} \cos(m[\phi - \Psi_m]), \end{aligned} \tag{5.6}$$

where boldface $\tilde{\mathbf{Q}}_m$ is an event-wise complex amplitude, $\tilde{Q}_m$ is its magnitude and Ψ_m its phase angle. Since $\rho(\phi)$ is a real function we arrive at the second line. $\tilde{Q}_m/2\pi = \rho_m$ is the amplitude of the density variation associated with the m^{th} sinusoid, and in the case of number correlations $\tilde{Q}_m$ is the number of particles in $2pi$ for a uniform density [166].

Now we apply Eq. (5.6) to the autocorrelation definition on a periodic variable in Eq. (5.5)

$$\begin{aligned} \tilde{\rho}_A(\phi_\Delta) &= \frac{1}{2\pi}\int_{\pi}^{\pi} d\phi \left(\sum_{m=-\infty}^{\infty} \frac{\tilde{\mathbf{Q}}_m}{2\pi} \exp(im\phi)\right)\left(\sum_{m'=-\infty}^{\infty} \frac{\tilde{\mathbf{Q}}^*_{m'}}{2\pi} \exp(-im'[\phi+\phi_\Delta])\right) \\ &= \sum_{m=-\infty}^{\infty} \frac{\tilde{Q}_m^2}{[2\pi]^2} \exp(-im\phi_\Delta) \\ &= \frac{\tilde{Q}_0^2}{[2\pi]^2} + 2\sum_{m=1}^{\infty} \frac{\tilde{Q}_m^2}{[2\pi]^2} \cos(m\phi_\Delta). \end{aligned} \tag{5.7}$$

We see that the autocorrelation of a Fourier series with coefficients $\tilde{Q}_m/2\pi$ is itself a Fourier series with coefficients $[\tilde{Q}_m/2\pi]^2$. The phase angle Ψ_m has been eliminated as the sinusoids are in terms of angle difference ϕ_Δ. This is an application of the Wiener-Khintchine theorem which relates power-spectrum elements to the autocorrelation.

The reverse transform is

$$\tilde{Q}_m^2 = n^2\langle r\cos(m[\phi - \Psi_m])\rangle^2 \tag{5.8}$$

$$
\begin{aligned}
&= 2\pi \int_{-\pi}^{\pi} d\phi_\Delta \tilde{\rho}_A(\phi_\Delta) \cos(m\phi_\Delta) \\
&= \sum_{i,j=1}^{n} r_i r_j \cos(m[\phi_i - \phi_j]) \\
&= n\langle r^2 \rangle + n(n-1)\langle r^2 \cos(m\phi_\Delta) \rangle \\
&\equiv \tilde{Q}^2_{ref} + \tilde{V}^2_m
\end{aligned}
$$

where the angle brackets represent event-wise averages. The term denoted $\tilde{Q}^2_{ref}$ is a "white-noise" background and the term denoted $\tilde{V}^2_m$ is the true two-particle azimuth correlation.

Since the terms are positive definite the relationship also holds for ensemble-averaged quantities. The ensemble-averaged Fourier transform is

$$\rho_A = \frac{Q^2_0}{[2\pi]^2} + 2 \sum_{m=1}^{\infty} \frac{Q^2_m}{[2\pi]^2} \cos(m\phi_\Delta), \tag{5.9}$$

while the reverse transform is [166]

$$Q^2_m = \overline{n\langle r^2 \rangle} + \overline{n(n-1)\langle r^2 \cos(m\phi_\Delta) \rangle}, \tag{5.10}$$

where the convention $Q^2_m = \overline{\tilde{Q}^2_m}$ has been adopted.

Recall from Sec. 4.2.1 that v_m coefficients are defined by a Fourier series in the single-particle density. We wish to relate the power-spectrum $\tilde{Q}_m$ coefficients to the conventional "flow" measure. To do this insert the event-wise reverse Fourier transform Eq. (5.8) into the ensemble-averaged Eq. (5.9). Note that there is no cross-term between the white-noise background and true two-particle correlation because they are uncorrelated by definition. The result is

$$\rho_A(\phi_\Delta) = \frac{\overline{n\langle r^2 \rangle}}{2\pi} \delta(\phi_\Delta) + \frac{\overline{n(n-1)\langle r^2 \rangle}}{[2\pi]^2} + 2 \sum_{m=1}^{\infty} \frac{V^2_m}{[2\pi]^2} \cos(m\phi_\Delta). \tag{5.11}$$

The first term is the self-pair term, which in our analysis is simply excluded. The second term is a uniform component $V^2_0 = \overline{n(n-1)\langle r^2 \rangle}$. The third term is the sinusoidal correlation structure. This is the basis for the relationship between two-particle correlations and conventional flow measurements.

We will now construct the quantity $\Delta\rho_A/\sqrt{\rho_{A,ref}}$. Assume for simplicity that our factorizable reference autocorrelation is $\rho_{A,ref}(\phi_1, \phi_2) = \rho_0(\phi_1)\rho_0(\phi_2)$ is a constant on ϕ—reasonable if ignoring detector artifacts—equal to $\rho_0 = \bar{n}/(2\pi\Delta\eta) \simeq d^2n/d\eta d\phi$, where $\Delta\eta$

is the acceptance on η. $\Delta\rho_A = \rho_A - \rho_{A,ref}$ which gives

$$\begin{aligned} \frac{\Delta\rho_A}{\sqrt{\rho_{A,ref}}} &= \frac{\sigma_n^2 - \bar{n}}{2\pi\bar{n}} + 2\sum_{m=1}^{\infty}\frac{V_m^2}{2\pi\bar{n}}\cos(m\phi_\Delta) \\ &\equiv \frac{\Delta\rho_A[0]}{\sqrt{\rho_{A,ref}}} + 2\sum_{m=1}^{\infty}\frac{\Delta\rho_A[m]}{\sqrt{\rho_{A,ref}}}\cos(m\phi_\Delta), \end{aligned} \tag{5.12}$$

where σ_n is the standard deviation. The first term is the density ratio average over the acceptance. The second term directly relates the correlations in this measure to the usual sinusoid V_m coefficients.

5.4.2 Relationship to v_m coefficients

Measuring the true v_m on ϕ alone in the presence of "nonflow" effects is very difficult. However it is possible to calculate a 2D correlation simultaneously on ϕ and η and use the characteristic η dependence to distinguish different physical contributions. This is because "flow" and "nonflow" contributions have very different η dependence. But first let's assume that there are only sinusoidal correlations. We will also omit the r_i weights for simplicity.

Now recall the definition of $v_m\{EP\}$ from Section 4.2.1

$$v_m\{EP\} = \frac{v_m^{obs}}{\langle\cos(m(\psi_m - \psi_r))\rangle}. \tag{5.13}$$

The two-particle correlation density V_m^2 is:

$$V_m^2 = \sum_{i=1}^{n}\sum_{j\neq i}^{n-1}\vec{u}(m\phi_i)\cdot\vec{u}(m\phi_j) = n^2 v_m^2\{2\}, \tag{5.14}$$

where n is the particle multiplicity of an event and $\vec{u}$ are unit vectors. The second part of the above expression introduces the relationship to the two-particle cumulant method, denoted by $v_2\{2\}$. The V_m here are strictly Fourier components of the total two-particle azimuth density and include "nonflow" effects that might be better described by non-Fourier terms.

If we use Eq. (4.3) in Eq. (5.14) then we arrive at the following relationship:

$$V_m = n\left\{\frac{1}{n}\sum_{i=1}^{n}\vec{u}(m\phi_i)\right\}\cdot\vec{u}(m\psi_m)\frac{Q_m}{V_m}. \tag{5.15}$$

In Ref. [166] an expression for the event-plane resolution was derived:

$$\langle\cos[m(\psi_m - \psi_r)]\rangle \approx \sqrt{\frac{n-1}{n}}\frac{V_m}{Q_m}. \tag{5.16}$$

Inserting this into Eq. (5.15) gives:

$$V_m \approx n \frac{v_m^{obs}}{\langle \cos(m(\psi_m - \psi_r)) \rangle} = n v_m\{EP\}, \tag{5.17}$$

recalling the definition of $v_2\{EP\}$ in Eq. 4.6. Thus we find that the event-plane method of measuring v_2, while often presented using different language, is nothing more but a type of two-particle correlation. This means that direct comparison between event-plane and autocorrelation methods is reasonable.

The Fourier coefficients of the correlation amplitude in Eq. 5.12 can be compared to the standard v_2 measure with the relation $\Delta\rho[m]/\sqrt{\rho_{ref}} = \rho_0(b) v_m^2$ where $\rho_0(b) = dn_{ch}/2\pi d\eta$. A simple Fourier decomposition would be all that is necessary if the only sources of correlations were related to flow. However, in real data there is also a significant contributions from "nonflow" terms, which have very different structure.

5.4.3 Gaussian Correlations

We observe structures besides sinusoids in data. One of the most common form of correlation we see are Gaussian peaks. There are several physical processes that can produce Gaussian peaks, such as minijets or HBT correlations. Any process that produces correlated clusters of particles has a tendency to make Gaussian correlations centered at the origin of $(\eta_\Delta, \phi_\Delta)$.

The autocorrelation of a single Gaussian peak is also a Gaussian peak. For a single-particle density of the form

$$\tilde{\rho}(x) = e^{-x^2/2\sigma^2} \tag{5.18}$$

the autocorrelation is then

$$\begin{aligned} \tilde{\rho}_A(x_\Delta) &= \int_{-\infty}^{\infty} e^{-x'^2/2\sigma^2} e^{-(x'-x_\Delta)^2/2\sigma^2} dx' \\ &= \int_{-\infty}^{\infty} e^{-(2x'' + \frac{1}{2}x_\Delta^2)/\sigma^2} dx'' \\ &= \sigma\sqrt{\pi} e^{-x_\Delta^2/4\sigma^2}, \end{aligned} \tag{5.19}$$

which other than the overall constant is just the same Gaussian with a $\sqrt{2}$ larger width. This was done for a non-periodic autocorrelation, however on a periodic variable there would

be a periodic array of Gaussians with centers shifted by 2π, 4π, etc. But the integral is the same as when integrating a single Gaussian from $-\infty$ to ∞.

However, a single-particle density with only one Gaussian peak is not a realistic scenario. What we actually observe in some real events is a number of Gaussian features, and there can be cross-terms between them. But the correlation term produced by particles within a single peak is *always* centered at $x_\Delta = 0$. This means that any Gaussian peaks in the single-particle correlation will contribute to a single peak at $x_\Delta = 0$. However the cross-terms *between* peaks will produce many peaks in the correlation, the positions of which can vary due to differing separation between peaks.

That is within a single event, but when we take the ensemble average over many events—or indeed if the number of peaks in a single event was large enough, though this is physically unlikely—in the absence of correlations between different peaks the cross-terms will average out to a constant background. But if some peaks are correlated then we will see that in the final correlation. For example, conservation of momentum will tend to produce back-to-back (dijet) peaks that result in another correlation centered at $\phi_\Delta = \pi$.

This peak will be elongated on η because of the nature of our coordinate system. The opposite momentum of a particle traveling in direction ϕ_i is $\phi_i - \pi$. This means that the difference between the emission angles of two particles with opposite momentum on azimuth is π. But even if two particles have opposite momenta on pseudorapidity—which isn't even necessarily true—that implies a change in sign from η_i to $-\eta_i$. The difference is then $2\eta_i$, which does nothing to constrain the correlation on η_Δ unless the single-particle distribution itself has an η-dependence. Within the STAR acceptance the η-dependence of the multiplicity distribution for most events is approximately flat and therefore we can expect correlations from momentum conservation to be flat on η_Δ.

Of course processes besides back-to-back jets must still conserve momentum. In events at RHIC with many produced particles it is possible to have thermal momentum conservation among most particles in an event. This produces a correlation structure which can be indistinguishable in shape from momentum conservation in dijets, though it would be expected to have different scaling properties with centrality, for instance.

5.5 Fit Models

The greatest strength of the autocorrelation method—its sensitivity to even small sources of correlations—can also be its greatest weakness. Since multiple distinct physical processes can contribute to observed correlations, direct comparison to simplified physical models—which may only account for a subset of what occurs in a nuclear collision—can be ambiguous. Of course an accurate model of every physical process in a nuclear collision would have to be consistent with the correlation data, but no such model exists. Instead we can isolate distinct components of a correlation by fitting them with model functions.

5.5.1 Observed Structures

So far we have compared these two-particle correlations to conventional v_2 measures under the assumption that all of the correlation structure present is naturally described in terms of a Fourier series expansion on azimuth. In real data that is not the case and it is necessary to account for other structures in our analysis. By using fits to the 2D correlation structure we can use the information on azimuth and pseudorapidity simultaneously in order to distinguish different correlation structures.

Our fit model is inspired by observation of detailed correlations in proton-proton collisions [138, 139]. As will be shown in Chapter 6, very peripheral Au-Au collisions are similar to proton-proton collisions. Thus, if we want a complete understanding of the Au-Au collision system as a function of centrality it is natural to start by understanding proton-proton correlation structures.

The principal structures we observe in proton-proton collisions are a 2D same-side Gaussian peak, a 1D Gaussian on η_Δ, and a dipole component $\cos(\phi_\Delta)$. There is also a sharp peak at the origin representing electron pairs and HBT effects which we model with a 2D exponential. The 2D Gaussian peak can be largely attributed to minijet production, as will be shown in Chapter 9. The dipole can be attributed to momentum conservation, whether primarily from back-to-back jet production or thermal momentum conservation. The 1D Gaussian on η_Δ is related to soft physics (projectile dissociation) and can be seen in the cuts made in Sec. 3.1.3.

When we go from the proton-proton collision system to heavy ions we find that all of these terms are still present and one additional term must be included: a quadrupole component $\cos(2\phi_\Delta)$. This is the term which directly corresponds to the conventional measure v_2. In order to measure the azimuth quadrupole we fit all components with a 2D model and extract the quadrupole term, which can then be related to the conventional v_2 measure as described above.

With all of these terms included the fit function is,

$$\begin{aligned} F &= A_D \cos(\phi_\Delta - \pi) + A_Q \cos(2\phi_\Delta) + A_{\rm soft} e^{-\frac{1}{2}\left(\frac{\eta_\Delta}{\sigma_{\rm soft}}\right)^2} + A_{2D} e^{-\frac{1}{2}\left\{\left(\frac{\phi_\Delta}{\sigma_{\phi_\Delta}}\right)^2 + \left(\frac{\eta_\Delta}{\sigma_{\eta_\Delta}}\right)^2\right\}} \\ &+ A_{exp} e^{-\left\{\left(\frac{\phi_\Delta}{w_{\phi_\Delta}}\right)^2 + \left(\frac{\eta_\Delta}{w_{\eta_\Delta}}\right)^2\right\}^{1/2}} + A_0. \end{aligned} \tag{5.20}$$

Including the amplitudes and widths there are 11 fit parameters: A_D, A_Q, A_0, $A_{\rm soft}$, A_{2D}, A_{exp}, σ_0, σ_{η_Δ}, σ_{ϕ_Δ}, w_{η_Δ}, and w_{ϕ_Δ}. We will see in Chapter 6 that these 11 parameters successfully describe heavy-ion collision data accurately from the most peripheral to the most central collisions.

5.5.2 Fit Methods

In order to fit these 2D histograms we invoke a standard χ^2 fit using the MINUIT MIGRAD minimization package [111]. Parameter errors are estimated using MINOS [111]. The fit function used is Eq. 5.20 with 11 free parameters. Six of these parameters are amplitudes and can be fit quite easily, but five terms correspond to the widths of Gaussian and exponential terms making this a nonlinear fit process.

Of course, as in any nonlinear fit there is no guarantee that the local minimum found by MIGRAD is the true global minimum. Unfortunately, there is no easy solution to this problem so we have have adopted a brute-force approach. Rather than simply fitting the histograms once, we first establish reasonable limits on the values of the parameters based on the range of the histogram. Overall amplitudes can vary dramatically depending on the correlation measure used, but common-sense limits can be adopted. For instance, the amplitude of a sinusoid term should never exceed the difference between the maximum and minimum points on the histogram. Limits are placed on the widths of Gaussian terms based

on experience observing these widths over a wide range of centrality and p_t conditions, but the limits are fixed for all histograms.

Once reasonable limits have been established it is possible to fit the histograms by randomly selecting starting values from within the acceptable ranges of parameters. The fitting process can then be repeated hundreds of times with a different random starting point each time. We seed the fitting algorithm with random starting points in the allowed parameter space and then repeat this procedure for each histogram 500-1000 times. This produces a distribution of χ^2 values for each histogram that provides a check on the stability of the fit. The the with the overall minimum χ^2 is taken to be the optimal fit, but with enough fitting attempts we can also learn something about the stability of the fitting procedure.

This procedure may seem unnecessary when fitting a few histograms, but as we will see in Chapter 7 when exploring the combined space of centrality and p_t for different collisions energies and studying the impact of variations on our fit model we can be fitting hundreds or even thousands of different histograms. Having a consistent and reproducible method for producing optimal fits is essential.

Chapter 6

P_T-INTEGRAL AZIMUTH QUADRUPOLE

6.1 Applied Correlations

As described in Chapter 5, we construct minimum-bias angular autocorrelations by considering all possible pairs of particles in an event within a defined acceptance and track quality standards. In general one can consider structures in the pair density on 6D momentum space $(p_{t1}, \eta_1, \phi_1, p_{t2}, \eta_2, \phi_2)$. In this analysis we study p_t-integrated correlations on the angular subspace $(\eta_1, \phi_1, \eta_2, \phi_2)$, where the angular variables for relativistic collisions are pseudorapidity η and azimuth ϕ.

6.1.1 Data Selection

Events are selected using the STAR Minbias trigger which requires a minimum energy threshold deposited in the Central Trigger Barrel, coincidence in both Zero-Degree Calorimeters, and a reconstructed event vertex as discussed in Chapter 2. Primary vertices were required to be within 25 cm of the TPC's axial center, well within the TPC's fiducial volume which extends to ± 100 cm in the longitudinal direction.

Once an event has been selected, pairs are formed from tracks measured in the TPC. However not all tracks in an event are necessarily suitable for a given analysis so track cuts are imposed. Track cuts can be set for kinematic restrictions, track reconstruction quality, and particle identification.

Kinematic cuts include restrictions on the momentum of measured particles as well as their angular (azimuth and pseudorapidity) variables. We wish to be as inclusive as possible in this analysis so the entire 2π azimuth range is included and $|\eta| \leq 1$. While the TPC actually does extend beyond $\eta = 1$, for very large η the reconstruction efficiency drops rapidly which can introduce correlation artifacts. Therefore these regions have been excluded [84].

The transverse momentum p_t of each particle is restricted to be between the STAR TPC's smallest measurable momentum $p_t = 0.15$ GeV/c and an upper limit of $p_t = 15$ GeV/c. This limit was chosen because very high p_t tracks can be problematic for track reconstruction. High momentum tracks do not curve much in the TPC's magnetic field so it can be difficult to even determine the sign of their charge.

Tracks are reconstructed by fitting hit points in the TPC. We can place restrictions on the number of fit points used for tracks that we accept. A large number of track fragments have only 11-13 points. To ensure that we are using good tracks we require them to have a minimum of 15 fit points. In addition, based on a track's position in the TPC we can get a rough estimate of the expected number of fit points. We only accept tracks with at least 52% of their expected fit points. This is to avoid problems with split tracks: points produced by a single particle that are actually reconstructed as two separate tracks. We also make cuts on the χ^2 of the helix fit to the tracks fit points to be within $0.0 < \chi^2 < 3.0$. And we exclude tracks with errors flagged by the track reconstruction program.

The distance-of-closest-approach (DCA) cut of a reconstructed track is used to distinguish the primary particles produced in the collision from secondary particles produced from weak decays or interaction with the detector material. We restrict the DCA of a track to be within 3 cm of the primary vertex which accepts a large fraction of true primary hadrons in addition to approximately 12% background contamination from weak decays and interactions with the material in the detector [21, 11].

This analysis does not deal directly with particle identification. However, there is a simple PID cut made in order to reduce the background from electrons and positrons, typically produced as pairs from photon conversions. This cut is made based on the dE/dx (energy loss per unit path length) in the TPC. Completely distinguishing electrons from hadrons with dE/dx measurements in STAR is impossible, and we only make this cut in regions were the electron band is distinct. Particles with dE/dx within 1.5σ of the expected values for electrons in the momentum ranges $0.2 < p < 0.45$ GeV/c and $0.7 < p < 0.8$ GeV/c are excluded. This cut reduces but does not eliminate the electron background. However, more aggressive cuts would affect our hadron correlations. Finally, we only accept particles with charge $\pm e$.

6.1.2 Event Mixing

As explained in Chapter 5, we combine pairs events in order to construct the mixed-pair correlation reference. If the events being paired have significantly different physical properties this can introduce artifacts in the correlations. Given N events there are $N(N-1)$ possible event pairs, but there is little statistical advantage to having the number of mixed event pairs exceed the number of events. Therefore we only use a subset of the possible event pairs and establish criteria for determining which events should be paired for mixing.

The first criterion is multiplicity. Certain correlation structures can vary rapidly with multiplicity, so mixing events with significantly different multiplicities can be problematic. We determine centrality from multiplicity, so the simplest rule we can make is to do event mixing only with events within the same centrality bin. In the more-peripheral bins this is sufficient, but in the more-central bins a single bin corresponds to a much larger range of multiplicities. We therefore divide the most central bins into additional sub-bins $\Delta n_{ch} = 50$ wide.

We also restrict event pairs based on the primary vertex z position. From our event cuts all events are restricted to $|z| \leq 25$ cm, but events for mixing are placed into 10 z-vertex bins that are each 5 cm wide which cover the full 5 cm range. Events are only paired with other events in the same z-vertex bin. Correlations are calculated separately for each multiplicity and z-vertex sub-bin and the final correlation is constructed from a weighted average of the correlations in each sub-bin.

6.1.3 Pair cuts

Since all two-particle correlations are constructed from particle-pair densities, we can also make cuts on particle pairs in addition to cuts on tracks and events. At first it may seem counter-intuitive, but pair cuts can actually avoid significant issues with tracks lost in the event reconstruction due to merging and crossing in the TPC.

There is already a track cut based on fit points designed to remove artifacts when a single track is reconstructed as two or more tracks. But the reverse process, called merging, can also happen when two nearby tracks are reconstructed as a single track. This creates a

pair loss which is highly biased towards closely-correlated tracks. The pair loss means that the density of sibling pairs with small angular separations is suppressed. In the mixed-event reference there is no angular bias. Track losses affect the correlation amplitude, so the final correlation pair ratio is suppressed for small η_Δ and ϕ_Δ [84].

In addition to track merging there can be pair losses from track crossings. When two tracks cross in the TPC there is a much greater chance of one or both tracks being reconstructed as split tracks. Since we make a track cut to remove split tracks, this means that tracks that cross are more likely to be excluded and further pair loss is produced. This pair suppression also depends on the total density of tracks in the TPC—higher density increases the chance of tracks crossing—so the effect is centrality-dependent.

Unlike track merging, track crossing affects particles with a small η_Δ separation but over a broad range of ϕ_Δ because different particles can bend different amounts in the magnetic field, or even in the opposite direction if the two particles have different charges. But the magnetic field only affects the particle's position in ϕ so the pair losses are still biased towards small η_Δ.

These pair losses can be corrected by making cuts that remove the *mixed-event reference pairs* as well as sibling pairs. If the pair loss is present in the reference as well as the sibling pairs then it will be corrected in the ratio. To avoid losses from merging tracks we cut particles with separations of 5 cm or less and to avoid losses from crossing tracks we cut particles with average longitudinal separations less than 5 cm [84].

6.1.4 Event-based Pileup Cut

Two-particle correlations of this form are very sensitive to pileup effects. Pileup occurs when there is sufficient beam luminosity such that particles from untriggered collisions in a different bunch crossing may appear in readout of a triggered collision event. The standard STAR track reconstruction procedure significantly reduces pileup effects, however some tracks may still be misidentified as belonging to the triggered event. The amount of pileup depends on the luminosity RHIC was run at, which varies significantly between different runs. About 0.5% of Run 4 events used in this analysis are estimated to contain

pileup tracks while only about 0.05% of Run 2 events do [37]. Despite these small numbers, pileup can have a real impact on the observed correlation structures. Since pileup tracks are biases towards large pseudorapidity values there is a "W"-shaped η_Δ-dependent correlation between pileup tracks and true tracks in the event. The pileup structure has no significant dependence on ϕ_Δ.

Events containing pileup tracks are identified by looking for distinctive patterns in the event-wise track end-point distributions in the longitudinal drift direction of the TPC that result from the bi-directional drift of the STAR TPC [37]. Particle tracks from pileup are either split by the TPC's central membrane or truncated before the TPC readout plane. But this cut is designed to look for patterns in the ensemble of tracks in an event, not on a track-by-track basis. So it can be used only to throw out whole events that contain pileup tracks. For this reason it is still necessary to have good track reconstruction that minimizes the number of pileup tracks or else we would be forced to throw out a significant fraction of events.

This procedure also does not completely eliminate pileup. However, if we calculate correlation histograms both with and without the pileup cut the difference between the two correlation histograms tells us the shape of correlations that come from pileup. A centrality-independent pileup detection efficiency $(1-f) = 0.25 \pm 0.1$ is assumed for this analysis based on the fraction of pileup events with insufficient tracks crossing the central membrane to be identified as pileup [37]. We then scale the pileup correlation by this efficiency and subtract that from the correlations with no pileup filter to estimate the real pileup-free correlation.

6.2 Two-Particle Correlations on Energy and Centrality

We wish to analyze correlation data to study the azimuth quadrupole component, which is the term most closely related to v_2. Rather than just treating the quadrupole contribution to these correlations as a background for jets or other physics, we wish to use the correlations themselves as a way to measure v_2. This requires an accurate fit model and a physical interpretation of the fit components.

6.2.1 Data Sets

We analyzed data from the STAR's TPC at a uniform 0.5 T magnetic field at collision energies of $\sqrt{s_{NN}} = 62$ and 200 GeV. As mentioned in Chapter 2 we use a minimum-bias trigger which requires a coincidence between the ZDC and CTB. The event, track, and pair cuts described above are applied.

This analysis used 6.7 million events at $\sqrt{s_{NN}} = 62$ GeV from RHIC Run 4 (in 2004) and 1.2 million events at $\sqrt{s_{NN}} = 200$ from RHIC Run 2 (in 2001). Older Run 2 data were used because RHIC operated at a much lower luminosity during early runs which produced a very clean data set with minimal pile-up. For the p_t-integrated analysis there was sufficient statistics in this dataset. For the p_t-differential analysis presented in the next chapter more events are required for sufficient statistics and the Run 4 data is used for 200 GeV collisions as well.

The centrality of each event is determined by the measured charge multiplicity, n_{ch}. We have found that it is important to use the same pseudorapidity acceptance $|\eta| < 1$ to determine centrality that is used for the correlation analysis. A standard reference multiplicity used in STAR is defined in the region $|\eta| < 0.5$. But if we base our analysis on this reference multiplicity significant artifacts arise in the correlation histograms due to canonical suppression. Correlations within the restricted reference-multiplicity pair acceptance are suppressed relative to those outside of it.

We determine centralities with the method developed in [169] based on the observed charged particle multiplicity in the TPC. There are nine $\sim 10\%$ bins from 100% (most peripheral) to 10% (most central), and the last 10% is divided into two 5% bins. We usually express centrality with the average path length parameter ν defined in Sec. 2.2.3.

6.2.2 2D Correlations

Following the procedure described in Chapter 5 we constructed 2D two-particle angular correlations on $(\eta_\Delta, \phi_\Delta)$ for the desired p_t acceptance and 11 centrality bins. Fig. 6.1 shows the correlations from 200 GeV Au-Au collisions and Fig. 6.2 shows the correlations from 62 GeV collisions. These correlations use the per-particle correlation measure $\Delta\rho/\sqrt{\rho_{ref}}$.

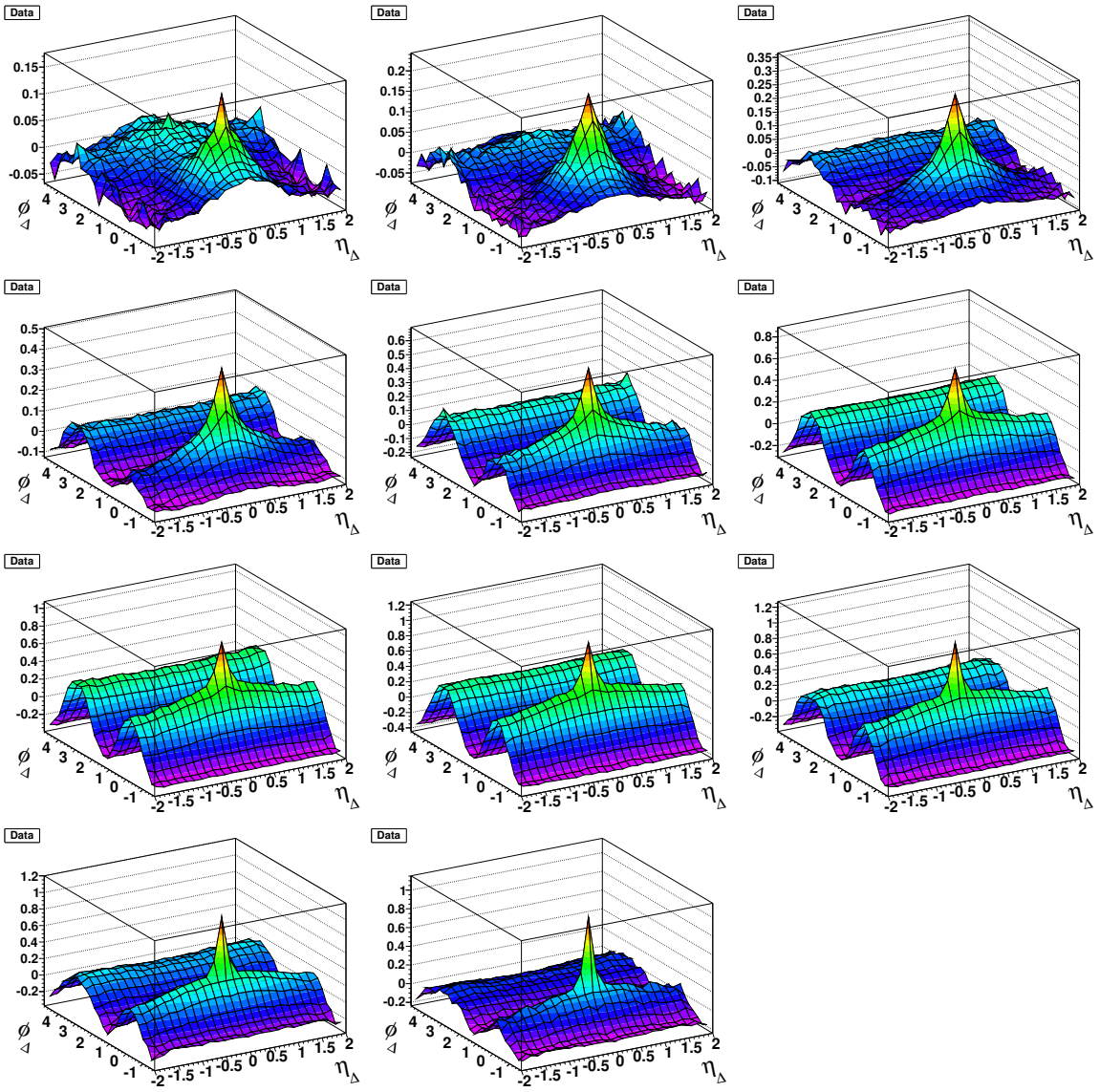

Figure 6.1: $\Delta\rho/\sqrt{\rho_{\mathrm{ref}}}$ data histograms for 200 GeV p_t-integrated correlations in 10% fractional centrality increments for the first 9 bins from 90-100% central collisions in the top right to 10-20% central collisions on the third line. The 0-10% range has been split into two bins, the last two histograms being 5-10% and 0-5% central collisions.

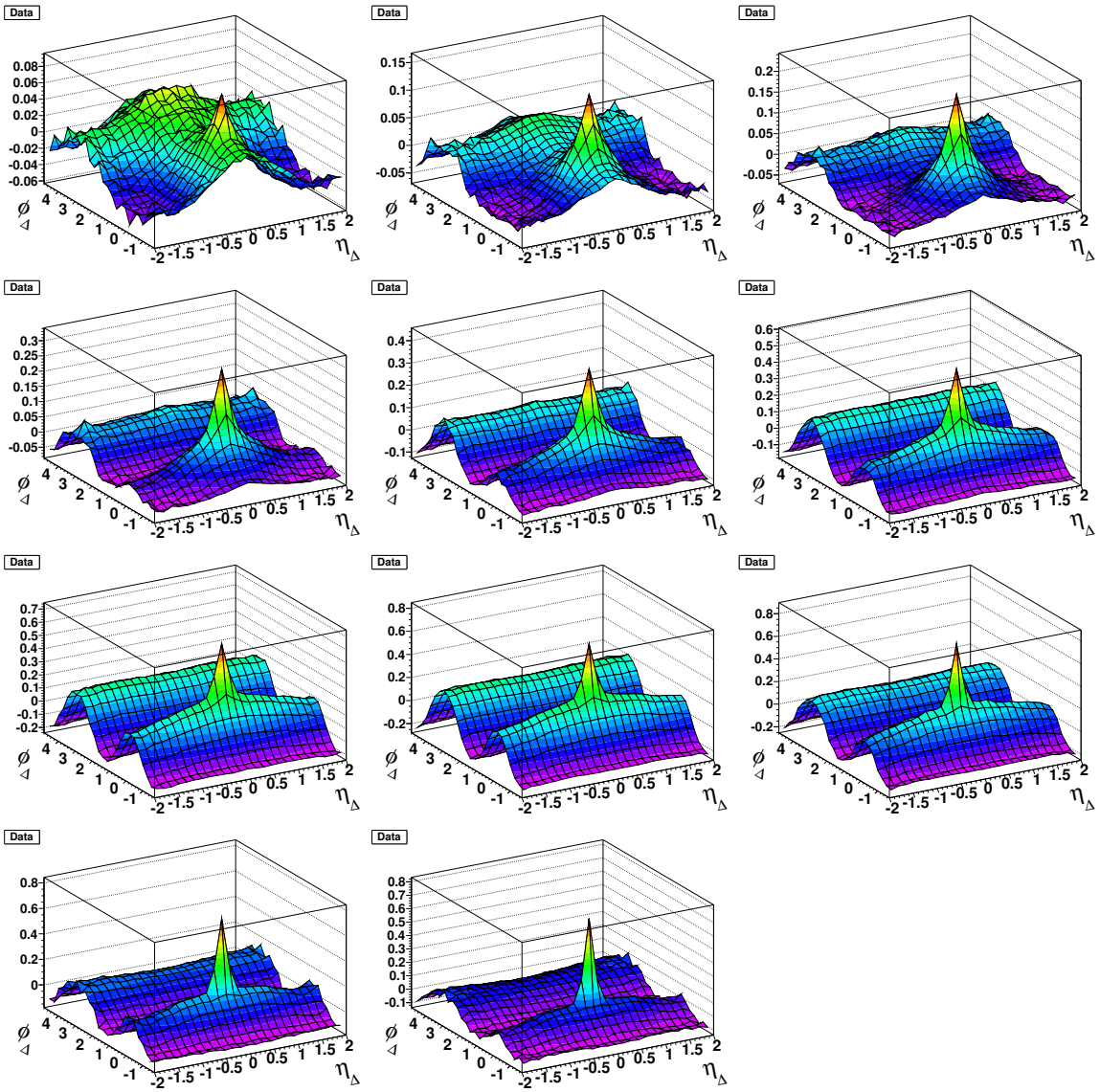

Figure 6.2: $\Delta\rho/\sqrt{\rho_{\mathrm{ref}}}$ data histograms for 62 GeV p_t-integrated correlations in 10% fractional centrality increments for the first 9 bins from 90-100% central collisions in the top right to 10-20% central collisions on the third line. The 0-10% range has been split into two bins, the last two histograms being 5-10% and 0-5% central collisions.

p_t-integrated 2D angular autocorrelations contain two dominate types of structure: η_Δ-dependent peaks and η_Δ-independent sinusoids $\cos(\phi_\Delta)$ and $\cos(2\phi_\Delta)$, where the $\cos(2\phi_\Delta)$ sinusoid can be identified with "elliptic flow", and the $m = 2$ Fourier component of the remaining structure is largely responsible for "nonflow". In this chapter we will focus primarily on the sinusoidal structures. In Chapter 9 we will return to discussing the peak structures.

6.2.3 Fits to 2D Correlations

The correlation data for each energy and centrality were fitted with a six-component model function that was given in Eq. 5.20 and motivated by structure observed in data from 200 GeV p-p collisions [138]. Figures 6.3 through 6.6 show the fits and residuals for all centralities from 200 GeV and 62 GeV Au-Au collisions. The eleven-parameter fit does an excellent job of describing 2D data for both energies and all centralities.

Figure 6.7 shows the major fit parameters as a function of centrality parameter ν. One of the most visibly striking features is the sudden increase of the same-side peak amplitude and η width above mid-central ($\nu \approx 3$) collisions. There is no corresponding kink in the quadrupole term or other parameters that corresponds to this sudden increase. The point where the same-side peak starts to increase rapidly is sometimes referred to as the sharp transition [84, 37]. This will be a major point when discussing a conjectured "ridge" structure in Chapter 9.

Here we focus on the quadrupole term and its relation to conventional v_2 measures. As described in Chapter 4, v_2 can be directly related to the $\Delta\rho/\sqrt{\rho_{\rm ref}}$ quadrupole amplitude by

$$A_Q\{2D\} = \frac{\Delta\rho[2]}{\sqrt{\rho_{\rm ref}}} \equiv \rho_0 v_2^2\{2D\}(b). \tag{6.1}$$

When written in terms of the standard v_2 measure we refer to this quantity as $v_2\{2D\}$ because it is produced from a two-dimensional fitting procedure. Fig. 6.8 (top two panels) compares 2D fit results for $\Delta\rho[2]/\sqrt{\rho_{\rm ref}}$ (first panel), with corresponding values of v_2 (second panel) from published analyses. Quadrupole fit results for 200 GeV (solid dots) and 62 GeV (solid upright triangles) data show a strong increase with centrality up to to mid-central

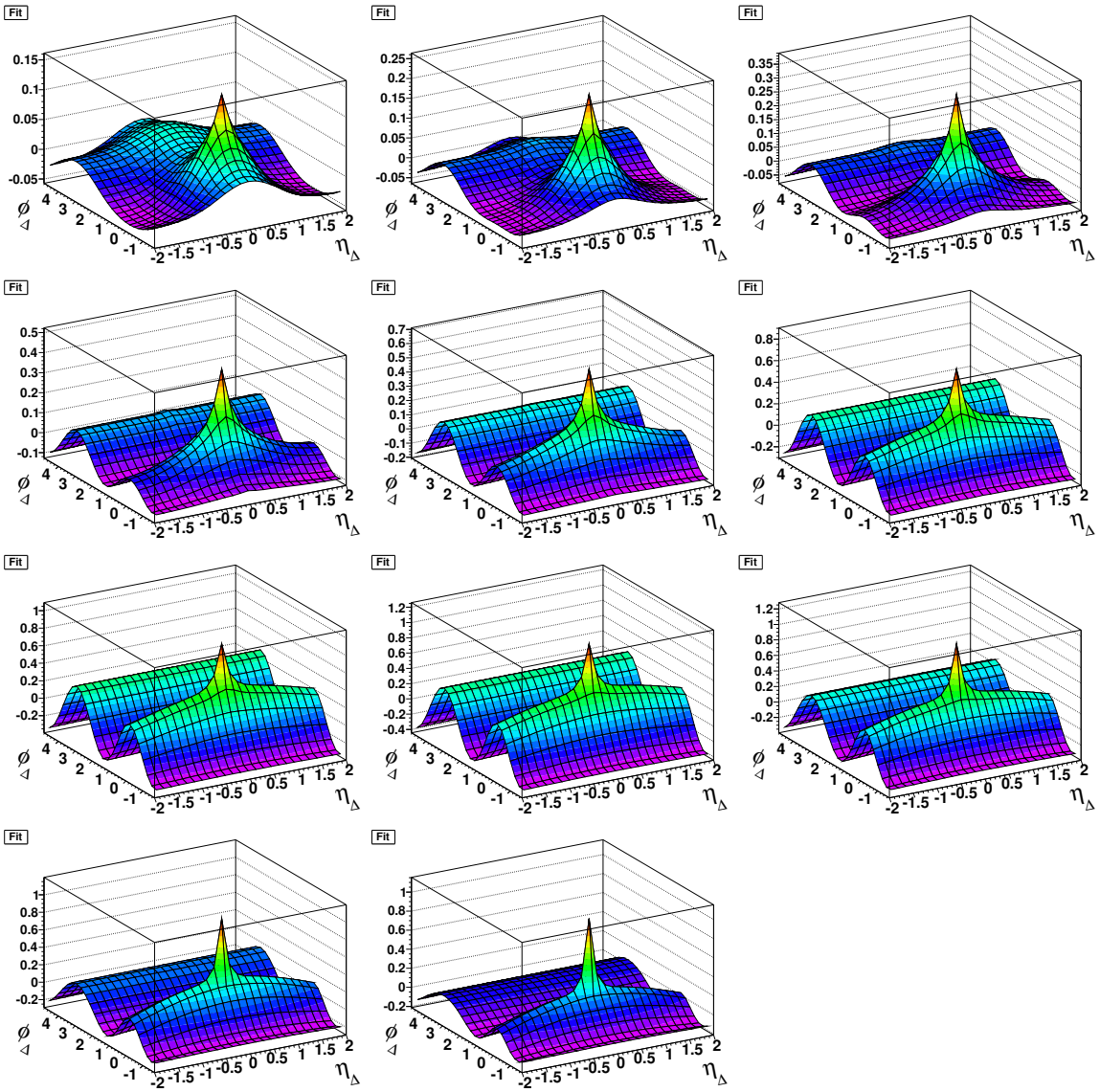

Figure 6.3: Fits to the $\Delta\rho/\sqrt{\rho_{\rm ref}}$ data histograms in Fig. 6.1 for 200 GeV p_t-integrated correlations in 10% fractional centrality increments for the first 9 bins from 90-100% central collisions in the top right to 10-20% central collisions on the third line. The 0-10% range has been split into two bins, the last two histograms being 5-10% and 0-5% central collisions.

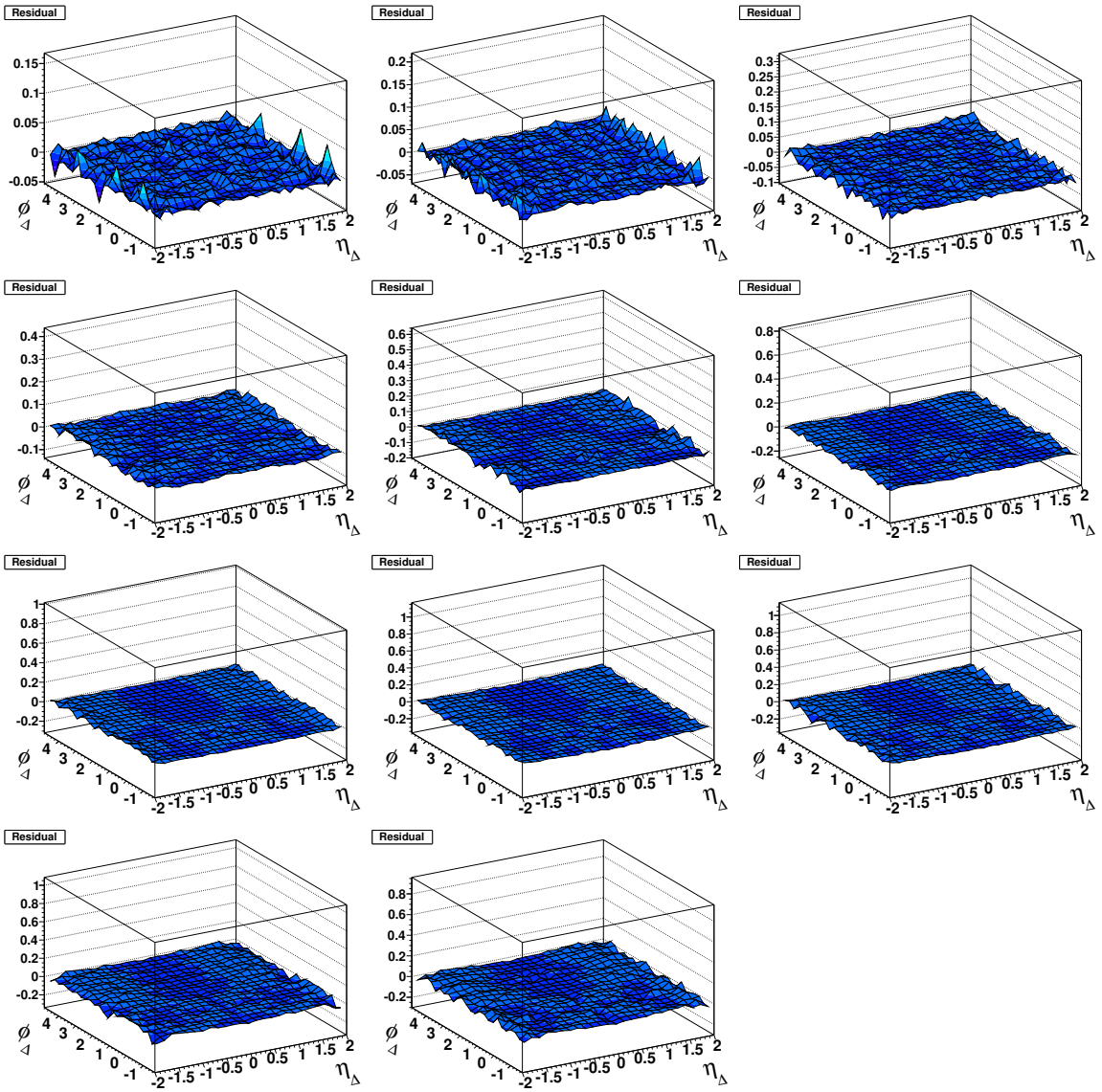

Figure 6.4: $\Delta\rho/\sqrt{\rho_{\rm ref}}$ residuals from the histograms fits in Fig. 6.3 for 200 GeV p_t-integrated correlations in 10% fractional centrality increments for the first 9 bins from 90-100% central collisions in the top right to 10-20% central collisions on the third line. The 0-10% range has been split into two bins, the last two histograms being 5-10% and 0-5% central collisions.

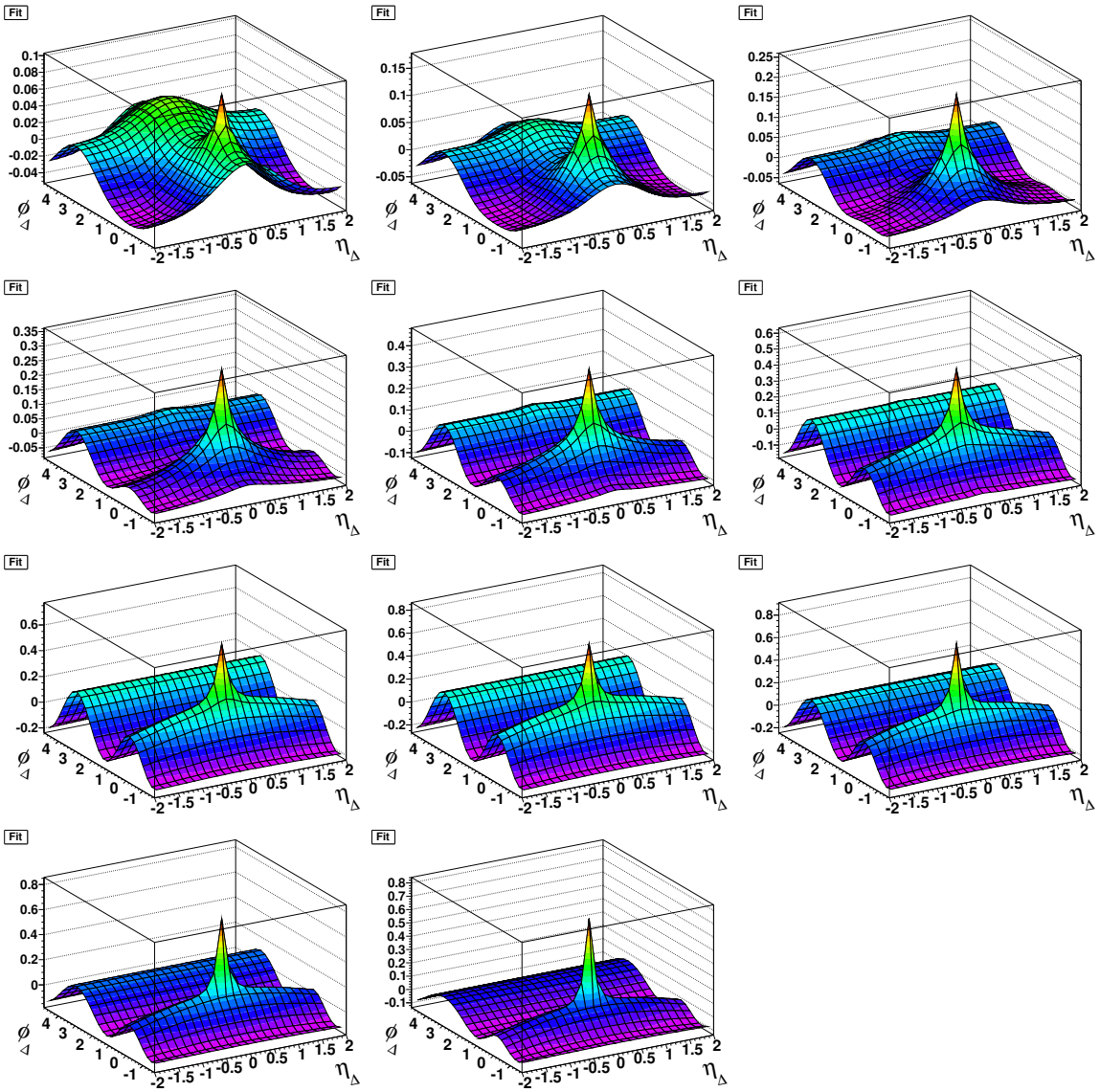

Figure 6.5: Fits to the $\Delta\rho/\sqrt{\rho_{\rm ref}}$ data histograms in Fig. 6.1 for 62 GeV p_t-integrated correlations in 10% fractional centrality increments for the first 9 bins from 90-100% central collisions in the top right to 10-20% central collisions on the third line. The 0-10% range has been split into two bins, the last two histograms being 5-10% and 0-5% central collisions.

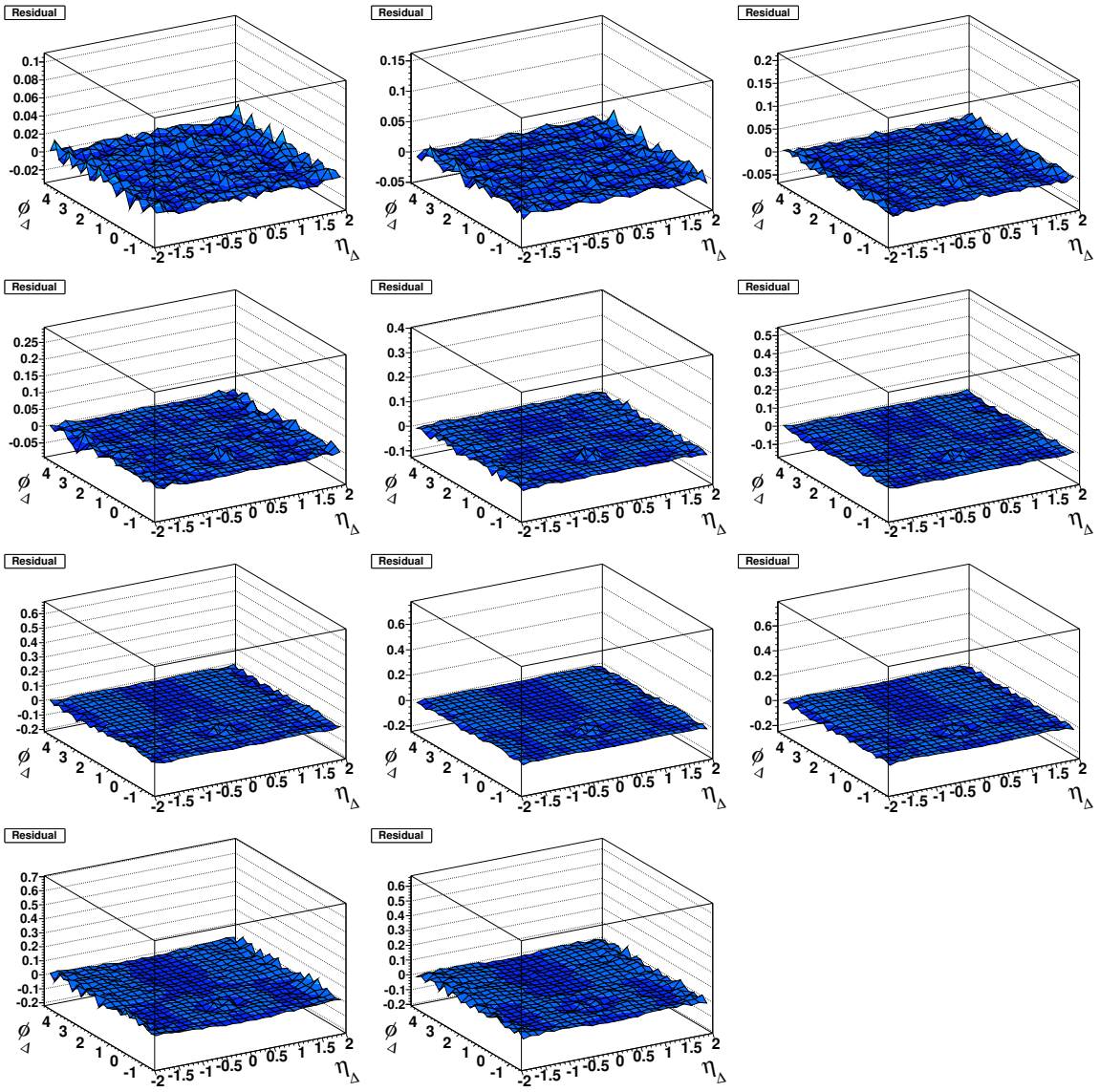

Figure 6.6: $\Delta\rho/\sqrt{\rho_{\rm ref}}$ residuals from the histograms fits in Fig. 6.3 for 62 GeV p_t-integrated correlations in 10% fractional centrality increments for the first 9 bins from 90-100% central collisions in the top right to 10-20% central collisions on the third line. The 0-10% range has been split into two bins, the last two histograms being 5-10% and 0-5% central collisions.

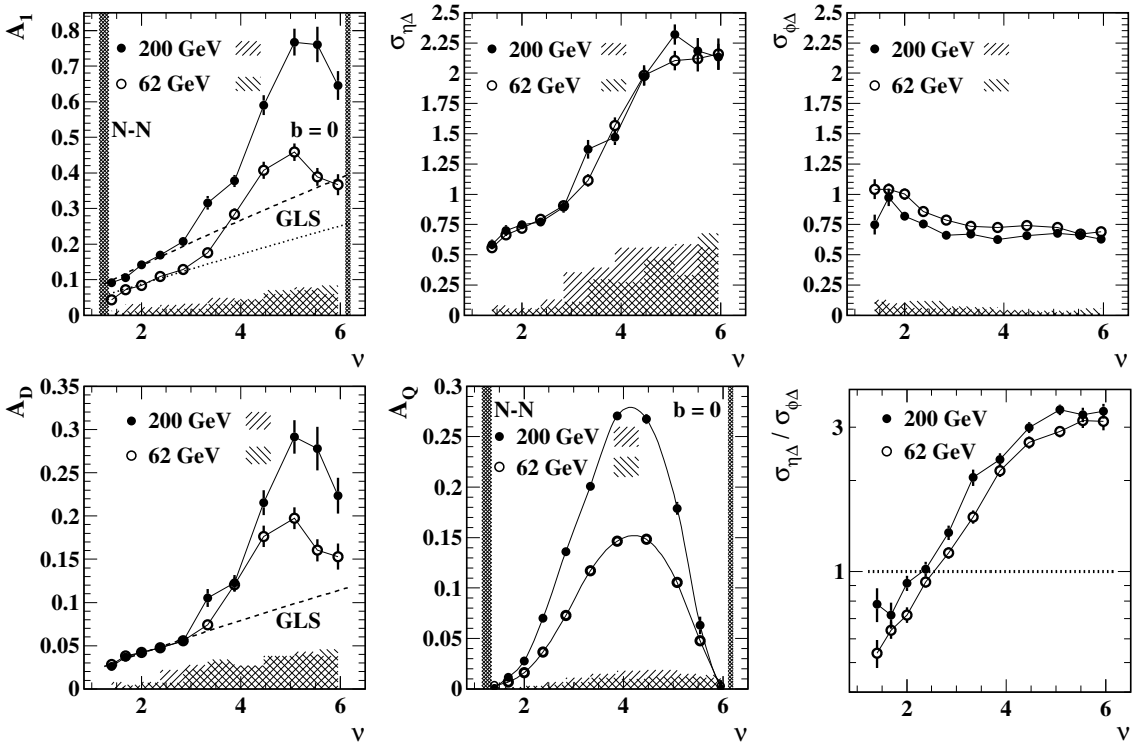

Figure 6.7: The major fit parameters for 200 and 62 GeV collisions as a function of centrality on centrality parameter ν [37]. In the order of the figures they are the amplitude of the same-side peak, the width of the same-side Gaussian peak on η, the width of the same-side Gaussian peak on ϕ, the amplitude of the dipole term, the amplitude of the quadrupole term, and the same-side peak width aspect ratio $\sigma_{\eta_\Delta}/\sigma_{\phi_\Delta}$. The dotted and dashed curves indicate Glauber linear superposition estimates for 62 and 200 GeV same-side peak amplitudes. The hatched regions indicate the full range of systematic uncertainties.

collisions followed by reduction to zero for the most central collisions. $v_2\{\mathrm{EP}\}$ data from NA49 (inverted solid triangles) [140] provide a reference for energy-dependence systematics.

Published data for two-particle $v_2\{2\}$ (open circles) and four-particle cumulant $v_2\{4\}$ (open squares) at 200 GeV [32] are compared to $v_2\{2D\}$ (solid points) from this 2D autocorrelation analysis. The $v_2\{1D\}$ (open triangles) are fits of $\cos(2\phi_\Delta)$ to 1D projections onto ϕ_Δ of the 200 GeV 2D autocorrelations, roughly consistent with the $v_2\{2\}$ analysis as expected [166, 158] and substantially larger than the 2D fits. That "nonflow" offset is expected from a conventional 1D flow analysis: the difference between open triangles and solid dots is exactly the $m = 2$ Fourier component of the same-side minijet peak [158]. $v_2\{4\}$

is expected to eliminate nonflow assuming that "elliptic" flow is a collective property of many particles, whereas "nonflow" describes independent "clusters" of a few particles [73]. The open squares in Fig. 6.8 (top two panels) are closer to the 2D analysis, but systematic deviations outside published uncertainties remain. We conclude that the main source of difference $v_2\{2\} - v_2\{4\}$ is the same-side minijet peak [158], not v_2 fluctuations [148, 50].

The comparison of $v_2\{2D\}$ and $v_2\{1D\}$ allows us to estimate the contribution of "nonflow" to uncorrected v_2 data from 200 GeV Au-Au collisions to be between 20-100%, varying with centrality. The problem is largest for the most central collisions, since not only is $v_2\{2D\}$ approaching zero but also the amplitude of the minijet term is near its maximum.

6.3 Trends and Parametrization

Measurements of the quadrupole moment over a broad range of centralities and energies provide qualitatively new insights into the correlation phenomenon thought to represent elliptic flow. Quadrupole amplitudes follow simple systematic trends on centrality and energy described by only two initial-state parameters for all systems down to 13 GeV.

6.3.1 Quadrupole Systematics

From the quadrupole data in Fig. 6.8 (upper-left panel) we have determined that data at different energies can be described by a common function on centrality and vary only in amplitude. The energy dependence of the amplitude is found to be proportional to $\log(\sqrt{s_{NN}}/13\text{ GeV})$. We introduce the energy scaling factor

$$R(\sqrt{s_{NN}}) \equiv \log(\sqrt{s_{NN}}/13\text{ GeV})/\log(200/13). \tag{6.2}$$

If we plot quadrupole amplitudes divided by the square of the eccentricity as a function of $R(\sqrt{s_{NN}})n_{bin}$ we observe the linear trend seen in Fig. 6.8 (lower-left panel). The complete set of quadrupole data can then be described as a function of energy and impact parameter b by

$$A_Q\{2D\} = \rho_0(b)v_2^2\{2D\}(b) = AR(\sqrt{s_{NN}})\epsilon_{opt}^2(b)n_{bin}(b). \tag{6.3}$$

where coefficient A is defined by $1000A = 4.5 \pm 0.2$, ϵ_{opt} is the eccentricity of the initial collision system defined in Sec. 4.3, and $n_{bin}(b)$ is the number of binary collisions. Eccentricity is not a measurable quantity and must be calculated in a model. We will be using the parametrization of the optical model of eccentricity given by Eq. (4.16).

Deviations of 17 GeV event-plane v_2 from the linear trend are consistent with expected crosstalk from minijets at that energy [158]. Eq. (6.3) accurately describes measured p_t-integrated azimuth quadrupole moments in heavy ion collisions for all centralities down to N-N collisions and all energies down to $\sqrt{s_{NN}} \sim 13$ GeV. Transformed to each plotting space it defines the dashed curves in Fig. 6.8. The dash-dotted curves passing through the 200 GeV 1D projection points in Fig. 6.8 are obtained by adding "nonflow" parametrization $g_2/2\pi = 0.004\nu^{1.5}$ to $A_Q\{2D\}$ [158].

We can contrast this simple description of the data with the hydro-inspired v_2/ϵ *vs* $1/Sdn_{ch}/d\eta$ format [172] shown in Fig. 6.8 (lower-right panel). For thermal equilibrium the expectation is the ideal-hydro limit $v_2/\epsilon \rightarrow$ constant. Previous v_2 measurements have been interpreted to suggest that central Au-Au collisions at 200 GeV attain the ideal hydro limit (full thermalization over some substantial space-time volume) [173]. The present analysis is *inconsistent with such expectations*.

We find a universal trend on $N_{\rm bin}$ and $\sqrt{s_{NN}}$ for all data as in Fig. 6.8 (third panel). We confirm the parametrization in Eq. (6.3) by observing the linear trend when plotting $(1/\epsilon^2)\Delta\rho[2]/\sqrt{\rho_{ref}}$ vs. $R(\sqrt{s_{NN}})n_{bin}(b)$. This parametrization of the quadrupole term gives a complete factorization of the energy and centrality dependence of the quadrupole term. In the next chapter we will also include p_t dependence.

6.3.2 Non-quadrupole Trends

We have also fitted the same-side minijet peak in the 62 and 200 GeV Au-Au autocorrelations. This 2D Gaussian peak centered at $(0, 0)$ in $(\eta_\Delta, \phi_\Delta)$ space is a major contributing term to correlations at all observed centralities and p_t. In studies of quadrupole (v_2) systematics the jet contribution is often dismissed as "nonflow". However, it has very interesting properties of its own. The centrality dependence of this peak in p_t-*integral* form reveals jet-

like systematics identical with those for p-p collisions in more-peripheral Au-Au collisions which scale with the number of binary collisions as expected of jets up to a transition point. Above the transition point a more rapid increase in amplitude and width of this peak is one of the most poorly-understood features in heavy-ion physics today. We will discuss it further in Chapter 9.

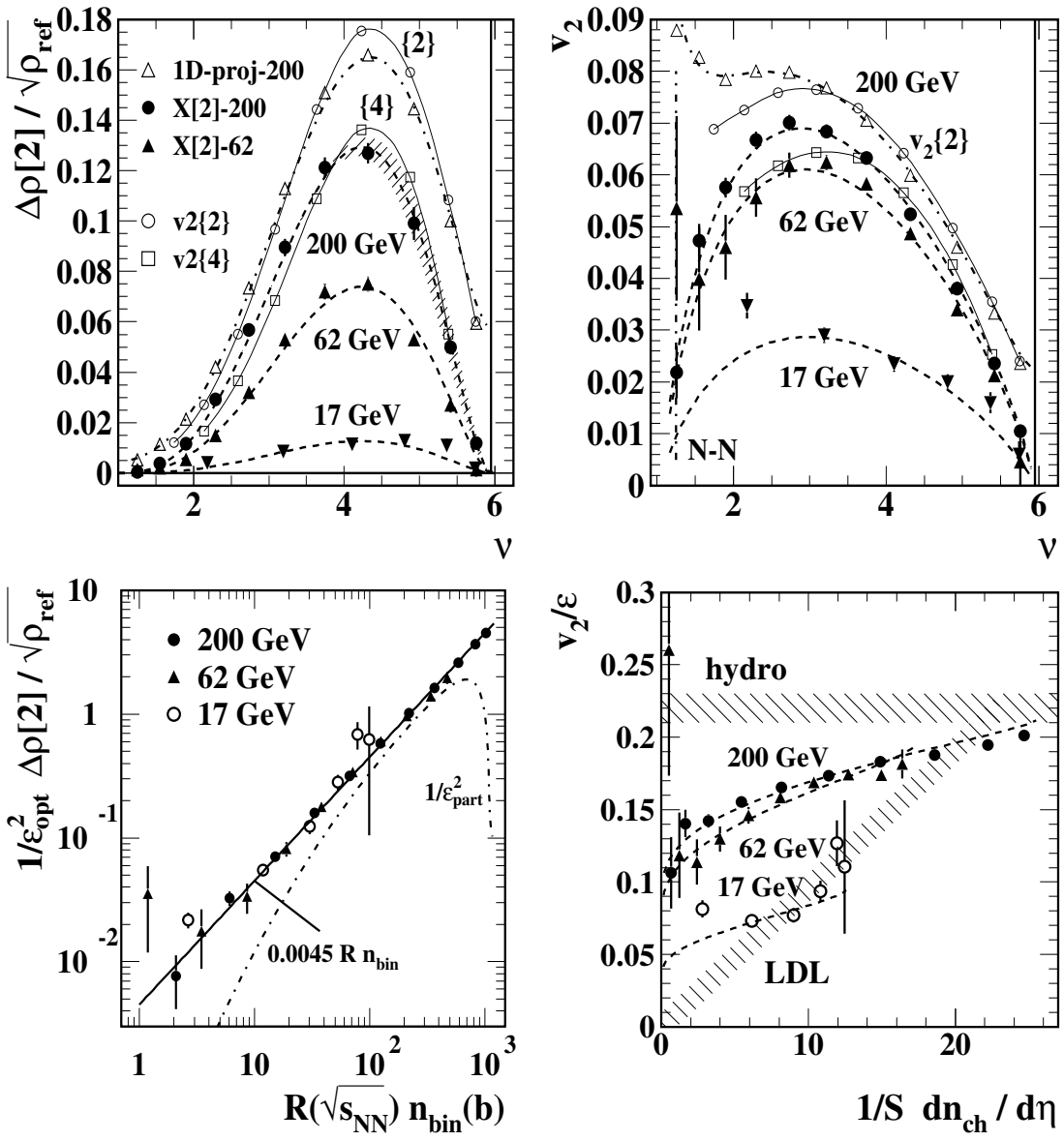

Figure 6.8: Top two panels: p_t-integrated quadrupole results in terms of $\Delta\rho/\sqrt{\rho_{\rm ref}}$ and v_2. The solid circles and solid triangles are quadrupole results from 2D fitting at 200 and 62 GeV respectively. The open circles and open squares are $v_2\{2\}$ and $v_2\{4\}$ results for 200 GeV collisions [32]. The upside-down solid triangles are 17 GeV results from NA49 [140]. The open triangles are from projecting the 2D correlations to just ϕ_Δ and fitting with only Fourier components. The dashed curves are from our parametrization of the data. Lower-left panel: Energy and centrality dependence of the quadrupole using the optical eccentricity for 200 and 62 GeV data from this study and 17 GeV results from NA49 [140]. Lower-right panel: A hydro-inspired plot of v_2/ϵ *vs* LDL (low-density limit) parameter $1/Sdn_{ch}/d\eta$ [172].

Chapter 7

P_T-DIFFERENTIAL AZIMUTH QUADRUPOLE

Studying the p_t dependence of the quadrupole instead of the p_t-integrated quantity can provide a greater understanding of the physical processes that produce these correlations. But first we must define p_t dependence in this system. Since the quadrupole is measured with two-particle correlations the correlation amplitude depends on the p_t of *both* particles. This defines a two-dimensional p_t space. In this chapter we will introduce the concept of marginal distributions for $v_2(p_t)$ measurements, defined by correlating particles within a given p_t bin with the entire event [116]. Then we will analyze the p_t-dependence of quadrupole correlations and construct a quadrupole spectrum.

7.1 $y_t \times y_t$ *Space and Cuts*

Angular correlations without a trigger particle are constructed by considering all possible pairs of particles in an event. For each particle the azimuth angle ϕ, pseudorapidity η and transverse momentum p_t are measured, defining a six dimensional two-particle space. In the previous chapter and published works we explored this space by integrating over all p_t and projecting to the angular difference variables [115, 84, 28]. We now wish to examine correlations in different p_t regions.

7.1.1 Marginal Distributions

We will be using transverse rapidity in place of p_t, as introduced in Sec. 2.2.2. Transverse rapidity y_t is defined by $y_t = \ln\{(p_t + m_t)/m\}$. For unidentified particles (hadrons) we assume m is the pion mass. y_t scales as $\ln(p_t)$ for larger p_t values but remains well defined for $p_t \to 0$ and can therefore be used over the entire kinematic range of particles produced at RHIC. Under the assumption that m is the pion mass y_t is simply a logarithmic transformation of p_t. But y_t is a convenient change of variables for the momentum scales we

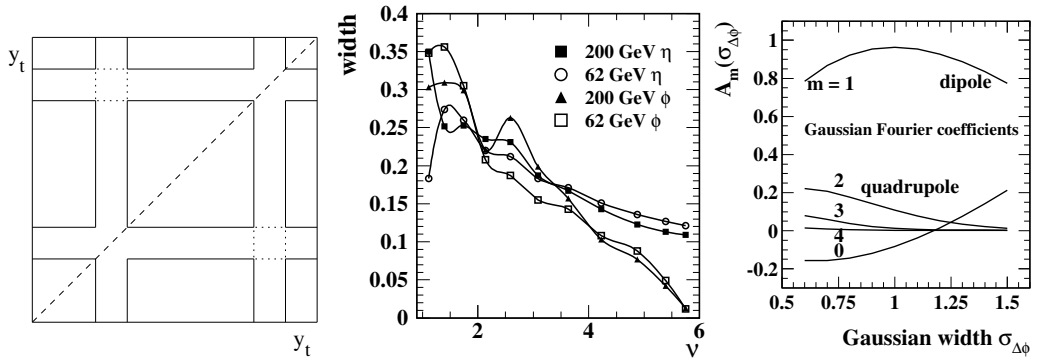

Figure 7.1: Left Panel: Two examples of marginal cuts in $y_t \times y_t$ space. Middle Panel: η and ϕ widths of the p_t-integrated exponential peak as a function of centrality from the analysis in Chapter 6. Right Panel: The Fourier decomposition of a periodic array of Gaussians as a function of the Gaussian width.

study.

We construct y_t-dependent correlations by defining several bins in $y_t \times y_t$ space and constructing two-particle correlations for each bin. A marginal distribution is defined by restricting the y_t of one of the particles to be within a certain range while allowing the second particle to span all y_t. Because of the inherent diagonal symmetry in $y_t \times y_t$ space this produces cross-shaped cuts as seen in Fig. 7.1 (left panel). Because of the cross shape of marginal distributions a complete set of marginal bins will overlap with each other in $y_t \times y_t$ space. A particular particle pair does not belong to a unique marginal y_t bin. When binning particles in practice it is better to define a two-dimensional grid of square bins in $y_t \times y_t$ which can then be summed in different combinations to produce the marginal cut spaces.

Marginal distributions are preferred because they yield the maximum possible statistical power for exploring higher p_t. Recall the definition of the two-particle correlation density V_m from Eq. 5.14, $V_m^2 = \sum_{i=1}^{n} \sum_{j \neq i}^{n-1} \vec{u}(m\phi_i) \cdot \vec{u}(m\phi_j) = n^2 v_m^2\{2\}$. This equation assumed that both indices were being summed over all particles. By restricting just one of the particles

we get,

$$V_m(b)V_m(b,p_t) = \sum_{i=1}^{n} \sum_{j\neq i, p_{min}<p_t(j)<p_{max}}^{n-1} \vec{u}(m\phi_i)\cdot\vec{u}(m\phi_j) = n^2 v_m(b) v_m(b,p_t) \qquad (7.1)$$

These cuts are analogous to the procedure in a standard event-plane $v_2(p_t)$ analysis [141] in which particles from the full momentum range are said to estimate the event plane and particles in the momentum interval are correlated to it. The marginal distributions allow us to study correlations at large p_t values and are easily converted into the usual $v_2(p_t)$ measure for comparison with published $v_2(p_t)$ data.

7.1.2 Alternative p_t Cuts

Of course marginal distributions are not the only possible way to divide a two-dimensional $p_t \times p_t$ space. It is possible to fully explore the two-dimensional p_t space with a two-dimensional grid of cuts, though the resolution of this grid would be limited with by the available statistics. Alternatively one could consider increasing the minimum p_t of both particles, but this reduces statistics rapidly compared to a marginal p_t cut.

In Chapter 3 we described an analysis of proton-proton collisions that cleanly separates "soft" and "hard" correlations [139]. It is tempting to apply the same approach to heavy-ion collisions. However, in practice the peak of the hard correlations moves to lower p_t as the centrality is increased and there is significant overlap between the two peaks, implying that a clean separation of these components with a single diagonal cut in $p_t \times p_t$ space is not possible for heavy-ion collisions.

Triggered high-p_t correlations have upper and lower bounds on the momentum of both the trigger particle and associated particles [10]. The trigger-particle momentum is higher than that for the associated particles, so this is equivalent to exploring an off-diagonal box in the untriggered $p_t \times p_t$ space. Using events from a high-p_t trigger to construct high-p_t correlations does provide access to a larger number of events that contain high-p_t particles than a minimum bias trigger and therefore improve statistics at high p_t. But it is difficult to study the complete p_t scaling and centrality dependence with triggered events.

7.2 Fitting

The fit procedure is similar to that used in the p_t-integrated results of Chapter 6 with one major exception: We no longer attempt to model the sharp exponential peak. Instead we simply exclude bins near the angular origin from the fit. This exclusion cut has the effect of making the fits more stable over a wide p_t range but it can be a problem for the most peripheral bins where the width of the exponential approaches that of the same-side 2D Gaussian.

7.2.1 Fit Models

In Chapter 5 we introduced a fit model that works well for describing p_t-integrated correlations for all centralities. This model also works well for the low-p_t region of p_t-differential correlations—as that region dominates p_t-integrated correlations. However if we want to study the p_t evolutions of mid-central and central collisions this model has limitations.

At high p_t the exponential peak which we attributed to HBT and electron pair production disappears. This should be expected as these are both low-p_t phenomena. As a result a naïve application of this fit model is under-constrained as it would mean fitting a single peak—the minijet peak—with both Gaussian and an exponential terms. This makes variations in either component difficult to interpret. But we can't just neglect the exponential peak either. Though it becomes negligible at high-p_t it is still an important component at low-p_t and we want to study the entire p_t range with a consistent model.

Fortunately in mid-central and central collisions the exponential peak is quite narrow. If we simply exclude a region near the origin of the correlations from our fit it is possible to accurately describe most centralities without including an exponential peak in the fit. This model does not work well in the most peripheral collisions where the exponential peak is wider. However in mid-central and central collisions it gives good fits with low residuals over the full p_t range.

The angular correlation histograms are constructed with 24 bins on ϕ_Δ with centers ranging from $-\pi/2$ to $17\pi/12$ in steps of $\pi/12$ and 25 bins on η_Δ with centers ranging from -1.92 to 1.92. A total of seven bins are excluded from the fit: bin centers of $\eta_\Delta = 0$,

$\phi_\Delta = 0, \pm\pi/12$ and $\eta_\Delta = \pm 0.08, \pm 0.16$, $\phi_\Delta = 0$. This is a cross shaped exclusion region elongated in the η direction because it requires more eta bins to cover the same numerical range. This has the effect of making the fits more stable over a wide p_t range but it can still be problematic for the most peripheral collisions.

The complete fitting function is then

$$\begin{aligned} F &= A_D \cos(\phi_\Delta - \pi) + A_Q \cos(2\phi_\Delta) + A_{\text{soft}} e^{-\frac{1}{2}\left(\frac{\eta_\Delta}{\sigma_0}\right)^2} \\ &+ A_{2D} e^{-\frac{1}{2}\left\{\left(\phi_\Delta/\sigma_{\phi_\Delta}\right)^2 + \left(\eta_\Delta/\sigma_{\eta_\Delta}\right)^2\right\}} + A_0. \end{aligned} \tag{7.2}$$

There are 5 terms and 8 parameters. Two of the terms are sinusoids on ϕ_Δ, one is a constant offset, and one term models only structure on η_Δ. Thus, the remaining term—the two-dimensional Gaussian—is solely responsible for describing "nonflow" [166].

7.2.2 Fit Applicability

As mentioned this fit model requires that the exponential term observed in the p_t-integrated data be either narrow or not present at all. The middle panel of Fig. 7.1 contains the η and ϕ widths of the p_t-integrated exponential peak measured in Chapter 6. Note that the maximum width of the exponential peak is around 0.35 in both η_Δ and ϕ_Δ in the most peripheral collisions. This extends significantly beyond the excluded region. Of course more bins could be excluded but the central region is still important for fitting the minijet peak. The more bins excluded from the fit the less reliable the fit of the Gaussian peak will be. But the widths of the exponential peak drop off rapidly in centrality and are already around 0.20 near the transition region. If we analyze the p_t-dependence of mid-central to central collisions with this technique the results should be reliable, but the most peripheral bins should be excluded.

We should also consider the possibility that the away-side ridge is modified. We are modeling the away-side ridge with a dipole for simplicity, but a more complete description of the away-side structure would be with a periodic array of Gaussian peaks centered at π, 3π, etc. The dipole description applies in the limit where the widths of the Gaussian peaks become large. Fig. 7.1 (right panel) shows the calculated Fourier coefficients of such an

array of Gaussians as a function of the Gaussian width. We find the dipole approximation works well in p_t-integrated correlations but the Gaussian width should narrow with p_t. If it narrows enough the dipole approximation will no longer be valid. Fits have been done with an away-side Gaussian rather than a dipole but for the momentum range in this study it did not appear to make a significant difference.

One final consideration is the possibility of a deformed same-side peak. In high-p_t triggered correlations the same-side peak is sometimes modeled with two separate "jet" and "ridge" components [10]. This will be explored further in Chapter 9. The present analysis does not extend as high in p_t as the triggered particle correlations and the marginal p_t cuts do not restrict the second ("associated") particle at all. Our p_t cuts appear to be less sensitive to this phenomenon and no significant deformation of the same-side peak is observed in this analysis. It's true that a single Gaussian may not be a perfect model either, but attempting to introduce additional terms seems premature for the available data. Some bins may contain small fit residuals but no clear systematic behavior is observed. And given the success of the single Gaussian approach in the low-p_t regime additional terms would potentially make the fit function under-constrained in that regime.

7.3 Results

This analysis is based on 14.5 million Au-Au collisions at $\sqrt{s_{NN}} = 200$ GeV and 6.7 million Au-Au collisions at $\sqrt{s_{NN}} = 62$ GeV observed with the STAR TPC. The acceptance was defined by transverse momentum $p_t > 0.15$ GeV/c, $|\eta| < 1$ and 2π azimuth. Minimum-bias event samples were divided into the standard 11 centrality bins: nine $\sim 10\%$ bins from near 100% to 10%, the last 10% divided into two $\sim 5\%$ bins. We apply the same event, track, and pair cuts as described in Sec. 6.1.

7.3.1 Data

In this analysis there is a minimum p_t cutoff of 150 MeV/c for all particles which corresponds to a pion y_t of 0.93. We have made nine marginal y_t cuts—as described in Sec. 7.1.1—for each centrality class of events and for both 62 and 200 GeV collisions. The first bin includes particles from y_t of 0.93 to 1.4. Above that there are 7 bins evenly spaced in y_t with a width

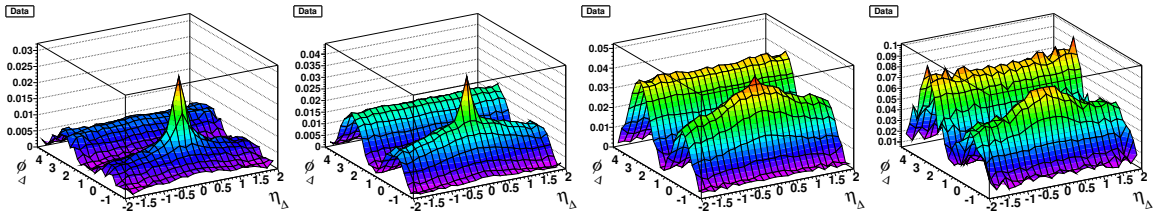

Figure 7.2: Example of the y_t evolution of correlation structures for 62 GeV 40-50% central collisions. The plots correspond to y_t bins of $y_t < 1.4$, $1.8 < y_t < 2.2$, $2.6 < y_t < 3.0$, and $3.4 < y_t < 3.8$.

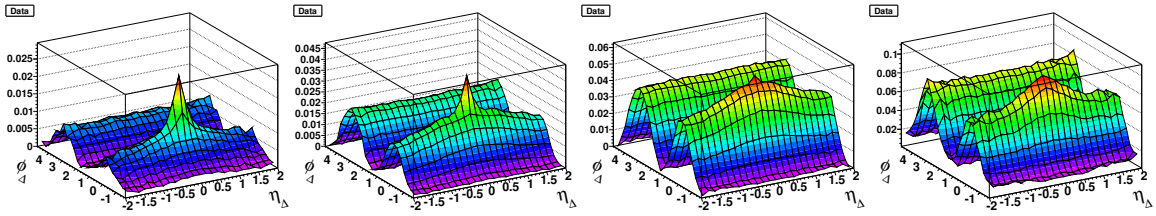

Figure 7.3: Example of the y_t evolution of correlation structures for 200 GeV 40-50% central collisions. The plots correspond to y_t bins of $y_t < 1.4$, $1.8 < y_t < 2.2$, $2.6 < y_t < 3.0$, and $3.4 < y_t < 3.8$.

of 0.4 units of transverse rapidity. The final bin includes all particles greater than $y_t = 4.2$. In p_t these bin edges correspond to 0.27 GeV/c, 0.41 GeV/c, 0.62 GeV/c, 0.94 GeV/c, 1.4 GeV/c, 2.1 GeV/c, 3.1 GeV/c, and 4.7 GeV/c. However the top p_t bin is excluded from the 62 GeV results due to the lack of statistics. This means that there are 187 histograms in this p_t-differential analysis, 99 for 200 GeV collisions and 88 for 62 GeV collisions. Due to the large number of histograms to fit, the automated fitting procedure described in Section 5.5.2 is used. This produces a very large number of figures so the complete set of data, fits, and residuals is provided in Appendix A. Figures 7.2 and 7.3 show an example of the p_t-evolution in mid-central collisions for 62 and 200 GeV collisions. For p_t-dependent correlations we are measuring the correlation amplitude in terms of $\Delta\rho/\rho_{\rm ref}$ rather than $\Delta\rho/\sqrt{\rho_{\rm ref}}$—see Sec. 5.2.4—so that it is not necessary to determine ρ_0 for each p_t bin. This also simplifies the conversion to the standard v_2 measure.

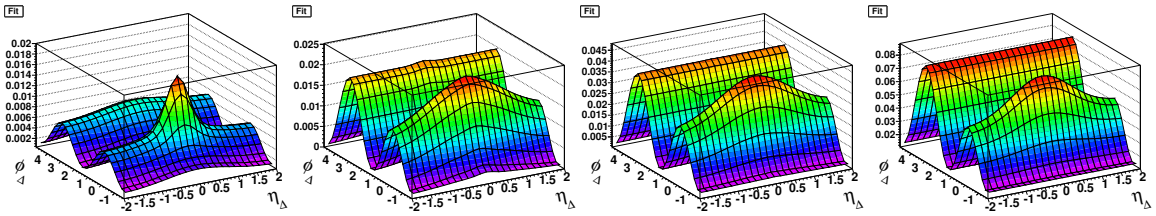

Figure 7.4: Example of the y_t evolution of the correlation fit for 62 GeV 40-50% central collisions. The plots correspond to y_t bins of $y_t < 1.4$, $1.8 < y_t < 2.2$, $2.6 < y_t < 3.0$, and $3.4 < y_t < 3.8$.

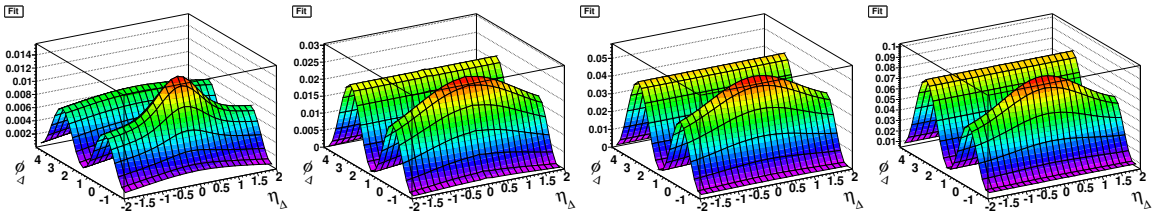

Figure 7.5: Example of the y_t evolution of the correlation fit for 200 GeV 40-50% central collisions. The plots correspond to y_t bins of $y_t < 1.4$, $1.8 < y_t < 2.2$, $2.6 < y_t < 3.0$, and $3.4 < y_t < 3.8$.

7.3.2 Fits

In Fig. 7.4 and 7.5 are examples of the p_t-dependence of the fit models for mid-central collisions for 62 and 200 GeV collisions respectively. Fig. 7.6 and 7.7 show the corresponding residuals. Again, the full set is in Appendix A.

The major fit parameters are shown in Fig. 7.8 for 62 GeV collisions and in Fig. 7.9 for 200 GeV collisions for several centralities. The 2D Gaussian amplitudes and azimuth widths follow expected trends for both energies. However, the widths on pseudorapidity seem to be largely independent of y_t over a large range. This unusual behavior is related to high-p_t observations that have been coined "the ridge". But in this chapter we will focus primarily on the quadrupole term. We will return to studying the same-side minijet peak in Chapter 9.

The quadrupole term follows similar p_t dependence for each centrality range shown, suggesting that there is a possibility of factorizing the centrality and p_t dependence. We will

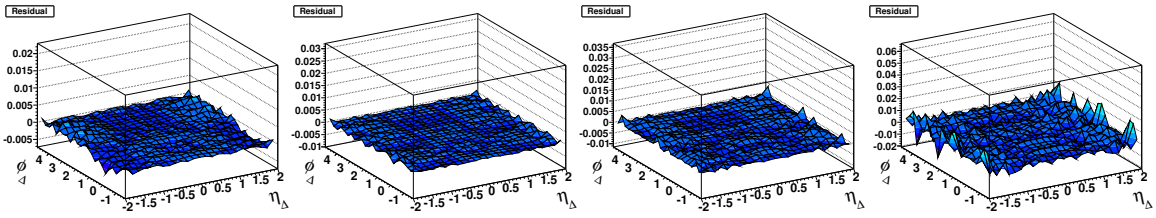

Figure 7.6: Example of the y_t evolution of fit residuals for 62 GeV 40-50% central collisions. The plots correspond to y_t bins of $y_t < 1.4$, $1.8 < y_t < 2.2$, $2.6 < y_t < 3.0$, and $3.4 < y_t < 3.8$.

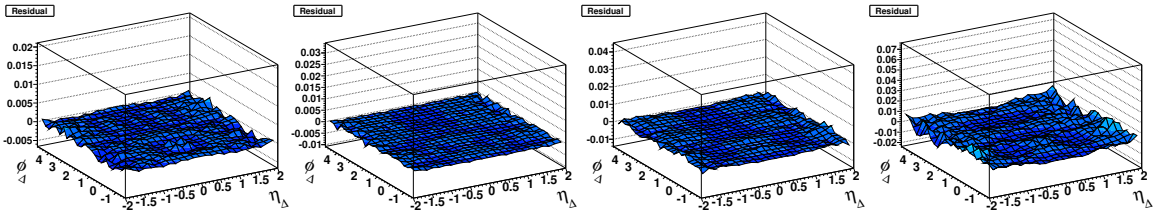

Figure 7.7: Example of the y_t evolution of fit residuals for 200 GeV 40-50% central collisions. The plots correspond to y_t bins of $y_t < 1.4$, $1.8 < y_t < 2.2$, $2.6 < y_t < 3.0$, and $3.4 < y_t < 3.8$.

explore that possibility in the next section. In Chapter 6 we already discussed the collision energy and centrality dependence, so total factorization and a simple parametrization are possible. However, the limitations of our fitting model prevent us from applying this approach to all centralities.

To compare these correlation amplitudes to published v_2 data, quadrupole amplitudes in $\Delta\rho/\rho_{\rm ref}$ can be converted into v_2 values by the simple relationship, $2v_2^2\{2D\} \equiv \Delta\rho[2]/\rho_{\rm ref}$. However, the marginal distribution produces data of the form $2v_2(b,p_t)v_2(b)$, not $2[v_2(b,p_t)]^2$. So the fit amplitude must be divided by p_t-integrated $v_2(b)$ results obtained in Chapter 6.

In our fit model the non-quadrupole term with the largest contribution to the second Fourier component on azimuth is the same-side 2D Gaussian peak. We can calculate the contribution to the second Fourier component of a 2D Gaussian of given amplitude and widths, which we know for the same-side peak from our fit parameters. Since the exponential peak is not significant at higher p_t, and other terms do not contribute to the second Fourier

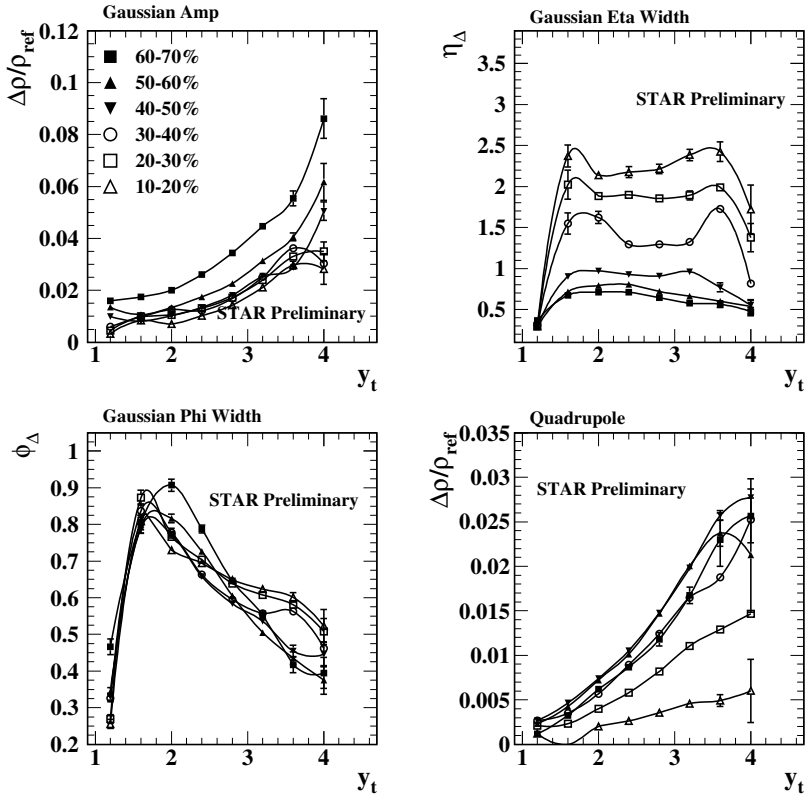

Figure 7.8: Fit parameters for 62 GeV collisions: Same-side peak amplitude, width in eta, width in phi, and quadrupole amplitude as a function of y_t for 10-20%, 20-30%, 30-40%, 40-50%, 50-60%, and 60-70% central collisions. Error bars are for fitting errors only.

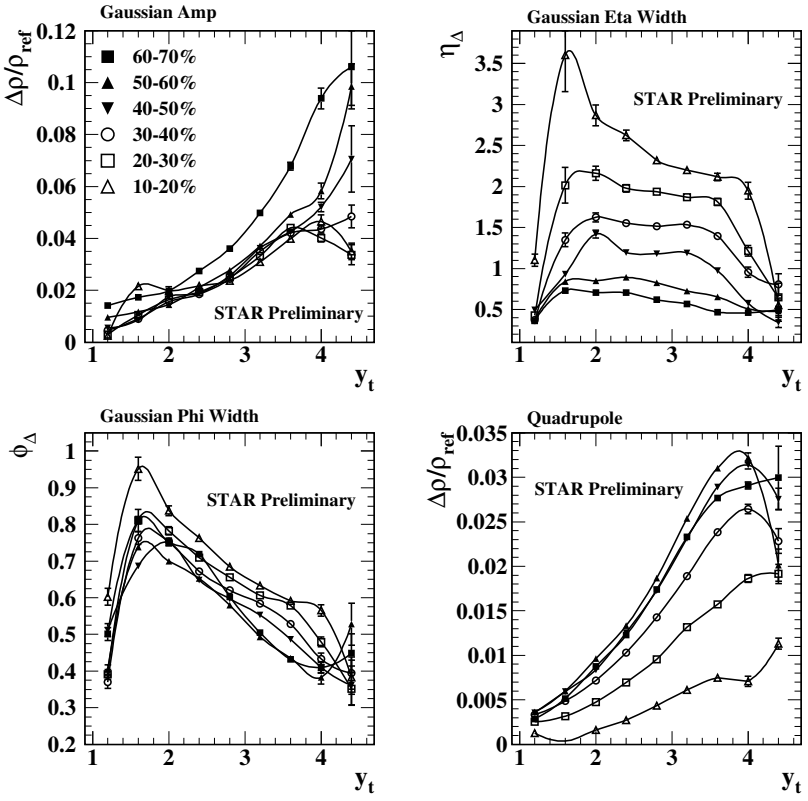

Figure 7.9: Fit parameters for 200 GeV collisions: Same-side peak amplitude, width in eta, width in phi, and quadrupole amplitude as a function of y_t for 10-20%, 20-30%, 30-40%, 40-50%, 50-60%, and 60-70% central collisions. Error bars are for fitting errors only.

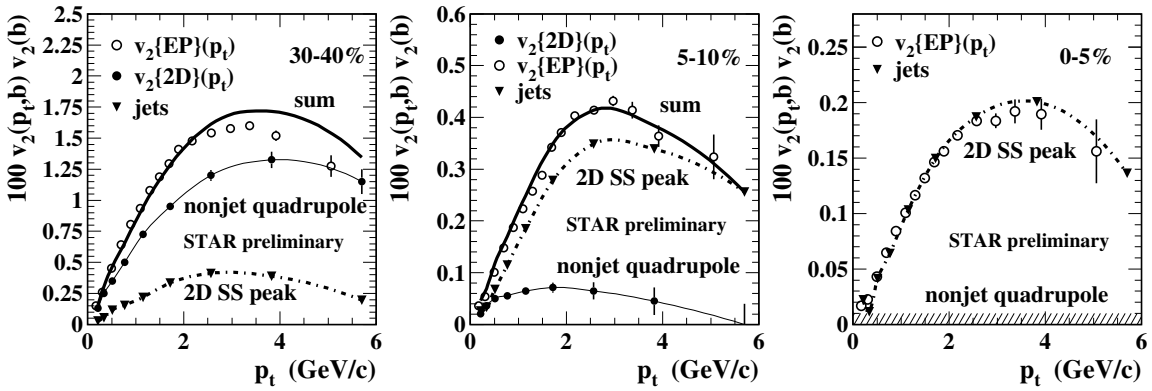

Figure 7.10: Comparison of quadrupole (closed circles) and the second Fourier component of the 2D same-side Gaussian (closed upside-down triangles) to $v_2\{EP\}$ results (open circles) [22] for 30-40%, 5-10%, and 0-5% central collisions. The dark solid curve in the first two panels is the sum of the quadrupole and same-side peak terms.

component on azimuth, this gives us a direct measure of the so-called "nonflow" contribution to v_2. Fig. 7.10 shows measured quadrupole results vs. p_t from this analysis compared to previously published $v_2\{\text{EP}\}$ results for 30-40%, 5-10% and 0-5% central collisions [22]. The curve labeled "2D SS peak" is the contribution to the second Fourier component calculated from our parametrization of the 2D Gaussian peak, while the "nonjet quadrupole" is the measured quadrupole amplitude converted to v_2. The curve labeled "sum" is the sum of these two components and it compares favorably with published $v_2\{EP\}$ results.

For 0-5% central collisions we do not observe a significant nonzero quadrupole term. An estimated upper limit is plotted as the lower hatched region. We see that published $v_2\{EP\}$ data are well-described by the jet curve alone, with *no* contribution from the nonjet quadrupole term. Not only does the 2D Gaussian peak dominate central collisions, the jet contribution to the total quadrupole is strongly dependent on both centrality and p_t. Simplified models of "nonflow" that do not take this dependence into account lead to a misrepresentation of v_2. What is often attributed to "elliptic flow" in more-central Au-Au collisions is actually the quadrupole component of the same-side jet peak. We find that there is negligible true (nonjet) quadrupole present in the most central collisions.

7.4 Quadrupole Properties

The p_t-dependence of the quadrupole term measured in two-particle correlations can be further analyzed to factorize the collision energy, centrality, and p_t dependence of the quadrupole term and develop a quadrupole spectrum. This leads to a very simple, compact, and complete representation of the quadrupole.

7.4.1 Quadrupole Spectrum

Consider the case of minimum-bias identified particles results from STAR [6]. In Ref. [158] it was shown that by plotting v_2/p_t on proper y_t for identified hadron species the particles appear to come from a single boosted source. This is reproduced in Fig. 7.11 (upper-left panel). This is most evident for the more massive particles. Since the pion mass is of the same order as the lowest p_t we can measure in STAR there are few observed pions in the necessary p_t range to see this boost. In Fig. 7.11 (upper-right panel) we plot just the lambdas, which makes the boost more explicit.

Now consider the centrality-dependent (denoted by b) production of an azimuth quadrupole term from a general boosted source. First make the general assumption that the single-particle density on y_t and ϕ can be decomposed into azimuth-dependent and azimuth-averaged terms:

$$\rho(y_t, \phi, b) = \rho_0(y_t, b) + \rho_2(y_t, \phi, b). \tag{7.3}$$

At this point we do not make any assumptions about the nature of the azimuth dependence. Then apply the continuum definition of v_2:

$$\begin{aligned} v_2(y_t, b) &\equiv \frac{\frac{1}{2\pi}\int_0^{2\pi} d\phi \rho(y_t, \phi, b)\cos[2(\phi - \psi_R)]}{\frac{1}{2\pi}\int_0^{2\pi} d\phi \rho(y_t, \phi, b)} \\ &\approx \frac{\frac{1}{2\pi}\int_0^{2\pi} d\phi \rho_2(y_t, \phi, b)\cos[2(\phi - \psi_R)]}{\rho_0(y_t, b)} \equiv \frac{V_2(y_t, b)}{\rho_0(y_t, b)}. \end{aligned} \tag{7.4}$$

Only the azimuth-dependent term contributes to the numerator, and the denominator is the single-particle spectrum [158]. What we study with correlations is actually the numerator of this expression which we denote by $V_2(y_t, b)$.

To calculate V_2 in terms of a quadrupole spectrum we need to introduce a boost model denoted $\rho_2(y_t, \phi)$. A general boost model for A-A collisions should have both monopole (radial flow, Hubble expansion) and quadrupole terms, which is easily expressed in y_t:

$$\Delta y_t(\phi) = \Delta y_{t0} + \Delta y_{t2} \cos(2[\phi - \psi_R]), \tag{7.5}$$

with $\Delta y_{t2} \leq \Delta y_{t0}$ a necessary condition for a positive-definite boost. Using a simple blast-wave model with a Maxwell-Boltzmann distribution for a locally-thermalized source the boosted spectrum's azimuth-dependent term then has the form [158]:

$$\rho_2(y_t, \phi) = A_{2y_t} \exp\{-\mu_2[\cosh(y_t - \Delta y_t(\phi)) - 1]\}, \tag{7.6}$$

where $\mu_2 = m_0/T_2$ and T_2 is the quadrupole spectrum's temperature. If we insert our boost model into Eq. (7.6) and factor the ϕ-dependent terms of ρ_2 into the form $\rho_2(y_t, \phi) = \rho_2(y_t) \times F_1(y_t, \phi) \times F_2(y_t, \phi)$ where

$$\begin{aligned} F_1(y_t, \phi) &= \exp\{m_t'[\cosh(\Delta y_{t2} \cos[2(\phi - \psi_r)]) - 1]/T_2\} \\ F_2(y_t, \phi) &= \exp\{p_t'[\sinh(\Delta y_{t2} \cos[2(\phi - \psi_r)])/T_2\}. \end{aligned} \tag{7.7}$$

We identify $\rho_2(y_t)$ as the azimuth-integrated quadrupole spectrum. Inserting this into the numerator of Eq. (7.4) and evaluating the integral yields

$$V_2(y_t, b) \approx \frac{p_t' \Delta y_{t2}(b)}{2T_2} \rho_2(y_t, b). \tag{7.8}$$

Finally, we want to isolate $\rho_2(y_t, b)$ by taking the unit-integral ratio of measured quantities:

$$Q(y_t, b) \equiv \frac{V_2(y_t, b)/p_t}{V_2(b)\,\langle 1/p_t \rangle} \approx \frac{\rho_2(y_t, b)}{\rho_2(b)}. \tag{7.9}$$

The parameters from the blast-wave model present in Eq. (7.8) drop out in the ratio and $Q(y_t, b)$, shown in Fig. 7.11 (lower-left panel), directly relates measured parameters to the quadrupole spectrum for 5-10%, 10-20%, 20-30%, 30-40%, 40-50%, 50-60%, and 60-70% central 200 GeV collisions. The universal scaling behavior revealed in this plotting form is remarkable. All centralities seems to exhibit approximately the same form, though there are some deviations for the most central cases at low-p_t. We conjecture that there is a

centrality-independent $Q_0(y_t)$ which is well-described by a boosted Lévy distribution with parameters $T_2 = 0.09$ GeV, $n_2 = 13.8$, and $\Delta y_{t0} = 0.58$ (dashed curve), though there are significant deviations for the more-central events at low p_t. This boost is the same that was observed in the case of minimum-bias identified hadrons in Fig. 7.11 (top two panels).

Similar behavior has been observed for published identified-particle v_2 data for minimum-bias collisions [158], as seen in the lower-right panel of Fig. 7.11 plotted against proper y_t for each particle species. The different particle species have different y_t dependence, which however corresponds to the same common m_t spectrum (solid curves) and the same common Δy_{t0} boost. The boost is a single, sharp value contradicting flow models that depend on Hubble expansion, which would result in a broad range of boosts.

7.4.2 Parametrization

A more detailed study of the systematics of the p_t-dependent quadrupole is possible. First, consider rearranging the definition of Q in Eq. (7.9) and use the definition of V_2 from Eq. (7.4) to get

$$v_2\{2D\}(p_t, b) = \left\langle \frac{1}{p_t} \right\rangle p_t v_2\{2D\}(b) \left[\frac{\rho_0(b) Q_0(p_t)}{\rho_0(p_t, b)} \right]. \tag{7.10}$$

The quantity $\rho_0(b)Q_0(p_t)/\rho_0(p_t, b)$ has a p_t dependence described by the ratio of the quadrupole Lévy distribution to the single-particle spectrum. This is approximately an exponential for larger values of p_t.

We can then construct a new parametrization of the form

$$v_2\{2D\}(p_t, b) \approx \left\langle \frac{1}{p_t} \right\rangle p_t v_2\{2D\}(b) \exp(-p_t/4) \times f(p_t, b), \tag{7.11}$$

where $f(p_t, b)$ is a dimensionless factor needed to describe deviations from the exponential form at low-p_t. It can be fit to the data with the form

$$f(p_t, b) = 1 + C(b)[\mathrm{erf}(y_t - 1.2) - \mathrm{erf}(1.8 - 1.2)], \tag{7.12}$$

where $C(b) = 0.12 - (\nu - 3.4)/5 - [(\nu - 3.4)/2]^5$. This parametrization provides a more accurate description of the quadrupole term over a wider range of p_t and centrality than the Lévy distribution alone. The factor $f(p_t, b)$ is approximately 1 above about 0.75 GeV/c.

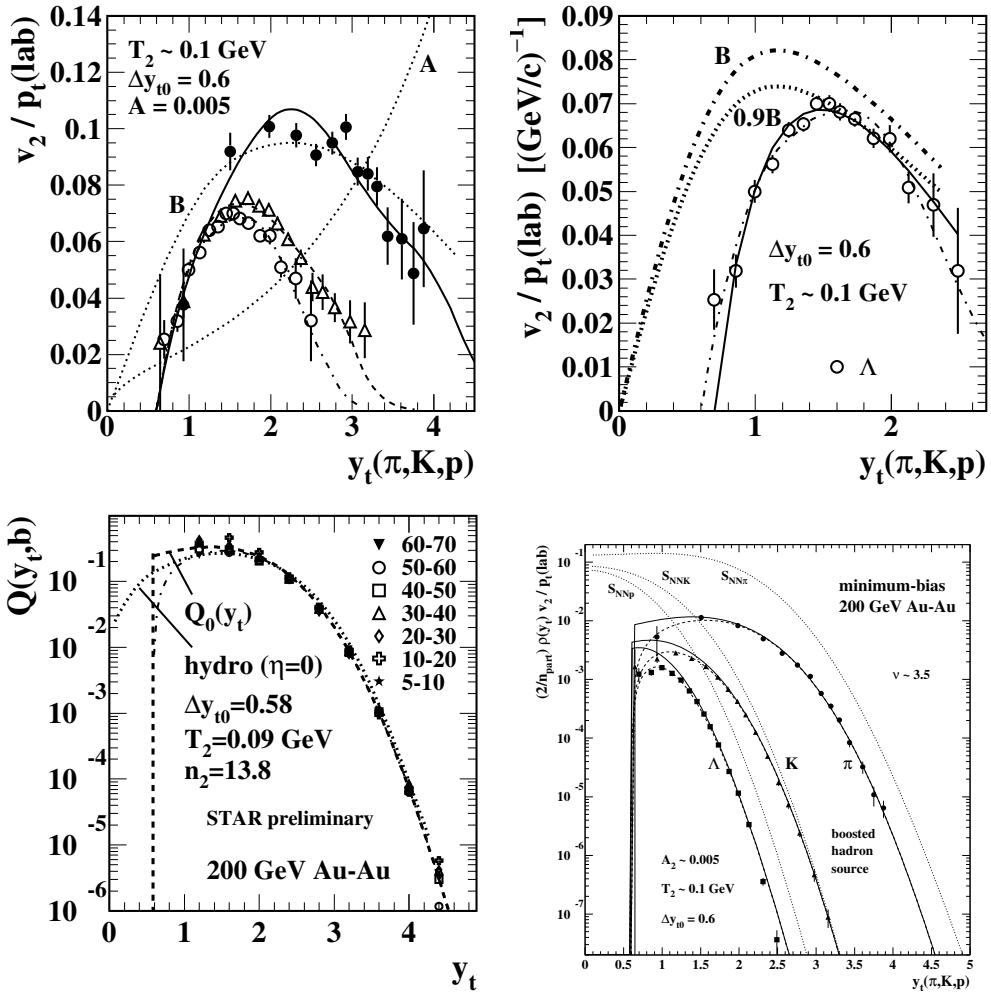

Figure 7.11: Upper-left panel: Identified $v_2(p_t)/p_t$ for pions (closed circles), kaons (open triangles), and protons (open circles) for minimum-bias collisions [6] vs. proper y_t for the particle species [158]. Upper-right panel: A magnification of the results for lambda particles. Lower-left panel: The quadrupole spectrum of unidentified particles for a range of centralities at 200 GeV. Lower-right panel: The minimum-bias quadrupole spectrum for different particle species [158].

Where the p_t dependence of $v_2\{2D\}(p_t, b)$ is entirely described by the factor $p_t \exp(-p_t/4)$. This leads to a factorization of the p_t and centrality dependence of $v_2(p_t, b)$ for higher p_t. This factorization can be combined with the factorization of collision energy and centrality dependence of the p_t-integrated quadrupole $v_2\{2D\}(b, \sqrt{s_{NN}})$described in Sec. 6.3.1 for a complete description of the azimuth quadrupole component, at least at higher p_t. This implies that there is very simple underlying behavior of the azimuth quadrupole.

We have developed a comprehensive understanding of the quadrupole term of p_t-dependent correlations. There is a universe quadrupole spectrum with a single, sharp boost. We will analyze the "nonflow" 2D Gaussian term in more detail in Chapter 9. But first we take a detour to study jet fragmentation in a much simpler system.

Chapter 8

FRAGMENTATION FUNCTIONS IN e^+-e^- COLLISIONS

8.1 Motivation

QCD theory predicts that an abundance of soft gluons (minijets) should be produced in relativistic collisions at RHIC [114]. Copious gluon production may drive formation of the colored medium in heavy ion collisions and global hydrodynamic phenomena [132, 133]. However, the degree of equilibration of minijets in heavy ion collisions remains uncertain theoretically and experimentally. In Chapters 6, 7, and Appendix A we see examples of significant jet-like correlations in heavy-ion collisions. We want to know if these correlations are really produced from parton fragmentation.

Fragmentation functions have been studied extensively in e^+-e^- collisions because it is a very clean system. In a standard dijet event a quark and antiquark are produced which subsequently fragment to produce two back-to-back jets. Since these two jets are all that is present in the event, momentum conservation demands that each parton have exactly half of the initial collision energy. This makes e^+-e^- collisions an ideal system for studying fragmentation, as the parton energy can is known and there is minimal background from other processes. It is very difficult to study fragmentation functions in heavy-ion collisions, but we will derived a parametrization of fragmentation in e^+-e^- collisions that can be applied to heavy-ion collisions.

Initial measurements of two-particle angular correlations in p-p collisions at Fermilab (fixed target) and the CERN ISR on momentum subspace (η, ϕ) (pseudorapidity and azimuth) [179] were described in terms of longitudinal (string) fragmentation [53]. Jets—correlated fragments from hard-scattered partons—were first observed at larger p_t and $\sqrt{s}$, establishing the nature of hard parton scattering and the validity of perturbative QCD (pQCD) [43]. A pioneering study of two-particle fragmentation functions in LEP e^+-e^- collisions is described in [19] (*cf.* a related theoretical treatment in [93]).

Minijet correlations in p-p and heavy-ion collisions observed at RHIC represent QCD in a *non*-perturbative context: parton scattering, energy loss and fragmentation at low Q^2. We wish to connect those measurements to QCD theory *via* parton fragmentation measurements at larger Q^2 in elementary collisions. A context for two-particle fragment distributions at RHIC can be established by studying single-particle fragmentation functions (FFs) from p-$\bar{\text{p}}$ and e^+-e^- collisions, the latter providing especially precise access to the fragmentation process down to very low parton Q (dijet energy) and hadron momentum.

Low-Q^2 fragmentation is related to *local parton-hadron duality* (LPHD) which provides a correspondence between pQCD parton predictions and hadronic observables [60, 61, 86]. According to LPHD conversion of partons to hadrons occurs locally in configuration space, with almost no distortion of the parton momentum distribution. The *structural* difference between a parton and a hadron should vanish for $Q \sim$ 1 - 2 GeV where parton production is *most abundant* in RHIC collisions. LPHD is important for low-Q^2 partons where 'fragmentation' may terminate with one or two partons (and hence hadrons). Minijet-related minimum-bias two-particle correlations studied in p-p and A-A collisions [170, 28, 157, 138, 29, 137] may therefore provide details of parton fragmentation at the energy scale where LPHD is most important.

Modification of parton scattering and fragmentation in the QCD medium of heavy ion collisions may reveal properties of the medium itself. A theoretical study of in-medium modification of the single-particle FF in A-A collisions is reported in [75]. The expectation is deformation of the *in vacuum* FF toward lower momentum, possibly corresponding to observed changes in the single-particle p_t spectrum ratio R_{AA} with collision centrality [31, 20]. A related study of two-particle correlations in heavy ion collisions, especially the asymptotic approach of fragment distributions to thermal equilibrium with increasing parton dissipation in the medium, is reported in [30]. Given the close connection between single-particle FFs and minijet-related two-particle fragment correlations, correlation measurements in heavy ion collisions may provide a more differential picture of properties of the QCD medium and its influence on low-Q^2 parton fragmentation.

In this chapter we establish a basis for *extrapolation* of measured e^+-e^- FFs to small energy scales as preparation for similar extrapolations in nuclear collisions. This is not a

theoretical analysis based on pQCD methods. For an example of such an analysis which consistently describes FFs over a large x_p (momentum fraction) range *cf.* [44] and the related discussion in Sec. 8.6.3. This is a phenomenological analysis of FF data intended to provide the best possible extrapolation down to small parton energies where pQCD assumptions such as colinearity and factorization become are not justified.

The chapter is organized as follows: We first present a new method of analyzing fragmentation functions, with emphasis on rapidity y as a preferred kinematic variable for low-Q^2 fragmentation studies. We then consider the general properties of FFs in the context of the double-log approximation (DLA), angular ordering and color coherence. We compare measured FFs from e^+-e^- collisions at three energies on several momentum variables and describe a new form of approximate energy-scale invariance on *normalized rapidity* u. We demonstrate that FFs on u are precisely modeled by the *beta distribution*. We consider FFs for identified hadrons and identified partons. Based on fits to measured FFs and jet multiplicity data we develop a simple, precise parameterization of e^+-e^- FFs valid over a broad energy range. Finally, we use our parameterization to study scaling violations and extrapolation to low Q^2.

8.2 Fragmentation Functions

The FF $D(x_E, Q^2)$ as used in this analysis is a single-particle density $2dn/dx_E$ of hadron fragments on energy fraction $x_E = E_{hadron}/E_{parton}$ produced by a pair of partons (dijet) with total energy Q ($Q^2 = -q^2$ is the negative invariant mass squared for the initial momentum transfer). Momentum fraction $x_p = p_{hadron}/p_{parton}$ approximates x_E if particle momenta are measured. At large x the distribution shape reflects energy conservation during the parton splitting cascade. At small x the shape is determined by quantum coherence of gluon emission (gluon or color coherence and the hadron size scale) [40, 88]. The FF data used in this study are hadron distributions reported on momentum fraction x_p, or $\xi_p \equiv \ln(1/x_p)$. Distributions on x_p emphasize pQCD aspects of parton fragmentation at large p (*e.g.,* scaling violations). For non-pQCD effects, especially the role of gluon coherence, logarithmic variable ξ_p provides better visual access to the relevant small-x_p (large-ξ_p) region.

8.2.1 Analysis Method

$D_p^h(x, Q^2$ or $s)$ is the FF for parton type p and hadron type h at the energy scale denoted by Q^2 or s. The parton-species-inclusive distribution $D^h(x, s)$ is discussed in Sec. 8.2.6, and the fragment-flavor-inclusive distribution $D_p(x, s)$ is discussed in Sec. 8.2.7. The total FF is $D(x, s) = \sum_h D^h(x, s)$. The corresponding FF on ξ is $D(\xi, s) = x\, D(x, s)$, with Jacobian factor x. FFs satisfy relations $\int_0^1 dx\, D(x, s) = 2n$ (dijet fragment multiplicity) and $\int_0^1 dx\, x\, D(x, s) = 2$ (dijet energy conservation) [69]. To simplify notation we adopt the convention that symbol D represents any fragmentation function, with the specific form [Jacobian relation to $D(x, s)$] implied by the first argument. Plot axes are labeled with the corresponding dijet particle density $D(x, s) \to 2dn/dx$, $D(\xi, s) \to 2dn/d\xi$, *etc.* to avoid confusion.

This study focuses on low-Q^2 parton fragmentation. Since ξ_p and pQCD expansion parameter $Y(Q) = \ln(Q/\Lambda)$ (Λ represents a reference energy scale) are undefined as p, $Q \to 0$ we introduce rapidity y (well-behaved in that limit) as an alternative logarithmic momentum/energy variable. The rapidity along axis $\hat{z}$ is $y_z(\vec{p}; m_0) \equiv \ln[(E + p_z)/m_t]$, with transverse (to $\hat{z}$) mass $m_t^2 = m_0^2 + p_t^2$. In frames co-moving on $\hat{z}$ $\vec{p} \to p_t$, $E \to m_t$ and $y \to y_t = \ln\{(m_t + p_t)/m_0\}$. In a frame where p is the only non-zero momentum component $y(p; m_0) = \ln[(E + p)/m_0]$, with $y \to \ln(2p/m_0)$ for $p \gg m_0$ and $\to p/m_0$ for $p \ll m_0$. m_0 may be a quark or hadron mass or energy scale Λ.

Given the limiting cases for y we note that $\ln(\sqrt{s}/m_0) \sim y(\sqrt{s}/2; m_0) \equiv y_{max}$, the kinematic limit for fragment rapidities. Similarly, $Y(Q) = \ln(Q/\Lambda) \sim y(Q/2; \Lambda)$ is a rapidity measure of the energy scale relative to a reference scale. We observe for data a lower limit y_{min} which may depend on fragment species and collision system (e^+-e^- *vs* p-$\bar{\text{p}}$). For unidentified fragments we assign the pion mass $m_0 \to m_\pi$ to all hadrons (but *cf.* Sec. 8.2.6). From data distributions on x_p or ξ_p for parton energy scale Q or CM energy $\sqrt{s}$ we extract fragment momenta p and calculate equivalent rapidities y (fragments) and y_{max} (partons). Data distributions on x_p or ξ_p are transformed to distributions on y using appropriate Jacobians. In [12] $\ln(1/x_p) \to \ln\{(E + p)_{parton}/(E + p)_{hadron}\} = y_{max} - y$ exactly.

Most e^+-e^- FFs plotted on normalized rapidity $u \equiv (y - y_{min})/(y_{max} - y_{min}) \approx 1 - \xi_p/Y$

have a particularly simple form described by the *beta distribution*. The unit-normal beta distribution defined on $u \in [0,1]$ is $\beta(u;p,q) = u^{p-1}\,(1-u)^{q-1}/B(p,q)$, with parameters p, $q \geq 0$ and beta function $B(p,q) = \frac{\Gamma(p)\,\Gamma(q)}{\Gamma(p+q)}$. Parameters p and q determine the shape of the distribution below and above the mode (most probable point) respectively. The mode is $u^* = \frac{p-1}{p+q-2}$, the mean is $\bar{u} = \frac{p}{p+q}$ and the variance is $\sigma_u^2 = \frac{p\,q}{(p+q)^2(p+q+1)} \approx \frac{1}{4(p+q+1)}$ (to 2%) [165].

8.2.2 e^+-e^- Fragmentation Functions

The double log approximation (DLA [88]) provides a context for extrapolating the fragmentation process to low Q^2. The fragment emission probability is approximated by a uniform density on logarithmic space $[\log(\theta), \log(p)]$, where θ is the radiated-parton emission angle and p is its momentum. The distribution is sketched in Fig. 8.1 (upper-left panel), where P is the leading-parton momentum and $\Theta \sim 1$ is the jet angular acceptance. The large solid triangle represents the kinematic boundary for the first radiated parton. The smaller triangles illustrate the *self-similar* nature of the splitting process (angular ordering [121]), each radiated parton becoming itself a DLA radiator. Alternatively, the DLA may be expressed in terms of $d\log(k_t)/dy$, where k_t is the transverse momentum component relative to the radiating parton momentum, and y is the radiated parton rapidity [54]. The flat DLA emission probability is terminated at some k_t (grey band in Fig. 8.1 upper-left panel) due to *gluon coherence* [88]. For sufficiently small k_t the conjugate transverse size of the virtual gluon overlaps the radiating parent parton and parton showering is terminated.

The general form of the FF and its evolution with p_{parton} corresponding to the DLA with angular ordering and gluon coherence (modified leading log approximation or MLLA [181]) is sketched in Fig. 8.1 (upper-right panel). We expect a monotonic increase with decreasing y below y_{max} due to showering. The available phase space (above the band in the left panel) is however reduced with decreasing y by gluon coherence, causing the FF to turn over, with a maximum at y^* (the mode). The distribution then falls to zero at some y_{min} which may be nearly independent of y_{max}. The FF is apparently self-similar at two levels: the internal cascade and its external boundary. Reducing the maximum opening angle Θ (dash-dot line)

or increasing the parton momentum P (dashed line) changes the boundary of the cascade (upper-left panel) and correspondingly the FF (upper-right panel).

8.2.3 Fragment Distribution on x_p and ξ_p

Single-particle FFs from e^+-e^- collisions have been studied extensively (*e.g.,* [78, 40, 17, 3, 16, 18]). The FF data plotted in Figs. 8.1 - 8.3 were obtained from collisions at three energy scales (CM energy $Q = \sqrt{s} = 14$, 44 and 91.2 GeV) measured at PETRA [78] and LEP [40] for unidentified hadrons from unidentified partons (flavor-inclusive jets). Those distributions are fiducial for this study because of the exceptional data quality and fragment momentum coverage. We consider the data in several presentation schemes and then develop a parameterized representation for extrapolation to low Q^2.

In Fig. 8.1 we plot fragment distributions on momentum fraction x_p (lower-left panel) and logarithmic equivalent ξ_p (lower-right panel). Distributions on x_p emphasize the large-x_p (small-ξ_p) region where pQCD is expected to best describe data, where the naïve parton model predicts 'scaling' or invariance of the parton distribution on energy scale Q. The dashed reference line in the third panel illustrates the exponential model sometimes used to characterize FFs on x_p. The vertical dotted line corresponds to $\xi_p = 1.5$ in the right panel: only a small fraction of fragments fall above that point. The data exhibit systematic scaling violations (Q dependence) described by the DGLAP evolution equations [165, 85, 48]. To study scaling violations FFs on x_p are parameterized by a model function such as $D_p^h(x, Q^2) = N\, x^\alpha\, (1-x)^\beta\, (1 + \gamma/x)$, where the four parameters depend on parton type p, hadron type h and energy scale Q [176, 122]. Distribution details in the small-x_p region (*e.g.,* below $x_p = 0.1$) are minimized in this format (*cf.* Sec. 8.6.3).

We can also plot data on ξ_p (lower-right panel) which emphasizes the small-x_p (large-ξ_p) region and better reveals non-perturbative details of fragmentation. The distribution is *approximately* Gaussian, with mode ξ_p^* and r.m.s. width σ_{ξ_p} predicted by pQCD (*cf.* Sec. 8.5). As noted, the fall-off at large ξ_p and maximum at ξ_p^* result from gluon coherence [40, 88]. Measurement of the full fragment distribution above and below the mode is important for a complete characterization of the fragmentation process.

The solid curves in Figs. 8.1 - 8.3 are obtained from beta distributions on normalized rapidity u determined by the systematic trends of beta parameters (p, q) plotted in Fig. 8.11 (left panel) (*cf.* Sec. 8.4.3) and transformed to each plotting space with appropriate Jacobians. Some approximation to 'scaling' or energy-scale independence is expected at large x_p (small ξ_p). Another form of scaling at small x_p (large ξ_p) may be explored by plotting distributions on rapidity y.

8.2.4 Fragment Distributions on y

Fragmentation functions plotted on ξ_p coincide at the kinematic limit $\xi_p = 0$ corresponding to the parton momentum. However, in Fig. 8.2 (upper-left panel) we observe that the FFs for three energies plotted on y have a common low-momentum limit $y_{min} \sim 0.35$ (vertical line, and *cf.* Sec. 8.3.1). That alignment is possible because y has the well-defined limiting value 0 as momentum $p \to 0$. Each data FF is terminated at the upper end by its kinematic limit $y_{max} = y(\sqrt{s}/2; m_0)$ (vertical lines) corresponding to $\xi_p = 0$ in Fig. 8.1 (lower-left panel). The distribution maxima increase monotonically with collision energy. The FFs in the left panel illustrate the self-similarity sketched in Fig. 8.1 (upper-right panel) and confirm an expectation for DLA scaling: fragmentation at small y should be nearly independent of the leading parton momentum.

In Fig. 8.2 (upper-right panel) we plot FFs from p-$\bar{\text{p}}$ collisions at FNAL [17] (the points are samples from the original data distributions used here to illustrate qualitative features). While the general features are similar to FFs for e^+-e^- collisions the lower limit y_{min} is considerably larger for p-$\bar{\text{p}}$ collisions (note the dotted reference line common to the two panels). The larger y_{min} for p-$\bar{\text{p}}$ collisions (~ 1.5) may be due to the finite jet-cone opening angle [17] and/or the presence of the underlying event [36] which must be distinguished from jet fragments. The Gaussian curve labeled MB represents a *minimum-bias* fragment distribution (no selection is imposed on the parton momentum spectrum) derived from the event-multiplicity dependence of p-p p_t spectra [24] which compares well with the systematics of FFs obtained from p-$\bar{\text{p}}$ jet reconstruction.

In Fig. 8.2 we compare FFs on $\xi_p \equiv \ln(Q/2p)$ (lower-left panel) and $y_{max} - y \sim \ln(Q/2p)$

(lower-right panel). The distributions are equivalent below the upper half-maximum points ($p \gg m_0$), above which distributions on $y_{max} - y$ drop rapidly toward well-defined limits at $y_{max} - y_{min}$. Distributions on ξ_p extend in principle to ∞, but the transformed beta distributions limit at $p_{min} \sim m_\pi/2$ or $\xi_p \sim \ln(Q/m_\pi)$, indicated by vertical lines in Fig. 8.2 (lower-left panel). This comparison suggests that rapidity $y(Q/2; m_0)$ or difference $y_{max} - y$ could replace ξ_p in FF studies. Rapidity $y(Q/2; \Lambda)$ could also replace pQCD expansion parameter $Y(Q) = \ln(Q/\Lambda)$, remaining well-defined for $Q \to 0$ while preserving established pQCD relations for larger Q. Fig. 8.2 also suggests that rescaling the rapidity by $y_{max} - y_{min}$ might provide more differential access to FFs.

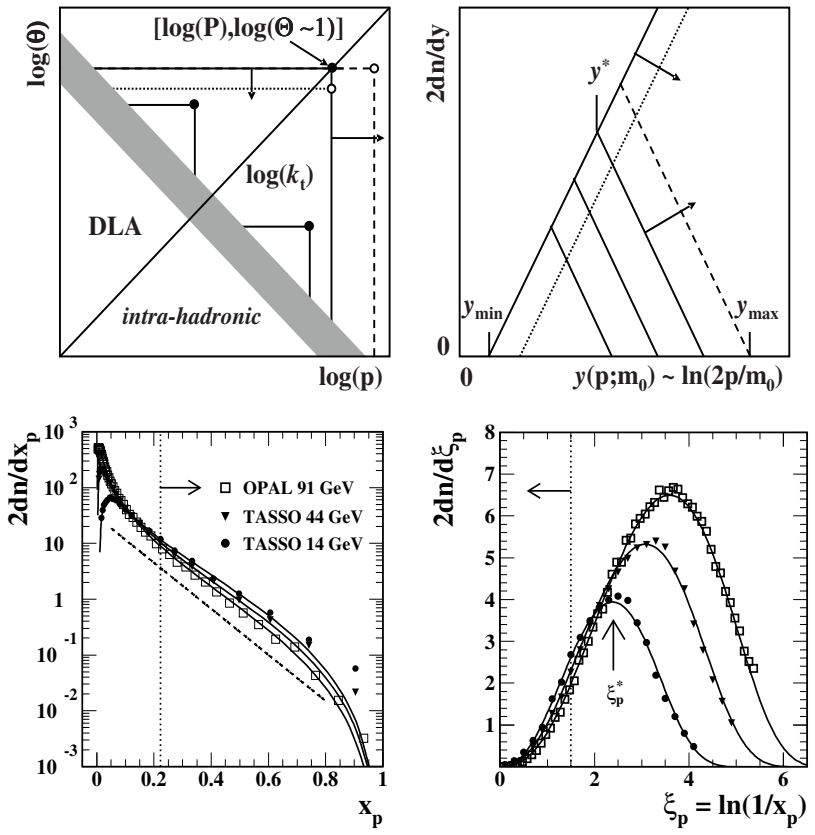

Figure 8.1: Upper-left panel: Schematic illustration of the double-log approximation (DLA) to parton fragmentation. Upper-right panel: Self-similar variation with energy of the the corresponding fragment distribution on y. Lower-left panel: e^+-e^- fragmentation functions on fractional momentum $x_p = p_{\rm fragment}/p_{\rm parton}$ for three CM energies. The dashed line is an exponential reference. Lower-right panel: The same fragmentation functions on logarithmic variable $\xi_p = \ln(1/x_p)$. The vertical dotted lines mark equivalent points on the two variables. The solid curves are determined by the parameterization from this analysis.

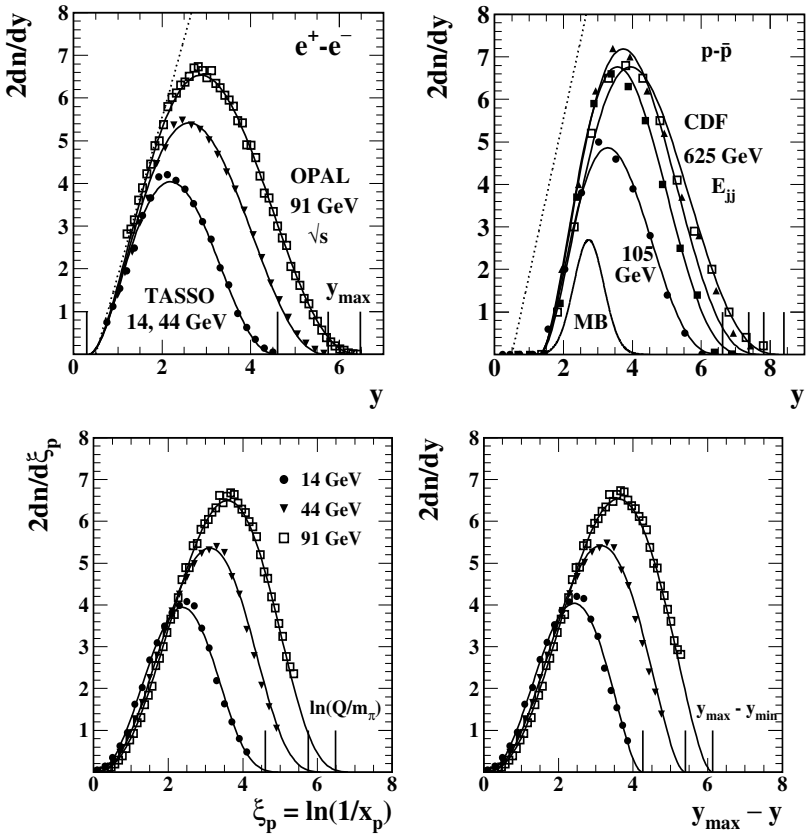

Figure 8.2: Upper-left panel: Fragmentation functions on rapidity y for e^+-e^- collisions. Upper-right panel: Fragmentation functions on rapidity y for p-$\bar{\text{p}}$ collisions. Lower-left panel: Comparison of fragmentation functions for three energies on ξ_p. Lower-right panel: The same comparison on $y_{max} - y$. Differences are noticeable only for small y or p (large ξ_p).

8.2.5 Fragment Distribution on u

Expectations of approximate energy scaling at large x_p and a different form of scaling (gluon coherence) at small x_p seem to require conflicting plotting strategies on ξ_p and y. However, both forms can be accommodated with normalized rapidity $u \equiv (y - y_{min})/(y_{max} - y_{min}) \in [0, 1]$. FFs from e^+-e^- collisions can be factored as $D(u, y_{max}) = 2n(y_{max})\, g(u, y_{max})$, with dijet multiplicity $2n(y_{max})$ (*cf.* Fig. 8.10) and unit-normal form factor $g(u, y_{max})$. In Fig. 8.3 we plot the three representative FFs transformed to $1/n(y_{max})\, dn/du \equiv g(u, y_{max})$. Multiplicity $2n(y_{max})$ can be obtained from fits to data, but also from the *shape* of $g(u, y_{max})$ based on an energy sum rule (*cf.* Sec. 8.4.2).

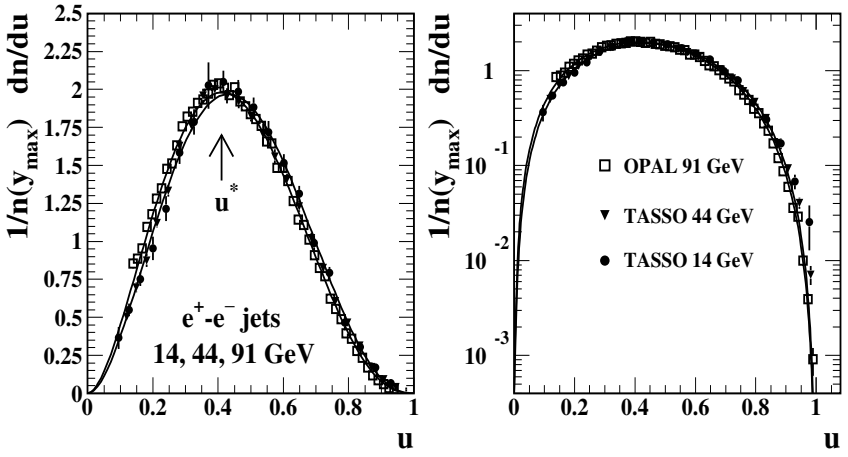

Figure 8.3: Fragmentation functions plotted on normalized rapidity u in linear (left panel) and semi-log (right panel) formats. The data distributions have been normalized by the corresponding di-jet multiplicity at each energy (lower solid curves in Fig. 8.10) determined by parameters (p, q). The data for three energies are plotted, but the curves for only 14 and 91 GeV are plotted to provide visible separation.

We have determined that form factor $g(u, y_{max})$ is well-described by beta distribution $\beta(u; p, q)$ defined in Sec. 8.2.1. While there are substantial 'scaling violations' on x_p or ξ_p [165], the normalized FF shapes on u in Fig. 8.3 are nearly independent of Q^2 or y_{max} over a large energy range. However, the remaining small variations with energy are significant, and well described by energy-dependent beta parameters (p, q) plotted in Fig. 8.11 and discussed in Sec. 8.4.3.

8.2.6 Identified Hadron Fragments

We define rapidities for unidentified hadrons by assigning the pion mass $m_0 \to m_\pi$ to several particle species. To assess the consequences we use identified-particle FF data for two CM energies. In Fig. 8.4 we show data $g(u, y_{max})$ and best-fit model $\beta(u; p, q)$ for identified charged pions $\pi^\pm$ (left panel) and kaons $\mathrm{K}^\pm$ (right panel) at 10 GeV [45] and 91 GeV [79]. Parton rapidity y_{max} is determined in each case with the identified *hadron fragment mass*. The distributions for identified protons ($\mathrm{p},\bar{\mathrm{p}}$) show similar behavior but with larger statistical errors. The pion FFs have widths similar to unidentified hadrons, but the peak modes are significantly lower (0.38 *vs* 0.41 at 91 GeV). The kaon peak modes are comparable to those for unidentified hadrons but the peak width at higher energy is significantly larger. The kaon FF shape seems to converge on the pion distribution at lower energy. The apparent blending of quark flavors could be related to the convergence of the gluon and quark FFs at lower energy in Fig. 8.11.

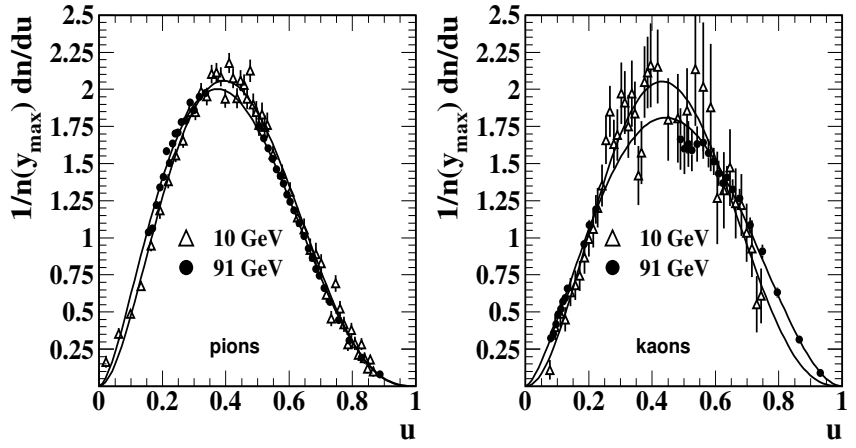

Figure 8.4: Fragmentation functions for two CM energies and for pion (left panel) and kaon (right panel) fragments plotted on normalized rapidity u.

To determine the effect of assigning the pion mass to unidentified fragments we used the following procedure. Data distributions on x_p for three identified fragment species (the 91 GeV data in Fig. 8.4) were transformed to normalized rapidity u with the proper mass assignments. Functions $\beta(u; p, q)$ were fitted to each species, transformed back to x_p and

plotted (dash-dot curves) with the data in Fig. 8.5 (left panel). The model functions on x_p were summed to represent the combination of unidentified hadrons and transformed to rapidity y assuming the pion mass, giving the solid curve in Fig. 8.5 (right panel). The dotted curve was obtained by assigning the pion mass to all data, transforming to u, fitting the resulting distribution and then transforming back to y. We conclude from the results that misidentifying kaons and protons as pions in unidentified hadrons shifts the FF peak mode at 91 GeV from the pion value ~ 0.38 to the inclusive hadron value ~ 0.41 in Fig. 8.3 (left panel). The dashed and dash-dot curves are fits to the individual fragment species with proper masses used to determine the rapidities.

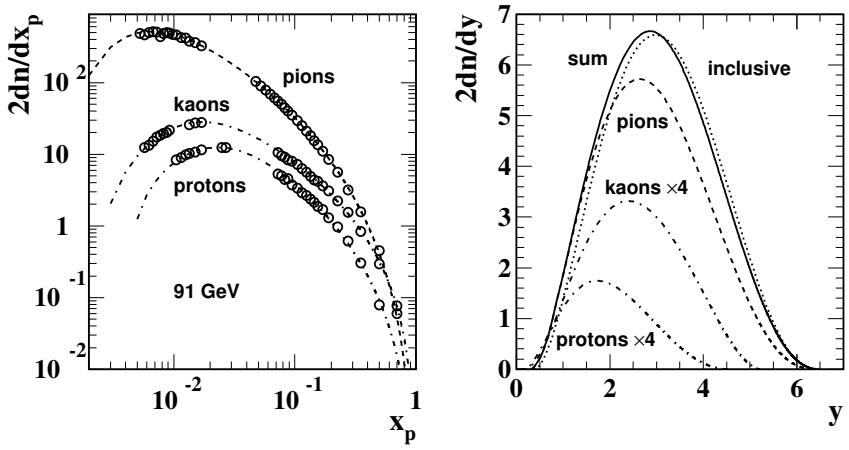

Figure 8.5: Left panel: Fragmentation function data for $\sqrt{s} = 91$ GeV and for three hadron species on fractional momentum x_p and corresponding beta-distribution fits on normalized rapidity u transformed to x_p (dash-dot curves). Right panel: Dashed and dash-dot curves for identified hadrons with proper mass assignments transformed from the left panel. The solid curve is a sum on x_p of the beta-distribution fits from identified fragments in the left panel transformed to rapidity y with a pion mass assignment. The solid curve is close to the distribution obtained from inclusive hadrons (dotted curve).

From this exercise certain trends are notable: Proton fragments have the largest momenta but the smallest rapidities. When transformed to normalized rapidity u the FFs for different fragment species are similar in shape (beta distribution) but exhibit small but significant mode variations with parton energy and hadron species (*cf.* Fig. 8.7 and the discussion following for a summary of flavor dependence). Unit-normal data distributions

$g(u, y_{max})$ for all light hadron species are well-described by model $\beta(u; p, q)$, establishing applicability of the beta distribution to FFs for identified light meson and baryon fragments as well as to inclusive hadrons.

8.2.7 Identified Partons

We now consider the role of parton identity in FF systematics. Normalized data distributions on u are shown in Fig. 8.6 for inclusive hadrons from udsc-quark jets (upper-left), gluon jets (upper-right) and b-quark jets (lower-left) for several parton energies in each case [4, 1]. The measured FFs for light quarks and gluons are well described by model $\beta(u; p, q)$, shape parameters (p, q) depending on parton species and energy scale. Dijet multiplicities are obtained as the best-fit coefficients of the unit-normal beta distribution. As expected, there is a substantial difference between quark and gluon FFs at larger jet energies, and a strong energy dependence of gluon jet shapes for smaller jet energies evident in the upper-right panel (the two solid curves correspond to $\sim$ 5 and 40 GeV gluons) (*cf.* Sec. 8.4.3). The b-quark data in the lower-left panel are not well described by the beta distribution. The best-fit beta distributions for $\sqrt{s} = 91.2$ GeV udsc quark and $Q = 80.2$ GeV (equivalent dijet energy) gluon jets (data with the best statistics) are repeated as the dashed ($\beta_{\rm q}$) and dash-dot ($\beta_{\rm g}$) curves respectively in all three panels to provide references.

In Fig. 8.6 (lower-right panel) we compare FFs from different parton types in a more differential format. As noted, $\beta_{\rm q}$ (dashed curves) for light fragments in udsc jets and $\beta_{\rm g}$ (dash-dot curves) for gluon jets are approximate limiting cases for all $\beta(u; p, q)$. We therefore define $v_{max} \equiv \ln(\beta_{\rm q} + \beta_{\rm g})$, $v_{min} \equiv -\ln(1/\beta_{\rm q} + 1/\beta_{\rm g})$ and normalized variable $v(\beta) \equiv (\ln\beta - v_{min})/(v_{max} - v_{min})$, with $v(\beta_{\rm q}) + v(\beta_{\rm g}) = 1$. We plot $v(\beta_{\rm q})$ (dashed), $v(\beta_{\rm g})$ (dash-dot) and $v(\beta_{\rm b})$ (solid) in the lower-right panel with the corresponding data for $\sqrt{s} = 91.2$ GeV quarks and $Q = 80.2$ GeV gluons (also *cf.* data and solid curves in Fig. 8.9 (first two panels)).

The light-fragment distribution from b quarks (solid dots) coincides with $v(\beta_{\rm q})$ (and open circles) for $u < 0.7$, but diverges sharply from the quark-jet trend above that point and descends towards $v(\beta_{\rm g})$ (and open triangles) for $u > 0.7$. The b-quark fragment data

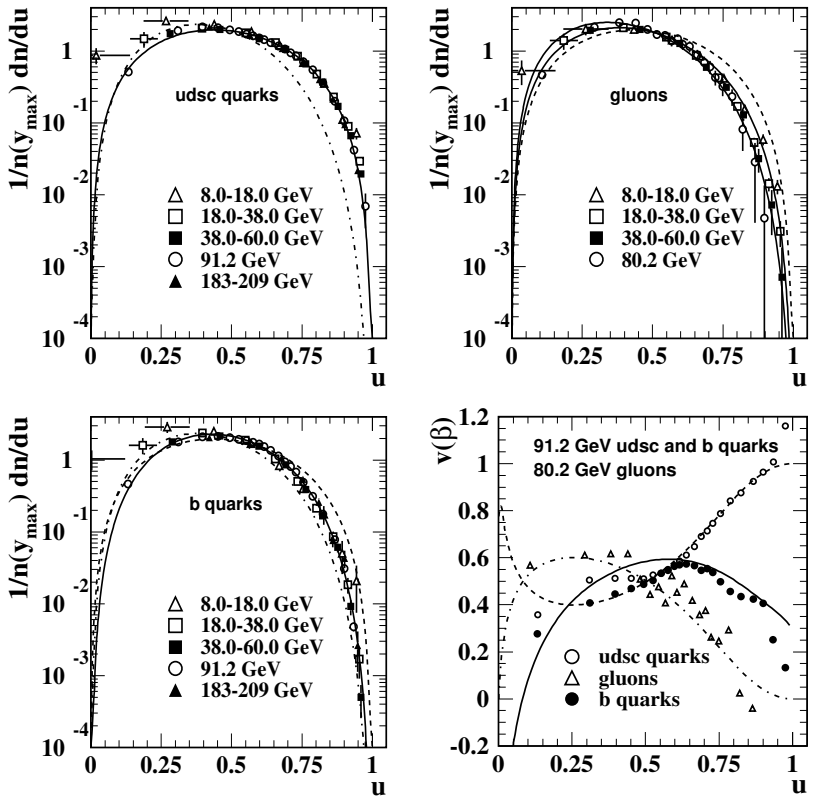

Figure 8.6: Unit-normal fragment distributions on normalized rapidity u for udsc quarks (upper left), b quarks (lower left) and gluons (upper right) fragmenting to inclusive hadrons. Lower-right panel: Normalized logarithmic variable $v(\beta)$ (see text) measures the FF shape for b-quark jets (solid) relative to those for gluon jets (dash-dot) and udsc-quark jets (dashed) as references.

were reduced by 10% to coincide with the quark-jet curve below $u \sim 0.7$. The initial normalization is represented by the beta-distribution fit $v(\beta_{\rm b})$ (solid curve) with mode near 0.5. With this more differential format we confirm that b-quark light-hadron fragments are not well described by a beta distribution. The exceptional softness of the b-quark FF (for unidentified fragments) was anticipated theoretically [177] (and *cf.* Fig. 8.7).

In Fig. 8.7 we summarize FF data and models for several fragment and parton types. The pion, kaon and proton FFs are beta-distribution fits to 91 GeV identified-fragment data (pion and kaon data are shown in Fig. 8.4). The gluon FF is the beta distribution defined at 80 GeV by (p, q) systematics in Fig. 8.11 (*cf.* comparison with FF data in Fig. 8.9 – second

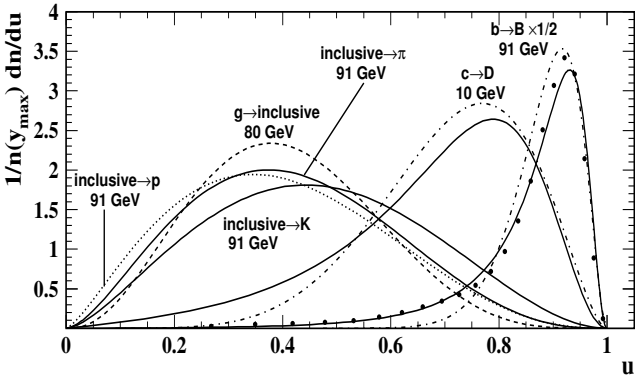

Figure 8.7: Distributions on u for several quark/meson flavor combinations, showing evolution of the $g(u, y_{max})$ shape with quark/meson mass. The c $\to$ D data are from [76, 46], and the b $\to$ B data are from [104]. The energies are dijet energies.

panel). The solid dots are b $\to$ B data from [104] compared to a best-fit beta distribution (dash-dot curve) and theory (solid curve). Low-statistics c $\to$ D data from [76, 46] are summarized by a best-fit beta distribution (dash-dot curve) and theory (solid curve).

The two solid curves on the right of Fig. 8.7 are from a theoretical treatment of heavy-quark fragmentation in which the FF for $Q \to H(Q\bar{q}) + q$ is approximated by $D_Q^H(x_p) \propto 1/\{1-1/x_p-\epsilon_Q/(1-x_p)\}^2/x_p$, with $\epsilon_Q \propto 1/m_Q^2$ [135]. The agreement of $D_b^B(u)$ (right-most solid curve) with b-quark data (solid points) [104] using $\epsilon_Q = 1.16/m_b^2 = 0.055$ and $m_b \sim 4.6$ GeV/c^2 is good. The dash-dot curve is the best-fit beta distribution with $(p, q) = (23, 3)$ which does not describe the $b \to B$ data. That failure may be related to the exceptional behavior of b $\to$ light hadrons discussed in connection with Fig. 8.6 (lower panels). The solid curve for $c \to D$ is $D_c^D(u)$ from the heavy-quark theory treatment, with $\epsilon_Q = 0.57/m_c^2 = 0.29$ and $m_c \sim 1.4$ GeV/c^2. The associated dash-dot curve is a beta distribution with $(p, q) = (7.0, 2.8)$ which best describes the data from [76, 46]. Both curves are consistent with the data, but the data errors are large below the FF peak mode.

FF modes increase monotonically with increasing meson and parton mass. However, the proton FF mode for udsc jets is lower than the inclusive hadron mode for gluon jets and the FF is significantly broader. The kaon FF shows the effect of the heavier s-quark mass, consistent with the trend for charm and bottom quarks (however, see the next paragraph).

The FF mass dependence on normalized rapidity u is subtle compared to the kinematic dependence on meson and parton masses encountered on p_t, ξ_p or y.

To summarize flavor dependence, the beta distribution describes the FF data for identified light quarks and gluons fragmenting to identified light mesons or baryons, providing a compact representation of the flavor dependence of fragmentation. The quality of the description is not good for heavy quarks fragmenting to light or heavy mesons. However, the region near $u = 1$ can be compared with non-perturbative trends for light-quark fragmentation extrapolated to small Q^2 in Fig. 8.11 (right panel), where the fragmentation 'cascade' is a single splitting or no splitting (parton $\rightarrow$ hadron).

8.3 Parametrization of Fragmentation Functions

We now fit the beta distribution to a sample of measured FFs falling in three groups: 1) the five fiducial FFs for unidentified fragments from flavor-inclusive partons distinguished by nearly complete coverage of the kinematically-allowed fragment momenta [40, 78] and a selection of data for 2) identified fragments and 3) identified partons to explore the role of hadron and parton species in fragmentation. Data in the form $D(u, y_{max})$ are fitted with model function $2n(y_{max})\,\beta(u; p, q)$ (*cf.* Sec. 8.2.1), minimizing χ^2 while freely varying parameters $2n$, p, and q, with $u = (y - y_{min})/(y_{max} - y_{min})$ and y_{min} constrained to specified values based on systematics studies.

8.3.1 Inclusive fragments from inclusive partons

We first fit FF data for inclusive hadrons and partons. Table 8.1 contains the best-fit parameters for the five fiducial FFs (OPAL [40] and TASSO [78] data) with $y_{min} = 0.35$ ($p = 0.05$ GeV/c). The model functions with starred energies are compared to data in Figs. 8.1 - 8.3. As noted, the FF shape is *nearly* independent of $\sqrt{s}$, but there is a significant trend for q to increase and p to decrease with increasing energy scale, shifting the FF mode to smaller u. The fitted multiplicities agree with the q-$\bar{\text{q}}$ multiplicity curves and data in Fig. 8.10.

Fig. 8.8 shows the systematic dependence of beta parameters (p, q) on the choice of y_{min}. The first three panels illustrate the variation of fits and data on u with y_{min} for energies

$\sqrt{s}$ (GeV)	2n	p	q	χ^2/ν
14*	8.8±0.10	2.95±0.08	3.52±0.07	16/18
22	10.7±0.15	2.91±0.06	3.52±0.08	25/20
35	13.4±0.05	2.84±0.02	3.50±0.02	148/22
44*	14.6±0.10	2.89 ±0.03	3.52±0.04	49/22
91.2*	20.4±0.05	2.84±0.01	3.67±0.01	86/51

Table 8.1: Unidentified fragments from unidentified partons: Beta-distribution parameters from χ^2 fits to fragmentation functions for five energies. The FFs for starred energies are plotted in Figs. 8.1 - 8.3.

14, 44 and 91 GeV. χ^2 variations are small over the interval shown. Variation with y_{min} is greater for smaller u and smaller y_{max}. Those trends are reflected in the summary of (p, q) variations in the lower-right panel: the p variation is greater, and more so for lower energy. The lines have slopes 0.8 (solid) and 1.6 (dashed). We set $y_{min} = 0.35$ for all inclusive fits and discuss the related systematic uncertainties in Sec. 8.4.3. The shift of OPAL (rescaled) q data in the lower-right panel (closed squares to open circles) results from increasing all particle momenta by 6.5% to test the effect of uncertainty in the momentum calibration. The p data are much less affected.

8.3.2 Identified fragments from inclusive partons

We next explore the role of hadron identity in fragmentation, with $m_0 \to m_{\rm hadron}$ assigned for both fragment and parton rapidities. Fits to identified hadron fragments from flavor-inclusive partons at $\sqrt{s} = 10$ GeV [45] and 91 GeV [79] plotted in Fig. 8.4 and Fig. 8.5 (left panel) are presented in Table 8.2. Trends for fragmentation to light hadrons are summarized in Fig. 8.7. For pions, parameter p is smaller and q larger than for inclusive hadrons in Table 8.1, shifting the peak mode to smaller u as noted previously and understood as an effect of misidentifying kaons and protons as pions in the inclusive hadron fragment mixture. The pion fit χ^2 is large; however the fit residuals are generally point-to-point random and

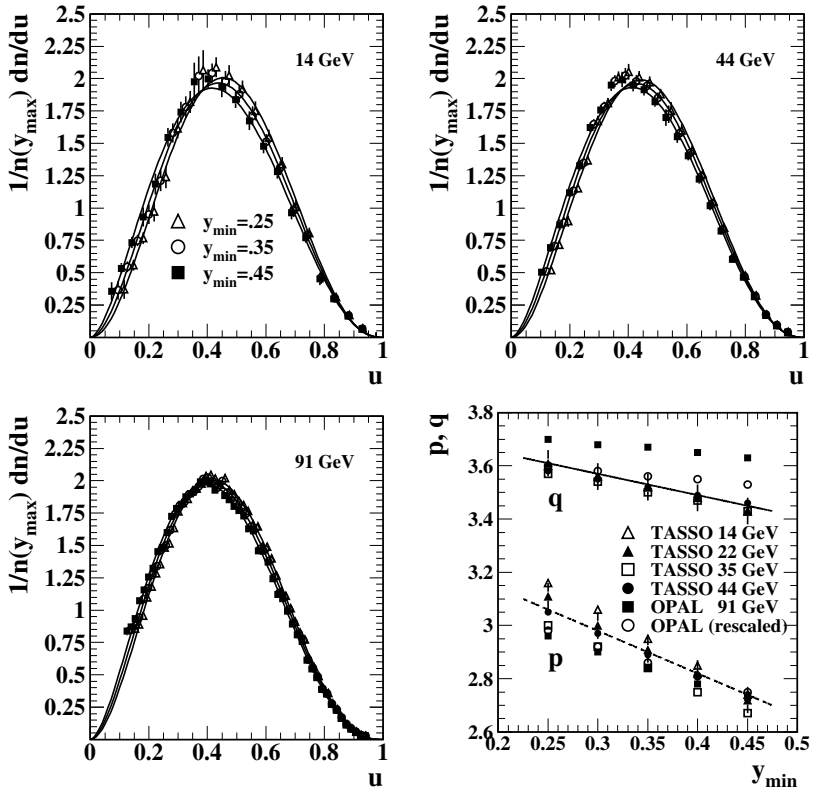

Figure 8.8: A study of the systematic effect on fiducial FFs and their beta parameters (p, q) of variations with y_{min}. The low ends of the FFs are most sensitive, and therefore p and FFs for low y_{max} are affected most. The trends in the lower-right panel may be compared with the (p, q) entries in Table 8.1.

substantially larger than the stated errors, especially toward the ends of the distribution.

The 10 GeV kaon peak is similar to the pion peak. However, the 91 GeV kaon peak is much wider ($p + q$ is reduced) and the mode is shifted substantially to the right ($q - p$ is reduced) relative to the pion peak, consistent with the quark mass-dependence trend in Fig. 8.7. The proton peak mode is shifted further to the left, beyond the pion and gluon peaks as shown in Fig. 8.7, mainly by reduction of p. We note in passing that $y_{min} \sim \ln\left[\frac{m_0+50\ \mathrm{MeV/c^2}}{m_0}\right]$.

FID	2n	p	q	y_{min}	χ^2/ν
$\sqrt{s}$ = 8 - 18 GeV					
$\pi^{\pm}$	5.63±0.02	2.92±0.03	3.96±0.05	0.35	89/49
$K^{\pm}$	0.88±0.025	3.15±0.12	3.84±0.19	0.10	33/39
p, $\bar{p}$	0.18±0.02	2.60±0.40	4.30±1.00	0.05	21/24
$\sqrt{s}$ = 91.2 GeV					
incl.	20.4±0.05	2.84±0.01	3.67±0.01	0.35	86/51
$\pi^{\pm}$	17.36±0.03	2.66±0.01	3.77±0.01	0.35	483/36
$K^{\pm}$	2.39±0.03	2.58±0.03	2.99±0.01	0.10	10/26
p, $\bar{p}$	1.10±0.02	2.36±0.04	3.58±0.07	0.05	17/23

Table 8.2: Identified fragments from unidentified partons: Beta-distribution parameters from χ^2 fits to fragmentation functions for pions, kaons and protons at $\sqrt{s}$ = 8 - 18 and 91.2 GeV

8.3.3 Inclusive fragments from identified partons

Finally, we consider data for unidentified hadron fragments from identified partons for two parton classes shown in Fig. 8.6: udsc quarks (in combination) and gluons. The fit results are shown in Fig. 8.9 (top two panels) and Table 8.3. The 'inclusive' table entry (first row) repeats the 91 GeV results from unidentified hadrons in Table 8.1 for reference. Parameters for the free χ^2 fit to the udsc FF data in the second row of the table reflect a width similar to the inclusive data ($q + p$ is similar), but the mode is shifted to slightly larger u ($q - p$ is smaller). Details of the fitting procedure are shown in Fig. 8.9 (upper-left panel). The points are substantially larger than the reported errors. The free fit (solid curve) is strongly influenced by the single point at $u \sim 0.13$. The χ^2 is large, and the fit function misses the data near the peak. As for the pion fragment FF data the udsc data errors appear to be underestimated.

The dashed curve is constrained by the (p, q) energy systematics in Fig. 8.11 (left panel) consistent with fits to the fiducial *inclusive* FFs (second udsc row of the table). The peak of

PID	2n	p	q	y_{min}	χ^2/ν
incl.	20.4±0.05	2.84±0.01	3.67±0.01	0.35	86/51
udsc	18.36±0.04	2.99±0.015	3.55±0.015	0.35	209/19
udsc	param. (p,q)	2.85±0.05	3.58±0.05	0.35	550/19
gluon	27.2±0.4	3.50±0.10	5.10±0.15	0.35	5.7/22
gluon	param. (p,q)	3.43±0.10	5.30±0.10	0.35	14.4/22

Table 8.3: Unidentified fragments from identified partons: Beta-distribution parameters from χ^2 fits to fragmentation functions for udsc quarks with $\sqrt{s} = 91.2$ GeV and gluons with $Q = 80.2$ GeV.

the data FF is better described, but the increased deviation from the small-u point greatly increases the χ^2. We expect the udsc FF to differ slightly from the flavor-inclusive FF (small shift to the right) due to the absence of gluon fragments, and the free fit is consistent with that expectation. We expect the udsc/inclusive multiplicity ratio to be 0.94 [2] but observe $18.36/20.4 = 0.90$, suggesting that the udsc FF height is underestimated by the free fit.

In Fig. 8.9 (upper-right panel) we show a free fit to FF data from gluon jets (solid curve) producing the fit parameters in the first gluon row of Table 8.3, which are plotted as open squares in Fig. 8.11 (left panel) and provide constraints on the gluon (p,q) energy systematics discussed in Sec. 8.4.3. The free fit has an unusually small χ^2; the data errors above the mode seem large compared to the residuals there. The dashed curve is a 'fit' with parameters constrained to the 80 GeV $(p_{\rm g}, q_{\rm g})$ systematic values from Fig. 8.11 (left panel) and reported with its χ^2 value in the second gluon row of Table 8.3.

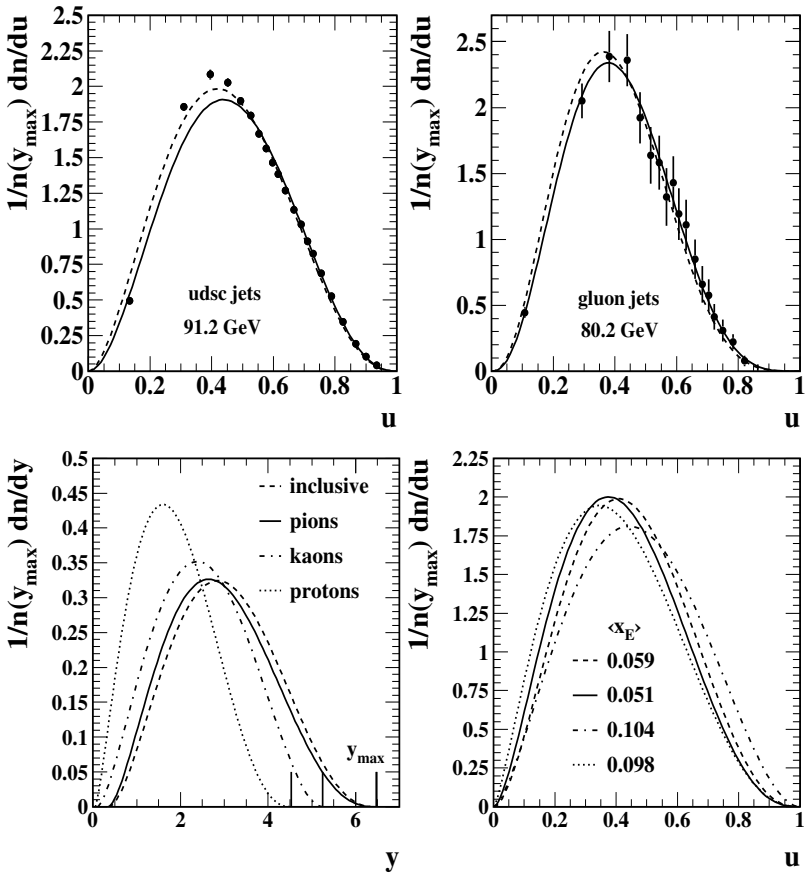

Figure 8.9: Upper two panels: Details of beta distribution fits to fragmentation functions for identified partons fragmenting to unidentified hadrons. The solid curves are free fits to data. The dashed curves are determined by the (p,q) systematics in Fig. 8.11 (left panel). Lower two panels: Unit-normal model functions $\beta(y \text{ or } u; p, q)$ from fits to FFs for identified fragments (pions, kaons and protons) and inclusive fragments, all from inclusive partons at $\sqrt{s} = 91.2$ GeV, plotted on rapidity y and normalized rapidity u.

8.4 Energy Scale Dependence

We can combine fits to fiducial FF data and dijet multiplicity data to determine the energy dependence of (p, q) for quark and gluon jets over a broad energy range. Fits to data $g(u, y_{max})$ with model $\beta(u; p, q)$ determine specific values (p, q) which constrain parameterized curves $(p(y_{max}), q(y_{max}))$. Fits to $2n(y_{max})$ data *via* the $\langle x_E \rangle$ integral of $\beta(u; p, q)$ also constrain the parameterizations, especially important in energy intervals where there are no FF data available. The resulting (p, q) energy trends efficiently represent e^+-e^- FFs over a broad energy range and provide a basis for extrapolating FFs to low Q^2.

8.4.1 Energy conservation sum rule

The total FF $D(x_E, s) = \sum_h D^h(x_E, s)$ (sum over all hadron species) integrates to total dijet multiplicity $\int_{2m_0/\sqrt{s}}^1 dx_E\, D(x_E, s) = 2n_{tot}(s)$ and satisfies the energy sum rule (ESR) $\int_{2m_0/\sqrt{s}}^1 dx_E\, x_E\, D(x_E, s) = 2$ [69]. The ratio of the integrals defines mean energy fraction $\langle x_E \rangle = 1/n_{tot}(s)$. Switching to (u, y, y_{max}), since $D(u, y_{max}) \equiv 2n_{tot}(y_{max})\, g(u, y_{max})$ and $g(u, y_{max}) \approx \beta(u; p, q)$ we have $\langle x_E \rangle \approx \int_0^1 du\, x_E(u, y_{max})\, \beta(u; p, q)$, with $x_E(u, y_{max}) = \cosh[y(u)]/\cosh(y_{max})$ and $y(u) = u\, y_{max} + (1-u)\, y_{min}$. Those relations connecting $\beta(u; p, q)$ to $n_{tot}(y_{max})$ are used below to obtain the energy dependence of (p, q) from multiplicity data.

Given several hadron species h with FFs $D^h(x_E)$ and dijet multiplicities $2n_h$ we expect $ESR = \sum_h 2n_h \langle x_E \rangle_h = 2$, provided *all* species are integrated. However, if only charged hadrons are detected we expect $ESR \sim 2/3 \times 2 \sim 1.33$. We can test the charged-fraction ESR using the fits to charged pion, kaon and proton data at 91 GeV from Table 8.2. The ESR for inclusive FFs can be tested with the fits from Table 8.1. In general, if f is the ESR fraction for detected particles ($f \sim 2/3$ for the charged-hadron fraction) we expect the relation $\langle x_E \rangle = f/n(y_{max})$ between monojet (charged-particle) multiplicity and energy fraction, which we use below to relate multiplicities to beta parameters (p, q).

Beta distribution fits to FFs $g^h(y \text{ or } u, y_{max})$ for identified pions, kaons and protons at 91.2 GeV from Table 8.2 and the FF for inclusive hadrons are plotted on rapidity y and normalized rapidity u in Fig. 8.9 (bottom two panels). The parameters for those curves are used to obtain $\langle x_E \rangle_h$ for each hadron species using the correct hadron mass and $\langle x_E \rangle_{incl}$ for

the inclusive distribution assigning the pion mass to all hadrons. We use the $2n$ fit values in the tables to obtain $\sum_h 2n_h \langle x_E \rangle_h = 1.25 \pm 0.03$ ($f = 0.62$) and $2n_{incl} \langle x_E \rangle_{incl} = 1.18 \pm 0.05$ ($f = 0.59$) for identified and inclusive charged fragments. If $\langle x_E \rangle_{incl}$ is calculated with the weighted-mean mass 0.2 GeV (weighted by the hadron multiplicities in Table 8.2) we obtain $ESR = 1.4 \pm 0.05$. The same procedure applied to the fits to lower-energy data from Table 8.2 gives $ESR \sim 1.1$. The exact energy scale for the lower-energy sum rule is not clear because of the scale range, but the result is roughly consistent with expectations. For the inclusive analysis below assuming the pion mass we use ESR factor 1.18.

8.4.2 Dijet multiplicities from $\beta(u; p, q)$ shapes

Dijet multiplicity $2n$ can be obtained directly by integrating measured and extrapolated FF data, as in Tables 8.1 - 8.3. However, as we have just shown there is a correspondence between $2n(y_{max})$ and the *shape* of data FF $g(u; y_{max})$ or fitted model function $\beta(u; p, q)$ determined by parameters $[p(y_{max}), q(y_{max})]$. We have obtained for inclusive charged fragments with pion mass assignment the relation $2n(y_{max}) = 1.18/\int_0^1 du\, x_E(u, y_{max})\beta(u; p, q)$ at 91.2 GeV which we now use to relate energy trends of FF shape parameters (p, q) to fragment multiplicities. Measured multiplicity trends on parton energy thereby provide constraints on the energy dependence of FF parameters (p, q), even in energy intervals where there are no measurements of FFs.

Fig. 8.10 shows dijet multiplicities $2n$ for g-g and q-$\bar{\text{q}}$ parton pairs. Precise multiplicity data for quark jets from two-jet events have been available for some time. New methods have produced similarly precise gluon-jet multiplicities from three-jet e^+-e^- events. Data for gluon jets were obtained from CDF (closed triangles) [18], CLEO (open triangles) [42], OPAL 'jet-boost' algorithm (open circles) [3] and OPAL inclusive (star) [16]. Data for quark jets were obtained from a compilation (Table 6 in [90]) and multiplied by factor 0.94 (the fraction of udsc jets in a flavor-inclusive sample [2]) to compare with the gluon jet multiplicities. The large points labeled π and K are multiplicities from fits to identified fragment data [79, 39, 45] in Table 8.2 plotted with the indicated multipliers. The hatched regions represent the domain of low-Q^2 partons which motivates this extrapolation study.

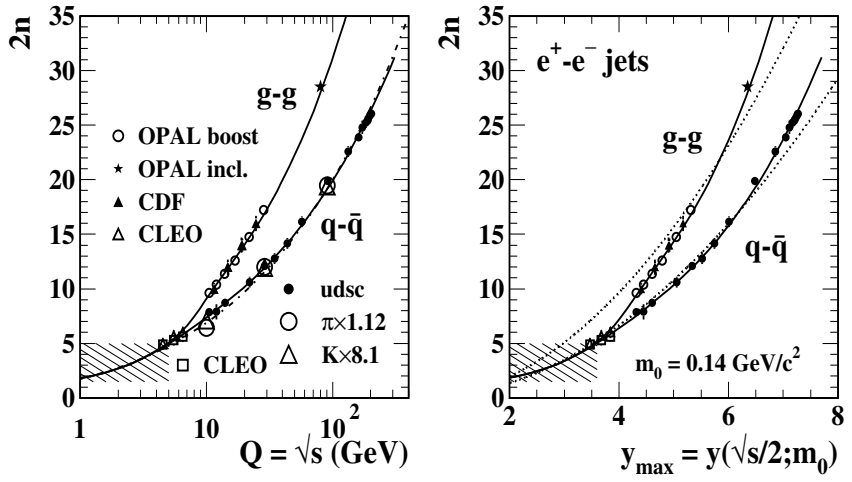

Figure 8.10: Dijet charged-particle multiplicity *vs* energy scale Q (dijet energy) plotted in a conventional format (left panel) and *vs* parton rapidity assuming the pion mass (right panel). The solid curves are quark and gluon dijet multiplicities $2n_{\rm q}$ and $2n_{\rm g}$ obtained from the (p, q) parameterizations in Fig. 8.11 (left panel). The dash-dot curve in the left panel is from a 3NLO pQCD expression. The udsc quark-jet multiplicities for unidentified hadrons (solid dots) are taken from a survey in [90]. The dotted curves in the right panel illustrate quadratic trends $A\,(y_{max} - y_{min})^2$ (see text).

The solid curves in Fig. 8.10 are multiplicities derived from the (p, q) energy trends using the relations defined above. The (p, q) parameterizations are adjusted to fit the multiplicity data but constrained by (p, q) values from fits to fiducial FFs. The resulting (p, q) energy dependence is described in the next subsection. Because $2n \propto 1/\langle x_E \rangle$ and $\langle x_E \rangle$ is monotonic with mean $\bar{u} = p/(p + q)$, multiplicities are mainly determined by ratio q/p or difference $q - p$ (*i.e.,* the mode or mean of the beta distribution), and only weakly dependent on sum $q + p$ (the width). A unique description of (p, q) over a broad energy range requires fits to multiplicity trends supplemented by the fits to fiducial FFs described in the previous section.

Quark-jet multiplicities are described in the MLLA by 3NLO expression $n_{\rm q}(Y) = K/2.25 \cdot Y^{-a_1\,C^2}\,\exp\{2C\,\sqrt{Y} + a\,\delta(Y)\}$, with $Y = \ln(\sqrt{s}/\Lambda)$, $C = \sqrt{4n_c/b}$ and $b = (11n_c - 2n_f)/3$ [89]. We used $a_1 = 0.3$ from [80] and $K = 0.13$ and $\Lambda = 0.15$ GeV from Table 8.1 and the functional form of $\delta_g(Y)$ from Fig. 3 in [89] for $\delta(Y)$ (all for $n_f = 5$). We set the coefficient of $\delta(Y)$ to $a = 1.8$ to obtain the best agreement with quark-jet data, shown by the dash-dot

curve in Fig. 8.10 (left panel) just visible relative to our parameterization (solid curve).

Variation of dijet multiplicities in the form $A\,(y_{max} - y_{min})^2$ would be expected for the self-similar scaling illustrated in Fig. 8.1 with fixed FF mode u^*. Quadratic trends for quark and gluon jets are illustrated by the dotted curves in Fig. 8.10 (right panel), with $A = 0.5$ for quarks and $1.45 \cdot 0.5$ for gluons. Deviations from the quadratic trend for quark-jet multiplicities in Fig. 8.10 correspond to the linear variation of $(p_{\rm q}, q_{\rm q})$ with y_{max} above $y_{max} = 4.5$ in Fig. 8.11 (left panel) which shift u^* to smaller values, as illustrated in the right panel of that figure. Gluon-jet multiplicities deviate more dramatically from the quadratic trend at lower energies, moving from the quark-jet curve to a gluon-jet trend about 50% larger within the energy interval $y_{max} = 3.5 - 5$ ($Q = 5 - 20$ GeV) as the quark-gluon color charge difference emerges. Above 20 GeV the gluon-jet multiplicities reflect the smaller linear variation of $(p_{\rm g}, q_{\rm g})$ with y_{max} in that energy interval.

8.4.3 Energy dependence of $\beta(u; p, q)$ parameters

Fig. 8.11 (left panel) shows the (p, q) energy dependence which produces the quark and gluon jet multiplicities (solid curves) in Fig. 8.10 and the solid curves compared to fiducial FFs in Figs. 8.1 - 8.3. Those curves summarize the energy dependence of udsc and gluon fragmentation to unidentified hadrons in e^+-e^- collisions. We assume that the shapes of inclusive (dominated by light quarks) and udsc FFs are approximately the same, as in Fig. 6 of [4]. Inclusive and udsc jet FFs at 91.2 GeV are compared in Table 8.3 and Fig. 8.9 (upper-left panel) and found to be similar. The vertical dotted lines mark the limits of multiplicity measurements, while the vertical dash-dot lines mark the limits of measured FFs used in this analysis. The upper ten solid points represent the fiducial FFs. The open squares represent the single gluon FF in Fig. 8.9 (upper-right panel) which constrains $(p_{\rm g}, q_{\rm g})$.

The (p, q) curves in Fig. 8.11 (left panel) are described by

$$
\begin{aligned}
p_{\rm q} &= 2.90 \pm 0.05 - (0.05 \pm 0.01)\,(y_{max} - 5.3) \qquad (8.1)\\
q_{\rm q} &= 3.50 \pm 0.05 + (0.05 \pm 0.01)\,(y_{max} - 5.3) - (0.8 \pm 0.2)\,(y_{max} - 4.5)[\tanh(y_{max} - 3.5) - 1]/2\\
p_{\rm g} &= p_{\rm q} + [(0.07 \pm 0.02)\,(y_{max} - 5.3) + 0.55 \pm 0.05] \times \{\tanh[(2.5 \pm 0.5)\,(y_{max} - 4.1 \pm 0.1)] + 1\}/2
\end{aligned}
$$

$$q_{\rm g} \;=\; q_{\rm q} + [(0.07 \pm 0.02)\,(y_{max} - 5.3) + 1.70 \pm 0.07] \times \{\tanh[(2.5 \pm 0.5)\,(y_{max} - 4.1 \pm 0.1)] + 1\}/2$$

The $p_{\rm q}$ expression in Eq. (8.1) is determined only by linear interpolation and extrapolation of fits to the hadron- and parton-inclusive fiducial FFs. Given that definition of $p_{\rm q}$ the curve for $q_{\rm q}$ is then defined only by the fit to the udsc quark-jet multiplicity data in Fig. 8.10. The agreement in Fig. 8.11 between $q_{\rm q}$ determined by fitting light-quark multiplicities $2n_{\rm q}$ (upper solid curve) and by fitting individual inclusive-parton FFs (upper solid points) indicates the consistency of the two methods. The expression for $p_{\rm g}$ is guided by the fit to a single gluon FF denoted by the open square point in Fig. 8.11 (left panel). For further discussion of its impact on scaling violations see Ref. [165].

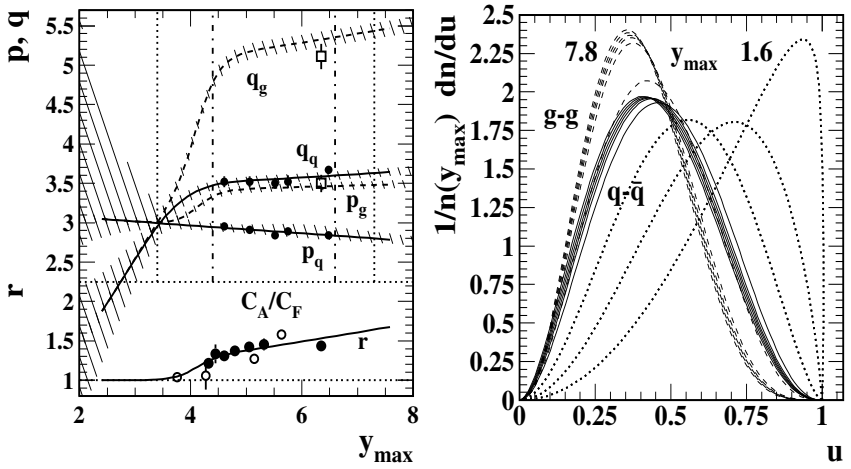

Figure 8.11: Left panel: Beta-distribution parameters $(p_{\rm q}, q_{\rm q})$ and $(q_{\rm g}, p_{\rm g})$ respectively for light-quark (solid) and gluon (dashed) jets and corresponding gluon-to-quark-jet multiplicity ratio r *vs* parton rapidity y_{max}. Right panel: Unit-normal FFs (beta distributions) obtained from parameters in the left panel plotted on normalized rapidity u for quark (solid) and gluon (dashed) jets and for nine equal-spaced values of parton rapidity y_{max} illustrating peak shape evolution with energy scale.

The error bands in the central region represent correlated systematic errors related to the uncertainty in y_{min}. As y_{min} varies the dominant effect is common displacement of p and q (*cf.* Fig. 8.8). Multiplicity depends mainly on the mode or mean of the fragment distribution, and therefore primarily on the ratio or difference of p and q. Multiplicity is

therefore insensitive to the choice of y_{min}. The FF width on the other hand depends directly on the sum $p + q$ and is therefore more influenced by the choice of y_{min}. To the right of the left dash-dot line the (p, q) vary slowly and linearly with increasing energy scale. The energy dependence for light quarks implies a slight reduction of the mode with the peak width unchanged, consistent with the fiducial FFs in this study (*e.g.,* Fig. 8.3). The gluon FF shows similar mode variation, but the width is also reduced with increasing energy.

Below the left dash-dot line ($Q \sim 10$ GeV) the (p, q) change rapidly. The multiplicity data, especially the CLEO data, require a sharp drop in q in that energy interval for both quarks and gluons which is effected by the tanh term in $q_{\rm q}$ of Eq. (8.1). The convergence of the quark and gluon (p, q) at the energy scale defined by the lower dotted line, again required by the CLEO data, is effected by the tanh terms in $p_{\rm g}$ and $q_{\rm g}$. Below $y_{max} = 3.6$ ($Q = 5$ GeV) there is no guidance from data, but we speculate as follows. At 5 GeV the average jet multiplicity is ~ 2.5 and there is no distinction between quark and gluon jets, $p \sim q$ and the FF is therefore symmetric about the midpoint on u. We argue that at lower energies the mean jet multiplicity approaches one and the FF approaches a delta function at $u = 1$, requiring $q \to 1$ and $p \to \infty$. We sketch those trends with large error bands in the left panel as a simple extrapolation of the trends derived from data.

In Fig. 8.11 (right panel) we show a sequence of model functions for nine equal y_{max} steps from 1.6 to 7.8, with parameters derived from the (p, q) curves in the left panel for gluon and quark FFs. The modes for quark jets (solid curves) and gluon jets (dashed curves) move from left to right with decreasing energy scale, and the dotted curves for $y_{max} < 3.6$ ($Q < 5$ GeV) represent both parton types in common. Below 5 GeV the FFs slew to the right and may approach a delta-function limit at $u = 1$. Those low-Q^2 trends can be compared with the theoretical description of heavy quark fragmentation on the right of Fig. 8.7.

The energy dependence of gluon-to-quark-jet multiplicity ratio $r = n_{\rm g}/n_{\rm q}$ derived from the beta parameters is plotted as the lowest solid curve in Fig. 8.11 (left panel). The open points are taken from [41] and the solid points are from [13]. r is expected to approach the ratio of color factors $C_A/C_F = 2.25$ at large Q. The ratio indeed increases monotonically with y_{max} from unity at $y_{max} \sim 3.5$ ($p \sim 2$ GeV/c and $n \sim 2$), but the approach to C_A/C_F is slow. The overall trend is in rough agreement with theory [92, 80].

The ratio slope $r' = dr/dy_{max} \sim dr/d\ln(Q)$ is also of theoretical interest but difficult to calculate since it is very sensitive to perturbative corrections [80]. Slope r' derived from (p, q) rises to peak value 0.45 at $y_{max} \sim 4$, then falls to 0.11 at $y_{max} = 5$ ($Q = 20$ GeV) and rises linearly to 0.13 at $y_{max} = 8$ ($Q = 400$ GeV). The value r' = 0.1 is in rough agreement with theory [80]. In contrast to the slow evolution of r the rapid separation of $q_{\rm q}$ and $q_{\rm g}$ with increasing energy between the lower dotted and dash-dot vertical lines of Fig. 8.11 (left panel) contrasted with a nearly fixed difference between them above that region may provide a clearer manifestation of the emergence of color charge.

8.4.4 Fragmentation functions on (y, y_{max})

We can use the parameterized beta distribution to construct a 2D fragment distribution on (y, y_{max}) as follows. Form factor $\beta(u; p, q)$ describes the shapes of FFs over a broad Q^2 interval. The beta distribution in turn determines multiplicity $n(y_{max})$ through $\langle x_E \rangle$ over the same range (Fig. 8.10). We combine the two factors to form $D(y, y_{max}) = 2n(y_{max})\,\beta[u(y, y_{min}, y_{max}); p(y_{max}), q(y_{max})]$.

In Fig. 8.12 (left panel) we plot $D(y, y_{max})$. The vertical dotted and dash-dot lines mark the same energies as in Fig. 8.11 (left panel). The dashed curve is a 'locus of modes' (positions of maxima) of conditional distributions on y for fixed y_{max}. The approach of that curve to the solid diagonal line ($y = y_{max}$) at lower left corresponds to the approach of the dotted curves in Fig. 8.11 (right panel) to $u = 1$. The horizontal dotted line denotes y_{min}, and $y_{max} = 8$ corresponds to $\sqrt{s} \sim 400$ GeV. This joint fragment density provides the basis for extrapolating FFs down to $Q \sim 1$ GeV ($y_{max} \sim 2$). Fig. 8.12 (right panel) is a transformation of the left panel onto $(y_{max}, y - y_{max})$, with $y - y_{max} \sim \ln x_p = -\xi_p$, which illustrates in the upper-right corner scaling violations: variation of the fragment density with increasing $\ln(Q/\Lambda) \to y_{max}$ at constant x_p or ξ_p (constant $y - y_{max}$) [165].

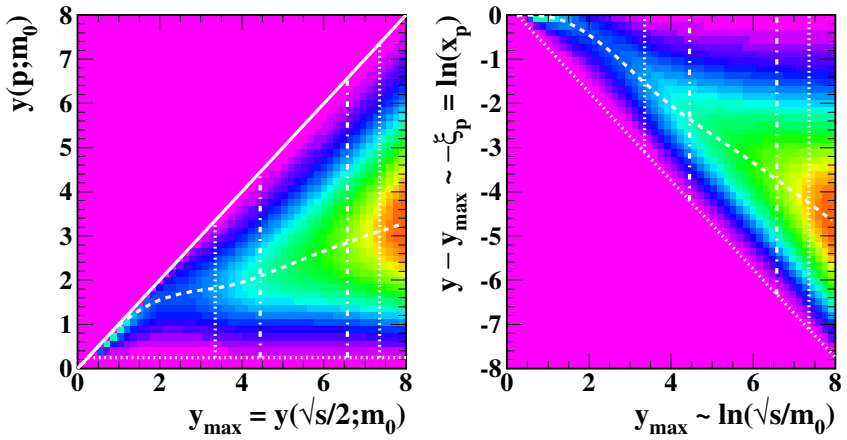

Figure 8.12: Left panel: Joint fragment distribution $D(y, y_{max})$ on fragment and parton rapidities for inclusive partons ($\sim$ udsc quarks) and inclusive hadrons. Fragmentation functions are vertical slices (conditional distributions) from the joint distribution. Right panel: The same distribution transformed to $(y - y_{max}, y_{max})$, with $y_{max} - y \sim \xi_p$, the logarithmic relative momentum. The vertical dash-dot lines define the interval determined by fiducial FFs plus dijet multiplicities. The intervals between vertical dash-dot and dotted lines are defined only by multiplicity trends. The upper-right region of the right panel illustrates scaling violations.

8.5 Peak statistics and pQCD

We have constructed a simple parameterized model of FFs for e^+-e^- collisions which compares well with data. In this section we compare the energy dependence of peak statistics on u and ξ_p inferred from our parameterization with predictions from pQCD. Fragmentation-function peak statistics predicted by pQCD [93, 69, 94, 14] can be compared to peak statistics u^* (mode), $\bar{u}$ (mean) and σ_u^2 (variance) for distribution $\beta(u; p, q)$. The mode for the β distribution is $u^* = \frac{p-1}{p+q-2}$ and the mean is $\bar{u} = \frac{p}{p+q}$, with (p, q) determined by the parameterizations in Fig. 8.11. The mode on y is $y^* = u^*\, y_{max} + (1 - u^*)\, y_{min}$.

In Fig. 8.13 (left panel) we show measured values of ξ_p^* in the form $y_{max} - \xi_p^* \sim y^*$ (consistent with Fig. 8.2) *vs* y_{max} [comparable to plots of ξ_p^* *vs* $\ln(Q/\Lambda)$] for eight quark-jet and fourteen gluon-jet energies [40, 78, 14]. The solid curve $y^*(y_{max})$ for quark jets inferred from our (p, q) parameterization is the same as the dashed curve in Fig. 8.12 (left panel). The five stars are obtained from our fits to the fiducial FFs in Table 8.1 (compare to peak

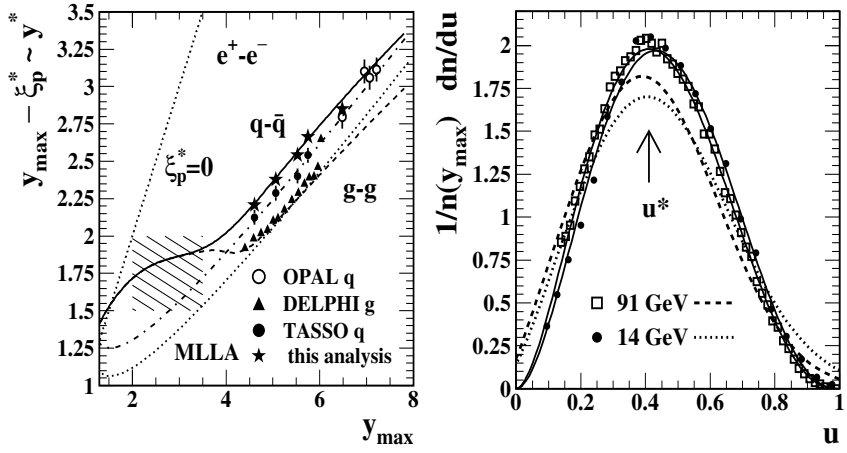

Figure 8.13: Left panel: Comparison of fragmentation-function modes *vs* parton rapidity from quark and gluon data (points) with 'locus of modes' trends (solid and dashed curves) derived from (p, q) energy systematics in Fig. 8.11 (left panel) and from the MLLA (dash-dot and dotted curves). Right panel: Comparison at two energies of FF data, beta distributions on u and MLLA Gaussians suitably transformed to u.

modes in Fig. 8.2). The errors are smaller than the points.

The MLLA predicts for inclusive jets $\xi^*_p = 0.5Y_2 + c_2\sqrt{Y_2} - c_2^2$, with $Y_2 \equiv \ln(Q/2\Lambda)$ (note the 2 in the denominator), $c_2 \equiv a/\sqrt{16b\,n_c}$, $a = b/n_c^2$ and $b = (11n_c - 2n_f)/3$ [181]. The MLLA prediction for ξ^*_p transformed to $y_{max} - \xi^*_p$ is plotted as the dash-dot curve in the left panel. The curve corresponds to $n_f = 5$, but changes with $n_f \to 3$ are within the data errors. The hatched area is the region of interest for study of low-Q^2 partons. The MLLA curve diverges from the $(p_{\rm q}, q_{\rm q})$ parameterization (solid curve) in that region.

We can also obtain a mode prediction for gluon jets. The MLLA prediction for the quark-gluon mode difference is $\Delta\xi^* = \xi^*_{\rm g} - \xi^*_{\rm q} \approx \frac{1}{12}\left(1 + \frac{n_f}{n_c^3}\right) + O(\sqrt{\alpha_s}) \sim 0.1$ [94, 14]. Taking the inclusive ξ^*_p prediction above as $\xi^*_{\rm q}$ we plot $y_{max} - \xi^*_{\rm g} = y_{max} - \xi^*_{\rm q} - \Delta\xi^*$ as the dotted curve in Fig. 8.13, which agrees fairly well above $y_{max} = 4.5$ ($Q \sim 12$ GeV) with the gluon y^* trend (dashed curve) obtained from parameters $(p_{\rm g}, q_{\rm g})$ in Fig. 8.11. Data from [14] for FF modes from gluon jets are plotted as solid triangles. The modes were obtained from Gaussian fits to gluon FF data over limited intervals on ξ_p. The data are well described by the dashed curve obtained from our (p, q) energy systematics and by the MLLA prediction.

The MLLA width prediction on ξ_p is $\sigma_{\xi_p} = Y^{3/4}/\sqrt{2c_1}$, with $c_1 = \sqrt{36n_c/b}$ [40]. The width on ξ_p should be equivalent to the width on y (*cf.* Fig. 8.2). The variance of the beta distribution on u is $\sigma_u^2 = \frac{p\,q}{(p+q)^2(p+q+1)} \simeq \frac{1}{4(p+q+1)} \sim 0.035$ for flavor-inclusive e^+-e^- jets. Thus, the observed r.m.s. width on y is $\sigma_y \sim 0.2\,y_{max} \sim 0.2Y$, the coefficient nearly independent of y_{max} per the (p,q) systematics in Fig. 8.11. That result is inconsistent with the MLLA width prediction $\sigma_y \sim 0.37\,Y^{3/4}$.

Measured FFs have been compared directly with analytic predictions of peak statistics from the MLLA and with Gaussians on ξ_p defined by parameters from perturbative approximations [93]. In Fig. 8.13 (right panel) we compare beta distributions and data for two energies on normalized rapidity u with corresponding MLLA Gaussians (normalized to unit integral) using the parameters described above. The Gaussian tails do not describe the data. Our parameterized model is consistent with pQCD predictions at larger Q^2, and the beta distributions (solid curves) demonstrate good sensitivity to small but meaningful systematic variations with energy of the FF data. The good fit of beta distributions to data over all fragment momenta insures a well-defined peak integral.

8.6 Discussion

Our intention in this study has been to provide the phenomenological means to extrapolate e^+-e^- parton fragmentation functions to low Q^2 where the perturbative description of QCD is not applicable. We have been guided by the many precise measurements of e^+-e^- fragmentation functions and their relationship to pQCD predictions now available. Parton scattering and fragmentation at low Q^2 are in turn important for understanding p-p and A-A collisions at RHIC. As a result of this study we have found that the beta distribution provides a simple but precise description of FFs which accomplishes the desired extrapolation but also reveals some interesting new aspects of parton fragmentation.

8.6.1 The beta distribution as compact representation

FFs for e^+-e^- collisions transformed to y are approximately self-similar with increasing y_{max}, as sketched in Fig. 8.1. They are bounded by parton rapidity y_{max} and lower limit y_{min}. Those trends suggest a further transformation to normalized rapidity $u = (y - y_{min})/(y_{max} -$

y_{min}). Measured FFs plotted on u are nearly independent of parton energy and can be factorized into dijet multiplicity $2n(y_{max})$ and unit-normal form factor $g(u, y_{max})$ which is modeled by the beta distribution. Since energy conservation relates the dijet multiplicity to the form-factor shape the fragmentation process is completely represented by the energy-scale dependence of parameters (p, q) of the beta distribution.

The beta distribution with two energy-dependent parameters thus precisely describes light-flavor FF data over the scale interval $Q \in [5, 100]$ GeV (*e.g.,* Figs. 8.1 - 8.3) and can be extended to lower energies, accomplishing the main goal of this study: extrapolation of fragmentation systematics down to fragment multiplicity $n \sim$ 1-2 and energy scale $Q \sim 1$ GeV. We also obtain simple representations of FFs on (x, s) or (y, y_{max}) (continuous 2D surface) for studies of scaling violations over the full kinematic range.

8.6.2 Fragmentation as an equilibration process

Why does the beta distribution provide a good description of e^+-e^- FFs? $\beta(u; p, q)$ describes systems in which entropy is maximized (*e.g.,* by a parton cascade) on a bounded interval (*e.g.,* bounded by the leading-parton energy). $\beta(u; p, q)$ is one instance of the *exponential family* of probability distributions $p(x)$ which can be defined in terms of a maximum-entropy condition with constraints [109]. The beta distribution defined on $x \in [0, 1]$ maximizes the Shannon entropy $S = -\int dx\, p(x) \ln[p(x)]$ subject to constraints on geometric means $\overline{\ln(x)} = \int dx\, p(x)\, \ln(x)$ and $\overline{\ln(1-x)}$. The Gaussian distribution can be similarly defined, with constraints on its first and second moments $\bar{x}$ and $\overline{x^2}$.

Given those properties of the beta distribution and its good description of FFs, fragmentation of light quarks and gluons can be viewed as an equilibration process controlled by two opposing tendencies: parton splitting as a form of downscale energy transport which increases entropy and gluon coherence which constrains the splitting at a scale conjugate to hadron size. The observed fragment distribution is then a maximum-entropy configuration balancing those two tendencies. Of the two beta parameters q reflects the splitting tendency and p reflects the hadron size constraint. The DGLAP equations which describe the perturbative splitting (transport) process are thus coupled to the soft part of the FF by

entropy maximization as well as energy conservation.

8.6.3 Conventional pQCD fragmentation functions

Do benefits from the introduction of (y, y_{max}), u and the beta distribution justify a new approach to fragmentation? In Fig. 8.14 we compare FF data to a beta distribution fit from this analysis and a pQCD model FF (KKP) obtained from a conventional scaling violations analysis using the DGLAP equations [122] and defined by 14 parameters for each parton-hadron combination. Fig. 8.14 (left panel) shows the OPAL 91 GeV FF data from Fig. 8.1 (third and fourth panels) with the KKP fragmentation function (dashed curve) and the FF from this analysis (solid curve). With the exception of a small deviation at large x_p the agreement in this format appears to be good (also *cf.* Fig. 8.1 – third panel).

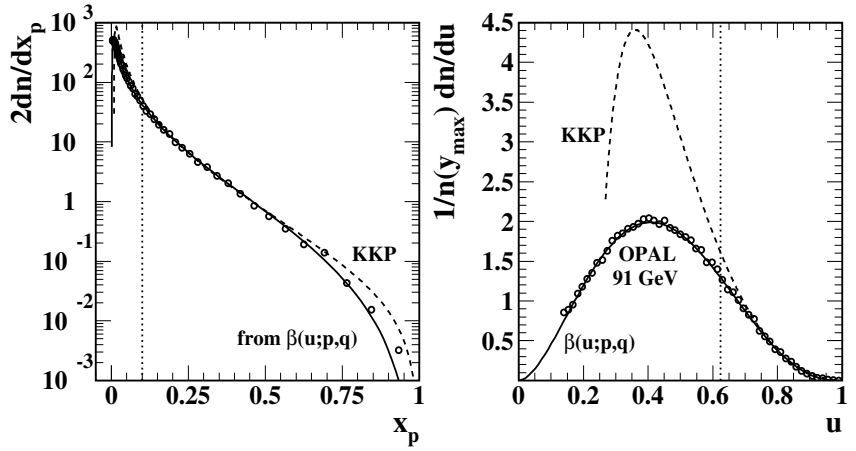

Figure 8.14: Left panel: Beta distribution (solid) and KKP FF (dashed) curves compared to OPAL 91 GeV data points (open circles) on linear momentum variable x_p. Right panel: The same curves and data transformed to normalized rapidity u. The vertical dotted lines both correspond to $x_p = 0.1$.

Fig. 8.14 (right panel) shows the same distributions on normalized rapidity u. The KKP FF based on DGLAP evolution deviates strongly from data below $u = 0.7$ and accurately represents less than 10% of the fragments at 91 GeV. The vertical dotted line in each panel shows the intended region of validity ($x_p > 0.1$) of the KKP and similar FFs. In contrast, the FF from our analysis, based on the beta distribution and defined by two parameters per

parton-hadron combination with simple energy dependence above $Q = 20$ GeV, accurately describes the data on x_p over six orders of magnitude and, extrapolating the full data distribution down to zero momentum, provides a well-defined multiplicity integral.

Recent improvements in the pQCD description of FFs have lead to much improved coverage on x_p. In [44] a consistent combination of DGLAP evolution, resummation of soft gluon logarithms and incorporation of hadron mass effects provides a semi-quantitative description below the FF mode on y or u while retaining good agreement above the mode. Such theoretical advances provide a context for the present phenomenological analysis.

8.6.4 Energy dependence and applications

We have studied the energy dependence of FFs as represented by beta distribution parameters (p, q) in Figs. 8.10 – 8.13. The direct relation between dijet multiplicities and FF shape parameters *via* the energy sum rule provides a new method for extending the FF description over a broad energy range. The connection between shape parameters (p, q) and dijet multiplicity $2n(y_{max})$ is particularly important for extrapolation to low Q^2 (*e.g.,* the CLEO multiplicity data provide strong constraints on low-energy FF evolution).

A striking feature of Fig. 8.10 is the bifurcation of quark and gluon trends near $Q \sim 5$ GeV and evolution to large separation by $Q \sim 20$ GeV, with a dramatic correspondence in Fig. 8.11 (left panel). Above 20 GeV the system exhibits simple pQCD trends which are most apparent in Fig. 8.11. Corresponding peak modes on u remain close to 0.4 over a broad energy range. It is not clear from Fig. 8.10 that peak modes increase rapidly near 5 GeV and approach unity below that point, but that trend can be inferred from Fig. 8.11 which provides important extrapolation guidance. Mode trends are illustrated in Fig. 8.13 and agree well with data and pQCD predictions in the energy range above 15 GeV. There is additional discussion of scaling violations in [165].

The beta distribution model provides and simple and complete description of fragmentation functions of light hadrons which suggests that at large enough energy scales fragmentation is an entropy-maximizing equilibration process. We will apply this parametrization to the same-side peak of heavy-ion collisions in the next chapter.

Chapter 9

THE SAME-SIDE PEAK

The bulk of the correlation analys presented thus far has focused on the quadrupole component and its relationship to conventional v_2 measures. Yet in exploring the quadrupole term we have also had to recognize the importance of another component: the same-side (SS) 2D Gaussian peak and its corresponding away-side (AS) ridge. We have found in Chapters 6 and 7 that the magnitude of this term is comparable or greater than the quadrupole term, and it has many unique properties. In fact it is the SS 2D peak that dominates in central A-A collisions.

In this chapter we present the hypothesis that the SS peak is dominated by jet fragmentation from low-Q^2 partons which is *modified*—but not quenched or suppressed—by the presence of a strongly-interacting medium.

9.1 Same-Side Peak Properties

The methods for constructing and fitting correlations were discussed in Chapters 5 through 7. Here we will review the final fit parameters but with an emphasis on the terms that describe the same-side peak and their properties.

9.1.1 Centrality Dependence

The centrality dependence of the p_t-integrated same-side peak established in Chapter 6 is reproduced in Fig. 9.1. The dashed and dotted curves in the first panel represent binary collision scaling in a Glauber linear superposition of nucleon-nucleon collisions for 200 and 62 GeV respectively [37]. These curves are what we would expect from hard scatterings in nuclear collisions if they were nothing more than a superposition of many nucleon-nucleon collisions with no collective behavior. The most peripheral collisions follow this trend exactly. When moving to more central collisions there is a significant deviation from this

trend which starts from about $\nu = 2.5$. At the same point there is more significant growth in η width of the same side peak. This growth only affects η while the ϕ width actually decreases from its value in the most peripheral collisions and then stays relatively constant for mid-central to central collisions.

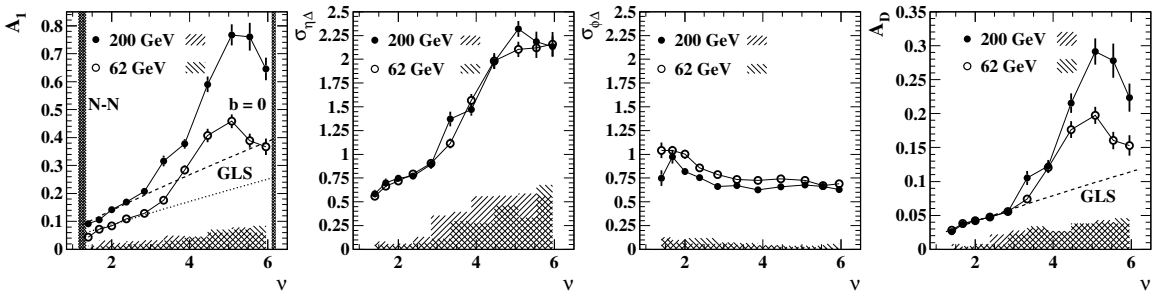

Figure 9.1: First panel: Centrality-dependence of the p_t-integrated same-side peak amplitude for 62 and 200 GeV collisions. Second panel: Width of the same-side peak on η. Third panel: Width of the same-side peak on ϕ. Fourth panel: Amplitude of the away-side dipole. [37]

The last panel of Fig. 9.1 shows the behavior of the away-side ridge. The shape of its centrality dependence for both 62 and 200 GeV collisions exactly matches the shape of the SS peak amplitudes. It should be noted that there is absolutely no requirement in the fit model that these parameters match. This trend is perfectly consistent with the assumption that the away-side peak is produced from momentum conservation in dijet production. Global momentum conservation of a thermal system, on the other hand, would scale with the number of participating nucleons.

Correlations in the most peripheral bin of Au-Au collisions are nearly identical to those observed in proton-proton collisions [138, 139]. This is because in a very peripheral collision the majority of the nucleons in the colliding nuclei do not even participate in the collision and just continue down the beampipe. The most peripheral bin of Au-Au collisions is essentially describing nucleon-nucleon collisions.

The same-side structure in p-p correlations is reproduced well by the PYTHIA Monte Carlo event generator and does not appear in PYTHIA simulations if hard parton scattering to jets is disabled [139]. Jets individually identified in event-wise analysis of energy

(calorimeter) angular distributions on (η, ϕ) follow the expected pQCD parton spectrum down to 5 GeV (3-4 GeV without background) [43, 8]. Trends for jet-like correlations and event-wise reconstructed jets are consistent: The most-probable hadron p_t for minimum-bias jet-like correlations in p-p collisions is 1 GeV/c, consistent with the observed 3-4 GeV lower limit to calorimeter-based reconstructed-jet energy spectra [43, 161].

The same-side peak trends are in sharp contrast to the simple behavior of the quadrupole component, which as we saw in Chapter 6 exhibits no sharp transition and is easily parametrized. With the away-side ridge behavior mirroring the same-side peak and the quadrupole following a separate and smooth trend there is no way for the sudden growth of the same-side peak to result from a poor fit. If the fit model mis-attributed some other aspect of the correlations to the same-side peak this should be visible in the quadrupole component. There aren't any other components in the fit model with sufficient magnitude to account for the difference. The large p_t-integrated same-side peak is a real phenomenon that contradicts the conventional heavy-ion collision scenario for more-central collisions.

9.1.2 p_t Dependence

With marginal y_t distributions we can study the y_t dependence of the SS peak as well. Measured $\Delta\rho/\rho_{\rm ref}$ amplitudes and widths in η_Δ and ϕ_Δ of the SS peak are plotted in Fig. 9.2. The amplitude of the SS peak increases significantly with y_t for all centralities although for this per-pair measure direct comparisons are complicated. However, the widths are not affected by the choice of correlation measure. The ϕ_Δ width appears to be basically independent of centrality and narrows significantly at higher y_t.

What is most remarkable that the large η_Δ widths above the transition point (third and fourth panel) persist even at large y_t. In fact, the SS peak's y_t dependence is roughly flat over a significant y_t interval (up to $p_t = 4$ GeV/c) for all centralities above the transition point. The naive (pQCD) expectation is that the peak should narrow in both η and ϕ as hadron p_t increases if the SS peak is describing correlations between fragments from higher-energy partons. While the mechanism behind this η broadening is not well understood, it should possible to develop a correspondence between the p_t-dependent Gaussian peak and

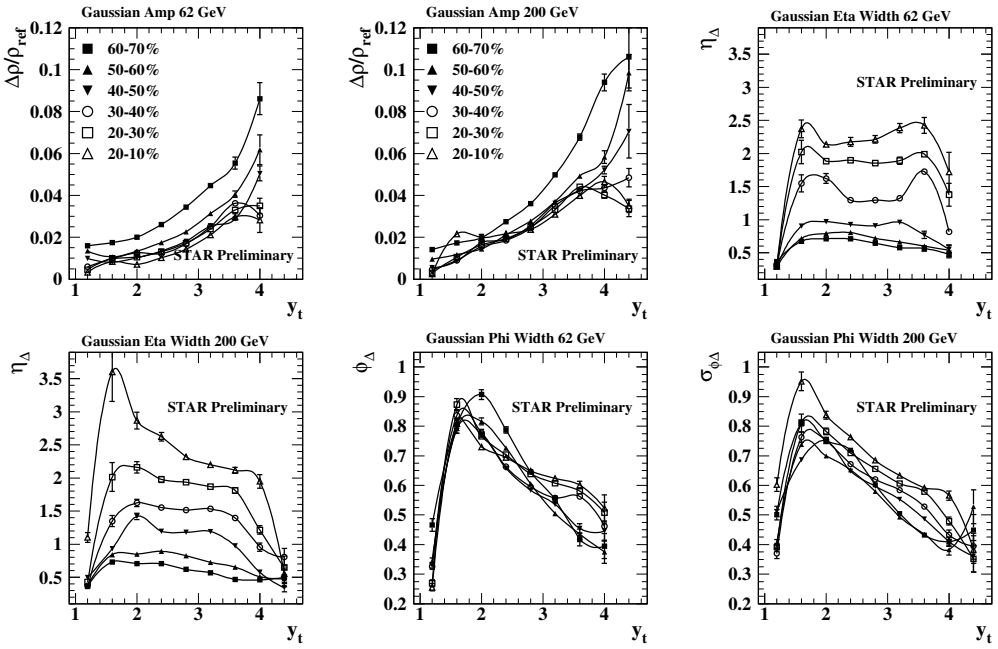

Figure 9.2: 62 and 200 GeV amplitudes and widths in η_Δ and ϕ_Δ of the Gaussian jet peak as a function of y_t for several different centralities.

hard components of single-particle spectra in a future analysis.

The existence of significant SS correlations at large η_Δ even at high p_t is closely related to the phenomenon that has been termed "the ridge". The mechanism for these "long-range" correlations is not well understood, but we do want to understand how this analysis relates to existing ridge observations.

9.2 The Ridge

The phenomenon known as "the ridge" is probably the single most poorly understood observation in modern heavy-ion physics. Many theories have been put forward to explain it, but they typically either lack detailed predictions or fail to be consistent with all existing observations.

The term was coined in the context of central collisions with high-p_t triggers. In that scenario it was observed that same-side two-particle correlations could be described by a narrow "jet" peak on top of a relatively flat background. The flat same-side correlation is

what is now referred to as "the ridge". The unusual properties of the p_t-integrated same-side correlations described above constitute another aspect of the ridge and are sometimes referred to collectively as the "soft ridge".

9.2.1 Ridge properties

Figure 9.3 is one of the most iconic examples of The Ridge [10]. It is a 2D correlation but unlike the analysis in this dissertation it was made using a high-p_t trigger. Rather than constructing the correlation from all pairs of particles in an event, the trigger particle is correlated with "associated" (non-triggered) particles. Typically there are additional p_t cuts imposed on the associated particles as well. While using a high-p_t trigger does make it possible to collect more events containing high-p_t particles than a minimum-bias trigger, it also limits the scope of the analysis. If we recall Fig. 7.1—the diagram of the y_t cuts used in constructing marginal distributions—a typical high-p_t triggered analysis with cuts on the associated particle momentum would be a small off-diagonal box in this space. Furthermore, high-p_t triggers are also frequently restricted to central collisions under the assumption that is where the physics of interest will be present. But we wish to examine the full centrality dependence.

The SS peak in this case is not a simple Gaussian. In the high-p_t triggered correlation analysis in Ref. [10] it is modeled with the combination of a Gaussian peak—which is labeled the "jet" part—and an η_Δ-independent component—which is labeled the "ridge" part. This is the origin of the ridge terminology. It is conventionally assumed that the ridge is some new physical phenomenon unrelated to jet physics.

Using the methods described in this dissertation we are in a unique position to examine the complete phenomenology of the ridge in both p_t and centrality. But first we need to understand the difference between the fit model introduced in Eq. (5.20) and these triggered correlations. Our fit model does not contain separate "jet" and "ridge" contributions. There is a contribution to the SS structure from the quadrupole term which is η_Δ-independent, but the high-p_t trigger results are also corrected for v_2 before introducing the separate "jet" and "ridge" contributions [10]. Differences in v_2 measurement methods are not enough to

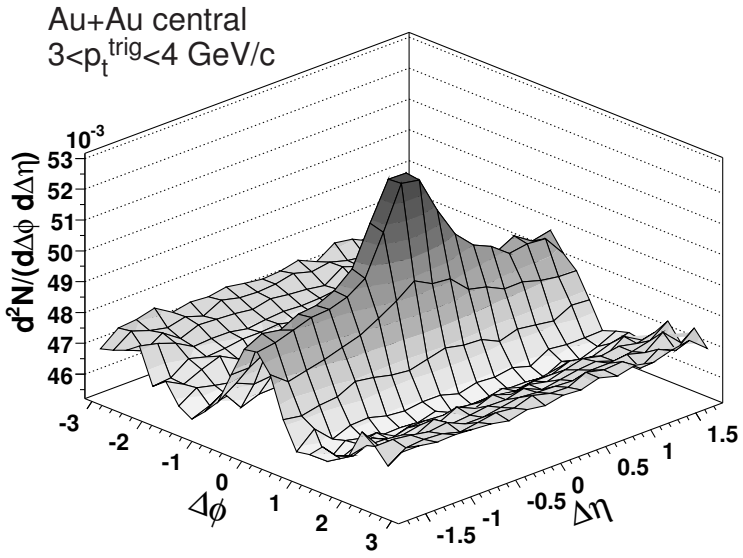

Figure 9.3: The charged di-hadron distribution in central Au-Au collisions for 2 GeV/c < p_t^{assoc} and 3 < p_t^{trig} < 4 GeV/c [10].

explain the difference in peak shapes.

To better understand the peak shape we subtract the quadrupole term and 1D η_Δ term—though this is a negligible contribution for more-central collisions and higher p_t—from measured p_t-dependent correlations. Two marginal p_t bins are shown in Fig. 9.4 for both 50-60% central collisions—just before the transition point—and 10-20% central collisions—where the amplitude and width of the SS peak are at maximum. The first p_t bin is 0.94 GeV/c < p_t < 1.4 GeV/c and the second is 2.1 GeV/c < p_t < 3.1 GeV/c. The first bin has large enough p_t to lack a significant electron peak but would still conventionally be considered part of the soft regime. The second bin has high enough p_t to be comparable to cuts made in the triggered analysis. Though it is not our highest p_t bin, higher bins begin to suffer from lack of statistics, and detailed comparisons of peak shapes become difficult.

The quadrupole-subtracted peaks and residuals in Fig. 9.4 provide no evidence for any significant deviation from a simple SS Gaussian. The Gaussian is very broad on η_Δ, but it is not broad enough to be require an η_Δ-independent function as part of the peak model.

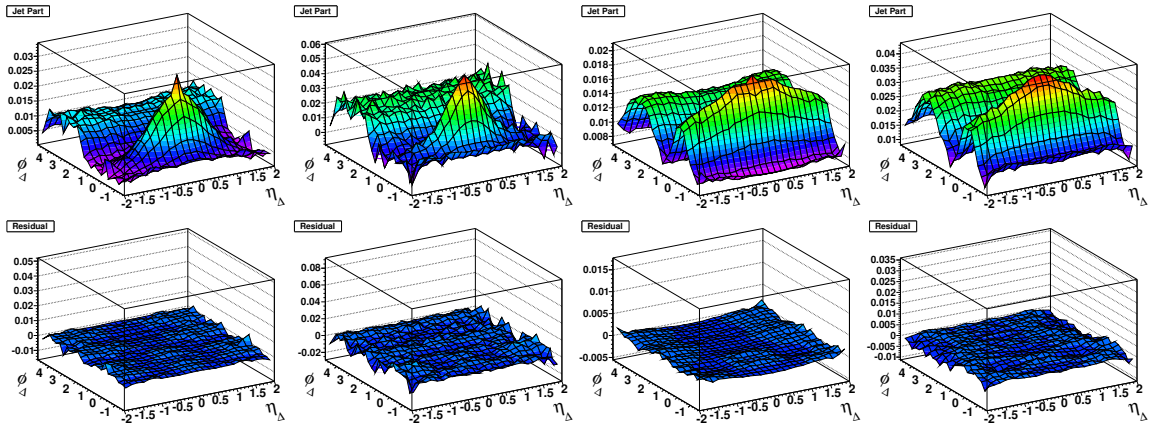

Figure 9.4: Top row: Quadrupole-subtracted correlations histograms in 200 GeV collisions for 50-60% central collisions with marginal p_t cuts 0.94 GeV/c $< p_t <$ 1.4 GeV/c and 2.1 GeV/c $< p_t <$ 3.1 GeV/c and 10-20% central collision with the same p_t cuts. Bottom row: Fit residuals for the same histograms as above.

This is what we observe for all centralities and p_t intervals in this study. While the p_t region explored in the triggered analysis does extend a bit higher than the data presented here the most significant distinction is which particles the p_t cuts are applied to. In the triggered analysis cuts are made on *both* the trigger and associated particles while the marginal p_t bins only impose a cut on the p_t of one particle. We conclude that it is necessary to restrict the p_t of both particles to see distinct "jet" and "ridge" components.

Centrality-dependence of the high-p_t triggered ridge is largely ignored, as the triggers are typically used to select more central events. But with the full complement of minimum-bias collisions we can study the centrality evolution as well. See Appendix A for the full set of plots. So long as the centrality is below the transition point we see a single narrow 2D Gaussian peak which becomes slightly narrower at higher p_t. This trend is expected for jets. For p_t-integrated and marginal p_t bins above the transition point we see a much broader 2D SS peak with an η_Δ-dependence largely independent of p_t, but the peak narrows on ϕ_Δ at higher p_t.

It is natural to propose three regimes: In peripheral collisions GLS scaling holds and we see jet peaks analogous to those in p-p collisions at all p_t. Above the transition point and at lower-p_t there is a single broad Gaussian peak *which evolves smoothly from the peak in*

more-peripheral collisions. Finally, when specific p_t cuts are made in more-central collisions there is a significant modification of the SS peak shape which introduces another component to the fit model.

Unfortunately, most attempts to explain the ridge have focused exclusively on the third regime. The ridge structure has been interpreted as evidence of a dense, flowing QCD medium [105, 82]. It is typically assumed that the low-p_t broad Gaussian is just a manifestation of the "soft ridge". The jet component is assumed to be negligible at lower-p_t since it is thought to be a high-p_t phenomenon that is washed out by the large number of low-p_t particles. But we see clear signs of jet physics in more peripheral collisions for *all* p_t bins. And the 2D SS jet peak smoothly evolves into the "soft ridge" with centrality. It is only with very specific kinematic cuts that distinct "jet" and "ridge" structures appear to emerge at all. A complete ridge theory needs to explain *all* of these observations.

9.2.2 Triangular Flow

One of the more-popular explanations for the ridge is the concept of "triangular flow", which states that the ridge is the result of *fluctuations* in the typical flow mechanism assumed to produce v_2. It is conjectured that these fluctuations manifest in such a way that they produce higher multipole terms, such as a sextupole component or v_3 term. While the collision system should be bilaterally symmetric on average, fluctuations in the nucleon positions at the time of the collision are said to actually produce a "triangular" distribution [51].

We do not observe any sextupole term in the residuals of our fits. It should be noted that the significant ϕ-dependent terms in our fit model are only the dipole, quadrupole, and SS Gaussian. The presence of the Gaussian means that this is not simply an orthogonal set of functions. It *is* possible that adding a sextupole to our fit function could change our results. However attempts to do so have shown that the sextupole term does nothing more than describe part of the Gaussian peak in the 1D projection onto ϕ_Δ. The Gaussian is still a necessary part of the fit function because even in the 1D case v_3 cannot accomodate all of the observed structure. We could of course add v_4, v_5, etc. terms to attempt to describe

the data without a Gaussian. However the result is just the Fourier decomposition of a Gaussian peak, which is a less compact and less useful description of the data than just using the Gaussian parameters. See App. B of Ref. [37] for a more detailed discussion of alternative fits.

It is common in v_3 analyses to only examine the ϕ_Δ dependence. But our fit model is further constrained in η_Δ. Even in the most central collisions—where the η_Δ width of the Gaussian is very large—a ridge that is perfectly flat in η_Δ does not describe the data well. Not only are higher multipoles a cumbersome way of describing the 1D data they can't describe the 2D data at all.

Finally, as stated above triangular flow depends on the presence of large flow fluctuations. But our observations in Chapter 6 and 7 indicate that there is essentially no quadrupole amplitude in the most central collisions. Fluctuation models predict significant v_2 (elliptic flow) in central collisions, because that is where conjectured fluctuations appear to be greatest. Our observations seem inconsistent with large flow fluctuations, and without large flow fluctuations there can be no physical motivation for a v_3 term. Thus, triangular flow appears to be an inadequate explanation for the ridge.

9.3 The p-p Ridge

The CMS collaboration has published a study of angular correlations in p-p collisions at the LHC [118, 167]. A notable result is the appearance of a same-side "ridge" structure with specific kinematic cuts. This ridge structure has been compared to that observed at RHIC [10]. It has been suggested that this correspondence implies that a dense medium may also form in p-p collisions at 7 TeV.

We can make a quantitative comparison between CMS results at 7 TeV and STAR results at 0.2 TeV. In the CMS study a quadrupole term was not considered because v_2 is usually assumed to be zero in p-p collisions. But it is possible for a small quadrupole component to be present even in p-p collisions. In Chapter 6 we established the energy dependence of the nonjet quadrupole. It is possible to perform a simple extrapolation to CMS energy. If we then introduce a proxy for "centrality" in p-p we find that observed trends in the quadrupole in Au-Au collisions can actually explain the SS "ridge" that CMS

observed with specific kinematic cuts.

9.3.1 SS ridge and curvatures at the azimuth origin

Appearance of a SS ridge depends on the total curvature at the azimuth origin $\phi_\Delta = 0$. A visible ridge is equivalent to a significant negative SS curvature over an extended η_Δ interval. The SS total azimuth curvature depends in part on curvature contributions from the AS 1D peak and nonjet quadrupole. Depending on the relative amplitudes of the two components a SS ridge feature may be visible or not. Other contributions to the SS curvature may be present. It is important to distinguish and understand the possible appearance of a visible SS ridge due to the nonjet quadrupole component, which may contribute to ridge formation *under some circumstances*. We now develop a description of SS curvature systematics.

A closed expression for the SS ($\phi_\Delta = 0$) curvature from a unit-amplitude AS 1D Gaussian periodic peak array with r.m.s. width σ_ϕ (approximated by two Gaussians centered at $\phi_\Delta = \pm\pi$) is given by

$$C(\sigma_\phi) = \left(\frac{\pi^4}{\sigma_\phi^4} - \frac{\pi^2}{\sigma_\phi^2} \right) \frac{2}{\pi^2} \exp\{-\pi^2/2\sigma_\phi^2\}. \tag{9.1}$$

The SS curvature is negligible for $\sigma_\phi < 0.6$ (Gaussians are fully resolved).

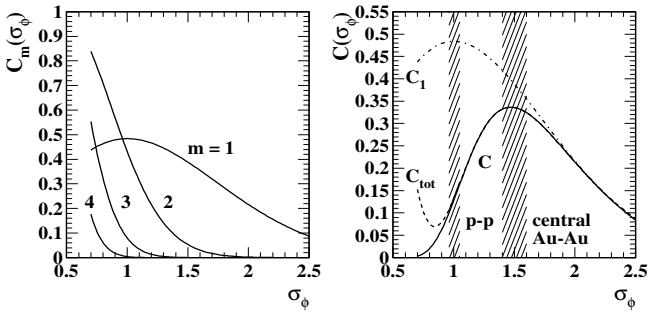

Figure 9.5: Left: Same-side curvature contributions C_m from four away-side (AS) 1D Gaussian multipoles $m = 1 \ldots 4$ as a function of the AS peak r.m.s. width. Right: Same-side curvature in closed form for an AS 1D Gaussian peak (solid curve) and for Eq. (9.3) truncated at $m = 3$ (dashed curve). The dipole curvature (dash-dotted curve) is included for reference.

The unit-amplitude AS 1D peak array can be expressed as a Fourier series with coeffi-

cients give by

$$F_m(\sigma_\phi) \;=\; \sigma_\phi\sqrt{2/\pi}\exp\{-m^2\sigma_\phi^2/2\}. \tag{9.2}$$

The curvature evaluated at $\phi_\Delta = 0$ for an AS 1D peak array with unit amplitude and r.m.s. width σ_ϕ is then given by

$$C_{tot}(\sigma_\phi) \;=\; \sum_{m=1}(-1)^{m-1}m^2F_m(\sigma_\phi), \tag{9.3}$$

Figure 9.5 (left panel) shows individual multipole contributions $C_m(\sigma_\phi) = m^2F_m(\sigma_\phi)$ to the curvature sum in Eq. (9.3) for $m = 1\ldots4$. Fig. 9.5 (right panel) shows the exact expression C in Eq. (9.1) (solid curve) and the series in Eq. (9.3) C_{tot} truncated at $m = 3$ (dashed curve). The deviation from the solid curve is consistent with neglect of the (negative of the) $m = 4$ term in the left panel. The dipole contribution C_1 (dash-dotted curve) is included for reference. The hatched region near $\sigma_\phi = 1$ represents 2D fits to 200 GeV NSD p-p data with an AS 1D Gaussian model. The hatched region near $\sigma_\phi = 1.5$ represents 2D fits to more-central Au-Au data where the AS 1D peak is well modeled by an AS dipole only.

For an AS 1D peak with amplitude A_{1D} and width $\sigma_\phi \geq 1$ (consistent with p-p minimum-bias and Au-Au data) Eq. (9.3) can be truncated to two multipoles

$$\begin{aligned} C_{AS}(\sigma_\phi) \;&=\; B_1(\sigma_\phi) - 4B_2(\sigma_\phi) \\ &\equiv\; A_D(\sigma_\phi)/2 - 4\times 2A_Q(\sigma_\phi). \end{aligned} \tag{9.4}$$

where $B_m(\sigma_\phi) = F_m(\sigma_\phi)A_{1D}$ [164], and 2D fit parameters A_D and A_Q are defined in Eq. (5.20). An additional (negative) curvature contribution comes from nonjet quadrupole $A_Q\{2D\}$. A SS ridge should appear if the total SS curvature is significantly negative or $16\left[A_Q(\sigma_\phi) + A_Q\{2D\}\right]/A_D > 1$. That relation is the central issue for this analysis.

9.3.2 Au-Au vs p-p collision geometry descriptions

A-A collision centrality is defined in the standard way described in Sec. 2.2.3. p-p collision centrality is of significant interest at the LHC [95]. We can in principle relate measured

n_{ch} to p-p collision centrality, but we currently have no p-p equivalent to the A-A Glauber model based on participant nucleons. An analogy might be made between participant nucleons in A-A collisions and "participant partons" in p-p collisions derived from the nucleon parton distribution function (PDF). Participant partons, the number depending on p-p centrality or soft momentum transfer, may engage in binary interactions, some of which would result in large-angle parton scattering. Hadron production then arises from projectile-nucleon fragmentation (soft component) and semi-hard parton scattering to form jets (hard component).

In the two-component study of single-particle p_t spectra from 200 GeV p-p collisions the spectrum hard component was found to scale in amplitude (*relative* to the soft component) approximately linearly with n_{ch} as n_{ch} was increased by a factor ten relative to the NSD value [24]. The spectrum hard component is quantitatively consistent with minijet correlations [168] and with pQCD-calculated fragment distributions [161]. The p-p hard-component *absolute* yield increases by a factor 50 as the total particle multiplicity near mid-rapidity increases ten-fold. Equivalently, the jet frequency per p-p collision within one unit of η increases from 2% to nearly 100% [24].

Based on the two-component model we interpret the n_{ch} systematics of spectra and correlations in terms of p-p centrality as follows. For all centralities the soft component arising from longitudinal fragmentation of projectile nucleons comprises no less than 90% of the hadron production, thus defining an "overlap volume" for the p-p collision determined by the large-scale soft momentum transfer. The hard-component *fraction* changes from 2% to 10%, but the hard-component *absolute yield* increases by factor 50, indicating a large increase in the number of participant-parton binary interactions (similar to N_{bin} in A-A collisions). Those systematics suggest that n_{ch} is closely correlated with p-p centrality despite strong event-wise fluctuations in nucleon shape and impact parameter. Increases with n_{ch} are not dominated by jet production but instead by p-p overlap volume.

The overlap of extended ($\approx$ spherical) objects also implies a geometric eccentricity which may be relevant to an azimuth quadrupole in the p-p hadronic final state. We argue by analogy that eccentricity in p-p collisions follows a similar trend to that in A-A collisions, that of two intersecting spheres. The eccentricity of minimum-bias p-p (N-N) collisions

may then be approximated by an average over more-peripheral A-A collisions. Just as for A-A collisions the p-p eccentricity may increase initially with increasing n_{ch} (centrality) but then fall off for more-central collisions, the extent depending on the magnitude of geometry fluctuations in p-p compared to Au-Au collisions. We estimate $\epsilon_{opt} \approx 0.3$ for minimum-bias p-p collisions based on ϵ_{opt} centrality dependence for more-peripheral Au-Au collisions [115].

9.3.3 2D histogram A-B comparisons

Angular correlation histograms for this study were binned as 25×28 on $(\eta_\Delta, \phi_\Delta)$ to match the CMS binning. Detailed comparisons of contour lines between data and model functions then permit quantitative inference of model parameters from the CMS data, typically accurate to 10% for the simple structures in p-p correlations. The CMS color palette includes 20 colors, whereas this study employs 50 colors, causing minor differences in shading in some regions but increasing sensitivity. The intervals spanned by vertical scales are nearly the same for model and CMS data in each comparison, although the offsets may differ. By careful A-B comparisons a good approximation to direct χ^2 model fits to histogram data can be achieved. Model uncertainties are discussed in more detail in Ref. [167].

We will use our standard 2D fit model from Eq. (5.20) to extrapolate parameters for comparison to the CMS data. We will also invoke the energy scaling observed in Eq. (6.2) and the energy and centrality dependence of the quadrupole term observed in Eq. (6.3).

9.3.4 p-p minijet collision-energy systematics

The parameters for the five most-peripheral Au-Au centrality bins in Chapter 6 are relevant to this study. The SS and AS peak amplitudes (A_{2D} and A_{1D} respectively) for those bins closely follow a Glauber linear superposition (GLS) trend $\propto \nu$ for $\nu \leq 3$ [37], with $\nu \approx 1.25$ equivalent to minimum-bias N-N collisions [169]. GLS scaling implies that jet correlations for Au-Au collisions within that centrality interval are predicted by jet correlations in p-p collisions, and the reverse. The relative error for each centrality and energy is given by $A_{2D} \pm 7\%$ and $A_{1D} \pm 5\%$.

The SS 2D Gaussian term can also be represented as $\rho_0(b)j^2(\eta_\Delta, \phi_\Delta, b)$, defining j^2 as a

measure for jet correlations statistically equivalent to v_2^2 for the azimuth quadrupole. See details in Sec. 9.4. We base extrapolation of 200 GeV jet correlations to 7 TeV on *quadrupole* energy scaling factor $R(\sqrt{s_{NN}})$) in Eq. (6.2). The predicted relation between 62 and 200 GeV is $\ln(200/13.5)/\ln(62/13.5) = 1.75$. The observed amplitude ratio for the SS 2D peak averaged over the five most-peripheral Au-Au centrality bins is $1.65 \pm 10\%$, in agreement with Eq. (6.2). However, the ratio for the AS 1D peak amplitude is $0.95 \pm 7\%$.

The difference between the two cases is consistent with jet systematics. The SS 2D peak amplitude represents the projected single-jet density on longitudinal rapidity y_z, while the AS 1D peak (AS ridge) amplitude represents the dijet density on 2D space (y_{z1}, y_{z2}). The two share a common dijet total cross section $\sigma_{dijet}(\sqrt{s})$. Longitudinal rapidity y_z is bounded kinematically by the beam energy $\sim \log(\sqrt{s})$. Since the kinematic bound for the 1D rapidity space goes as $\log(\sqrt{s})$ and that for the 2D space goes as $\log^2(\sqrt{s})$ the difference between SS and AS energy scaling trends may differ by one factor $\log(\sqrt{s})$. That substantial difference in energy scaling between AS 1D peak and azimuth quadrupole amplitudes is of central importance to appearance of the SS ridge at LHC energies but not at RHIC energies (see Sec. 9.3.13).

9.3.5 p-p minijet multiplicity and p_t systematics

Jet angular correlations in p-p collisions scale with n_{ch} as follows (consistent with spectrum hard-component trends from Ref. [24]). The mean jet fragment multiplicity (~ 2.5, dominated by 3 GeV jets) does not change significantly with p-p n_{ch} (the number of correlated pairs per jet is fixed), but the jet frequency increases by a factor 50 with $10\times$ increase in n_{ch}, rising to about one dijet per p-p collision. Jet correlations measured by $\rho_0\, j^2$ then scale up as $10 \times (50/10^2) = 5$, since pair ratio j^2 represents correlated pairs / reference pairs.

For p-p correlations on $y_t \times y_t$ at 200 GeV [138, 139] the SS jet correlation structure (single 2D peak) extends down to $p_t \approx 0.35$ GeV/c, with mode at 1 GeV/c . Nearly half the SS-correlated pairs appear below the mode. In contrast, AS correlations are cut off near 0.7 GeV/c due to initial-state k_t effects. Thus, a smaller fraction of AS pairs appears below 1 GeV/c. For $p_t \in [1, 3]$ GeV/c cuts at 7 TeV imposed on corresponding angular correlations

the SS 2D peak amplitude should be reduced approximately by factor 1/3 and the AS 1D peak reduced by factor 1/2.

9.3.6 Minimum-bias angular correlations

We compare minimum-bias angular correlations at RHIC energies to equivalent results from 7 TeV p-p data. Comparison of jet correlations from minimum-bias p-p collisions for the two cases tests an assumed energy extrapolation of RHIC data. We also compare responses to applied n_{ch} and p_t cuts. Correlation parameters for two energies and several cut conditions are summarized in Table 9.1. Comparison of quadrupole and jet extrapolations to CMS data tests the hypothesis that the SS ridge in 7 TeV p-p data results from a combination of nonjet quadrupole and AS dipole structure in angular correlations.

Energy extrapolation of minimum-bias nonjet azimuth quadrupole amplitude $A_Q\{2D\}$ to 7 TeV follows Eq. (6.2) established below 200 GeV, and extrapolation of the corresponding SS 2D peak amplitude A_{2D} follows the same trend. We then scale those 200 GeV parameters to CMS results at 7 TeV as $R_X = [R(7\text{ TeV})\,2\pi\Delta\eta]\;A_X$, with $R(7\text{ TeV}) = 2.3$ and $\Delta\eta = 4.8$, or $R_X \approx 70A_X$. As noted in Sec. 9.3.4, energy dependence of the AS 1D peak amplitude near 200 GeV is consistent with no change with energy. Only the acceptance factor is include and $R_D \approx 30A_D$. The resulting extrapolation in Fig. 9.6 (first panel) compares well with CMS minimum-bias data in the second panel. It is notable that the large ϕ elongation (2:1) of the SS 2D peak observed in 200 GeV p-p collisions [139] seems to persist in 7 TeV collisions, as does the 1D Gaussian on η_Δ associated with longitudinal projectile-nucleon fragmentation [138].

9.3.7 High-multiplicity cut

Figure 9.6 (third panel) shows the model function in Fig. 9.6 (first panel) with the following changes: (i) The SS 2D peak amplitude is scaled up by factor 3, (ii) The AS 1D peak amplitude is scaled up by factor 4, (iii) the SS peak ϕ width is reduced from 0.9 to 0.65 and the η width from 0.64 to 0.58, and (iv) the 1D η Gaussian is eliminated. Those changes relative to the minimum-bias case are required to achieve agreement between model and

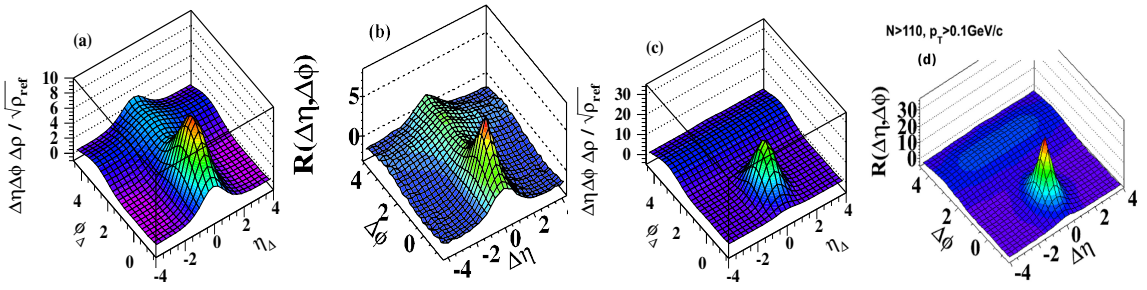

Figure 9.6: (a) The parametrization of 200 GeV p-p data from [138, 139] (left panel) rescaled by energy-dependent factor $R(7\text{ TeV}) = 2.3$ and CMS acceptance factor $\Delta\eta\Delta\phi$. The AS ridge is not scaled up by the energy factor. (b) CMS angular correlations for minimum-bias 7 TeV p-p collisions [118]. (c) Model function from (a) with jet structure increased by factor 3 and quadrupole increased by factor 6, with SS peak narrowed on η_Δ and with 1D η_Δ Gaussian removed. (d) CMS p_t-integral angular correlations for high-multiplicity 7 TeV p-p collisions [118].

data in this figure and in Fig. 9.7. The extrapolated jet structure in the third panel compares well with CMS data in the fourth panel with the exception of the narrow contribution from quantum correlations and electron pairs at the origin not included in the model.

Selecting high-multiplicity p-p collisions biases the jet frequency per event to larger values [24]. As argued in Sec. 9.3.2 the increased hard scattering can be interpreted as the result of increased p-p centrality induced by the multiplicity cut. For 200 GeV p-p correlations a similar multiplicity cut increases jet correlation structure by a factor 5 [138] compared to factor 3 noted for the SS 2D peak in 7 TeV data. The difference is discussed in Sec. 9.3.11.

Figure 9.7 shows the results in Fig. 9.6 with the vertical axis range reduced by a factor 5 to enhance small-amplitude details. Correspondence of the SS jet peaks near the base is evident. The AS ridge shows significant reduction in the data at larger η_Δ (lower-left panel) which is not included in the model function (upper-right panel) inferred within the STAR TPC η acceptance. The approximately 20% falloff at larger η_Δ is not critical to this analysis.

The nonjet-quadrupole amplitude is increased by factor 6 for this figure to $2R_Q\{2D\} = 0.42$ (relative to the extrapolated minimum-bias value). The larger quadrupole amplitude is

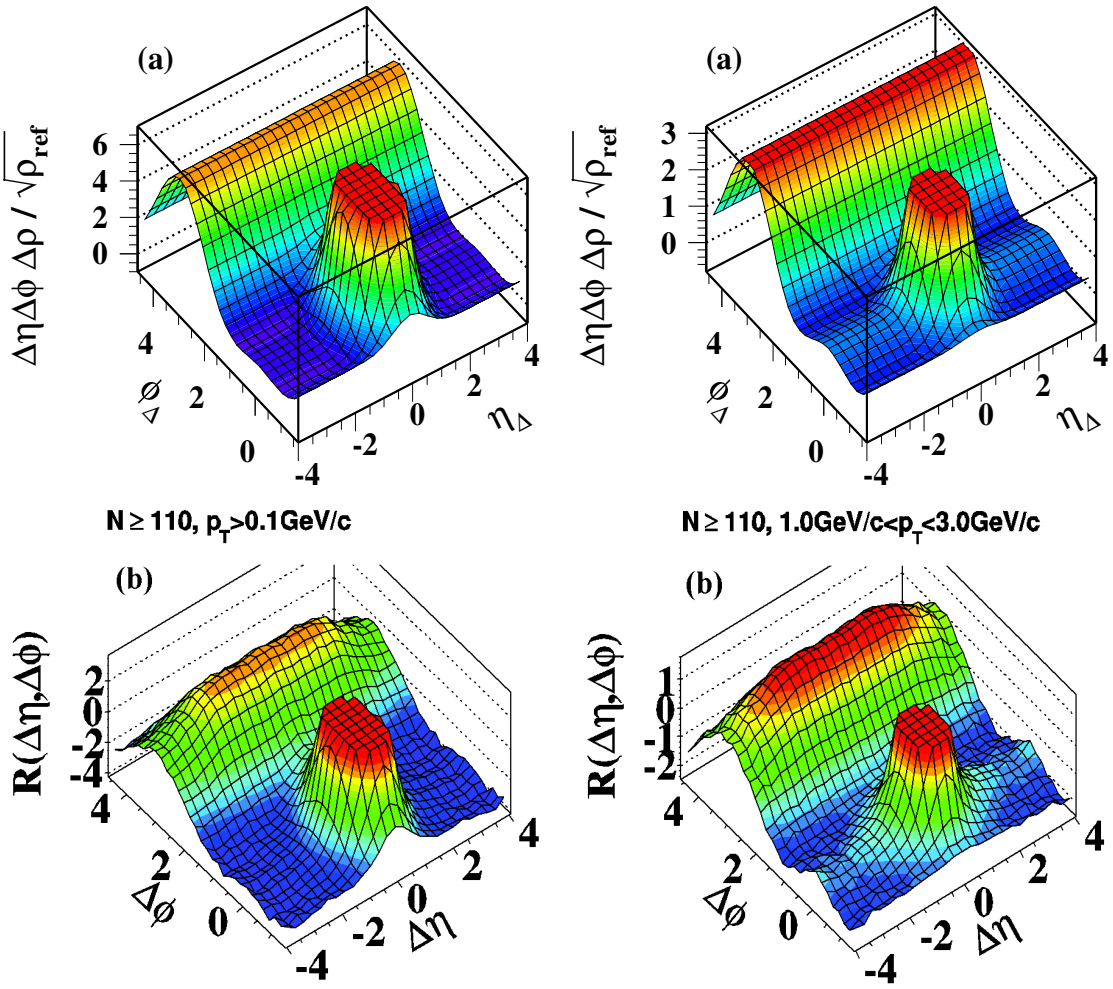

Figure 9.7: Histograms from Fig. 8.2 rescaled by factor 5. Upper-left panel: Model function from Fig. 9.6 (third panel) but with quadrupole amplitude increased by factor 6 to $R_Q = 0.42$. Lower-left panel: CMS p_t-integral correlations for high-multiplicity cut [118]. Upper-right panel: Model function from the top left panel with the same quadrupole amplitude but with jet correlation amplitudes and peak widths reduced (see text). Lower-right panel: CMS correlations for high-multiplicity cut and $p_t \in [1, 3]$ GeV/c [118].

$\sqrt{s}$ (TeV)	Condition	$2A_Q$	$A_D/2$	A_{2D}	$16A_Q/A_D$	$2R_Q$	$R_D/2$	R_{2D}	σ_η	σ_ϕ
0.2	MB	$0.001 + .0023$	0.023	0.058	0.57±0.16	$0.03 + 0.069$	0.69	1.74	0.64	0.9
7	MB	$0.0023 + 0.0023$	0.023	0.133	0.80±0.22	$0.07 + 0.069$	0.69	4.0	0.64	0.9
7	n_{ch} cut	$0.014 + 0.0092$	0.092	0.39	1.01±0.28	$0.42 + 0.29$	2.9	12.0	0.58	0.65
7	p_t, n_{ch} cuts	$0.014 + 0.0047$	0.047	0.13	1.59±0.44	$0.42 + 0.14$	1.45	4.0	0.55	0.55

Table 9.1: p-p correlation systematics. Entries represent systematics inferred from RHIC data at 200 GeV and parameters inferred by modeling CMS angular correlation histograms at 7 TeV from Ref. [118]. The left columns indicate collision energy and cut conditions, including minimum-bias (MB) data. The A_X represent parameters from STAR per-particle analysis with an intensive correlation measure. The R_X represent corresponding CMS data including extensive acceptance factor $2\pi\Delta\eta \approx 30$. The two entries in the $2A_Q$ and $2R_Q$ columns correspond to nonjet and jet-related (AS peak) quadrupoles respectively.

required to change the SS curvature in $|\eta_\Delta| > 2$ from concave upward (positive curvature) to slightly concave downward (negative curvature). The 6-fold quadrupole increase is thus already required by CMS data prior to imposition of p_t cuts. The SS curvature issue is further discussed in Sec. 9.3.13.

9.3.8 High-multiplicity plus high-p_t cuts

Figure 9.7 (upper-right panel) shows the model in Fig. 9.7 (upper-left panel) with the following changes: (i) The ϕ width of the SS 2D peak is further reduced from 0.65 to 0.55 leading to a symmetric SS peak on $(\eta_\Delta, \phi_\Delta)$, (ii) The SS peak amplitude is reduced by factor 1/3 and AS 1D peak by factor 1/2 compared to the high-multiplicity cut alone and (iii) the nonjet quadrupole amplitude remains the same as for the high-multiplicity cut alone—$2R_Q\{2D\} = 0.42$ increased by factor 6 from minimum-bias 0.07. Those changes provide good agreement between model (upper-right panel) and CMS data (lower-right panel), especially near the base of the SS 2D peak. With high-p_t cuts we expect to eliminate some fraction of the jet contribution and possibly to change the quadrupole amplitude. The required changes in jet structure at 7 TeV agree well with the effects of reduced p_t acceptance for jet-correlated pairs at 200 GeV [138, 139]. Appearance of the SS ridge in relation to factors affecting the SS curvature is further discussed in Sec. 9.3.13.

9.3.9 Quadrupole/jet ratio and SS curvatures

Appearance of a SS ridge depends on the condition $16A_{Q,tot}/A_D > 1$, where $A_{Q,tot} = A_Q(\sigma_\phi) + A_Q\{2D\}$. The first term in $A_{Q,tot}$ scales with the AS 1D (jet) peak amplitude A_{1D}, the second is the nonjet quadrupole amplitude. The AS 1D peak model in Fig. 9.6 (first panel) is a Gaussian with $\sigma_\phi \approx 1$. The *jet-related* quadrupole component of the AS peak is then $2A_Q(\sigma_\phi = 1) \approx 0.1A_D$ [164]. For the curvature discussion in Sec. 9.3.13 the 1D Gaussian is approximated as the sum of AS dipole and quadrupole terms only. Requiring an equivalent net curvature at $\phi_\Delta = 0$ leads to $2A_Q(\sigma_\phi) \approx 0.05A_D$. The jet-related quadrupole then includes estimated curvature contributions from higher Fourier components of the AS peak (mainly the sextupole). Nonjet and jet-related quadrupoles (in that order) are shown in both $2A_Q$ and $2R_Q$ columns of Table 9.1.

The split between $A_Q\{2D\}$ and $A_Q(\sigma_\phi)$ is the dominant uncertainty in characterization of 2D angular correlations in peripheral and central A-A collisions and low-multiplicity p-p collisions, where the nonjet quadrupole amplitude is small relative to the jet amplitudes. The uncertainty in the latter dominates the uncertainty in $16A_Q/A_D$. Combining relative uncertainties in $A_Q\{2D\}$ (25%), $A_Q(\sigma_\phi)$ (10%) and A_D (10%) leads to $16A_Q/A_D \pm 28\%$, included in the corresponding column of Table 9.1.

9.3.10 Inferred model parameters

This analysis reveals that minimum-bias jet structure at 7 TeV is remarkably similar to that at RHIC energies. The same-side 2D peak amplitude continues to follow the $\log(\sqrt{s})$ energy scaling established between 17 and 200 GeV, while any change in the AS 1D amplitude is much less, consistent with the AS trend at lower energies. Changes in jet structure with applied n_{ch} and p_t cuts at 7 TeV are also similar to those observed in 200 GeV p-p collisions.

Novel structure in the form of a same-side ridge does appear at 7 TeV with application of certain multiplicity and p_t cuts. Does the ridge structure imply novel physics in LHC p-p collisions, or is it simply related to phenomena observed at lower energies? In the following sections we review jet and quadrupole correlation systematics in p-p and Au-Au collisions and consider how a combination of increased collision energy plus n_{ch} and p_t cuts can lead

to a visible SS ridge.

Table 9.1 presents results from extrapolation of RHIC p-p data to 7 TeV and from modeling CMS data histograms for several cut conditions. The first row summarizes results for p-p collisions at 200 GeV (jet parameters) or extrapolated from Au-Au centrality trends (nonjet quadrupole parameter). In general, STAR (A_X) and CMS (R_X) parameters are related by $R_X = 2\pi\Delta\eta A_X \approx 30 A_X$, since $\Delta\eta = 4.8$.

In the second row, the SS peak and quadrupole amplitudes determined at 200 GeV have been scaled up with energy by factor $R(\sqrt{s}) = 2.3$ inferred from jet and quadrupole energy systematics below 200 GeV. AS dipole amplitude A_D remains the same, consistent with jet structure trends below 200 GeV. The comparison in Fig. 9.6 indicates that energy extrapolation of 200 GeV jet correlations provides good agreement with 7 TeV data.

In the third row, parameters have been modified in response to the n_{ch} cut. Jet peak amplitudes are further increased by factors 3 (SS) and 4 (AS) and the quadrupole amplitude by factor 6 to match the structure observed in Figs. 9.6 and 9.7 (left panels). In the fourth row, parameters have been further modified in response to the p_t cut. The quadrupole amplitude is unchanged. SS 2D peak amplitude A_{SS} is reduced by factor 1/3 and AS dipole amplitude A_D is reduced by factor 1/2 to match the structure in Fig. 9.7 (right panels).

Figure 9.6 (first two panels) tests extrapolation of jet structure from 200 GeV to 7 TeV. The extrapolation is reasonably accurate. Fig. 9.6 (last two panels) tests the effect of the n_{ch} cut on 7 TeV jet structure compared to the response at 200 GeV. Response to cuts at the two energies is quantitatively similar. Figure 9.7 probes the effect of applied cuts on the extrapolated nonjet quadrupole and its possible contribution to formation of the SS ridge.

9.3.11 p-p and Au-Au centrality trends

From CMS data we conclude that both $A_Q\{2D\}$ (nonjet quadrupole) and A_D (jets) increase with increasing p-p multiplicity (by factors 6 and 3 respectively for a factor-7 increase in n_{ch}), and that the ratio $A_Q\{2D\}/A_D$ may therefore double). Are such trends consistent with p-p and Au-Au collisions at 200 GeV? We have two sources of information about p-p multiplicity trends at RHIC energies: a) measured 200 GeV p-p systematics and b)

arguments by analogy with Au-Au collision centrality.

p-p minijet multiplicity systematics at 200 GeV As noted in Sec. 9.3.2 selection of high-multiplicity p-p events is expected to bias toward more-central collisions with larger dijet production [95]. Two-component analysis of 200 GeV p-p p_t spectra revealed that with a ten-fold increase in multiplicity the jet frequency increased by a factor 50 (100% of collisions), which should correspond to a factor-5 increase in jet correlations (Sec. 9.3.5) [24]. Jet correlation measurements at 200 GeV confirmed that the per-particle jet correlation amplitude increases by about a factor 5 [138, 139].

At 7 TeV the minimum-bias jet frequency is expected to increase relative to 200 GeV by factor $R(7\text{ TeV}) = 2.3$ to almost 5%. The maximum frequency increase should then be $50/2.3 = 22$. With a 7-fold increase in event multiplicity we expect the jet correlation amplitude to increase by factor $7(22/7^2) \approx 3$. In Sec. 9.3.7 we confirm from CMS data that application of a factor-7 high-multiplicity cut does increase the jet correlation amplitude by factor 3.

Au-Au quadrupole centrality systematics The nonjet quadrupole in A-A collisions below 200 GeV depends only on collision energy and initial geometry in the form b/b_0 (the relative geometry of intersecting spheres), not on absolute system size. The two trends are factorized as in Eq. (6.3). We argue by analogy between p-p and Au-Au centrality that the same increase in p-p centrality which leads to increased jet production should produce a corresponding quadrupole increase.

The measured nonjet quadrupole amplitude is expressed in terms of A-A centrality parameters by $A_Q\{2D\} = \rho_0(b)v_2^2\{2D\} \propto n_{bin}\epsilon_{opt}^2$ [115]. The AS 1D peak amplitude) scales with A-A centrality as $A_D/2 \propto \rho_0(b)j^2 \propto \nu/(1+x(\nu-1)) \approx \nu$][84]. The Glauber parameters are related by $n_{bin} \sim \nu^4$ and $n_{part} \sim \nu^3$. Thus, A_Q/A_D scales with Au-Au centrality as $\nu^3 \sim n_{part}$, which increases by a factor 50 up to the maximum of A_Q beyond which the rapid decrease of $\epsilon_{opt}^2(b)$ dominates.

We assume that ϵ_{opt}^2 changes (increases) slowly with n_{ch} in p-p collisions and that the quadrupole amplitude increases *at least as fast* as the AS 1D peak amplitude and probably

faster with n_{ch} based on Au-Au centrality systematics. A nonjet quadruple increase twice the jet increase as required by CMS data (SS curvature) is thus consistent with measured p-p and Au-Au centrality trends at RHIC energies.

9.3.12 p-p minijet response to p_t cuts

In Sec. 9.3.8 we observed that with $p_t \in [1, 3]$ GeV/c cuts imposed the 7 TeV SS peak amplitude is reduced by factor 1/3 and the AS ridge is reduced by factor 1/2. As noted in Sec. 9.3.5 in p-p correlations on $y_t \times y_t$ at 200 GeV [138, 139] SS jet correlations extend down to $p_t = 0.3$ GeV/c with the mode at 1 GeV/c. Nearly half the SS peak correlated pairs appear below the mode on p_t. In contrast, AS correlations are cut off near 0.7 GeV/c due to initial-state k_t effects. A smaller fraction of AS pairs appears below 1 GeV/c. The p_t cut systematics at 7 TeV are thus consistent with 200 GeV jet structure on $y_t \times y_t$. With the high-multiplicity cut (more-central p-p collisions) the SS peak azimuth width decreases from 0.9 to 0.65. With the high-p_t cut the SS 2D azimuth width is further reduced to 0.55 leading to a symmetric on $(\eta_\Delta, \phi_\Delta)$ SS jet peak. Similar reductions in SS peak azimuth width are observed at 200 GeV and are consistent with centrality trends in Au-Au collisions [84].

9.3.13 Azimuth curvatures and SS ridge phenomenon

This analysis tests the hypothesis that the ridge observed in p-p data at 7 TeV results from a competition between two curvature contributions on ϕ_Δ within $|\eta_\Delta| > 2$ (excluding the SS 2D peak). A visible ridge may appear when the sum of correlation structure near $\phi_\Delta = 0$ becomes significantly concave downward (negative curvature). In minimum-bias p-p collisions at 7 TeV and all p-p collisions at RHIC energies we observe only a positive curvature in that region (no visible ridge).

The dominant structures within $|\eta_\Delta| > 2$ are the AS dipole $\cos(\phi_\Delta - \pi)$ and the azimuth quadrupole $\cos(2\phi_\Delta)$. The curvature of $\cos(2\phi_\Delta)$ at $\phi_\Delta = 0$ is four times the curvature of $\cos(\phi_\Delta - \pi)$ with opposite sign. Like the CMS ridge, the 200 GeV nonjet quadrupole and AS 1D jet peak (dipole) are insensitive to charge combination, with equal amplitude for like-sign and unlike-sign charge pairs [27]. The SS net curvature is then determined by

the coefficients of two sinusoids—$A_D/2$ for the dipole and $2A_Q$ for the quadrupole. Zero net curvature corresponds to $4 \times 2A_Q = A_D/2$ or $16A_Q/A_D = 1$. That ratio is included in Table 9.1. A ridge (negative curvature) is observed if that ratio is significantly greater than 1. A small relative change in correlation amplitudes may result in qualitative appearance or disappearance of a SS ridge.

As revealed in Table 9.1 the increase in amplitude with increased collision energy (factor 2) plus applied p_t (factor 2) and n_{ch} (factor 1.5) cuts at 7 TeV increases the nonjet quadrupole amplitude relative to the AS dipole by an overall factor 6, changing the SS curvature sign and producing a visible SS ridge.

9.3.14 Relevance of the Au-Au SS ridge to p-p collisions

The jet-related SS "ridge" observed in more-central Au-Au collisions at RHIC energies has been compared with the SS ridge observed in 7 TeV p-p collisions. Two manifestations of the Au-Au ridge phenomenon are notable: (i) η elongation of a monolithic SS peak accurately described by a single 2D Gaussian [28, 84] and (ii) development of a seemingly separate ridge-like structure beneath a symmetric 2D jet peak with certain applied p_t cuts [10]. Item (i), well established for "untriggered" (no p_t cuts) jet correlations and for some combinations of p_t cuts, has been referred to as a "soft ridge," although there is no separate ridge per se. Item (ii) is inferred from other combinations of p_t cuts ("trigger-associated" dihadron analysis).

Elongation of the p_t-integral SS 2D peak (i) undergoes a sharp transition on centrality in A-A collisions (both Au-Au and Cu-Cu collisions) [84]. For more-peripheral A-A and p-p collisions the SS peak is strongly elongated in the ϕ direction (3:2) [139]. For more-central collisions the SS peak transitions to strong elongation in the η direction (3:1) [37]. The (sharp) transition in peak properties occurs within a small centrality interval. Variation of SS jet peak structure with p_t cuts (ii) is complex, depending strongly on different charge-sign combinations, hadron p_t and hadron species. Assignment of certain aspects of peak structure to a distinct ridge phenomenon for some p_t cuts is questionable.

We observe that for p-p collisions the minimum-bias SS 2D peak η and ϕ widths have the

same value at 7 TeV as at 200 GeV and are reduced slightly with p_t and dn_{ch} cuts. Thus, item (i) η broadening is not observed. The appearance of a SS "ridge" in CMS p-p data for some cut combinations could be associated with item (ii). However, the absence of item (i) and consistency with known azimuth quadrupole systematics makes interpretation (ii) unlikely. There is thus no indication from p-p data that the CMS ridge is directly associated with the SS 2D (jet) peak. A more definitive resolution may come from systematic study of Pb-Pb centrality systematics.

The $R(\sqrt{s})$ trend Eq. (6.2) inferred from angular correlation energy systematics below 200 GeV in Chapter 6 also describes NSD p-p particle densities above 200 GeV. The NSD value $dn_{ch}/d\eta = 2.5$ at 200 GeV combined with $R(7\text{ TeV}) = 2.3$ predicts 5.75 consistent with the CMS measurement ~ 5.8 [119]. The CMS high-multiplicity cut produces a 7-fold increase over the NSD angular density to $dn_{ch}/d\eta = 40$. In a study of 200 GeV p-p p_t spectra [24] the multiplicity variation included a 10-fold increase (to $dn_{ch}/d\eta = 25$). The maximum particle density studied at 200 GeV is 60% of the maximum at 7 TeV. Thus, RHIC and LHC p-p particle densities are directly comparable, and much smaller than densities achieve in more-central Au-Au collisions at RHIC.

9.4 Parton Fragment Yields

We introduced the concept of minijets in Chapter 1. In Chapter 3 we introduced the two-component model of p-p spectra that includes a "hard" component dominated by jet fragmentation. Ref. [159] expands the two-component model to A-A collisions. In Chapters 6 and 7 we examined the behavior of the quadrupole component of two-particle correlations. In Sec. 9.1.1 we examined the centrality dependence of the same-side peak. Chapter 8 established a detailed description of minijets in e^+-e^- collisions. Ref. [161] shows how this simple parametrization might be modified in heavy-ion collisions. We now wish to use those results to examine the nature of the SS peak in heavy-ion collisions.

We wish to establish a direct connection between minimum-bias jet angular correlations and spectrum hard components . We test the following hypothesis: (i) a jet-like "same-side" 2D peak at the origin in angular correlations (*intra*jet correlations within single jets) represents all minimum-bias parton fragments and (ii) those same fragments also appear as the

spectrum hard component. Measured spectrum hard components from p-p and Au-Au collisions have been described by pQCD [161]. By establishing a quantitative relation between jet-like correlations and spectrum yields we relate minimum-bias jet (minijet) correlations directly to pQCD theory.

9.4.1 Parton Fragment Distributions

The quantitative correspondence between spectrum hard components [24, 159] and pQCD fragment distributions established in Ref. [161] strongly suggests that the parton fragment interpretation for hard components is valid. However, no such correspondence has been established for minimum-bias angular correlations (without p_t "trigger/associated" cuts). Interpretation of low-p_t jet-like features as true jet structure [138, 139, 28, 84] is questioned by many as outside the scope of high-p_t hard processes nominally described by pQCD (e.g. [96, 7]). Coupling spectrum hard components *and* minimum-bias jet-like correlations to pQCD predictions within a single quantitative system would provide compelling support for a comprehensive interpretation in terms of parton fragmentation to minijets. To achieve the connection we transform two-particle jet correlations to the equivalent single-particle fragment distributions by factorization of the correlated-pair density.

The context of this analysis is a two-component model of fragmentation—longitudinal [53] and transverse [147]—manifested in 1D p_t spectra and 2D two-particle angular correlations [24, 159, 161]. The two-component model as invoked here represents two orthogonal fragmentation systems: longitudinal projectile-nucleon fragmentation (soft component) and transverse large-angle-scattered parton fragmentation (hard component). That picture is consistent with the PYTHIA Monte Carlo model of p-p collisions [147]. The terminology "soft" and "hard" refers to the initial N-N or parton-parton momentum transfer, not to the hadron fragment p_t which may extend down to zero momentum. In this analysis we focus on fragmentation of large-angle-scattered partons manifesting as hard components in p_t spectra and jets in angular correlations.

The spectrum hard component (HC) was discovered in a p-p spectrum analysis [24]. The HC was later interpreted as hadron fragments from minimum-bias jets. The HC is

defined as the measured p_t {or $y_t = \ln[(m_t + p_t)/m_\pi]$ with $m_t^2 = p_t^2 + m_\pi^2$} hadron spectrum minus a fixed soft component (SC). The SC (interpreted as longitudinal projectile-nucleon fragmentation) is in turn defined as the limiting case of spectrum variation with event multiplicity (p-p) or centrality (A-A), which limit should correspond to no transversely-scattered parton fragmentation [24, 159]. Two-component analysis of Au-Au collisions revealed that the HC undergoes strong evolution with increasing centrality: Suppression at larger $p_t \sim 10$ GeV/c [31] is closely correlated with much larger enhancement at smaller $p_t \sim 0.5$ GeV/c [159]

In Chapter 8 fragmentation functions (FF) for light quarks and gluons fragmenting to unidentified hadrons were accurately parametrized over a large kinematic domain down to zero fragment momentum. A parametrization of so-called "medium-modified" FFs (mFFs) [75] has also been developed [161]. By folding a pQCD parton spectrum with parametrized e^+-e^- or p-$\bar{\text{p}}$ FFs or calculated mFFs we obtain fragment distributions (FDs) which provide a good description of spectrum hard components down to small fragment momentum ($p_t \sim 0.3$ GeV/c) [161].

9.4.2 Analysis Method

p_t-integrated jet angular correlations on 4D angle space $(\eta_1, \eta_2, \phi_1, \phi_2)$ (pseudorapidity η and azimuth ϕ) represented by pair density $J^2(\eta_1, \eta_2, \phi_1, \phi_2, b)$—representing our correlation measurements—are converted to single-particle 2D density $J(\eta, \phi, b)$ via calculated pQCD "jet frequency" $f(b)$ (b is the A-A impact parameter). $J(b)$ (averaged over the angular acceptance) is in turn compared with spectrum hard component $H_{AA}(b)$, and therefore with pQCD calculations as in Ref. [161].

To convert jet angular correlations to fragment yields we require a model of the single-particle angular density. We denote the charged-particle 2D density on (η, ϕ) by $\rho_0 = dn_{ch}/2\pi d\eta$, with the two-component spectrum model (first line) [120]

$$\begin{aligned} \frac{2}{n_{part}}\,\rho_0(b) &= S_{NN} + \nu\, H_{AA}(b) \\ &\approx \rho_{pp}\,\{1 + x\,(\nu - 1)\}\,, \end{aligned} \tag{9.5}$$

where S_{NN} is the soft component, by hypothesis independent of Au-Au centrality, and

$H_{AA}(b)$ is the hard component. Eq. (9.5) (second line) is an alternative two-component model proposed in Ref. [120]. Parameter x represents the (fixed) hard-component fraction of particle production. The 2D charged-particle density for $\sqrt{s_{NN}} = 200$ GeV NSD p-p (N-N) collisions is assumed in this analysis to be $\rho_{pp} = 2.5/2\pi \approx 0.4$. The alternative (KN) model is further discussed in Ref. [168].

To convert jet-correlated pairs to single-particle fragment yields we must factorize the pair distribution. The first step is to average the SS 2D peak over the angular acceptance to obtain 4D density $J^2(b) = \rho_0^2(b)\, j^2(b)$. Schematically,

$$\frac{\Delta\rho}{\rho_{ref}}(\eta_\Delta, \phi_\Delta, b) \stackrel{\text{model fit}}{\rightarrow} j^2(\eta_\Delta, \phi_\Delta, b) \stackrel{\text{average}}{\rightarrow} j^2(b). \tag{9.6}$$

Combining measured pair ratio $j^2(b)$ with measured single-particle 2D angular density $\rho_0(b)$ we obtain the mean two-particle 4D angular density of fragment pairs

$$J^2(b) \;=\; n_j(b) \left(\frac{n_{ch,j}}{2\pi\Delta\eta}\right)^2, \tag{9.7}$$

where $n_j(b)$ is the pQCD calculated per-event jet number in acceptance $\Delta\eta$, and $n_{ch,j}(b)$ is the inferred jet fragment multiplicity. That expression represents the hypothesis that the SS 2D peak includes all intrajet correlated pairs.

Eq. (9.7) leads to a factorization assumption: The mean number of correlated hadron pairs in a jet is approximately the square of the mean jet fragment multiplicity (significant fluctuation effects are discussed in Ref. [168]. Given jet-number hypothesis $n_j(b)$ within acceptance $\Delta\eta$ the 2D fragment density on (η, ϕ) is then

$$\begin{aligned} J(b) &\equiv n_j(b)\sqrt{J^2(b)/n_j(b)} \\ &= n_j(b)\,\rho_0(b)\sqrt{j^2(b)/n_j(b)} \\ &= n_j(b)\,\frac{n_{ch,j}(b)}{2\pi\Delta\eta}. \end{aligned} \tag{9.8}$$

$J(b)$ is the 2D angular density of parton fragments within the acceptance inferred from jet angular correlations. Note that $J^2(b) \neq [J(b)]^2$. The relation between measured two-particle and inferred single-particle angular densities in Eq. (9.8) is based on a jet hypothesis.

Jet correlations are related through $J(b)$ to spectrum hard component $H_{AA}(b)$ by

$$\left(\frac{2\pi}{n_{bin}}\right) J(b) \;=\; f(b)\, n_{ch,j}(b) = \frac{dn_h}{d\eta} \equiv 2\pi H_{AA}(b), \tag{9.9}$$

where $f(b) \equiv (1/n_{bin})\, dn_j(b)/d\eta$ is the calculated jet frequency defined in Ref. [24] for NSD p-p (N-N) collisions, and $dn_h/d\eta$ is the hard-component multiplicity density on η (see Sec. 9.4.7). Equation (9.8) (third line) is consistent with Eq. (9) of Ref. [161]. Combined with Eq. (9.9) it relates measured jet angular correlations directly to hard-component yield $H_{AA}(b)$ {integral of spectrum hard component $H_{AA}(y_t, b)$ [159]} assuming that H_{AA} represents a jet fragment density [161].

There are two acceptance issues for jets: (i) fragment losses from jets at η acceptance boundaries and (ii) the number of jets per dijet (fraction of jets with a partner) within η acceptance $\Delta\eta$. The first depends on jet size relative to η acceptance ($\sigma_\eta/\Delta\eta$), the second on fractional η acceptance relative to 4π ($\Delta\eta/\Delta\eta_{4\pi}$), where $\Delta\eta_{4\pi}$ is defined by $n_{j,tot} = \Delta\eta_{4\pi} \times dn_j/d\eta(\eta = 0)$. Jet fragment multiplicities $n_{ch,j}$ are reduced from a pQCD ideal [168]. The reduced multiplicity is then assumed to be point-like at the jet (parton) location on (η, ϕ). Ideal (4π) values are indicated in relevant plots. The number of jets per dijet which appear in acceptance $\Delta\eta$ is denoted by $\epsilon_j \in [1, 2]$ (see Sec. 9.4.3).

9.4.3 Jet angular correlations

Figure 9.8 (first two panels) shows smooth parametrizations of data for the SS 2D peak amplitude, η and ϕ widths from $\sqrt{s_{NN}} = 200$ GeV Au-Au collisions. The data are described to a few percent except for the interval $\nu > 5$ where A_{2D} and σ_η data typically fall below the parametrizations. The systematic uncertainty in A_{2D} and σ_η in that interval increases to 10%.

Figure 9.8 (third panel) shows the angle-averaged SS peak pair yield (solid curve) in the form $\rho_0(b)\, j^2(b)$ for pairs within the angular acceptance and the yield extrapolated to 4π (dashed curve). Angle average $j^2(b)$ is defined in terms of SS peak parameters. The dash-dotted curve is the GLS reference. The difference between the 4π and $(\Delta\eta = 2, 2\pi)$ curves is large for this pair measure because the pair acceptance depends on the square of the relative η acceptance $\Delta\eta/\Delta\eta_{4\pi}$. The curve labeled 4π is related to the SS 2D peak "volume" V in Ref. [84] by $V/2\pi\Delta\eta = V/4\pi$, where $\Delta\eta = 2$.

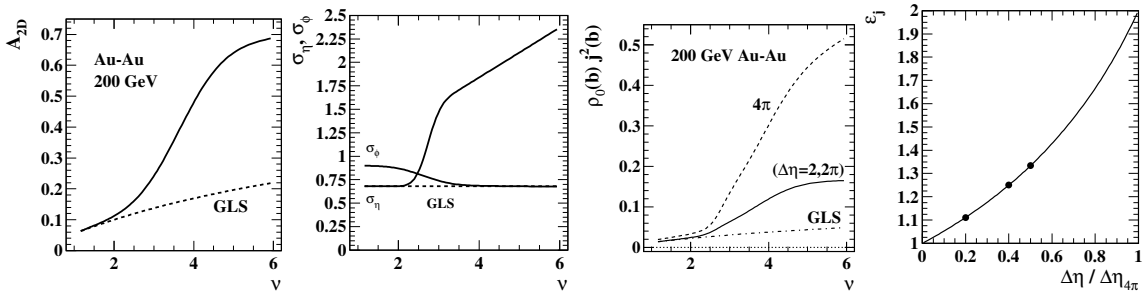

Figure 9.8: Fit parameters versus centrality measure ν for the same-side 2D peak in correlation data on $(\eta_\Delta, \phi_\Delta)$ from Au-Au collisions at $\sqrt{s_{NN}} = 200$ GeV [84]. First panel: The same-side 2D Gaussian amplitude. Second panel: The 2D peak rms widths. Third panel: The product of single-particle 2D angular density $\rho_0(b)$ and angle-averaged pair ratio $j^2(b)$ representing the same-side 2D peak in jet angular correlations. Fourth panel: The number of jets per dijet ϵ_j within acceptance $\Delta\eta$ as a function of the η acceptance relative to an effective 4π acceptance.

9.4.4 Jet Properties from Correlations

We combine measured jet correlations in the form $j^2(b)$ with a pQCD estimate of jet production to determine jet frequency $f(b)$ and mean jet multiplicity $n_{ch,j}(b)$. By removing n_{bin} from jet systematics in A-A collisions we obtain two slowly-varying factors which can be studied in detail.

A parton fragment distribution (FD) on rapidity y can be defined for individual NSD N-N collisions by the pQCD folding integral [161]

$$\begin{aligned}
\frac{d^2n_h}{dy\,d\eta} &= \frac{\epsilon_j(\Delta\eta)/2}{\sigma_{NSD}\,\Delta\eta_{4\pi}} \int_0^\infty dy_{max}\, D_{\rm xx}(y, y_{max}, b)\, \frac{d\sigma_{dijet}}{dy_{max}} \\
&= \frac{f(b)}{2\sigma_{dijet}} \int_0^\infty dy_{max}\, D_{\rm xx}(y, y_{max}, b)\, \frac{d\sigma_{dijet}}{dy_{max}} \\
&= f(b)\, D_{\rm xx}(y, b)/2 = \frac{2\pi}{n_{bin}} J(y, b). \qquad (9.10)
\end{aligned}$$

$D_{xx}(y, y_{max}, b)$ is an FF ensemble from collision system xx which may therefore include "in-medium" modifications in p-p collisions or in Au-Au depending on centrality b. $d\sigma_{dijet}/dy_{max}$ is the pQCD dijet spectrum on parton rapidity $y_{max} = \ln(2E_{jet}/m_\pi)$. The FD shape is ensemble-mean FF $D_{\rm xx}(y, b)$. Below fragment momentum 2 GeV/c the FD is dominated by the FF of 3 GeV jets. $\epsilon_j(\Delta\eta) \in [1, 2]$ measures the mean number of jets per

dijet in acceptance $\Delta\eta$ (assuming point-like jets). $\Delta\eta_{4\pi}$ is the effective 4π η acceptance. Relating pQCD FDs to measured spectrum hard components provides constraints on parton spectrum parameters: the exponent of the power law and the effective spectrum cutoff energy which determines dijet total cross section $\sigma_{dijet}(b)$.

The integral of $D_{xx}(y, y_{max})$ over fragment rapidity y is dijet fragment multiplicity $2n_{ch,j}(y_{max})$. Integrating both sides of Eq. (9.10) over fragment rapidity gives the per-participant-pair fragment angular density on η

$$\begin{aligned} \frac{dn_h}{d\eta} &= \frac{\epsilon_j(\Delta\eta)}{\sigma_{NSD}\,\Delta\eta_{4\pi}} \int_0^\infty dy_{max}\, n_{ch,j}(y_{max})\, \frac{d\sigma_{dijet}}{dy_{max}} \\ &= f(b)\, n_{ch,j}(b) = \frac{2\pi}{n_{bin}} J(b), \end{aligned} \tag{9.11}$$

where $n_{ch,j}$ is the per-jet fragment multiplicity averaged over the minimum-bias parton spectrum, effectively the fragment multiplicity for partons near the 3 GeV spectrum cutoff. Eq. (9.9) was used to obtain the second line. The jet properties in Eq. (9.11)—minimum-bias jet frequency $f(b)$ and mean jet fragment multiplicity $n_{ch,j}(b)$—relate jet angular correlations to spectrum hard components and pQCD fragment distributions [161].

9.4.5 Jet frequency from pQCD

Jet frequency $f(b)$ is defined via Eq. (9.11) by

$$\begin{aligned} f(b) &\equiv \frac{1}{n_{bin}(b)} \frac{dn_j(b)}{d\eta} \\ &= \frac{\epsilon_j(b)\,\sigma_{dijet}(b)}{\sigma_{NSD}\Delta\eta_{4\pi}(b)}, \end{aligned} \tag{9.12}$$

where $\sigma_{NSD} = 36.5$ mb is the total cross section for non-single-diffractive (NSD) N-N collisions [47], and n_{bin} is the mean number of N-N binary collisions per Au-Au collision. The $f(b)$ estimate is constrained by comparisons between pQCD FD calculations and measured HCs [161]. $\sigma_{dijet}(b)$ is determined by the parton spectrum cutoff inferred from hadron spectrum hard components.

In Fig. 9.8 (last panel) the number of jets per dijet within acceptance $\Delta\eta$ is $\epsilon_j(\Delta\eta) = 1/(1 - a/2)$, with fractional η acceptance $a = \Delta\eta/\Delta\eta_{4\pi}$ [161]. The points correspond to $a = 1/5, 2/5, 2/4$, three cases relevant to this analysis. The first two cases are for 200 GeV

p-p collisions with $\Delta\eta = 1, 2$, the last for central Au-Au collisions with $\Delta\eta = 2$ and $\Delta\eta_{4\pi}$ reduced by 20% (e.g. from a shift in projectile-nucleon parton distributions).

In Fig. 9.9 (first panel) the solid curve describes the estimated centrality variation of jet frequency $f(b)$ for 200 GeV Au-Au collisions in acceptance $\Delta\eta = 2$. The single data point is from Ref. [24], where an analysis of p_t spectra from 200 GeV NSD p-p collisions within $\Delta\eta = 1$ invoked Eq. (9.11) (second line) with $H_{AA} = dn_h/2\pi d\eta$ and an estimate of $n_{ch,j} = 2.5$ for $E_{jet} \sim 4$ GeV from Ref. [35] to determine $f_{pp} = (dn_h/d\eta)/n_{ch,j} = 0.03/2.5 = 0.012 \pm 0.004$. The pQCD prediction for $f(b)$ from Eq. (9.12) for p-p collisions within $\Delta\eta = 1$ is

$$\begin{aligned} f_{pp} &= \frac{1.1 \times 2.5 \text{ mb}}{36.5 \text{ mb} \times 5} \\ &\approx 0.015 \pm 0.0025, \end{aligned} \tag{9.13}$$

consistent with Ref. [24] and represented by the lower hatched band. For increased acceptance $\Delta\eta = 2$ $\epsilon_j \to 1.26$ from 1.1, so $f_{pp} \to 0.0175$ which fixes the left end of the solid curve, with 15% uncertainty.

In more-central Au-Au collisions a 1.6-fold increase in the dijet cross section relative to p-p is inferred from comparisons of FDs to measured spectrum hard-component shapes [161]. Retaining the effective 4π jet acceptance on η assumed for p-p collisions the f(b) value is therefore

$$\begin{aligned} f_{\text{Au-Au}}(b = 0) &= \frac{1.26 \times 4 \text{ mb}}{36.5 \text{ mb} \times 5} \\ &\approx 0.028 \pm 0.0045. \end{aligned} \tag{9.14}$$

If $\Delta\eta_{4\pi}(b)$ were to decrease by 20% in central Au-Au collisions then ϵ_j increases to 1.35 and $f_{\text{Au-Au}}(b{=}0) \to 0.037$. The two values establish limits on the estimated $f(b)$ for central Au-Au collisions. The combined uncertainty for more-central collisions is then $\pm 20\%$. The transition from the p-p estimate to the range of values for more-central Au-Au collisions is assumed to be step-like based on observed sharp transitions in the p_t spectrum hard component [159] and jet angular correlations [84]. The transition begins near $\nu = 2.5$ and ends near $\nu = 3.5$. See also Fig. 9.8 (second panel).

Figure 9.9 (second panel) shows the number of jets $n_j(b) = n_{bin}\, \Delta\eta\, f(b)$ within $\Delta\eta = 2$ for 200 GeV Au-Au collisions (solid curve) and the corresponding GLS reference (dashed

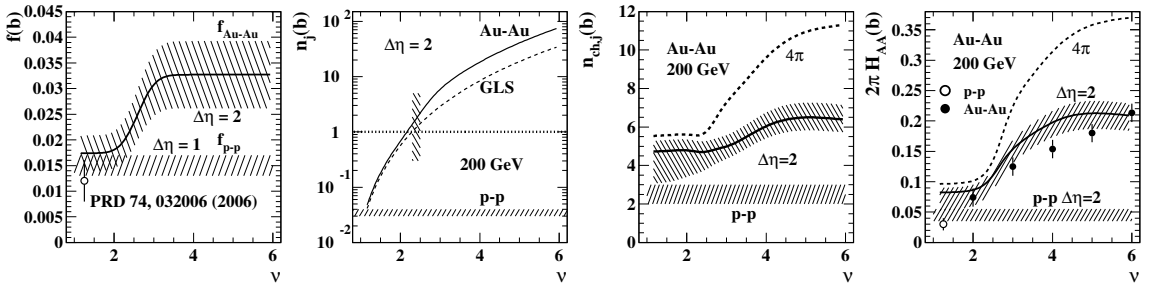

Figure 9.9: First panel: Jet frequency $f(b) = (1/n_{bin})\, dn_j/d\eta$ vs centrality parameter ν for $\sqrt{s_{NN}} = 200$ GeV Au-Au collisions (upper hatched band) and for NSD p-p collisions (open circle [24], lower hatched band). Second panel: Corresponding total jet number $n_j(b)$ in angular acceptance $\Delta\eta = 2$. Third panel: Mean jet fragment multiplicity $n_{ch,j}(b)$ vs centrality parameter ν for $\sqrt{s_{NN}} = 200$ GeV Au-Au collisions (upper hatched band) and p-p collisions (lower hatched band). Fourth panel: Spectrum hard-component yield $2\pi\, H_{AA}(b)$ vs ν inferred from two-particle jet correlations (solid curve) and from single-particle spectra (solid points) [159]. The lower hatched band and open point represent the hard-component yield obtained from NSD p-p collisions [24].

curve) representing binary-collision scaling of p-p (N-N) collisions. The lower hatched band represents the value for p-p collisions. It is notable that deviations of jet properties from the GLS reference become significant where the jet number per unit η becomes substantially greater than unity (upper hatched region) near $\nu \sim 2.5$, the location of the sharp transition in spectrum hard components and jet angular correlations.

9.4.6 Fragment multiplicity from angular correlations

We can now combine estimated jet frequencies with measured jet angular correlations to predict mean jet fragment multiplicities. The minimum-bias fragment multiplicity is obtained by introducing the $n_j(b)$ hypothesis into Eq. (9.7) to obtain

$$\begin{aligned} n_j(b)\, n_{ch,j}^2(b) &= (2\pi\Delta\eta)^2\, J^2(b) \\ &= n_{ch}^2(b)\, j^2(b) \quad \text{fragment pairs} \\ n_{ch,j}(b) &= n_{ch}(b)\, \sqrt{j^2(b)/n_j(b)}, \end{aligned} \tag{9.15}$$

where $n_{ch}(b) = 2\pi\Delta\eta\, \rho_0(b)$ (charged multiplicity in the angular acceptance) and $j^2(b)$ are measured quantities.

Figure 9.9 (third panel) shows rms jet multiplicity $n_{ch,j}(b)$ inferred from Eq. (9.15) (third line) as a function of Au-Au centrality. The solid curve is the result within 2D angular acceptance $(\Delta\eta, \Delta\phi) = (2, 2\pi)$ including edge losses. The dashed curve is the result for a 4π acceptance with 100% jet fragment efficiency.

While the detected jet fragment multiplicity for more-central Au-Au collisions is reasonably well determined, that for peripheral collisions appears to be overestimated when compared to single-particle results [161]. From p-p spectrum hard-component measurements and from $e^{=}$-e^{-} and p-$\bar{\text{p}}$ FF systematics we expect a mean p-p jet fragment multiplicity of 2-3 [35, 24, 165]. For minimum jet energy 3 GeV and mean fragment multiplicity 2-3 we obtain a most-probable fragment momentum $\sim$ 1.2 GeV/c, consistent with observations [24]. $n_{ch,j} \sim$ 4-5 from jet correlations suggests a significant contribution to $j^2(b)$ from fluctuations, as discussed in Ref. [168].

9.4.7 Jet fragment angular density

We now combine jet properties inferred from angular correlations to predict jet fragment densities which can be compared with measured spectrum hard components.

Differential hard component $H_{AA}(y_t, b)$ represents the mean parton fragment spectrum per N-N binary collision within an A-A collision. For A-A transparency (GLS reference) $H_{AA}(b) = H_{NN}$ independent of centrality. H_{AA} has been obtained from measured spectra by a subtraction procedure [24, 159] and compared quantitatively to pQCD fragment distributions [161]. *Integral* hard component $H_{AA}(b)$ represents by hypothesis the angular density of large-angle-scattered-parton fragments within an acceptance. In the present analysis we can infer $H_{AA}(b)$ from jet angular correlations by

$$\begin{aligned} 2\pi H_{AA}(b) &= f(b)\, n_{ch,j}(b) \\ H_{AA}(b) &= \frac{1}{n_{bin}}\, \rho_0(b)\, \sqrt{n_j(b)\, j^2(b)}, \end{aligned} \tag{9.16}$$

where the second line follows from Eq. (9.15).

Figure 9.9 (fourth panel) shows $2\pi H_{AA}(b)$ obtained from jet angular correlations for limited η acceptance and jet edge losses (solid curve) and for 4π acceptance with 100%-efficient fragment detection (dashed curve). The p-p datum (open circle) was inferred from

spectrum data with $\Delta\eta = 1$ [24]. The value $2\pi H_{pp} = 2.5 \times 0.012 = 0.03$ was based on a naïve Gaussian model for $H_{pp}(y_t)$ without exponential tail. For $\Delta\eta = 2$ and a more accurate model function we obtain

$$2\pi\, H_{AA}(b) \;\approx\; 2.5 \times 0.018 = 0.045, \tag{9.17}$$

defining a revised GLS reference with uncertainty marked by the lower hatched band.

The Au-Au data (solid points) are derived from the "total hadrons" data in Fig. 15 (left panel) of Ref. [159]. The consistency between jet correlations and spectrum hard components is good, except for peripheral A-A collisions where there may be a significant fluctuation contribution to jet correlations, as discussed in App. C of Ref. [168]. A factor 4-5 increase in H_{AA} with Au-Au centrality is suggested by spectrum and minimum-bias jet correlation data.

Multiplying Eq. (9.16) through by $\nu/2\pi$ or ν gives

$$\begin{aligned} \nu H_{AA}(b) &= \frac{2}{n_{part}}\, n_{ch,j} \frac{dn_j}{2\pi d\eta} \\ &= \frac{2}{n_{part}} \rho_0(b) \sqrt{n_j(b)\, j^2(b)}. \end{aligned} \tag{9.18}$$

$\nu H_{AA}(b)$ is the total hard component of the two-component spectrum model in Eq. (9.5) (first line). Figure 9.10 (left panel) shows the two-component particle yield $S_{NN} + \nu H_{AA}(b)$ predicted by measured jet angular correlations (bold solid curve). Soft component S_{NN} is by hypothesis fixed at ≈ 0.4 [2D density on (η, ϕ)] for all centralities. The solid points are the "total hadrons" data in Fig. 15 (left panel) of Ref. [159] divided by 2π. The dash-dotted line is the Kharzeev-Nardi (KN) approximation to per-participant charged-hadron 2D density $(2/n_{part})\rho_0(b)$ assumed for this analysis [120]. νH_{AA} increases by a factor $6\times$(4-5) = 25-30 relative to the hard component in p-p collisions.

Figure 9.10 (right panel) shows 2D angular density $\rho_0(b)$ on (η, ϕ). The solid curve is KN model $\rho_0(b) = (n_{part}/2)\rho_{pp}\,[1 + x(\nu - 1)]$ with $\rho_{pp} = 0.4$ and fixed $x = 0.09$ for Au-Au at 200 GeV [120]. The KN model describes minimum-bias data in more-central collisions but fails in more-peripheral collisions where corrected yield data are sparse. For more-peripheral collisions we expect a GLS trend extrapolated from p-p collisions with $x \sim$ 0.018-0.035

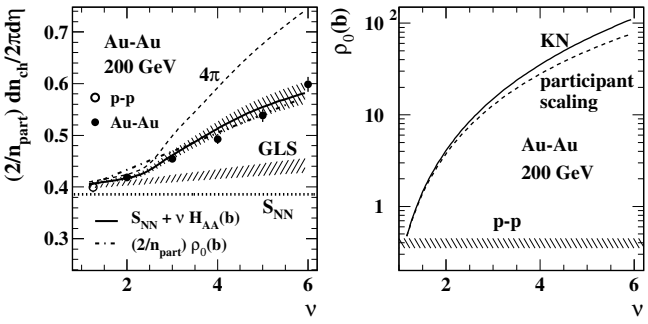

Figure 9.10: Left: The per-participant-pair total hadron angular density $(2/n_{part})\,\rho_0(b)$ derived from two-particle jet correlations (solid curve) and from spectrum data (open [24] and solid [159] points). Note the suppressed zero. The lower hatched band represents a Glauber linear superposition (GLS) reference. Right: The corresponding Kharzeev-Nardi (KN) two-component model (solid curve) for the single-particle angular density (dash-dotted line in the left panel).

(lower hatched band in the left panel). The sharp transition in jet angular correlations near $\nu = 2.5$ explains the large change in KN parameter x.

According to Eq. (9.18) (second line) the *fractional hard component*

$$F \equiv \nu\, H_{AA}/\{(2/n_{part})\,\rho_0\} \approx 0.3, \tag{9.19}$$

from spectrum analysis of central Au-Au collisions [159]. It can also be obtained from angular correlations via $\sqrt{n_j(b)\,j^2(b)}$. (F is the same quantity defined in Ref. [120].) The first factor in the radicand is obtained from pQCD (relative systematic uncertainty $< 20\%$). The second factor is from measured jet angular correlations (relative uncertainty small). For central Au-Au collisions we obtain $\rho_0\, j^2 \sim 0.165$, $\rho_0 \sim 110$ and $n_j \sim 70$, leading to $F = 0.32$. That result is consistent with the analysis in Ref. [120], but in this case inferred directly from jet correlations.

We conclude that the observed increase in particle production beyond participant scaling in central Au-Au collisions is fully explained in terms of jet angular correlations. Combining angular correlation measurements and a pQCD estimate of jet number we find that *one third of the final state* in 200 GeV central Au-Au collisions is associated with *resolved jet correlations* (relative uncertainty $< 10\%$).

9.4.8 Systematic uncertainties

Systematic uncertainties for jet-related particle production have different trends below and above the "sharp transition" in jet characteristics near $\nu = 2.5$. The primary data source for this SS peak analysis is pair ratio $j^2(b)$ derived from fits to the same-side 2D peak and averaged over the angular acceptance. The numerical uncertainty in the underlying 2D histograms is negligible compared to other uncertainties in the analysis. Derivation of $j^2(b)$ from 2D histograms involves model fits which, for the same-side 2D peak, have uncertainties of order 5% since the 2D peak is a dominant correlation structure.

Uncertainty in mean event-wise jet number $n_j(b) \leftrightarrow f(b)$ is substantial due to uncertainty in $\sigma_{dijet}(b)$ and $\Delta\eta_{4\pi}$, as shown in Fig. 9.9 (left panel). $\sigma_{dijet}(b)$ depends on comparisons between calculated pQCD fragment distributions and spectrum hard components in p-p and Au-Au collisions, specifically the location of the mode of the hard component on y_t [161]. For p-p collisions the cross-section estimate was 2.5±0.6 mb, or a 25% relative uncertainty. Evolution of the spectrum hard component with centrality led to inference of a 4±1 mb cross section in central Au-Au due to a 10% downward shift of the effective cutoff energy [161]. We also include the possibility that the effective 4π η acceptance may be reduced in more-central Au-Au collisions due to "slowing" of the projectile, but this is very speculative. The uncertainties are summarized by the hatched regions in Fig. 9.9 (left panel).

Uncertainties in mean jet fragment multiplicity $n_{ch,j}(b)$ are indicated by the hatched regions in Fig. 9.9 (third panel). The upper hatched region describes the multiplicity estimate derived from angular correlations assuming pair factorization. Uncertainties for more-central A-A collisions are dominated by the 20% contribution from the jet frequency. However, the square root reduces the relative uncertainty to approximately 10%. In more-peripheral collisions possible fluctuation contributions to $j^2(b)$ substantially increase the uncertainty in $n_{ch,j}(b)$ (see App. C of Ref. [168]). However, information from elementary collisions can be invoked to supplement the multiplicity estimate there. The lower hatched region describes a fragment multiplicity estimate based on measured fragmentation functions and their uncertainties.

Jet fragment yields can be estimated by $2\pi\, H_{AA}(b) = f(b)\, n_{ch,j}(b)$. However, because

the uncertainties in the factors are strongly correlated they do not add quadratically. In fact, the relative uncertainties in $H_{AA}(b)$ and $n_{ch,j}(b)$ are the same, since $n_{ch,j}(b) \propto \sqrt{j^2(b)/n_j(b)}$ and $H_{AA} \propto \sqrt{j^2(b)\, n_j(b)}$. Factors $n_{ch}(b)$ and Glauber parameters omitted in that comparison have relatively small uncertainties. The factors in the radicands have independent uncertainties, with the 20% for n_j dominating. Because of the square root the relative uncertainty in both quantities is $\pm 10\%$ for more-central collisions. For peripheral collisions the uncertainty increases because of the fluctuation contribution.

The per-participant-pair total charged-particle yield in the two-component model is $(2/n_{part})\, \rho_0(b) = S_{NN} + \nu H_{AA}(b)$. The relative uncertainty in the *total* hadron yield as inferred from jet correlations is significant for central collisions but negligible for peripheral collisions, since νH_{AA} increases by a factor 30 with centrality.

9.4.9 pQCD jets and low-p_t structure

The direct comparison in Figs. 9.9 (fourth panel) and 9.10 (left panel) between previously-measured spectrum hard components and comparable data inferred from a jet-like feature in angular correlations (present analysis) seems to provide substantial additional support for a minimum-bias jet interpretation. Thus, we find that independent procedures based on a jet hypothesis agree within estimated uncertainties and with a pQCD calculation.

According to pQCD theory jets (correlated hadron fragments of scattered partons) should contribute significant structure in both correlations and single-particle spectra. Jets should appear in spectra as a hard-component contribution over some p_t interval. Jets should also appear as a same-side 2D peak and away-side ridge in combinatoric two-particle correlations. But, how far down in p_t does "true" jet structure extend? Is a jet description valid for minimum-bias jets with energy peaked near 3 GeV and fragments with $p_t \approx 1$ GeV/c?

Phenomenologically, spectrum hard component H_{AA} is defined for more-peripheral A-A collisions in the two-component model as the part of the spectrum that scales as n_{bin}, or as ν relative to $n_{part}/2$ (participant scaling) [159]. That definition emerged from a physical-model-independent analysis of p-p collisions [24]. Later comparisons to pQCD calculations

lent support to a jet fragment interpretation down to ~ 0.3 GeV/c [161].

In the present study jet-like structure in p_t-integral two-particle correlations [84] is compared with $H_{AA}(y_t, b)$ from spectra integrated to obtain yields $H_{AA}(b)$ [159]. The detailed analysis assumes a jet mechanism for correlation structure and the validity of pQCD applied to that structure. The agreement is remarkable. Since the mode of jet-correlated particles is equivalent to $p_t = 1$ GeV/c [138, 139] we conclude that true jet correlations must extend significantly below 1 GeV/c. The quantitative agreement of spectrum structure, correlation structure and pQCD calculations supports a consistent minimum-bias jet picture: Correlated fragments from minimum-bias partons (~ 3 GeV) play a major role in all RHIC collisions for hadron momenta down to about 0.3 GeV/c.

References [162, 163] provide several examples of the consequences of format choices. Some conventional plotting formats effectively minimize manifestations of parton fragmentation. A comparison between Fig. 9.10 (left panel) and Fig. 9.9 (fourth panel) provides an illustration.

In Fig. 9.10 (left panel) both spectrum data (points) and correlations (solid curve) seem to be consistent with the linear KN model (dash-dotted line). Even with the substantial plot offset it is difficult to see any effect of the sharp transition, and it could be argued from that plot that there is none.

In Fig. 9.9 (fourth panel) the more differential format clearly shows significant deviations, since the KN model in that format would correspond to a constant value proportional to the fixed KN x parameter (see App. D of Ref. [168]). Correlation and spectrum data provide clear evidence for a sharp transition in jet characteristics as the rapid increase to the right of $\nu = 2.5$ in data points (spectra) and solid curve (correlations) relative to the GLS extrapolation $2\pi H_{AA} = 0.045$.

Comparing the structure in Fig. 9.8 and the examples above we observe a progression of reduced sensitivity to jet properties from correlated pairs (transition dominating) to differential hard-component particle yields (transition clearly apparent) to total hadron yields (transition effectively concealed).

Factorization of minimum-bias jet correlations provides new access to pQCD processes at low parton energies and fragment momenta where most of the fragment yield appears in

nuclear collisions. The SS 2D peak, interpreted in terms of minimum-bias jets, is quantitatively connected to pQCD through pair factorization and the spectrum hard component. The connection persists down to parton energy 3 GeV and hadron momentum zero.

Jet fragment yield $n_{ch,j}(b)$ is effectively the fragment multiplicity of 3 GeV jets because of the parton power-law spectrum cutoff. Fragment yields inferred from correlations can be compared with 3 GeV multiplicities extrapolated from e^+e^- FFs in Chapter 8 and from p-$\bar{\text{p}}$ jets [161], with and without proposed medium-modification effects.

Inferred jet frequency $n_j(b)$ is of central importance to RHIC physics. It describes the number of jets that appear as correlated fragments in the final state, integrated over the entire parton spectrum and some η acceptance $\Delta\eta$. Minimum-bias correlation data establish a constraint on $n_j(b)$ that agrees with the spectrum hard-component analysis. Those results imply that essentially all initial-state large-angle-scattered partons down to 3 GeV observed in p-p collisions also survive to the final state in central Au-Au collisions (scaled per binary N-N collision) as resolved jet angular correlations.

Chapter 10

CONCLUSIONS

In Chapter 3 we explored the conflict which is central both to heavy-ion physics and this document: namely the dispute between the roles of the soft and hard components in nuclear collisions. The conventional interpretation of RHIC physics heavily emphasizes the soft component and claims that there is a locally-thermalized hydrodynamically expanding medium which is the dominant source of correlations in nuclear collisions. Studies of hard process exist of course, but are typically restricted to high-p_t triggered correlations and treated as an exception. We have found evidence that minijets appear to play a significant role in heavy-ion collisions. While these processes are not as "hard" as jets as described by pQCD theory we nevertheless find that they exist on a continuum with standard pQCD physics. Far from being an exception, minijets appear to dominate much of the physics of RHIC collisions.

10.1 Quadrupole

The azimuth anisotropy typically measured with v_2 is one of the most important observables in conventional flow theory. In Chapter 4 we described the conventional approaches for measuring v_2 and their limitations. We introduced a new approach using 2D two-particles correlations in Chapter 5 and extracted a quadrupole term from fits to those correlations that can be directly related to v_2. The nonjet quadrupole term can be distinguished from η-dependent "nonflow", which we argued in Chapter 9 is dominated by minijets. Several properties of the nonjet quadrupole itself seem to conflict with hydrodynamic expectations and suggest that it could be due to a novel QCD phenomenon.

In Chapter 6 we analyzed the quadrupole term of p_t-integrated two-particle correlation histograms over the complete centrality range of collisions at RHIC. Using the optical Glauber model of eccentricity we find that the trend $\Delta\rho[2]/\sqrt{\rho_{\rm ref}} \propto R(\sqrt{s_{NN}})n_{bin}(b)\epsilon^2_{\rm opt}(b)$

with $R(\sqrt{s_{NN}}) \propto \log(\sqrt{s_{NN}}/13 \text{ GeV})$ describes the data for all energies below $200GeV$ and Au-Au centralities. All p_t-integrated Au-Au azimuth quadrupole data from 13 to 200 GeV are represented by two initial-state parameters. This is in sharp contrast to the standard hydrodynamical expectation of an equation-of-state, for which we see no evidence.

The p_t-differential histograms in Chapter 7 exhibit simple trends on collision energy and centrality. The dependence on collisions energy and centrality can be factorized to produce a very accurate description of p_t-integrated data. We found that the low-p_t identified-particle data are inconsistent with transverse Hubble expansion. The p_t-dependent quadrupole component is used to construct a boosted quadrupole spectrum that is approximately centrality-independent and well described by a fixed boosted Lévy distribution. Quadrupole systematics reveal a system with remarkably simple scaling behavior and a possible factorization of the collision energy, centrality, and p_t dependence. This system seems to contradict typical hydrodynamic expectations in nuclear collisions. The observed energy scaling provides a prediction for the LHC.

Hydro interpretation of the azimuth quadrupole as representing "elliptic flow" may be questioned. Strong jet ("nonflow") contributions to published v_2 data have confused their interpretation [160]. When jet contributions are eliminated from v_2 by using 2D angular correlations systematic trends inconsistent with hydro are revealed [115]. We also see no evidence for large flow fluctuations. Reassessment of published v_2 data in a broader context suggests the possibility of an alternative interpretation in terms of novel QCD field phenomena [160, 158].

10.2 Minijets

A two-component spectra model describes proton-proton collisions well [24] but attempts to measure radial flow in heavy-ion collisions with identified-hadron spectra in the context of a two-component spectrum model failed [159]. Contrary to expectations all spectrum evolution with centrality was confined to a jet-related hard component. The spectrum hard component can be quantitatively related to pQCD calculations [161], supporting the conclusion that the hard component represents minimum-bias parton fragmentation. The correlations observed in proton-proton collisions can be clearly associated with hard processes

[138, 139]. In heavy-ion collisions we see that these structures are modified in a continuous fashion as a function of centrality. The two-component spectrum analysis strongly suggests that the fragmentation process is modified in heavy-ion collisions but jets are not "quenched" [159, 161].

To understand fragmentation functions better we analyzed e^+-e^- collisions. In Chapter 8 we described a simple phenomenological parametrization of fragmentation functions (FF) in e^+-e^- collisions that is accurate even at very low-Q^2. In Chapter 9 we describe a simple modification of this parametrization that is capable of accounting for RHIC data under the assumption that fragmentation is modified in mid to central collisions.

We have examined the variation of FFs with parton energy on conventional kinematic variables x_p and ξ_p, on rapidity y and on normalized rapidity u. We find that FFs plotted on rapidity y vary with energy in a nearly self-similar manner. FFs transformed to u are well described by the product of dijet multiplicity and a unit-normal form factor modeled by the beta distribution. The latter is determined by parameters (p, q) which exhibit modest linear variations within perturbative energy scale range $2E_{jet} = Q > 20$ GeV. The beta distribution shape, when combined with an energy-conservation sum rule, also determines dijet multiplicities. The factored representation on u thus provides a simple and compact representation of e^+-e^- FFs over a broad energy range and permits extrapolation to small energy scales.

The beta distribution model suggests that fragmentation of light partons (at larger energy scales) can be viewed as an entropy-maximizing equilibration process. In this analysis the energy dependence of fragmentation has been extrapolated down to a kinematic region not accessed by conventional methods. Such low-Q^2 extrapolation provides a phenomenological context for minijet-related two-particle correlations in p-p and A-A collisions at RHIC, forming a basis for theoretical treatments of in-medium dissipation of low-Q^2 partons and the subsequent hadronization process in heavy ion collisions. The observed fragment spectrum in heavy ion collisions can be related to modified fragmentation functions from elementary collisions [161].

The centrality dependence of the jet peak observed in 2D angular correlations in heavy-ion collisions at RHIC exhibits a remarkable transition in its amplitude and width on pseudo-

rapidity. The large η width of the SS peak—sometimes referred to as "the ridge"—remains one of the least understood phenomena in heavy-ion collisions. But the claim that the same-side peak is due to "triangular flow" caused by large flow fluctuations is not consistent with the data. There is also a "proton-proton" ridge claimed to be observed in CMS collisions with certain kinematic cuts but it is actually a manifestation of the quadrupole term [118, 167].

The amplitude and widths of the 2D jet peak can be used to derive parton fragment yields [168]. Minimum-bias jet (minijet) angular correlations have been converted to absolute parton fragment yields which are found to comprise approximately one third of the hadronic final state in 200 GeV central Au-Au collisions. Direct comparison of minijet correlations with previously-measured spectrum hard-component yields reveals good agreement within data uncertainties.

pQCD fragment distributions calculated by folding a minimum-bias parton energy spectrum with a parametrization of measured fragmentation functions accurately describe measured spectrum hard components. The combined results reveal that almost all large-angle-scattered partons down to 3 GeV parton energy survive as true jet manifestations in spectra and correlations, albeit with significant modification of fragmentation.

The large number of jets we observe in more-central heavy ion collisions and newly discovered quadrupole systematics seem to conflict with much of the conventional interpretation of RHIC collisions in terms of a dense partonic medium with small viscosity (perfect liquid). Large jet contributions to spectra and correlations quantitatively described by pQCD theory contradict claims of early thermalization by parton multiple scattering and formation of a strongly-coupled, small-viscosity QGP. We certainly observe significant modification of parton fragmentation, but the basic pQCD processes persist even in the most-central Au-Au collisions at RHIC.

10.3 Implications for RHIC

The claims in this document contradict much of the "standard" interpretation of heavy-ion physics. This should not be perceived as a rejection of the RHIC program or experiments. There is a huge quantity of quality data that has been recorded at RHIC, and this analysis

would not have been possible without it. The problem we address is strictly about the interpretation of those data. The study of QCD dynamics at RHIC competes with a strong emphasis on hydro models and possible QGP formation. The importance of fragmentation in RHIC collisions has become more apparent in several recent studies. The issue for A-A collisions is the major changes in parton scattering and fragmentation that occur at smaller p_t within larger A-A space-time volumes.

Hydro-motivated analysis of RHIC data tends to interpret the large parton fragment contribution below 2 GeV/c in terms of flow phenomena. pQCD descriptions are artificially restricted to small regions of momentum space (high p_t). The role of parton fragmentation is thereby minimized. Model-independent analysis of spectrum and correlation structure reveals new fragmentation features described quantitatively by pQCD over the full hadron momentum range [168].

A significant consequence of this analysis is the confirmation of less-direct indications that a substantial fraction of the final state in central Au-Au collisions consists of resolved jets with energies as low as 3 GeV [28, 84, 159, 161]. The evolution of nuclear collisions is apparently dominated by parton scattering and fragmentation even in the most central Au-Au collisions, albeit the fragmentation process may be strongly modified [75]. The evolution of nuclear collisions is apparently dominated by parton fragmentation even in the most central Au-Au collisions. Those results pose significant difficulties for the RHIC "perfect liquid" paradigm. Several examples follow.

Multiple scattering of partons and hadrons might lead to formation of thermalized partonic and/or hadronic media. However, in these studies we find no loss of initial scattered partons to thermalization, only redistribution of parton energy *within jets* during fragmentation. Strong jet correlations persist for low-energy partons and low-momentum hadrons, contradicting significant multiple scattering of either partons or hadrons. In particular, the same-side 2D peak *narrows* on azimuth, which is inconsistent with parton or hadron multiple scattering in a dense medium.

Parton multiple scattering might establish a dense thermalized medium (opaque core) which absorbs most partons. Any surviving jets would then be emitted from a "corona" region at the (radial) surface of the collision system. Imposition of high-p_t triggers would

bias toward "tangential emission" from the corona and unmodified jet pairs. However, focusing only on yield reductions in high-p_t bins (R_{AA} [31], "triggered" jet correlations [10]) to conclude parton absorption in a dense medium is misleading. Reduced fragment number at larger p_t should not be interpreted as a reduction in the *precursor-parton number*. The inference error may be large due to the steepness of the fragment spectrum arising from the underlying parton power-law spectrum. Final-state jet structure should be studied over the full hadron p_t acceptance to best understand parton precursors. The present analysis combined with other studies suggests that the number of *resolved* final-state jets per N-N collision *increases* with A-A centrality. Fragmentation is modified, with more fragments at smaller hadron momentum as the general trend.

It has been suggested that energetic partons passing through a dense medium might produce "Mach shocks" manifested as a distortion in the "away-side" jet. Distortions in background-subtracted data (azimuth double peak near π) are interpreted to imply formation of Mach shocks in the dense medium. However, all jets within the angular acceptance must appear in the *minimum-bias* same-side (SS) jet peak. Any deformation of "away-side" jets should then appear in the SS peak. But that is not observed. The "away-side" jet is a fiction. The away-side peak at π radians in minimum-bias angular correlations reflects *inter*jet correlations *between* jets, not a single "away-side" jet. Broadening of the away-side peak reflects acoplanarity of the parton partners (e.g. k_t broadening), not internal jet structure. Even the lowest-energy jets are not deformed azimuthally [84]. We conclude that the double-peaked structure attributed to Mach cones arises from biased v_2 data which may include a substantial jet contribution ("nonflow") [164]. Such double peaks do not appear in the great majority of unsubtracted or "raw" dihadron correlation data.

Scattered partons at energy scales of a few GeV might undergo multiple scattering to form a dense thermalized partonic medium. The large thermalized parton flux could then lead to large energy densities and pressure gradients which could drive hydrodynamic flows [107]. However, analysis of parton fragment yields [168] combined with two-component spectrum analysis [159] and direct comparisons of spectrum data with pQCD calculations [161] indicates that all initial-state large-angle-scattered partons appearing as jets in p-p collisions (down to a 3 GeV parton spectrum cutoff) also appear as resolved

jets in central Au-Au collisions. None of the expected pQCD parton spectrum is lost to thermalization. Partons do not contribute to large (thermal) energy densities or pressure gradients. These conclusions are consistent with failure to observe significant radial flow in differential spectrum analysis of 200 GeV Au-Au collisions with identified hadrons [159].

There are still many challenges that remain. Work is in progress to use the TOF detectors at STAR to do minimum-bias correlations with identified particles. Such an analysis should add another layer of understanding to correlation structures at RHIC. The mechanism behind the large-η_Δ "ridge" observations is still poorly understood. The details of the p_t-dependence of the same-side peak have not been fully explored and that could potentially provide new insights into this puzzle. Of course there are challenges for theorists as well. Some aspects of this work have focused on the importance of minijets at RHIC, but compared to high-p_t jets minijets are still poorly understood theoretically. The modification of fragmentation functions in more-central heavy-ion collisions as proposed in this dissertation is empirically driven, and a more rigorous theoretical understanding would be helpful. We have also presented a complete parametrization of nonjet quadrupole systematics that seems to contradict hydro theory. The nonjet quadrupole does not exhibit the transition observed in jet production and appears to be a distinct phenomenon but it could potentially be related to QCD field interactions driven by the initial collision geometry [160, 158]. We have only begun to scratch the surface of an exciting new aspect of QCD physics.

BIBLIOGRAPHY

[1] G. Abbiendi et al. Experimental properties of gluon and quark jets from a point source. *Eur. Phys. J.*, C11:217–238, 1999.

[2] G. Abbiendi et al. Particle multiplicity of unbiased gluon jets from e^+e^- three jet events. *Eur.Phys.J.*, C23:597–613, 2002. 34 pages, 9 figures, Submitted to Eur. Phys. J. C Report-no: CERN-EP-2001-076.

[3] G. Abbiendi et al. Experimental studies of unbiased gluon jets from e+ e- annihilations using the jet boost algorithm. *Phys. Rev.*, D69:032002, 2004.

[4] G. Abbiendi et al. Scaling violations of quark and gluon jet fragmentation functions in e+ e- annihilations at s**(1/2) = 91.2-GeV and 183-GeV - 209-GeV. *Eur. Phys. J.*, C37:25–47, 2004.

[5] J. Abele et al. The laser system for the STAR time projection chamber. *Nucl. Instrum. Meth.*, A499:692–702, 2003.

[6] B. I. Abelev et al. Mass, quark-number, and s(NN)**(1/2) dependence of the second and fourth flow harmonics in ultra-relativistic nucleus nucleus collisions. *Phys. Rev.*, C75:054906, 2007.

[7] B.I. Abelev et al. Identified baryon and meson distributions at large transverse momenta from Au+Au collisions at s(NN)**(1/2) = 200-GeV. *Phys.Rev.Lett.*, 97:152301, 2006.

[8] B.I. Abelev et al. Longitudinal double-spin asymmetry and cross section for inclusive jet production in polarized proton collisions at s**(1/2) = 200-GeV. *Phys.Rev.Lett.*, 97:252001, 2006.

[9] B.I. Abelev et al. Indications of Conical Emission of Charged Hadrons at RHIC. *Phys.Rev.Lett.*, 102:052302, 2009. 6 pages, 4 figures, 1 table.

[10] B.I. Abelev et al. Long range rapidity correlations and jet production in high energy nuclear collisions. *Phys.Rev.*, C80:064912, 2009.

[11] B.I. Abelev et al. Systematic Measurements of Identified Particle Spectra in pp, d^+ Au and Au+Au Collisions from STAR. *Phys.Rev.*, C79:034909, 2009. 60 pages, 46 figures, 37 tables.

[12] P. Abreu et al. Determination of alpha-s from the scaling violation in the fragmentation functions in e+ e- annihilation. *Phys. Lett.*, B311:408–424, 1993.

[13] P. Abreu et al. The Scale dependence of the hadron multiplicity in quark and gluon jets and a precise determination of C(A) / C(F). *Phys.Lett.*, B449:383–400, 1999.

[14] P. Abreu et al. Measurement of the gluon fragmentation function and a comparison of the scaling violation in gluon and quark jets. *Eur.Phys.J.*, C13:573–589, 2000.

[15] K. H. Ackermann et al. STAR detector overview. *Nucl. Instrum. Meth.*, A499:624–632, 2003.

[16] K. Ackerstaff et al. Multiplicity distributions of gluon and quark jets and tests of QCD analytic predictions. *Eur. Phys. J.*, C1:479–494, 1998.

[17] D. Acosta et al. Momentum distribution of charged particles in jets in dijet events in p anti-p collisions at s**(1/2) = 1.8-TeV and comparisons to perturbative QCD predictions. *Phys. Rev.*, D68:012003, 2003.

[18] D. Acosta et al. Measurement of charged particle multiplicities in gluon and quark jets in proton anti-proton collisions at s**(1/2) = 1.8-TeV. *Phys. Rev. Lett.*, 94:171802, 2005.

[19] P. D. Acton et al. A Study of two particle momentum correlations in hadronic Z0 decays. *Phys. Lett.*, B287:401–412, 1992.

[20] J. Adams et al. Transverse momentum and collision energy dependence of high p(T) hadron suppression in Au + Au collisions at ultrarelativistic energies. *Phys. Rev. Lett.*, 91:172302, 2003.

[21] J. Adams et al. Identified particle distributions in pp and Au+Au collisions at s(NN)**(1/2) = 200 GeV. *Phys.Rev.Lett.*, 92:112301, 2004.

[22] J. Adams et al. Azimuthal anisotropy in Au + Au collisions at s(NN)**(1/2) = 200-GeV. *Phys. Rev.*, C72:014904, 2005.

[23] J. Adams et al. Distributions of charged hadrons associated with high transverse momentum particles in pp and Au + Au collisions at s(NN)**(1/2) = 200-GeV. *Phys.Rev.Lett.*, 95:152301, 2005.

[24] J. Adams et al. The Multiplicity dependence of inclusive p(t) spectra from p-p collisions at s**(1/2) = 200-GeV. *Phys. Rev.*, D74:032006, 2006.

[25] J. Adams et al. The Energy dependence of p_t angular correlations inferred from mean-p(t) fluctuation scale dependence in heavy ion collisions at the SPS and RHIC. *J.Phys.G*, G34:451–466, 2007.

[26] John Adams et al. Experimental and theoretical challenges in the search for the quark gluon plasma: The STAR collaboration's critical assessment of the evidence from RHIC collisions. *Nucl. Phys.*, A757:102–183, 2005.

[27] John Adams et al. Hadronization geometry and charge-dependent number autocorrelations on axial momentum space in Au-Au collisions at s(NN)**(1/2) = 130-GeV. *Phys.Lett.*, B634:347–355, 2006.

[28] John Adams et al. Minijet deformation and charge-independent angular correlations on momentum subspace (eta, phi) in Au-Au collisions at s(NN)**(1/2) = 130-GeV. *Phys. Rev.*, C73:064907, 2006.

[29] John Adams et al. Transverse-momentum p(t) correlations on (eta,Phi) from mean-p(t) fluctuations in Au - Au collisions at s(NN)**(1/2) = 200-GeV. *J. Phys.*, G32:L37–L48, 2006.

[30] John Adams et al. Transverse momentum correlations and minijet dissipation in Au Au collisions at s(NN)**(1/2) = 130-GeV. *J. Phys.*, G34:799–816, 2007.

[31] C. Adler et al. Centrality dependence of high p(T) hadron suppression in Au+Au collisions at s**(NN)(1/2) = 130-GeV. *Phys. Rev. Lett.*, 89:202301, 2002.

[32] C. Adler et al. Elliptic flow from two- and four-particle correlations in Au + Au collisions at s(NN)**(1/2) = 130-GeV. *Phys. Rev.*, C66:034904, 2002.

[33] C. Adler et al. The STAR level-3 trigger system. *Nucl. Instrum. Meth.*, A499:778–791, 2003.

[34] C. Adloff et al. A measurement of the proton structure function F2(x,Q**2) at low x and low Q**2 at HERA. *Nucl. Phys.*, B497:3–30, 1997.

[35] T. Affolder et al. Charged particle multiplicity in jets in $p\bar{p}$ collisions at $\sqrt{s} = 1.8$ TeV. *Phys.Rev.Lett.*, 87:211804, 2001.

[36] T. Affolder et al. Charged jet evolution and the underlying event in proton - anti-proton collisions at 1.8-TeV. *Phys. Rev.*, D65:092002, 2002.

[37] G. Agakishiev et al. Anomalous centrality evolution of two-particle angular correlations from Au-Au collisions at $\sqrt{s_{\rm NN}} = 62$ and 200 GeV. *Phys.Rev.*, C86:064902, 2012.

[38] M. M. Aggarwal et al. Scaling of particle and transverse energy production in 208-Pb + 208-Pb collisions at 158-A-GeV. *Eur. Phys. J.*, C18:651–663, 2001.

[39] H. Aihara et al. Charged hadron inclusive cross-sections and fractions in e^+e^- annihiliation $\sqrt{s} = 29$ GeV. *Phys.Rev.Lett.*, 61:1263, 1988.

[40] M. Z. Akrawy et al. A Study of coherence of soft gluons in hadron jets. *Phys. Lett.*, B247:617–628, 1990.

[41] M.S. Alam et al. Shape studies of quark jets versus gluon jets at s**(1.2) = 10-GeV. *Phys.Rev.*, D46:4822–4827, 1992.

[42] M.S. Alam et al. Study of gluon versus quark fragmentation in $\Upsilon \to gg\gamma$ and $e^+e^- \to q\bar{q}\gamma$ events at s**(1/2) = 10-GeV. *Phys.Rev.*, D56:17–22, 1997.

[43] C. Albajar et al. Production of Low Transverse Energy Clusters in anti-p p Collisions at s**(1/2) = 0.2-TeV to 0.9-TeV and their Interpretation in Terms of QCD Jets. *Nucl. Phys.*, B309:405, 1988.

[44] S. Albino, B. A. Kniehl, G. Kramer, and W. Ochs. Resummation of Soft Gluon Logarithms in the DGLAP Evolution of Fragmentation Functions. *Phys. Rev.*, D73:054020, 2006.

[45] H. Albrecht et al. Inclusive Production of Charged Pions, Charged and Neutral Kaons and Anti-Protons in e+ e- Annihilation at 10-GeV and in Direct Upsilon Decays. *Z. Phys.*, C44:547, 1989.

[46] H. Albrecht et al. Inclusive production of D0, D+ and D*+ (2010) mesons in B decays and nonresonant e+ e- annihilation at 10.6-GeV. *Z. Phys.*, C52:353–360, 1991.

[47] G.J. Alner et al. Antiproton-proton cross sections at 200 and 900 GeV c.m. energy. *Z.Phys.*, C32:153–161, 1986.

[48] Guido Altarelli and G. Parisi. Asymptotic Freedom in Parton Language. *Nucl. Phys.*, B126:298, 1977.

[49] B. Alver et al. System size, energy, pseudorapidity, and centrality dependence of elliptic flow. *Phys. Rev. Lett.*, 98:242302, 2007.

[50] B. Alver et al. Event-by-Event Fluctuations of Azimuthal Particle Anisotropy in Au + Au Collisions at $\sqrt{s_{NN}} = 200$ GeV. *Phys.Rev.Lett.*, 104:142301, 2010.

[51] B. Alver and G. Roland. Collision geometry fluctuations and triangular flow in heavy-ion collisions. *Phys.Rev.*, C81:054905, 2010.

[52] M. Anderson et al. The STAR time projection chamber: A unique tool for studying high multiplicity events at RHIC. *Nucl. Instrum. Meth.*, A499:659–678, 2003.

[53] Bo Andersson, G. Gustafson, G. Ingelman, and T. Sjostrand. Parton Fragmentation and String Dynamics. *Phys. Rept.*, 97:31–145, 1983.

[54] Bo Andersson, G. Gustafson, and J. Samuelsson. Discrete QCD: A New approximation for QCD cascades. *Nucl.Phys.*, B463:217–237, 1996. Revised version.

[55] A. L. S. Angelis et al. A Measurement of the Transverse Momenta of Partons, and of Jet Fragmentation as a Function of s**(1/2) in p p Collisions. *Phys. Lett.*, B97:163, 1980.

[56] H. Appelshauser et al. Directed and elliptic flow in 158-GeV/nucleon Pb + Pb collisions. *Phys. Rev. Lett.*, 80:4136–4140, 1998.

[57] G. Arfken. *Mathematical Methods for Physicists*. Academic Press, third edition, 1985.

[58] G. Arnison et al. Hadronic Jet Production at the CERN Proton - anti-Proton Collider. *Phys.Lett.*, B132:214, 1983.

[59] Data assembled by W. Fischer. Run overview of the relativistic heavy ion collider. http://www.agsrhichome.bnl.gov/RHIC/Runs/.

[60] Yakov I. Azimov, Yuri L. Dokshitzer, Valery A. Khoze, and S. I. Troyan. Similarity of Parton and Hadron Spectra in QCD Jets. *Z. Phys.*, C27:65–72, 1985.

[61] Yakov I. Azimov, Yuri L. Dokshitzer, Valery A. Khoze, and S. I. Troyan. Humpbacked QCD Plateau in Hadron Spectra. *Zeit. Phys.*, C31:213, 1986.

[62] R. Baier, Alfred H. Mueller, D. Schiff, and D. T. Son. 'Bottom-up' thermalization in heavy ion collisions. *Phys. Lett.*, B502:51–58, 2001.

[63] J. Barrette et al. Energy and charged particle flow in 10.8-A-GeV/c Au + Au collisions. *Phys. Rev.*, C55:1420–1430, 1997.

[64] F. Becattini, M. Gazdzicki, and J. Sollfrank. On chemical equilibrium in nuclear collisions. *Eur. Phys. J.*, C5:143–153, 1998.

[65] F. Bergsma et al. The STAR detector magnet subsystem. *Nucl. Instrum. Meth.*, A499:633–639, 2003.

[66] Rajeev S. Bhalerao and Jean-Yves Ollitrault. Eccentricity fluctuations and elliptic flow at RHIC. *Phys. Lett.*, B641:260–264, 2006.

[67] R.S. Bhalerao, N. Borghini, and J.Y. Ollitrault. Analysis of anisotropic flow with Lee-Yang zeroes. *Nucl.Phys.*, A727:373–426, 2003. 32 pages, 7 eps figures, RevTeX Report-no: Saclay-T03/098,TIFR/TH/03-15.

[68] A. Bialas, M. Bleszynski, and W. Czyz. Multiplicity Distributions in Nucleus-Nucleus Collisions at High-Energies. *Nucl. Phys.*, B111:461, 1976.

[69] O. Biebel, P. Nason, and B. R. Webber. Jet fragmentation in e+ e- annihilation. 2001.

[70] J. P. Blaizot and Alfred H. Mueller. The Early Stage of Ultrarelativistic Heavy Ion Collisions. *Nucl. Phys.*, B289:847, 1987.

[71] N. Borghini and J. Y. Ollitrault. Azimuthally sensitive correlations in nucleus nucleus collisions. *Phys. Rev.*, C70:064905, 2004.

[72] Nicolas Borghini, Phuong Mai Dinh, and Jean-Yves Ollitrault. Are flow measurements at SPS reliable? *Phys.Rev.*, C62:034902, 2000.

[73] Nicolas Borghini, Phuong Mai Dinh, and Jean-Yves Ollitrault. Flow analysis from multiparticle azimuthal correlations. *Phys.Rev.*, C64:054901, 2001.

[74] Nicolas Borghini, Phuong Mai Dinh, and Jean-Yves Ollitrault. Thermalization and elliptic flow at RHIC. 2001.

[75] Nicolas Borghini and Urs Archim Wiedermann. Distorting the Hump-backed Plateau of Jets with Dense QCD Matter. 2005.

[76] D. Bortoletto et al. Charm Production in Nonresonant e+ e- Annihilations at s**(1/2) = 10.55-GeV. *Phys. Rev.*, D37:1719, 1988.

[77] P. Braun-Munzinger, I. Heppe, and J. Stachel. Chemical equilibration in Pb + Pb collisions at the SPS. *Phys. Lett.*, B465:15–20, 1999.

[78] W. Braunschweig et al. Global Jet Properties at 14-GeV to 44-GeV Center-of-Mass Energy in e+ e- Annihilation. *Z. Phys.*, C47:187–198, 1990.

[79] D. Buskulic et al. Inclusive pi+-, K+- and (p, anti-p) differential cross- sections at the Z resonance. *Z. Phys.*, C66:355–366, 1995.

[80] A. Capella, I.M. Dremin, J.W. Gary, V.A. Nechitailo, and J. Tran Thanh Van. Evolution of average multiplicities of quark and gluon jets. *Phys.Rev.*, D61:074009, 2000. 23 pages including 3 figures. Version 2 contains small correction to equation (41) Report-no: FIAN-TD22-99, LPT-9974, UCRHEP-E264.

[81] Fred Cooper and Graham Frye. Comment on the Single Particle Distribution in the Hydrodynamic and Statistical Thermodynamic Models of Multiparticle Production. *Phys. Rev.*, D10:186, 1974.

[82] Laszlo P. Csernai, Joseph.I. Kapusta, and Larry D. McLerran. On the Strongly-Interacting Low-Viscosity Matter Created in Relativistic Nuclear Collisions. *Phys.Rev.Lett.*, 97:152303, 2006.

[83] P. Danielewicz and G. Odyniec. Transverse Momentum Analysis of Collective Motion in Relativistic Nuclear Collisions. *Phys. Lett.*, B157:146–150, 1985.

[84] Michael Daugherity. Anomalous centrality variation of minijet angular correlations in Au-Au collisions at 62-GeV and 200-GeV from STAR. *J.Phys.G*, G35:104090, 2008.

[85] Yuri L. Dokshitzer. Calculation of the Structure Functions for Deep Inelastic Scattering and e+ e- Annihilation by Perturbation Theory in Quantum Chromodynamics. *Sov. Phys. JETP*, 46:641–653, 1977.

[86] Yuri L. Dokshitzer. QCD Phenomenology, Lectures at the International CERN-Dubna School, Pylos. 2002.

[87] Yuri L. Dokshitzer, Dmitri Diakonov, and S. I. Troian. Hard Processes in Quantum Chromodynamics. *Phys. Rept.*, 58:269–395, 1980.

[88] Yuri L. Dokshitzer, Victor S. Fadin, and Valery A. Khoze. Coherent Effects in the Perturbative QCD Parton Jets. *Phys. Lett.*, B115:242–246, 1982.

[89] I.M. Dremin and J.W. Gary. Energy dependence of mean multiplicities in gluon and quark jets at the next-to-next-to-next-to leading order. *Phys.Lett.*, B459:341–346, 1999.

[90] I.M. Dremin and J.W. Gary. Hadron multiplicities. *Phys.Rept.*, 349:301–393, 2001.

[91] Loyal Durand and Hong Pi. Semihard QCD and High-Energy p p and anti-p p Scattering. *Phys. Rev.*, D40:1436, 1989.

[92] Patrick Eden, Gosta Gustafson, and Valery A. Khoze. On particle multiplicity distribution in three jet events. *Eur.Phys.J.*, C11:345–350, 1999.

[93] C. P. Fong and B. R. Webber. One and two particle distributions at small x in QCD jets. *Nucl. Phys.*, B355:54–81, 1991.

[94] C.P. Fong and B.R. Webber. Higher Order QCD Corrections to Hadron Energy Distributions in Jets. *Phys.Lett.*, B229:289, 1989.

[95] L. Frankfurt, M. Strikman, and C. Weiss. Dijet production as a centrality trigger for *pp* collisions at CERN LHC. *Phys.Rev.*, D69:114010, 2004.

[96] R.J. Fries, Berndt Muller, C. Nonaka, and S.A. Bass. Hadron production in heavy ion collisions: Fragmentation and recombination from a dense parton phase. *Phys.Rev.*, C68:044902, 2003.

[97] M. Gazdzicki and S. Mrowczynski. A Method to study 'equilibration' in nucleus-nucleus collisions. *Z.Phys.*, C54:127–132, 1992.

[98] V. Greco, C. M. Ko, and P. Levai. Parton coalescence and antiproton/pion anomaly at RHIC. *Phys. Rev. Lett.*, 90:202302, 2003.

[99] G. Hanson et al. Evidence for Jet Structure in Hadron Production by e+ e- Annihilation. *Phys. Rev. Lett.*, 35:1609–1612, 1975.

[100] M. Harrison, Stephen G. Peggs, and T. Roser. The RHIC accelerator. *Ann. Rev. Nucl. Part. Sci.*, 52:425–469, 2002.

[101] Ulrich W. Heinz and Peter F. Kolb. Early thermalization at RHIC. *Nucl. Phys.*, A702:269–280, 2002.

[102] Henning Heiselberg. Event-by-event physics in relativistic heavy ion collisions. *Phys.Rept.*, 351:161–194, 2001.

[103] Henning Heiselberg and Anne-Marie Levy. Elliptic flow and HBT in non-central nuclear collisions. *Phys. Rev.*, C59:2716–2727, 1999.

[104] A. Heister et al. Study of the fragmentation of b quarks into B mesons at the Z peak. *Phys. Lett.*, B512:30–48, 2001.

[105] Tetsufumi Hirano and Miklos Gyulassy. Perfect fluidity of the quark gluon plasma core as seen through its dissipative hadronic corona. *Nucl.Phys.*, A769:71–94, 2006.

[106] C.M. Hung and Edward V. Shuryak. Equation of state, radial flow and freezeout in high-energy heavy ion collisions. *Phys.Rev.*, C57:1891–1906, 1998.

[107] P. Huovinen and P.V. Ruuskanen. Hydrodynamic Models for Heavy Ion Collisions. *Ann.Rev.Nucl.Part.Sci.*, 56:163–206, 2006.

[108] Rudolph C. Hwa. Thermalization of Quarks and Gluons in Heavy Ion Collisions. *Phys. Rev.*, D32:637, 1985.

[109] N. Kapur J. and K. Kesavan H.˙ *Entropy Optimization Principles with Applications*. Academic Press, 1992.

[110] Peter Jacobs and Glenn Cooper. Spatial Distribution of Initial Interactions in High Energy Collisions of Heavy Nuclei. 2000.

[111] F. James and M. Roos. Minuit: A System for Function Minimization and Analysis of the Parameter Errors and Correlations. *Comput. Phys. Commun.*, 10:343–367, 1975.

[112] P. G. Jones et al. Hadron yields and hadron spectra from the NA49 experiment. *Nucl. Phys.*, A610:188c–199c, 1996.

[113] T. Kafka et al. One, Two, and Three Particle Distributions in p p Collisions at 205-GeV/c. *Phys. Rev.*, D16:1261, 1977.

[114] K. Kajantie, P. V. Landshoff, and J. Lindfors. Minijet Production in High-Energy Nucleus-Nucleus Collisions. *Phys. Rev. Lett.*, 59:2527, 1987.

[115] David Kettler. Universal centrality and collision energy trends for v(2) measurements from 2D angular correlations. *Eur. Phys. J.*, C62:175–181, 2009.

[116] David Kettler. The azimuth quadrupole in nuclear collisions. *PoS*, CERP2010:011, 2010.

[117] David Kettler. Azimuth Quadrupole Systematics in Au-Au Collisions. *J. Phys. Conf. Ser.*, 270:012058, 2011.

[118] Vardan Khachatryan et al. Observation of Long-Range Near-Side Angular Correlations in Proton-Proton Collisions at the LHC. *JHEP*, 1009:091, 2010.

[119] Vardan Khachatryan et al. Transverse-momentum and pseudorapidity distributions of charged hadrons in pp collisions at $\sqrt{s} = 7$ TeV. *Phys.Rev.Lett.*, 105:022002, 2010.

[120] Dmitri Kharzeev and Marzia Nardi. Hadron production in nuclear collisions at RHIC and high density QCD. *Phys. Lett.*, B507:121–128, 2001.

[121] K. Kimura, M. Kitazawa, and K. Tesima. Corrections to angular ordering in multiple hadroproduction. *Z.Phys.*, C72:271–280, 1996.

[122] Bernd A. Kniehl, G. Kramer, and B. Potter. Fragmentation functions for pions, kaons, and protons at next-to-leading order. *Nucl. Phys.*, B582:514–536, 2000.

[123] Yuri V. Kovchegov and Anastasios Taliotis. Early time dynamics in heavy ion collisions from AdS/CFT correspondence. *Phys. Rev.*, C76:014905, 2007.

[124] J. M. Landgraf et al. An overview of the STAR DAQ system. *Nucl. Instrum. Meth.*, A499:762–765, 2003.

[125] Kang Seog Lee, Ulrich W. Heinz, and Ekkard Schnedermann. Search for Collective Transverse Flow Using Particle Transverse Momentum Spectra in Relativistic Heavy Ion Collisions. *Z. Phys.*, C48:525–541, 1990.

[126] Michael Annan Lisa, Scott Pratt, Ron Soltz, and Urs Wiedemann. Femtoscopy in Relativistic Heavy Ion Collisions: Two Decades of Progress. *Ann. Rev. Nucl. Part. Sci.*, 55:357–402, 2005.

[127] Qing-jun Liu, Duncan J. Prindle, and Thomas A. Trainor. Autocorrelations from the scale dependence of transverse- momentum fluctuations in Hijing-simulated Au-Au collisions at s(NN)**(1/2) = 200-GeV. *Phys. Lett.*, B632:197–202, 2006.

[128] W.J. Llope. Multigap RPCs in the STAR experiment at RHIC. *Nucl.Instrum.Meth.*, A661:S110–S113, 2012.

[129] T. Ludlam. Experimental results from the early measurements at RHIC: Hunting for the quark-gluon plasma. *Nucl. Phys.*, A750:9–29, 2005.

[130] Larry D. McLerran. The Physics of the Quark - Gluon Plasma. *Rev. Mod. Phys.*, 58:1021–1064, 1986.

[131] Michael L. Miller, Klaus Reygers, Stephen J. Sanders, and Peter Steinberg. Glauber modeling in high energy nuclear collisions. *Ann. Rev. Nucl. Part. Sci.*, 57:205–243, 2007.

[132] Alfred H. Mueller. Toward equilibration in the early stages after a high energy heavy ion collision. *Nucl. Phys.*, B572:227–240, 2000.

[133] Gouranga C. Nayak, Adrian Dumitru, Larry D. McLerran, and Walter Greiner. Equilibration of the gluon-minijet plasma at RHIC and LHC. *Nucl. Phys.*, A687:457–474, 2001.

[134] Jean-Yves Ollitrault. Anisotropy as a signature of transverse collective flow. *Phys. Rev.*, D46:229–245, 1992.

[135] C. Peterson, D. Schlatter, I. Schmitt, and Peter M. Zerwas. Scaling Violations in Inclusive e+ e- Annihilation Spectra. *Phys.Rev.*, D27:105, 1983.

[136] R. J. Porter and T. A. Trainor. Soft and hard components of two-particle distributions on (y_t, η, ϕ) from p-p collisions at $\sqrt{s} = 200$ GeV.

[137] R. J. Porter and T. A. Trainor. Correlation structures from soft and semi-hard components in p - p collisions at s**(1/2) = 200-GeV. *Acta Phys. Polon.*, B36:353–359, 2005.

[138] R. Jefferson Porter and Thomas A. Trainor. Correlations from p-p collisions at s**(1/2) = 200-GeV. *J. Phys. Conf. Ser.*, 27:98–107, 2005.

[139] R. Jefferson Porter and Thomas A. Trainor. Correlations in p p collisions. *PoS*, CFRNC2006:004, 2006.

[140] Arthur M. Poskanzer et al. Centrality dependence of directed and elliptic flow at the SPS. *Nucl. Phys.*, A661:341–344, 1999.

[141] Arthur M. Poskanzer and S. A. Voloshin. Methods for analyzing anisotropic flow in relativistic nuclear collisions. *Phys. Rev.*, C58:1671–1678, 1998.

[142] Duncan J. Prindle and Thomas A. Trainor. The equivalence of fluctuation scale dependence and autocorrelations. *J. Phys. Conf. Ser.*, 27:118–127, 2005.

[143] W. Reisdorf and H. G. Ritter. Collective flow in heavy-ion collisions. *Ann. Rev. Nucl. Part. Sci.*, 47:663–709, 1997.

[144] R. E. Renfordt et al. Stopping Power and Collective Flow of Nuclear Matter in the Reaction Ar + Pb at 0.8-GeV/U. *Phys. Rev. Lett.*, 53:763–766, 1984.

[145] Ina Sarcevic, Stephen D. Ellis, and Peter Carruthers. QCD Minijet Cross-Sections. *Phys. Rev.*, D40:1446, 1989.

[146] Edward V. Shuryak. What RHIC experiments and theory tell us about properties of quark-gluon plasma? *Nucl. Phys.*, A750:64–83, 2005.

[147] Torbjorn Sjostrand. High-energy physics event generation with PYTHIA 5.7 and JETSET 7.4. *Comput.Phys.Commun.*, 82:74–90, 1994.

[148] Paul Sorensen. Elliptic flow fluctuations in Au+Au collisions at s(NN)**(1/2) = 200-GeV. *J.Phys.G*, G34:S897, 2007.

[149] Paul Sorensen. Elliptic Flow: A Study of Space-Momentum Correlations In Relativistic Nuclear Collisions. 2009.

[150] H. Sorge. Highly sensitive centrality dependence of elliptic flow: A novel signature of the phase transition in QCD. *Phys. Rev. Lett.*, 82:2048–2051, 1999.

[151] Misha A. Stephanov, K. Rajagopal, and Edward V. Shuryak. Event-by-event fluctuations in heavy ion collisions and the QCD critical point. *Phys. Rev.*, D60:114028, 1999.

[152] R. Stock et al. Compression Effects in Relativistic Nucleus Nucleus Collisions. *Phys. Rev. Lett.*, 49:1236–1239, 1982.

[153] Reinhard Stock. Quark Matter 99 summary: Hadronic signals. *Nucl.Phys.*, A661:282–299, 1999.

[154] D. Teaney, J. Lauret, and Edward V. Shuryak. Flow at the SPS and RHIC as a quark gluon plasma signature. *Phys. Rev. Lett.*, 86:4783–4786, 2001.

[155] T. A. Trainor, R. J. Porter, and D. J. Prindle. Autocorrelations from fluctuation scale dependence by inversion. *J. Phys.*, G31:809–824, 2005.

[156] T.A. Trainor. Event-by-event analysis and the central limit theorem. 2000.

[157] Thomas A. Trainor. Low-Q**2 partons in p - p and Au - Au collisions. *AIP Conf. Proc.*, 828:238–243, 2006.

[158] Thomas A. Trainor. Azimuth quadrupole component spectra on transverse rapidity $\mathbf{y_t}$ for identified hadrons from Au-Au collisions at $\sqrt{s_{NN}} = 200$ GeV. *Phys. Rev.*, C78:064908, 2008.

[159] Thomas A. Trainor. Centrality evolution of p_t and y_t spectra from Au-Au collisions at $\sqrt{s_{NN}} = 200$ GeV. *Int. J. Mod. Phys.*, E17:1499–1540, 2008.

[160] Thomas A. Trainor. The RHIC azimuth quadrupole: "Perfect liquid" or gluonic radiation? *Mod.Phys.Lett.*, A23:569–589, 2008.

[161] Thomas A. Trainor. Evolution of minimum-bias parton fragmentation in nuclear collisions. *Phys.Rev.*, C80:044901, 2009.

[162] Thomas A. Trainor. Examination of the relevance of hydrodynamics for data measured at the BNL relativistic heavy ion collider. *J.Phys.*, G37:085004, 2010.

[163] Thomas A. Trainor. Parton fragmentation in nuclear collisions. *PoS*, CERP2010:003, 2010.

[164] Thomas A. Trainor. Zero yield at minimum (ZYAM) method and v2: Underestimating jet yields from dihadron azimuth correlations. *Phys. Rev.*, C81:014905, 2010.

[165] Thomas A. Trainor and David T. Kettler. Extrapolating parton fragmentation to low Q^2 in e^+ - e^- collisions. *Phys. Rev.*, D74:034012, 2006.

[166] Thomas A. Trainor and David T. Kettler. The azimuth structure of nuclear collisions. I. *Int. J. Mod. Phys.*, E17:1219–1272, 2008.

[167] Thomas A. Trainor and David T. Kettler. Comparing the same-side 'ridge' in CMS p-p angular correlations to RHIC p-p data. *Phys.Rev.*, C84:024910, 2011.

[168] Thomas A. Trainor and David T. Kettler. Parton fragment yields derived from minimum-bias jet angular correlations. *Phys. Rev.*, C83:034903, 2011.

[169] Thomas A. Trainor and Duncan J. Prindle. A power-law description of collision centrality applied to Hijing-1.37-simulated Au - Au collisions at s(NN)**(1/2) = 200-GeV. 2004.

[170] Thomas A. Trainor and Duncan J. Prindle. Transverse momentum correlations in relativistic nuclear collisions. *J. Phys. Conf. Ser.*, 27:134–143, 2005.

[171] S. Voloshin and Y. Zhang. Flow study in relativistic nuclear collisions by Fourier expansion of Azimuthal particle distributions. *Z.Phys.*, C70:665–672, 1996.

[172] S. A. Voloshin and Arthur M. Poskanzer. The physics of the centrality dependence of elliptic flow. *Phys. Lett.*, B474:27–32, 2000.

[173] Sergei A. Voloshin. Energy and system size dependence of elliptic flow: Using rapidity gaps to suppress non-flow contribution. *AIP Conf.Proc.*, 870:691–694, 2006.

[174] Sergei A. Voloshin, Arthur M. Poskanzer, Aihong Tang, and Gang Wang. Elliptic flow in the Gaussian model of eccentricity fluctuations. *Phys.Lett.*, B659:537–541, 2008.

[175] Xin-Nian Wang and Miklos Gyulassy. HIJING: A Monte Carlo model for multiple jet production in p p, p A and A A collisions. *Phys. Rev.*, D44:3501–3516, 1991.

[176] B. R. Webber. Measuring alpha-s from scaling violation in fragmentation functions. *J. Phys.*, G17:1579–1584, 1991.

[177] B. R. Webber. Hadronization. 1994.

[178] Klaus Werner. Core-Corona Separation in Ultra-Relativistic Heavy Ion Collisions. *Phys. Rev. Lett.*, 98:152301, 2007.

[179] J. Whitmore. Multiparticle Production in the Fermilab Bubble Chambers. *Phys. Rept.*, 27:187–273, 1976.

[180] G. Wilk and Z. Wlodarczyk. On the interpretation of nonextensive parameter q in Tsallis statistics and Levy distributions. *Phys. Rev. Lett.*, 84:2770, 2000.

[181] A. H. Mueller Yu. L. Dokshitzer, V. A. Khoze and S. I. Troyan. *Basics of perturbative QCD.* Editions Frontières, 1991.

Appendix A

P_T-DEPENDENT CORRELATIONS PLOTS

The following several pages shows the complete dataset of p_t-differential two-particle correlations for all centralities, p_t bins, and both 200 GeV and 62 GeV collision energies. First we show the data for a given collision system and centrality for each p_t bin, then the fit to those histograms, and finally the residuals from the fit. For the plots of residuals the bins excluded from the fit—see Chapter 7—are set to zero.

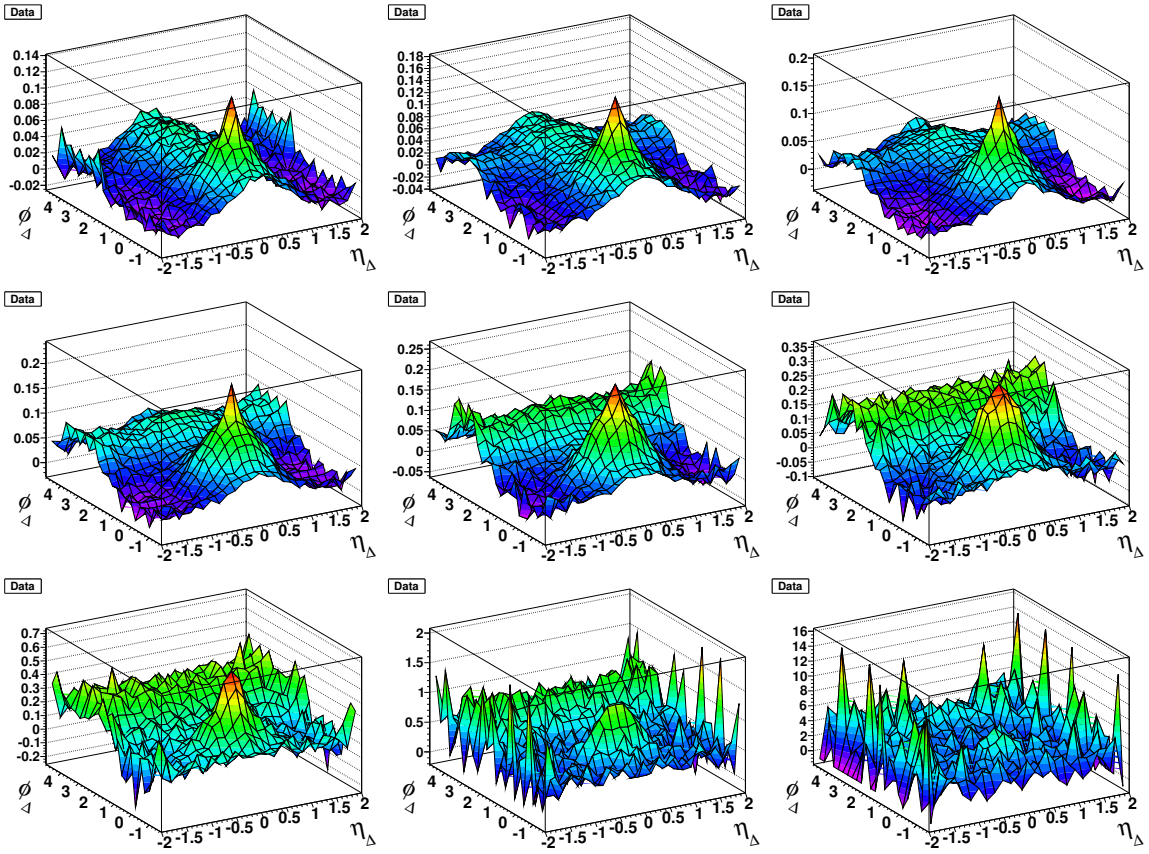

Figure A.1: Data histograms for 200 GeV 90-100% central collisions. Starting from the upper left the y_t bins are $y_t < 1.4$, $1.4 < y_t < 1.8$, $1.8 < y_t < 2.2$, $2.2 < y_t < 2.6$, $2.6 < y_t < 3.0$, $3.0 < y_t < 3.4$, $3.4 < y_t < 3.8$, $3.8 < y_t < 4.2$, and $y_t > 4.2$.

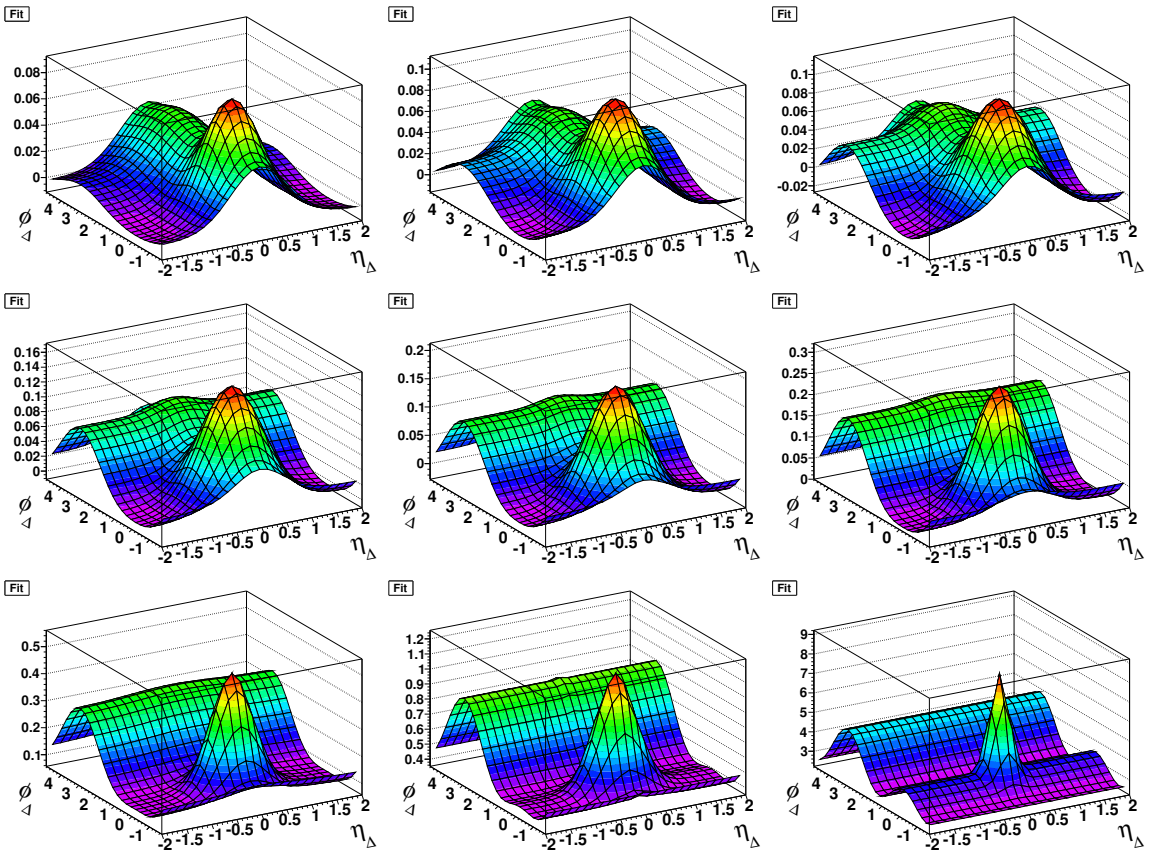

Figure A.2: Fits to the histograms for 200 GeV 90-100% central collisions. Starting from the upper left the y_t bins are $y_t < 1.4$, $1.4 < y_t < 1.8$, $1.8 < y_t < 2.2$, $2.2 < y_t < 2.6$, $2.6 < y_t < 3.0$, $3.0 < y_t < 3.4$, $3.4 < y_t < 3.8$, $3.8 < y_t < 4.2$, and $y_t > 4.2$.

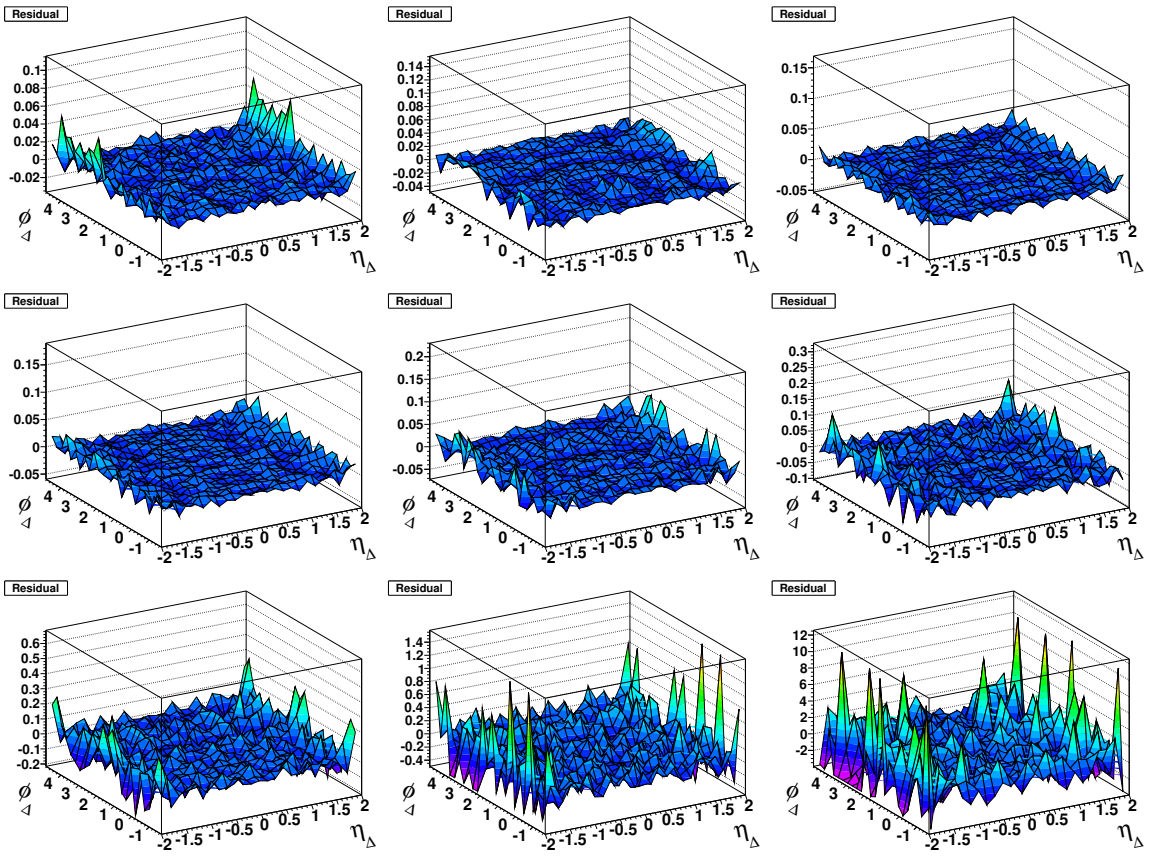

Figure A.3: Residuals for the fits to the histograms for 200 GeV 90-100% central collisions. Starting from the upper left the y_t bins are $y_t < 1.4$, $1.4 < y_t < 1.8$, $1.8 < y_t < 2.2$, $2.2 < y_t < 2.6$, $2.6 < y_t < 3.0$, $3.0 < y_t < 3.4$, $3.4 < y_t < 3.8$, $3.8 < y_t < 4.2$, and $y_t > 4.2$.

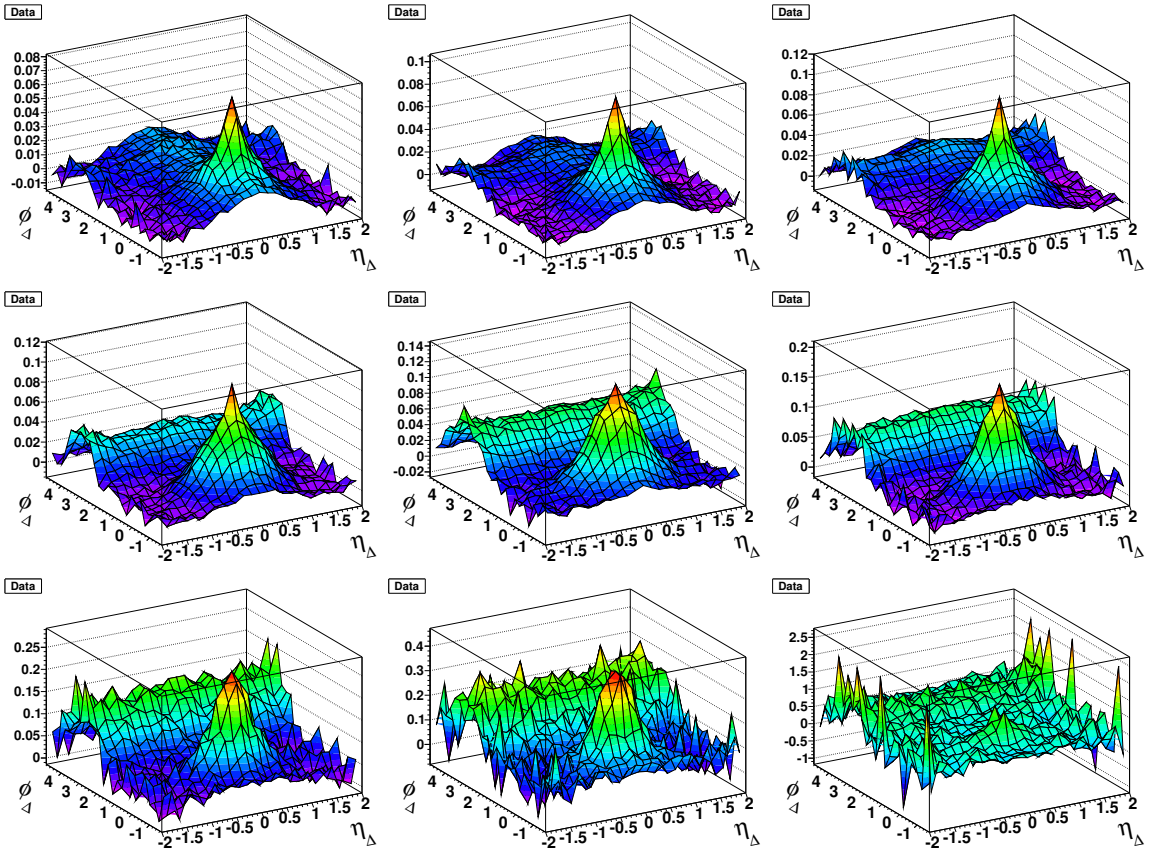

Figure A.4: Data histograms for 200 GeV 80-90% central collisions. Starting from the upper left the y_t bins are $y_t < 1.4$, $1.4 < y_t < 1.8$, $1.8 < y_t < 2.2$, $2.2 < y_t < 2.6$, $2.6 < y_t < 3.0$, $3.0 < y_t < 3.4$, $3.4 < y_t < 3.8$, $3.8 < y_t < 4.2$, and $y_t > 4.2$.

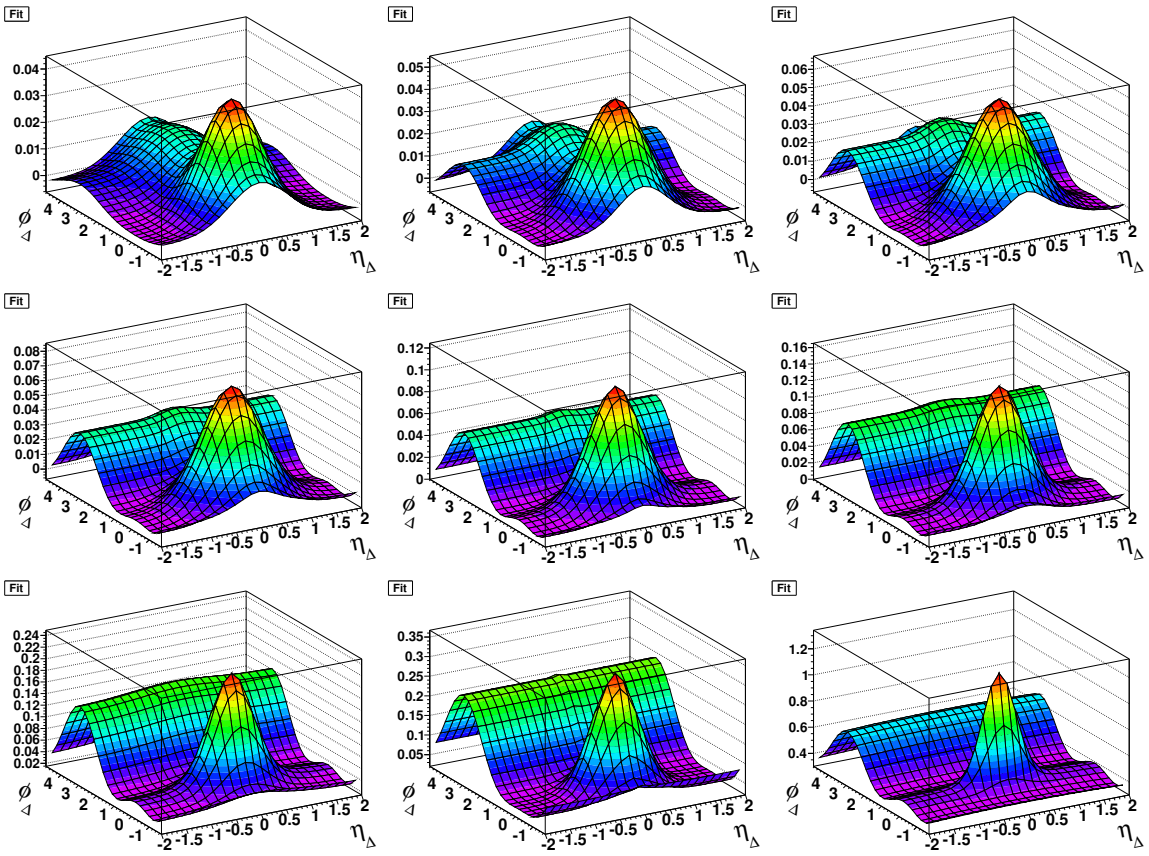

Figure A.5: Fits to the histograms for 200 GeV 80-90% central collisions. Starting from the upper left the y_t bins are $y_t < 1.4$, $1.4 < y_t < 1.8$, $1.8 < y_t < 2.2$, $2.2 < y_t < 2.6$, $2.6 < y_t < 3.0$, $3.0 < y_t < 3.4$, $3.4 < y_t < 3.8$, $3.8 < y_t < 4.2$, and $y_t > 4.2$.

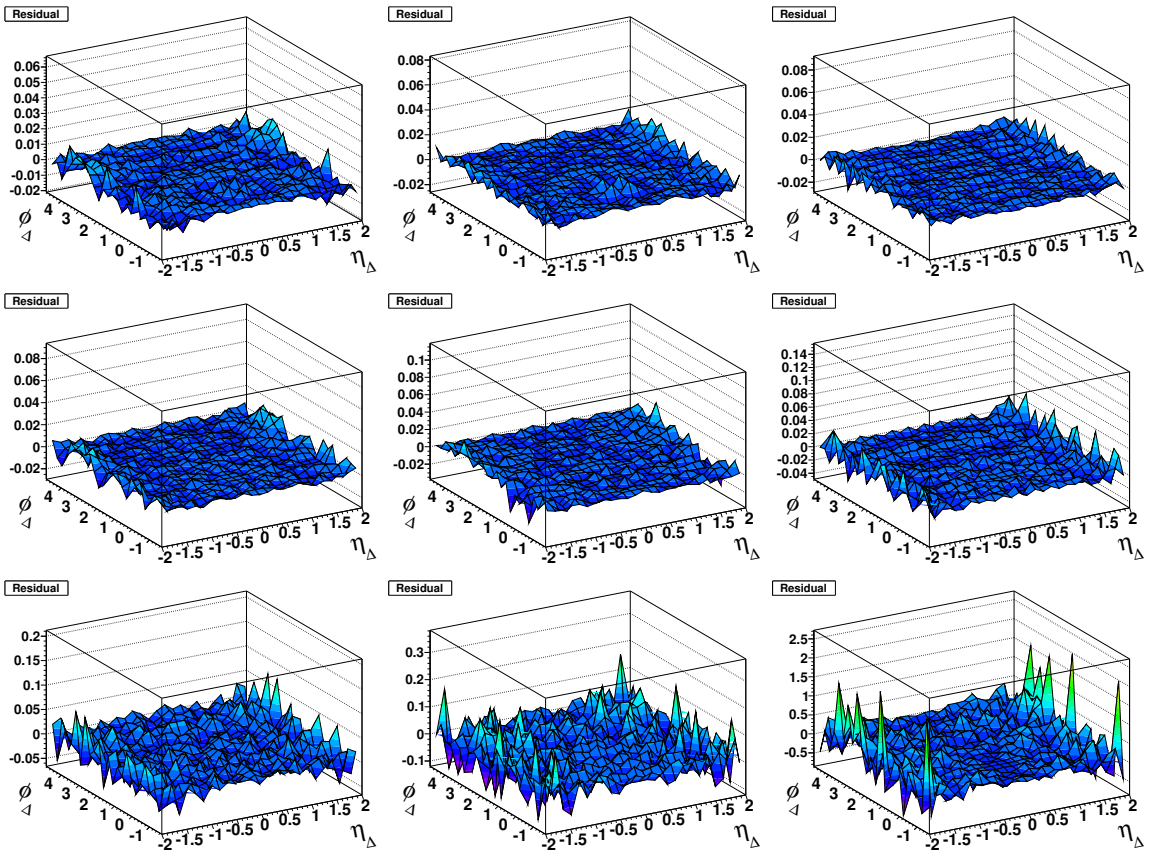

Figure A.6: Residuals for the fits to the histograms for 200 GeV 80-90% central collisions. Starting from the upper left the y_t bins are $y_t < 1.4$, $1.4 < y_t < 1.8$, $1.8 < y_t < 2.2$, $2.2 < y_t < 2.6$, $2.6 < y_t < 3.0$, $3.0 < y_t < 3.4$, $3.4 < y_t < 3.8$, $3.8 < y_t < 4.2$, and $y_t > 4.2$.

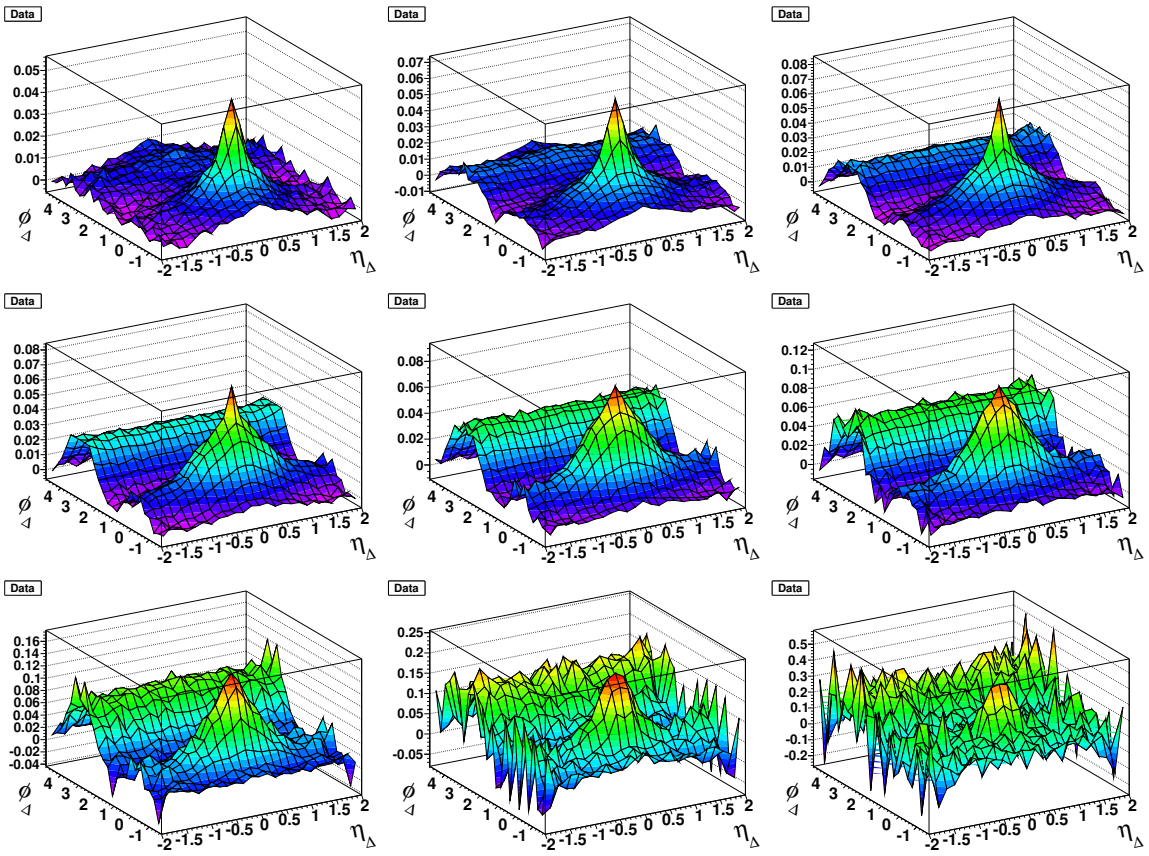

Figure A.7: Data histograms for 200 GeV 70-80% central collisions. Starting from the upper left the y_t bins are $y_t < 1.4$, $1.4 < y_t < 1.8$, $1.8 < y_t < 2.2$, $2.2 < y_t < 2.6$, $2.6 < y_t < 3.0$, $3.0 < y_t < 3.4$, $3.4 < y_t < 3.8$, $3.8 < y_t < 4.2$, and $y_t > 4.2$.

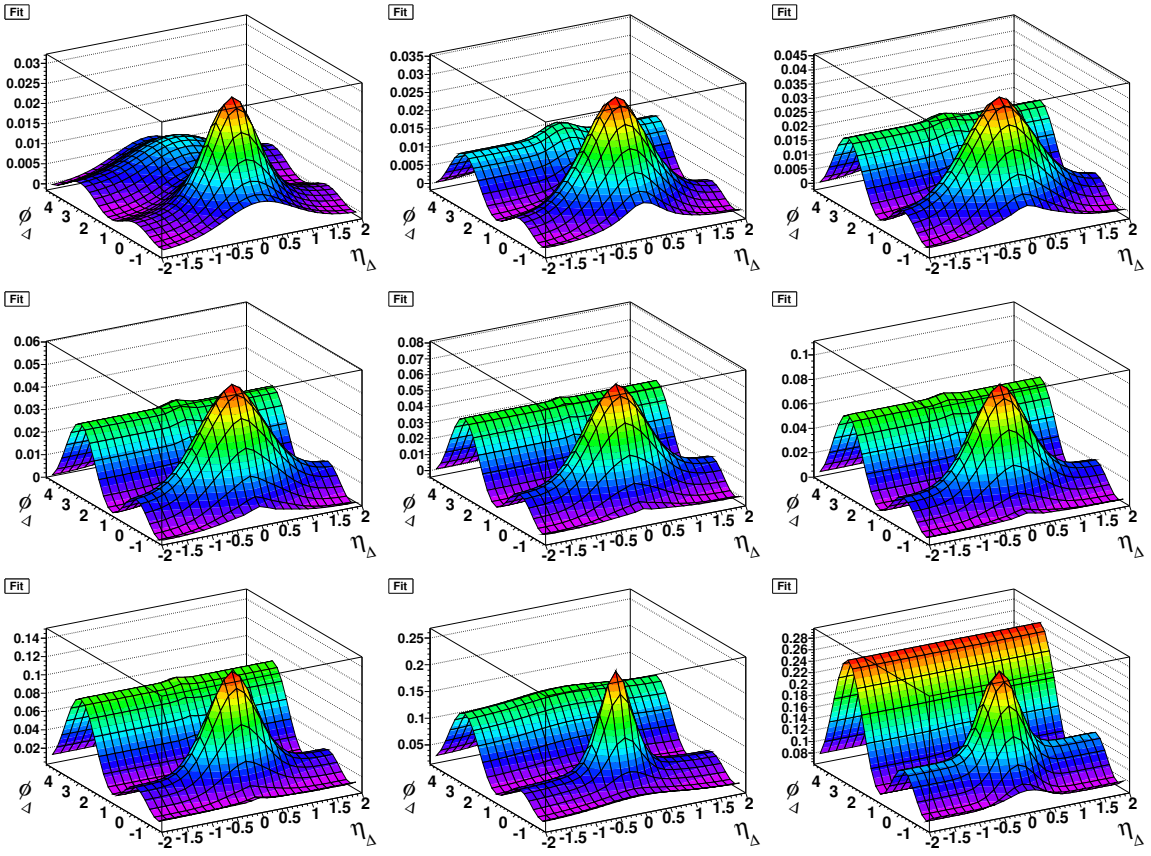

Figure A.8: Fits to the histograms for 200 GeV 70-80% central collisions. Starting from the upper left the y_t bins are $y_t < 1.4$, $1.4 < y_t < 1.8$, $1.8 < y_t < 2.2$, $2.2 < y_t < 2.6$, $2.6 < y_t < 3.0$, $3.0 < y_t < 3.4$, $3.4 < y_t < 3.8$, $3.8 < y_t < 4.2$, and $y_t > 4.2$.

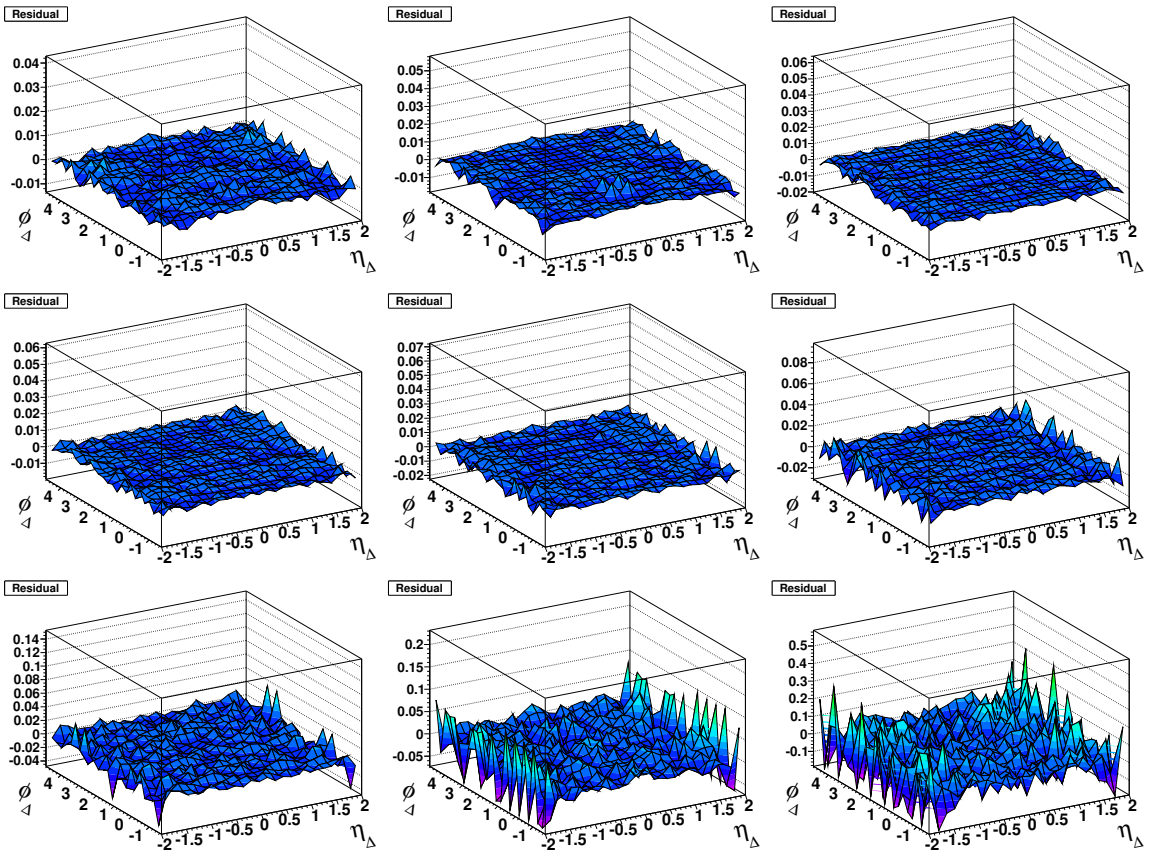

Figure A.9: Residuals for the fits to the histograms for 200 GeV 70-80% central collisions. Starting from the upper left the y_t bins are $y_t < 1.4$, $1.4 < y_t < 1.8$, $1.8 < y_t < 2.2$, $2.2 < y_t < 2.6$, $2.6 < y_t < 3.0$, $3.0 < y_t < 3.4$, $3.4 < y_t < 3.8$, $3.8 < y_t < 4.2$, and $y_t > 4.2$.

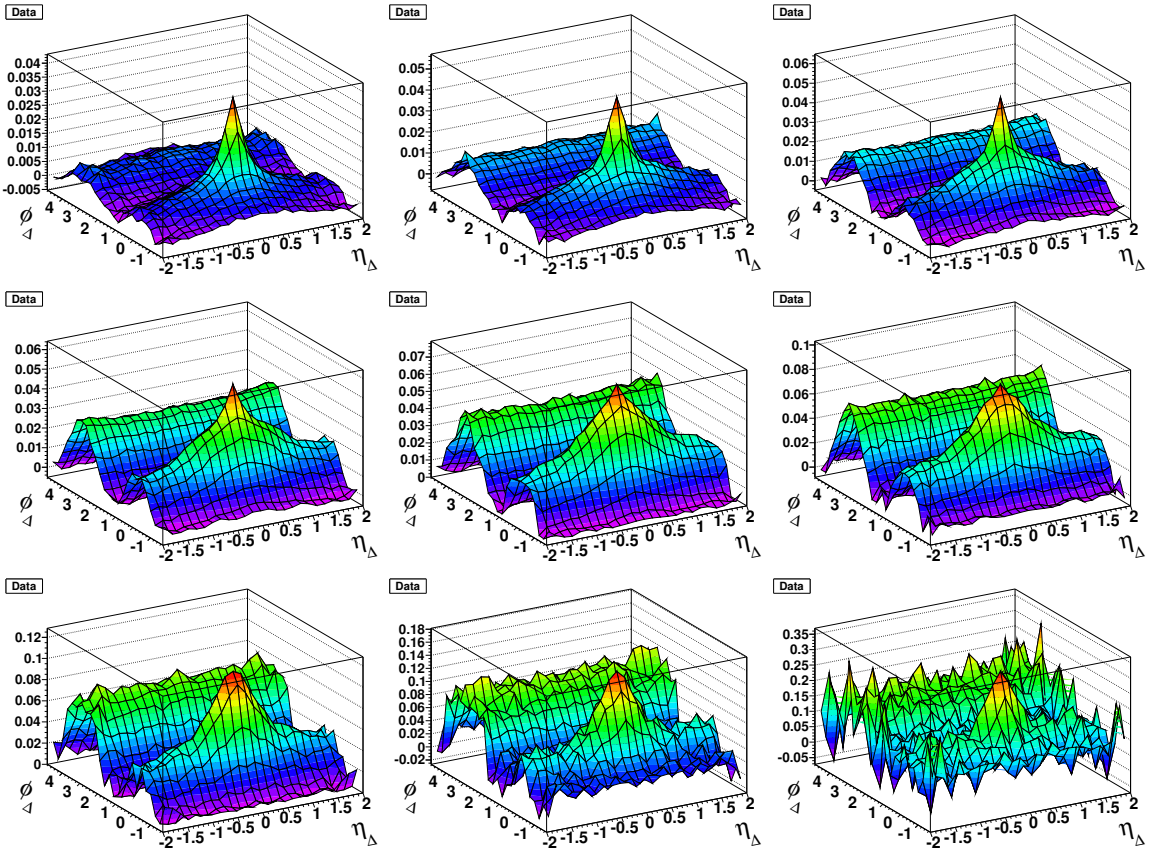

Figure A.10: Data histograms for 200 GeV 60-70% central collisions. Starting from the upper left the y_t bins are $y_t < 1.4$, $1.4 < y_t < 1.8$, $1.8 < y_t < 2.2$, $2.2 < y_t < 2.6$, $2.6 < y_t < 3.0$, $3.0 < y_t < 3.4$, $3.4 < y_t < 3.8$, $3.8 < y_t < 4.2$, and $y_t > 4.2$.

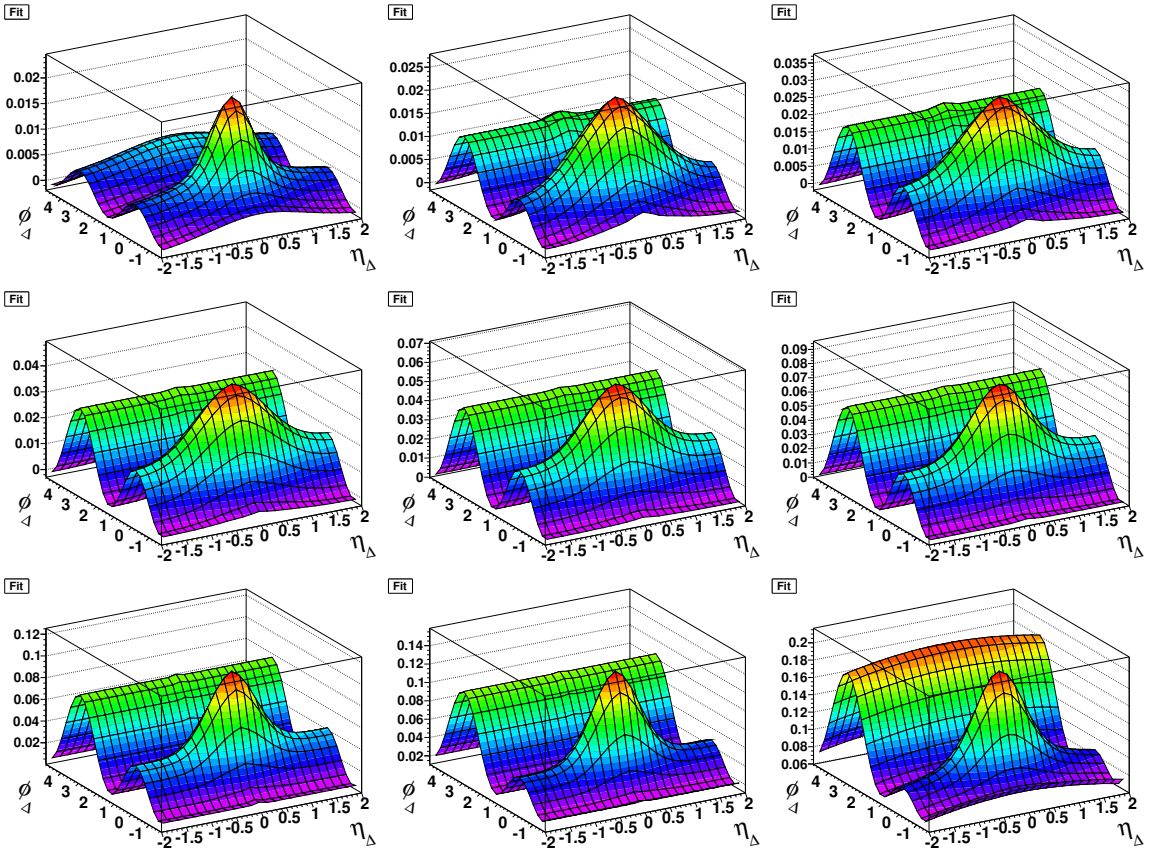

Figure A.11: Fits to the histograms for 200 GeV 60-70% central collisions. Starting from the upper left the y_t bins are $y_t < 1.4$, $1.4 < y_t < 1.8$, $1.8 < y_t < 2.2$, $2.2 < y_t < 2.6$, $2.6 < y_t < 3.0$, $3.0 < y_t < 3.4$, $3.4 < y_t < 3.8$, $3.8 < y_t < 4.2$, and $y_t > 4.2$.

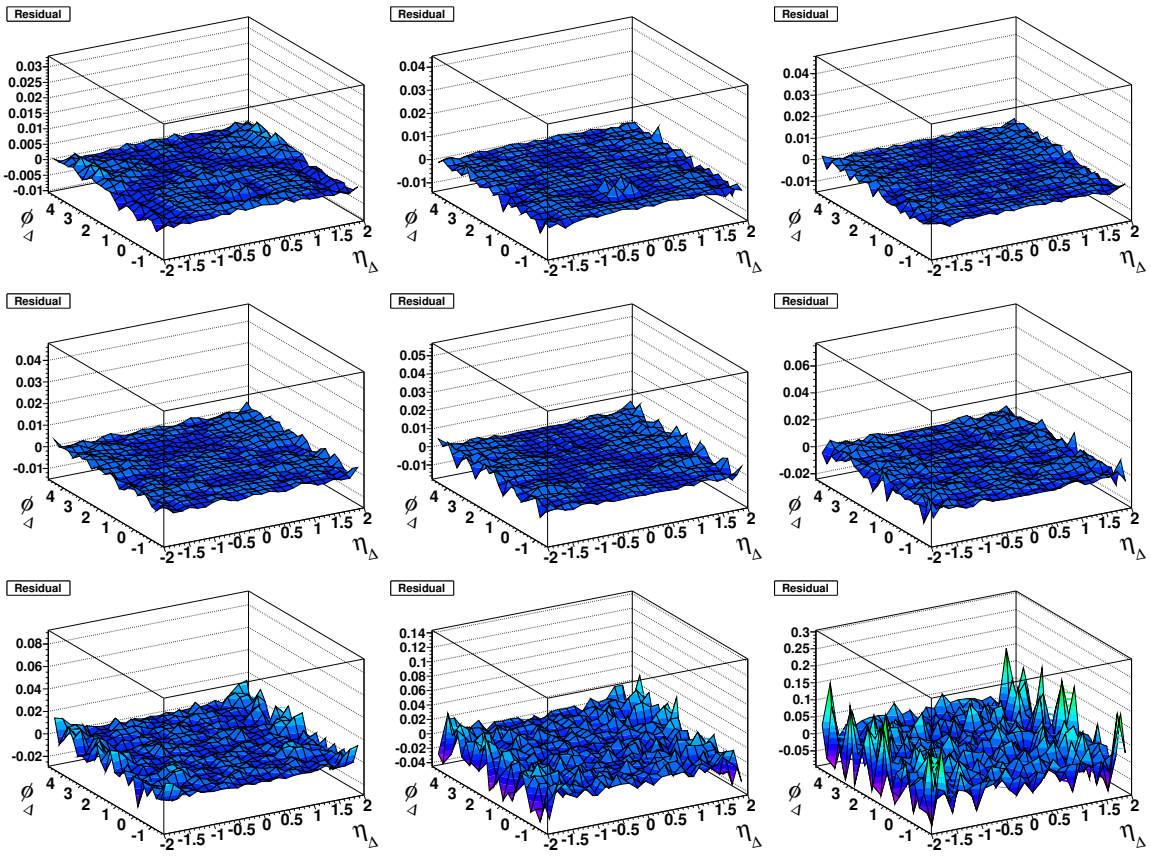

Figure A.12: Residuals for the fits to the histograms for 200 GeV 60-70% central collisions. Starting from the upper left the y_t bins are $y_t < 1.4$, $1.4 < y_t < 1.8$, $1.8 < y_t < 2.2$, $2.2 < y_t < 2.6$, $2.6 < y_t < 3.0$, $3.0 < y_t < 3.4$, $3.4 < y_t < 3.8$, $3.8 < y_t < 4.2$, and $y_t > 4.2$.

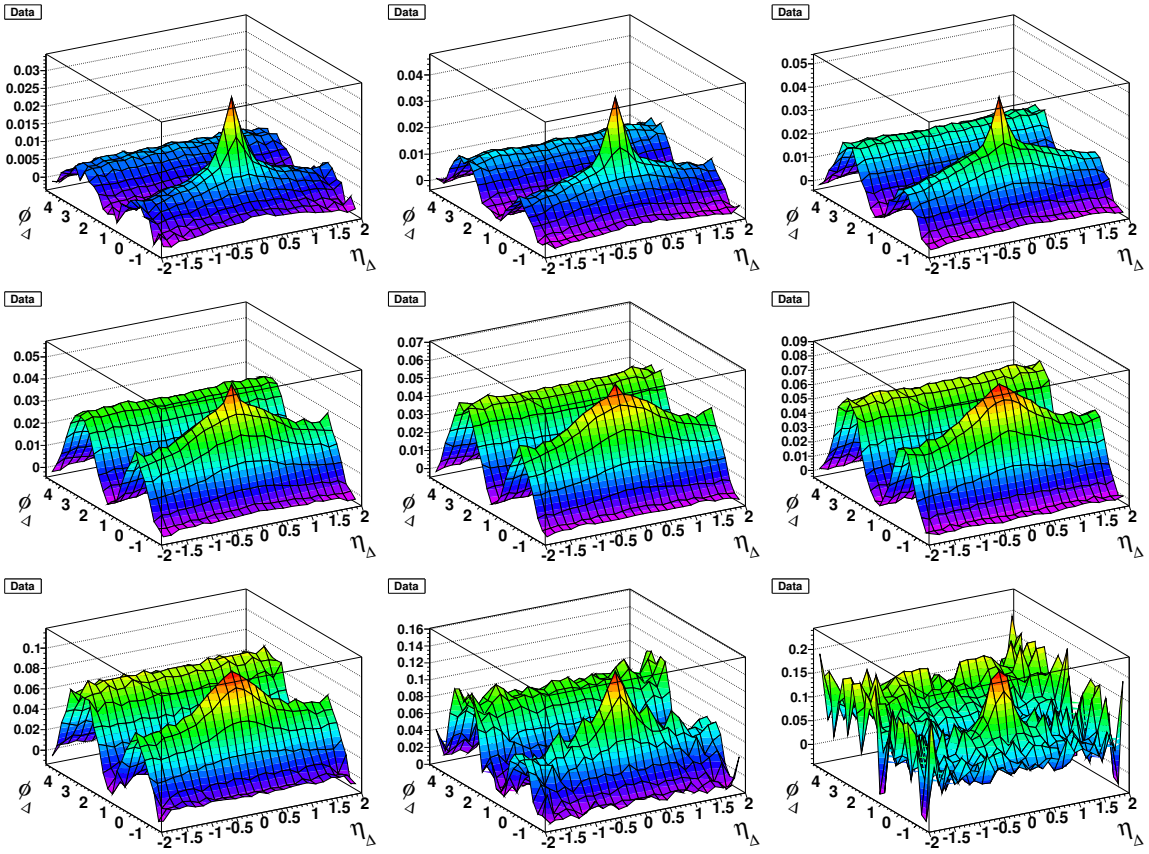

Figure A.13: Data histograms for 200 GeV 50-60% central collisions. Starting from the upper left the y_t bins are $y_t < 1.4$, $1.4 < y_t < 1.8$, $1.8 < y_t < 2.2$, $2.2 < y_t < 2.6$, $2.6 < y_t < 3.0$, $3.0 < y_t < 3.4$, $3.4 < y_t < 3.8$, $3.8 < y_t < 4.2$, and $y_t > 4.2$.

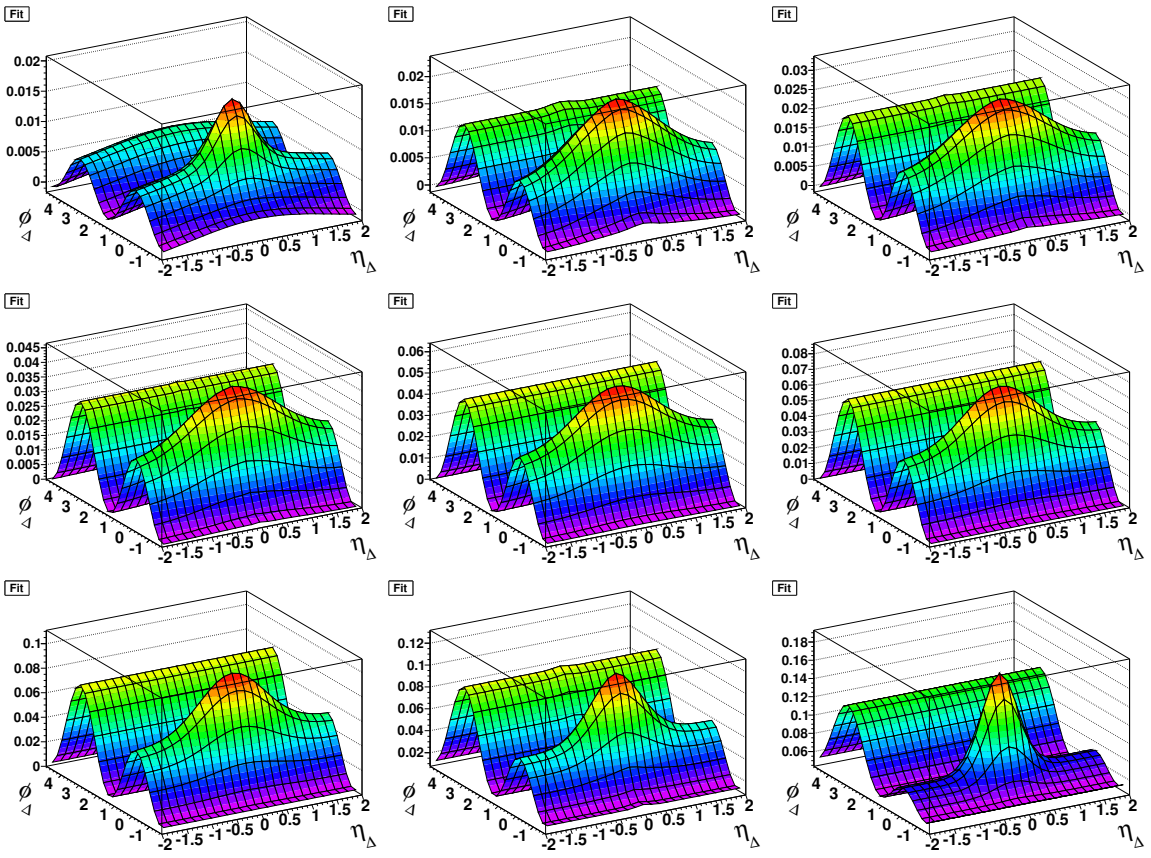

Figure A.14: Fits to the histograms for 200 GeV 50-60% central collisions. Starting from the upper left the y_t bins are $y_t < 1.4$, $1.4 < y_t < 1.8$, $1.8 < y_t < 2.2$, $2.2 < y_t < 2.6$, $2.6 < y_t < 3.0$, $3.0 < y_t < 3.4$, $3.4 < y_t < 3.8$, $3.8 < y_t < 4.2$, and $y_t > 4.2$.

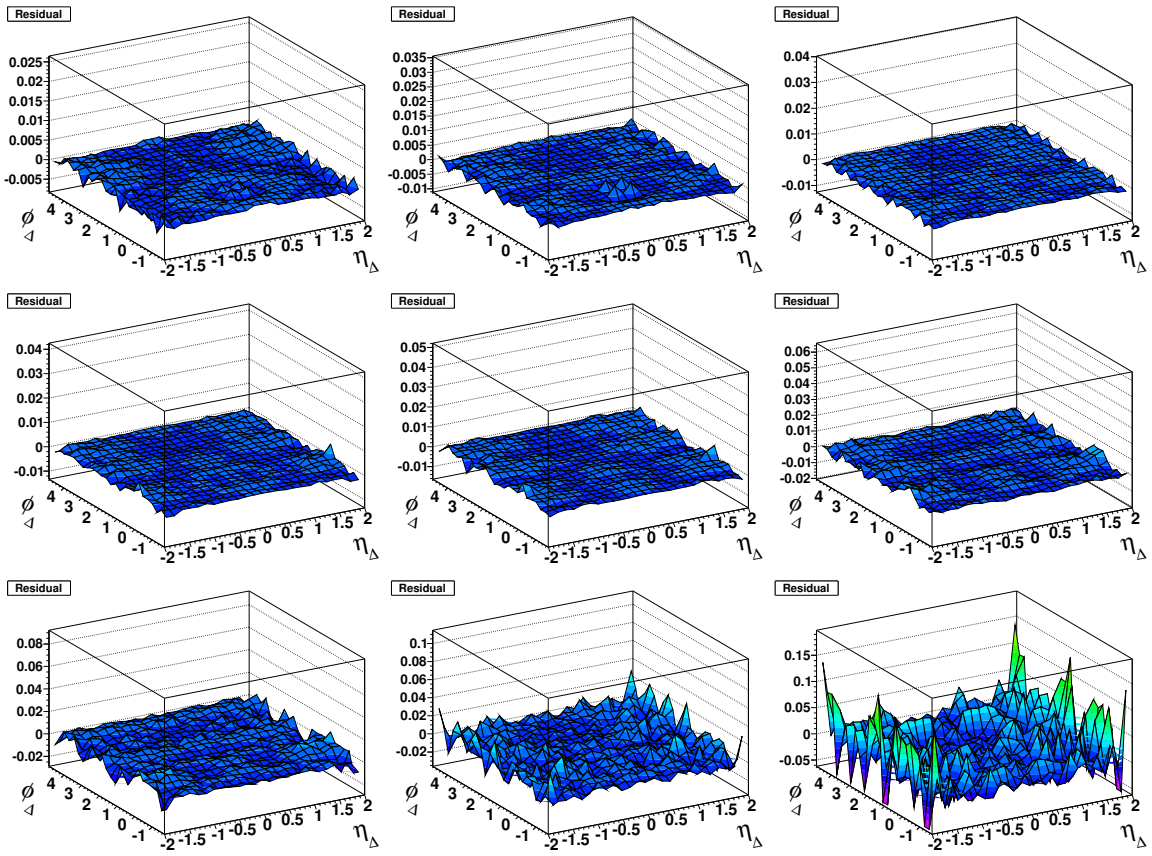

Figure A.15: Residuals for the fits to the histograms for 200 GeV 50-60% central collisions. Starting from the upper left the y_t bins are $y_t < 1.4$, $1.4 < y_t < 1.8$, $1.8 < y_t < 2.2$, $2.2 < y_t < 2.6$, $2.6 < y_t < 3.0$, $3.0 < y_t < 3.4$, $3.4 < y_t < 3.8$, $3.8 < y_t < 4.2$, and $y_t > 4.2$.

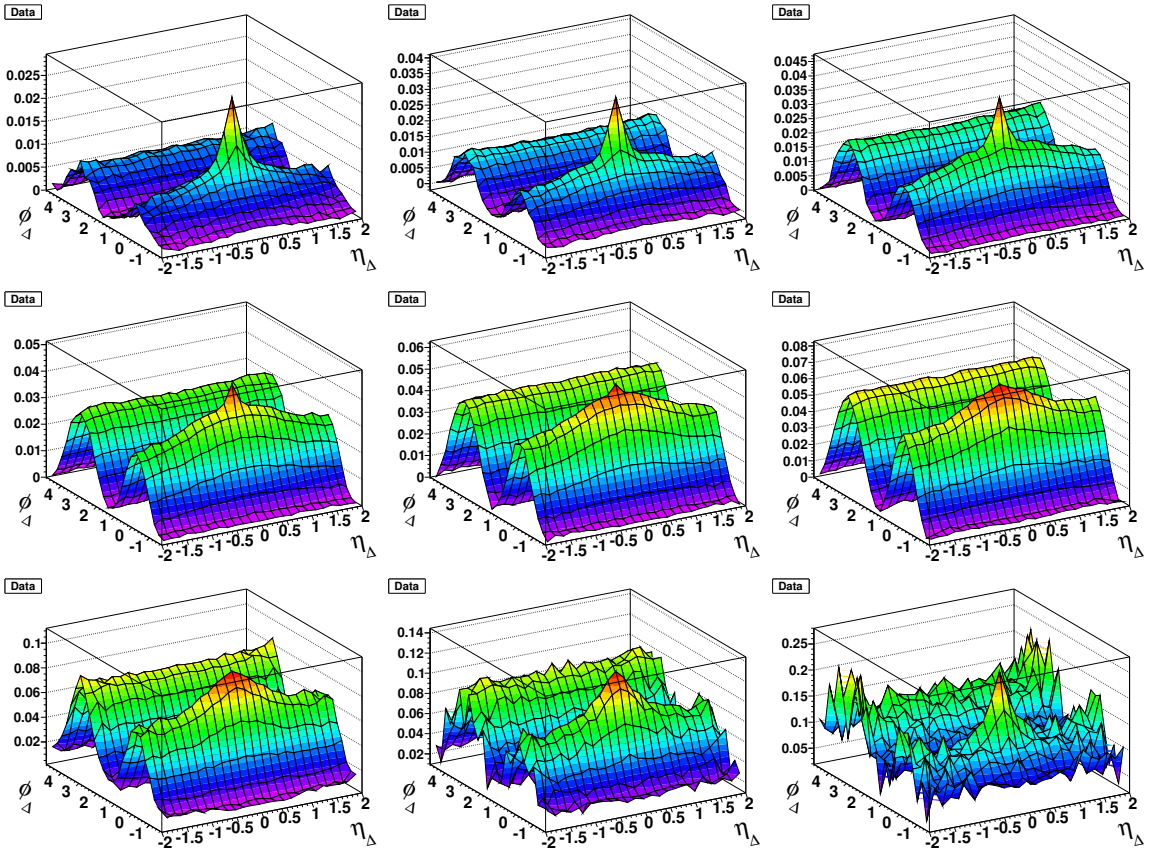

Figure A.16: Data histograms for 200 GeV 40-50% central collisions. Starting from the upper left the y_t bins are $y_t < 1.4$, $1.4 < y_t < 1.8$, $1.8 < y_t < 2.2$, $2.2 < y_t < 2.6$, $2.6 < y_t < 3.0$, $3.0 < y_t < 3.4$, $3.4 < y_t < 3.8$, $3.8 < y_t < 4.2$, and $y_t > 4.2$.

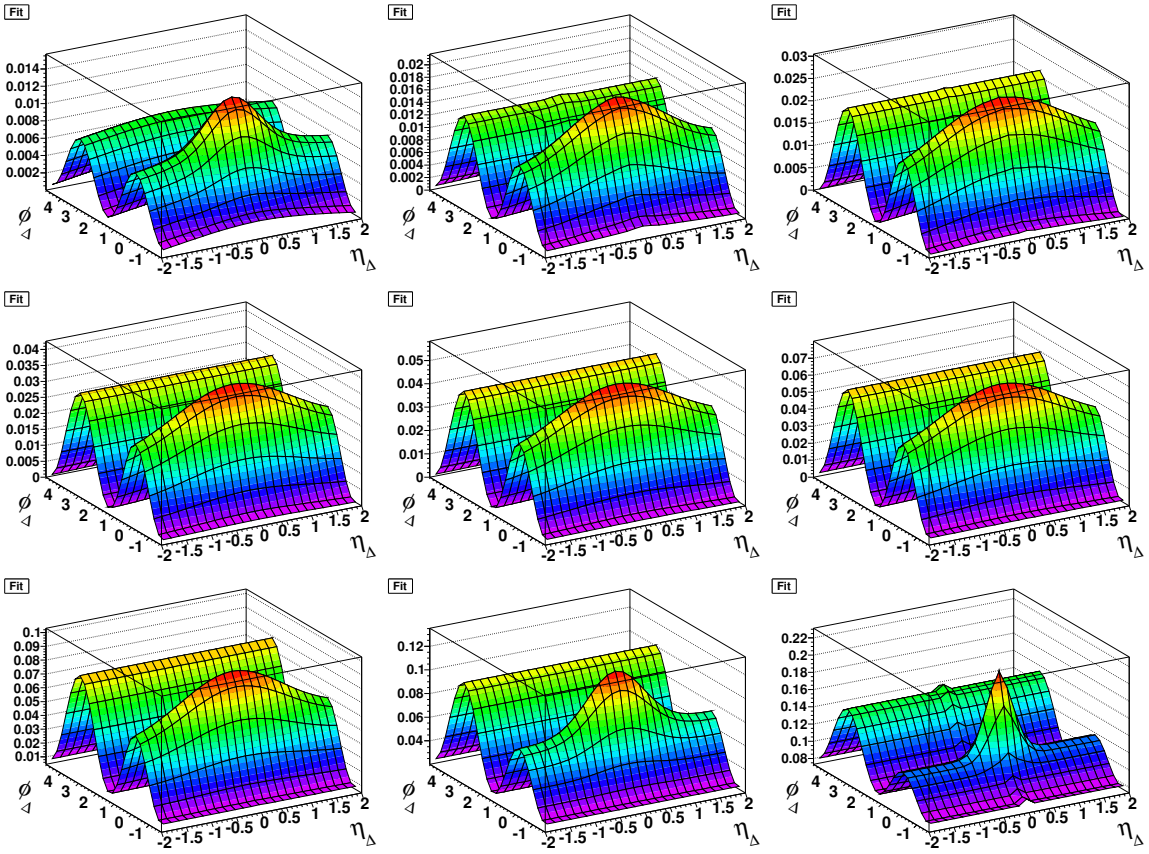

Figure A.17: Fits to the histograms for 200 GeV 40-50% central collisions. Starting from the upper left the y_t bins are $y_t < 1.4$, $1.4 < y_t < 1.8$, $1.8 < y_t < 2.2$, $2.2 < y_t < 2.6$, $2.6 < y_t < 3.0$, $3.0 < y_t < 3.4$, $3.4 < y_t < 3.8$, $3.8 < y_t < 4.2$, and $y_t > 4.2$.

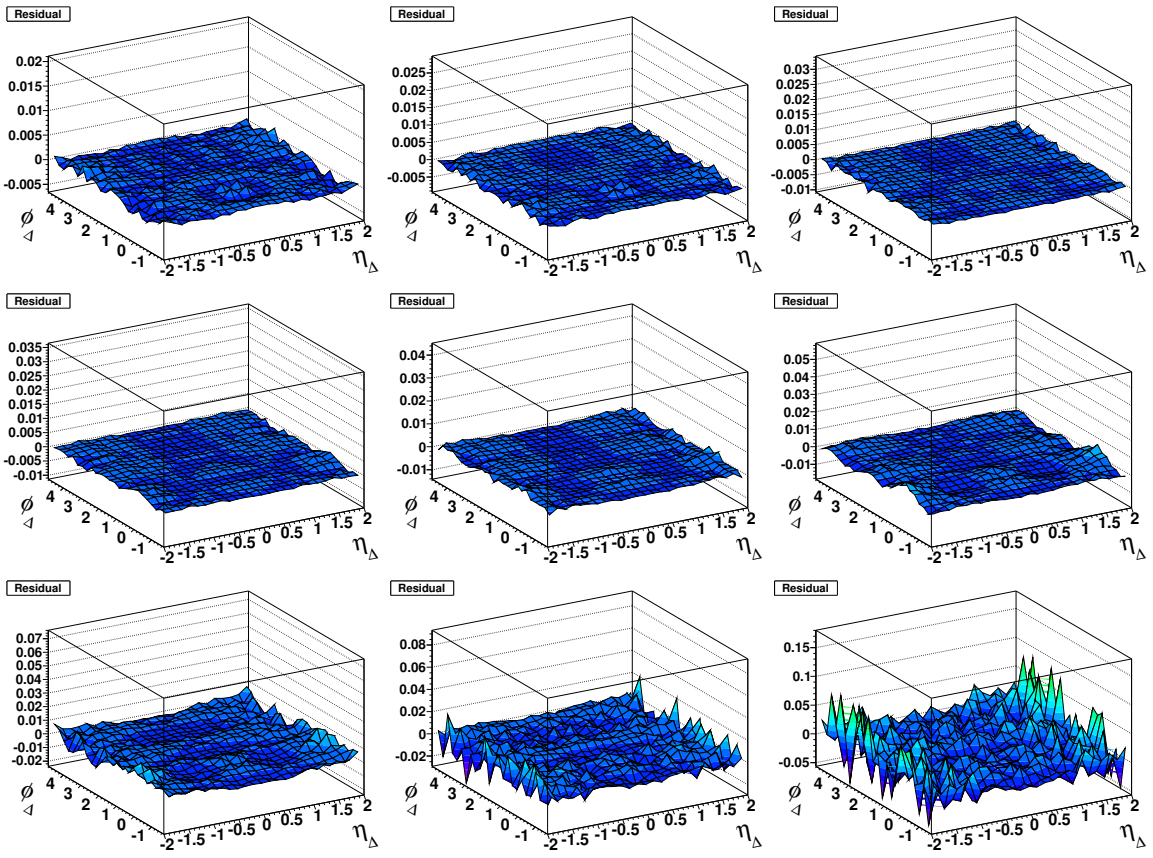

Figure A.18: Residuals for the fits to the histograms for 200 GeV 40-50% central collisions. Starting from the upper left the y_t bins are $y_t < 1.4$, $1.4 < y_t < 1.8$, $1.8 < y_t < 2.2$, $2.2 < y_t < 2.6$, $2.6 < y_t < 3.0$, $3.0 < y_t < 3.4$, $3.4 < y_t < 3.8$, $3.8 < y_t < 4.2$, and $y_t > 4.2$.

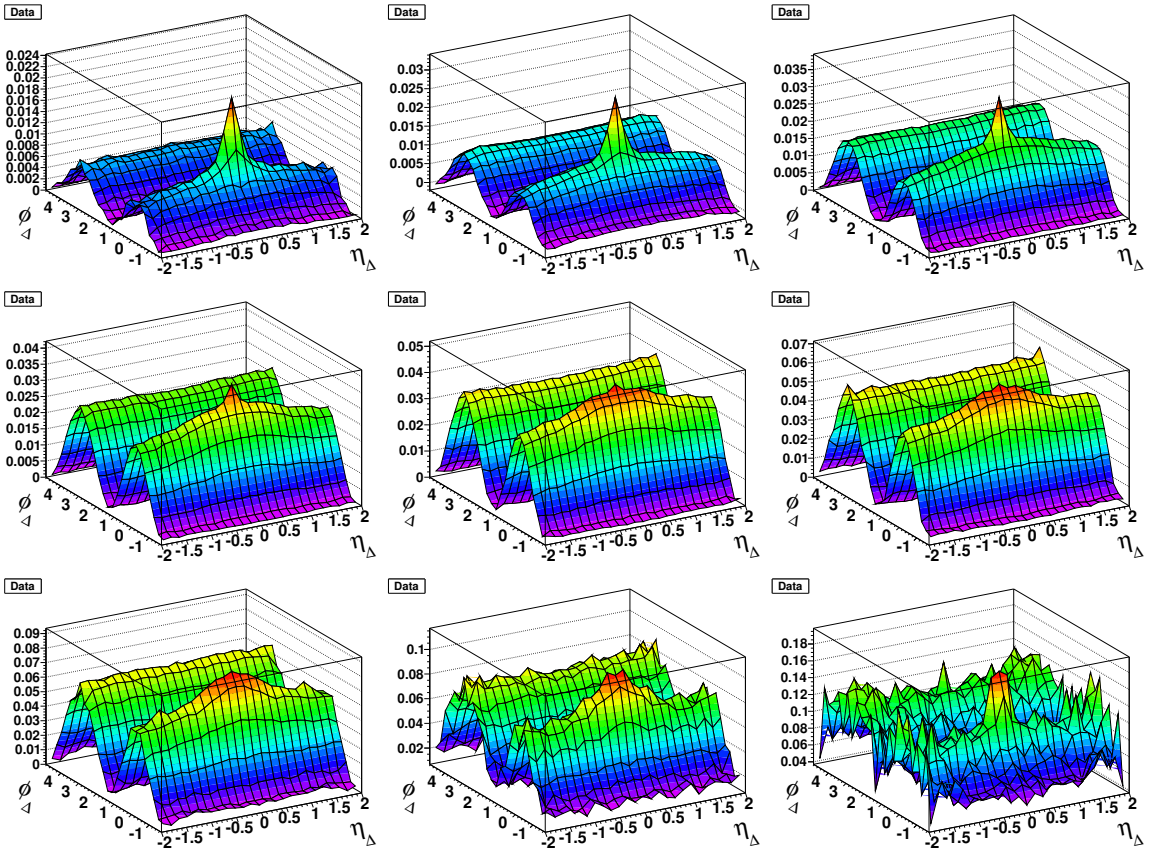

Figure A.19: Data histograms for 200 GeV 30-40% central collisions. Starting from the upper left the y_t bins are $y_t < 1.4$, $1.4 < y_t < 1.8$, $1.8 < y_t < 2.2$, $2.2 < y_t < 2.6$, $2.6 < y_t < 3.0$, $3.0 < y_t < 3.4$, $3.4 < y_t < 3.8$, $3.8 < y_t < 4.2$, and $y_t > 4.2$.

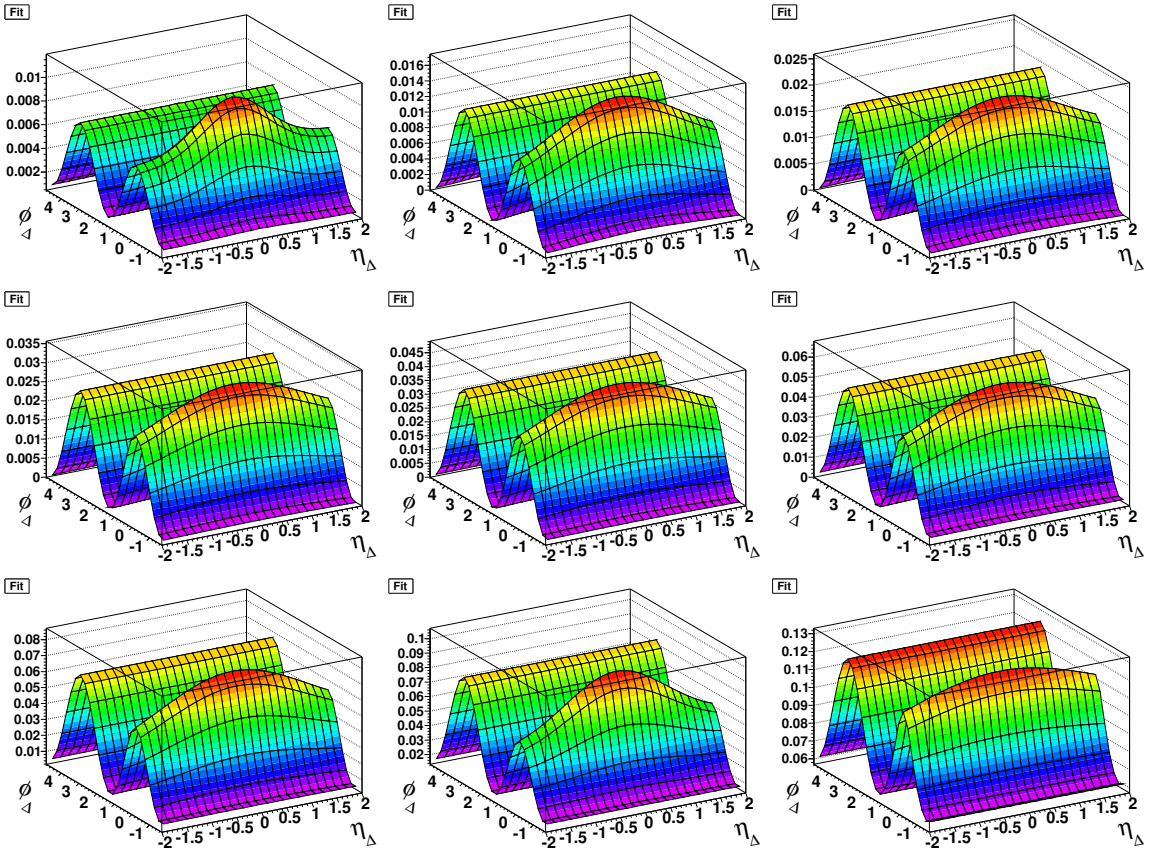

Figure A.20: Fits to the histograms for 200 GeV 30-40% central collisions. Starting from the upper left the y_t bins are $y_t < 1.4$, $1.4 < y_t < 1.8$, $1.8 < y_t < 2.2$, $2.2 < y_t < 2.6$, $2.6 < y_t < 3.0$, $3.0 < y_t < 3.4$, $3.4 < y_t < 3.8$, $3.8 < y_t < 4.2$, and $y_t > 4.2$.

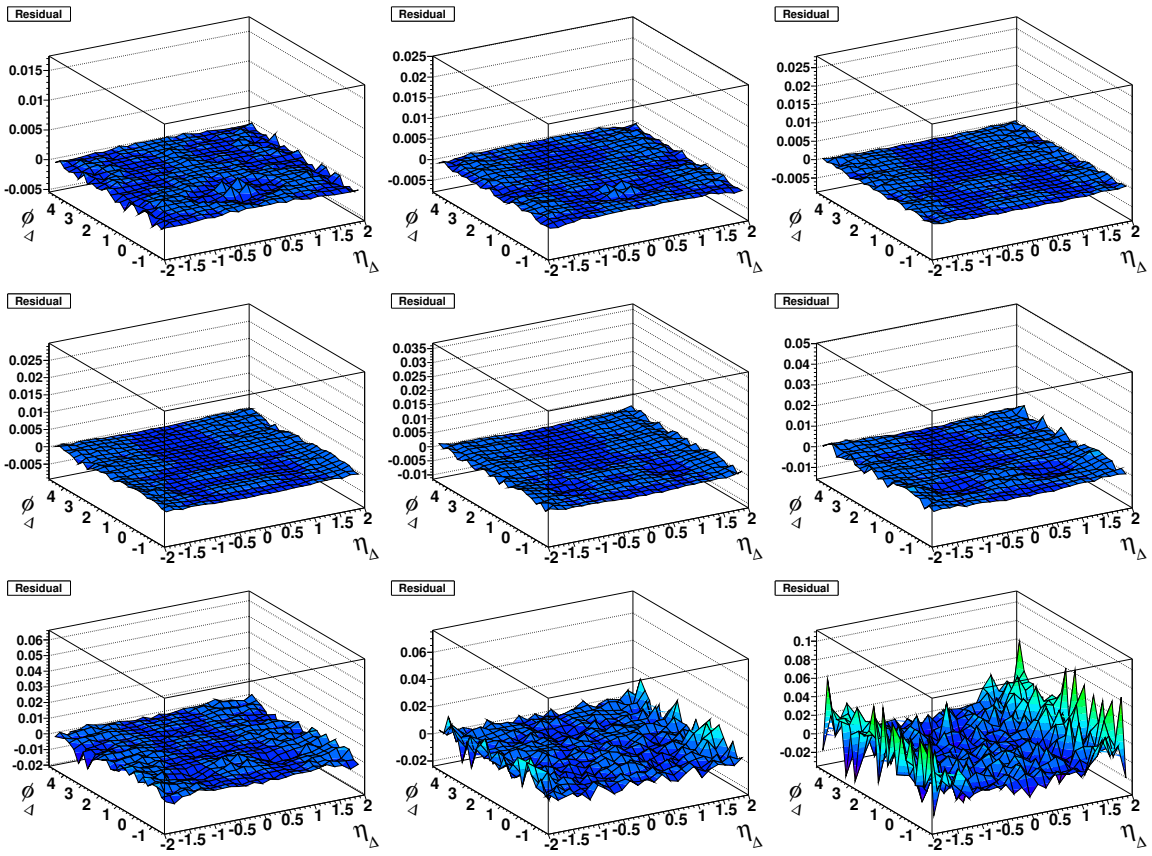

Figure A.21: Residuals for the fits to the histograms for 200 GeV 30-40% central collisions. Starting from the upper left the y_t bins are $y_t < 1.4$, $1.4 < y_t < 1.8$, $1.8 < y_t < 2.2$, $2.2 < y_t < 2.6$, $2.6 < y_t < 3.0$, $3.0 < y_t < 3.4$, $3.4 < y_t < 3.8$, $3.8 < y_t < 4.2$, and $y_t > 4.2$.

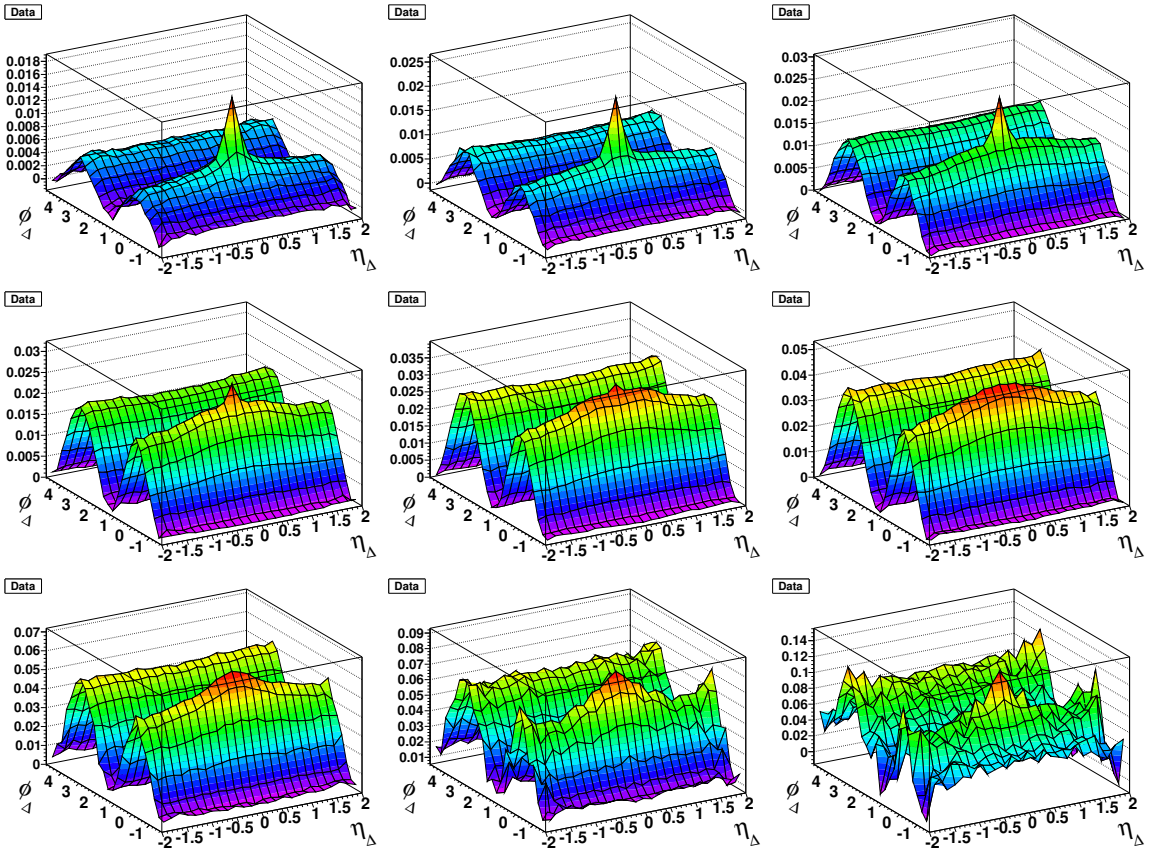

Figure A.22: Data histograms for 200 GeV 20-30% central collisions. Starting from the upper left the y_t bins are $y_t < 1.4$, $1.4 < y_t < 1.8$, $1.8 < y_t < 2.2$, $2.2 < y_t < 2.6$, $2.6 < y_t < 3.0$, $3.0 < y_t < 3.4$, $3.4 < y_t < 3.8$, $3.8 < y_t < 4.2$, and $y_t > 4.2$.

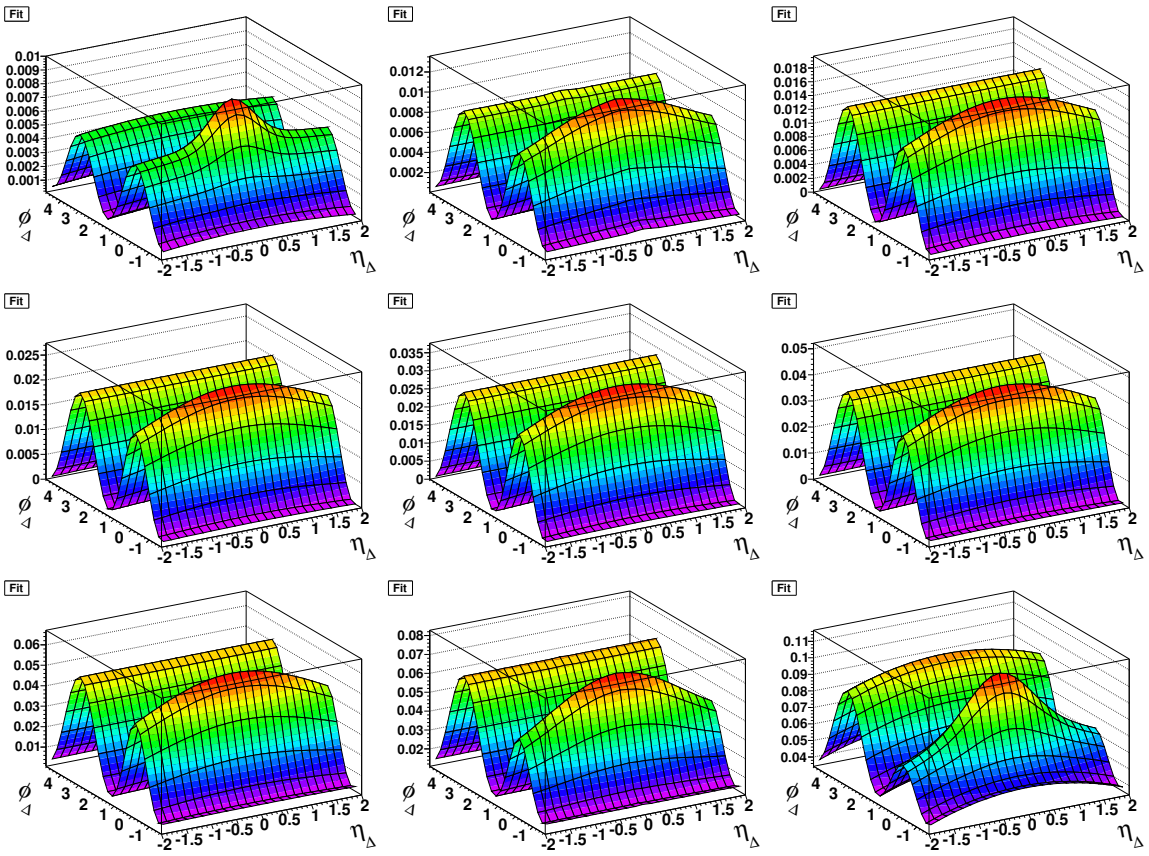

Figure A.23: Fits to the histograms for 200 GeV 20-30% central collisions. Starting from the upper left the y_t bins are $y_t < 1.4$, $1.4 < y_t < 1.8$, $1.8 < y_t < 2.2$, $2.2 < y_t < 2.6$, $2.6 < y_t < 3.0$, $3.0 < y_t < 3.4$, $3.4 < y_t < 3.8$, $3.8 < y_t < 4.2$, and $y_t > 4.2$.

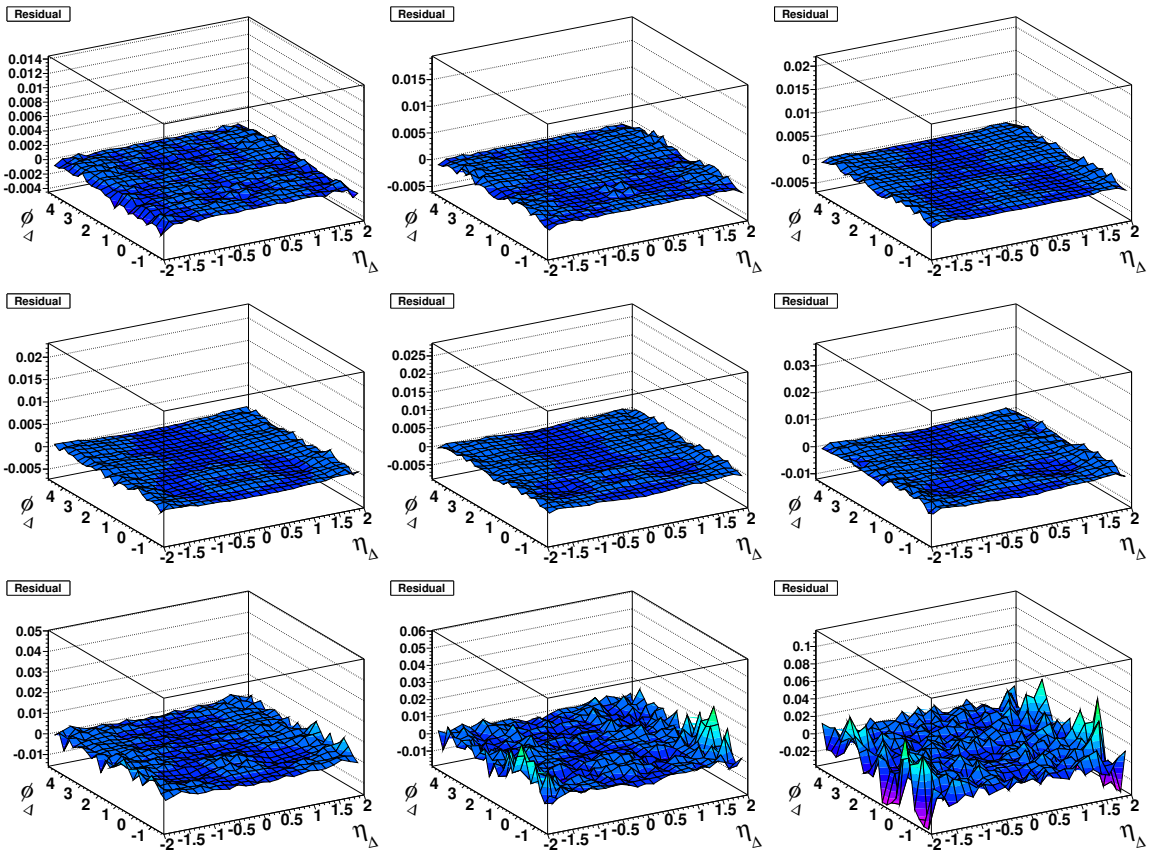

Figure A.24: Residuals for the fits to the histograms for 200 GeV 20-30% central collisions. Starting from the upper left the y_t bins are $y_t < 1.4$, $1.4 < y_t < 1.8$, $1.8 < y_t < 2.2$, $2.2 < y_t < 2.6$, $2.6 < y_t < 3.0$, $3.0 < y_t < 3.4$, $3.4 < y_t < 3.8$, $3.8 < y_t < 4.2$, and $y_t > 4.2$.

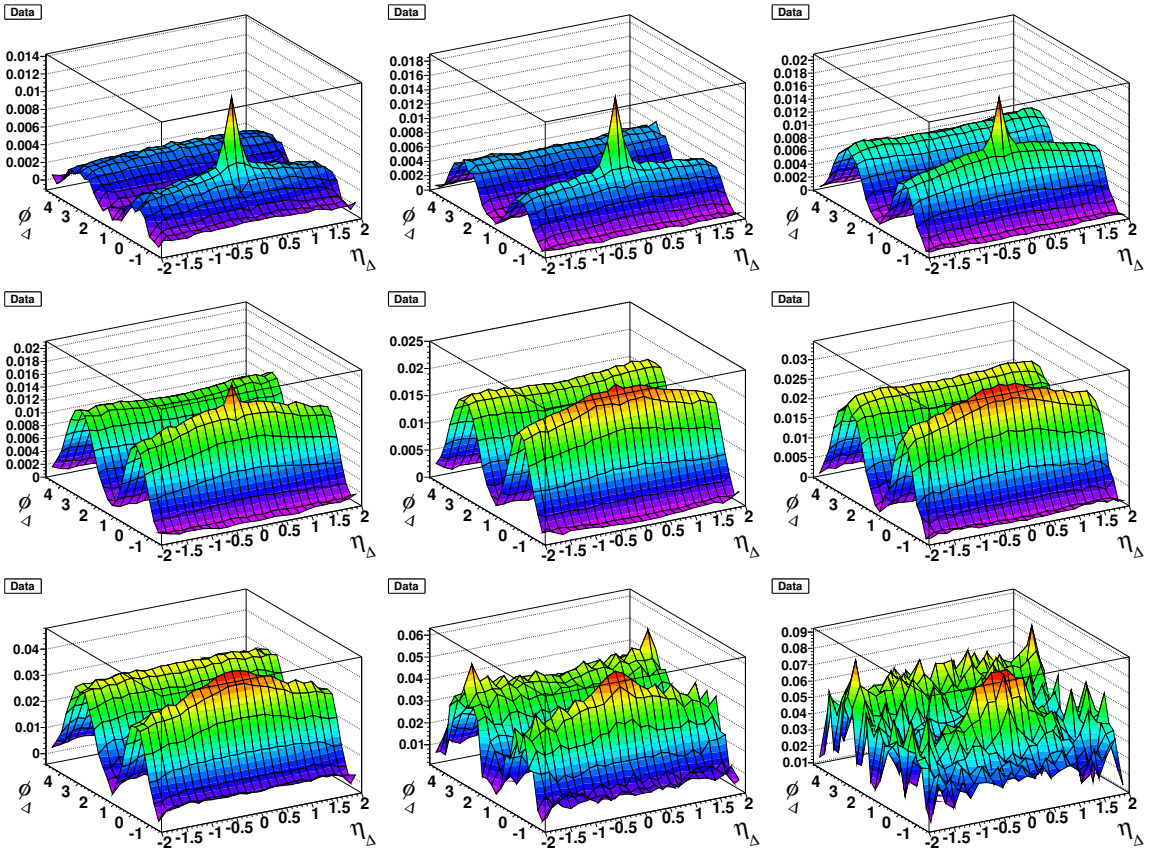

Figure A.25: Data histograms for 200 GeV 10-20% central collisions. Starting from the upper left the y_t bins are $y_t < 1.4$, $1.4 < y_t < 1.8$, $1.8 < y_t < 2.2$, $2.2 < y_t < 2.6$, $2.6 < y_t < 3.0$, $3.0 < y_t < 3.4$, $3.4 < y_t < 3.8$, $3.8 < y_t < 4.2$, and $y_t > 4.2$.

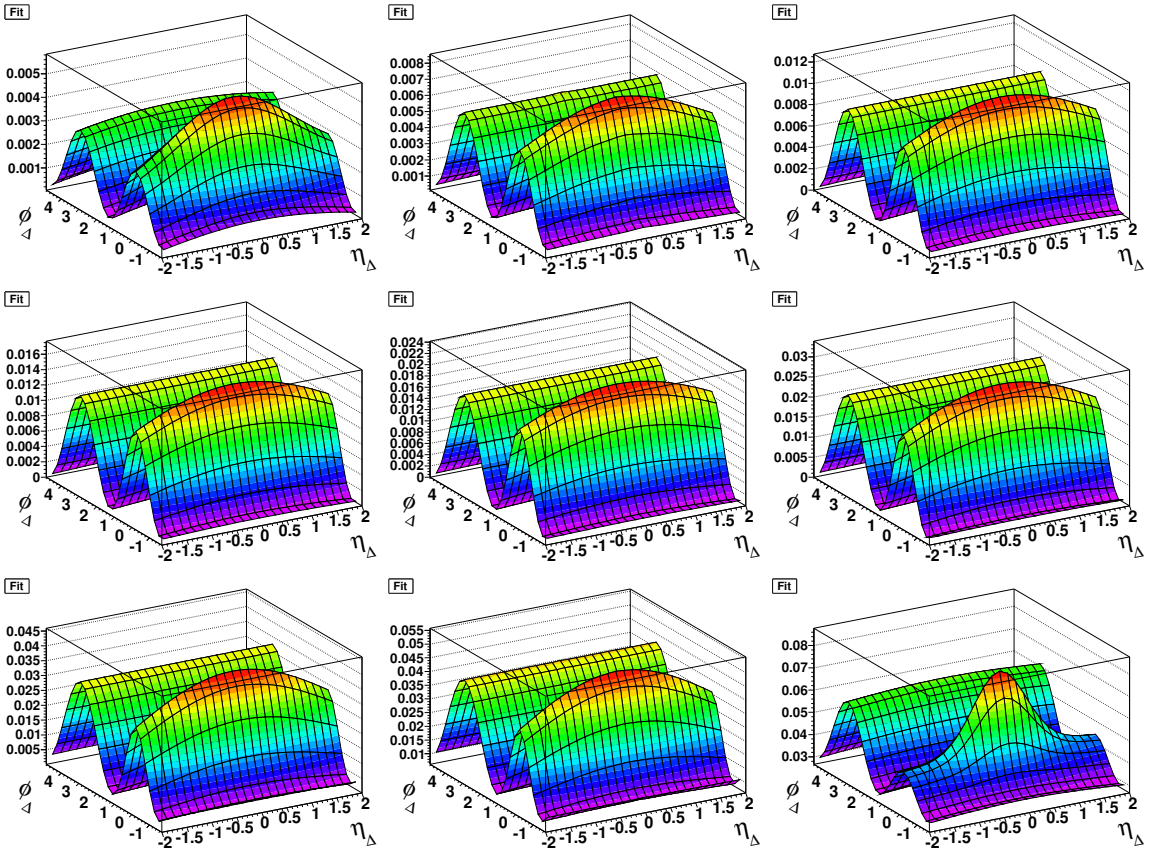

Figure A.26: Fits to the histograms for 200 GeV 10-20% central collisions. Starting from the upper left the y_t bins are $y_t < 1.4$, $1.4 < y_t < 1.8$, $1.8 < y_t < 2.2$, $2.2 < y_t < 2.6$, $2.6 < y_t < 3.0$, $3.0 < y_t < 3.4$, $3.4 < y_t < 3.8$, $3.8 < y_t < 4.2$, and $y_t > 4.2$.

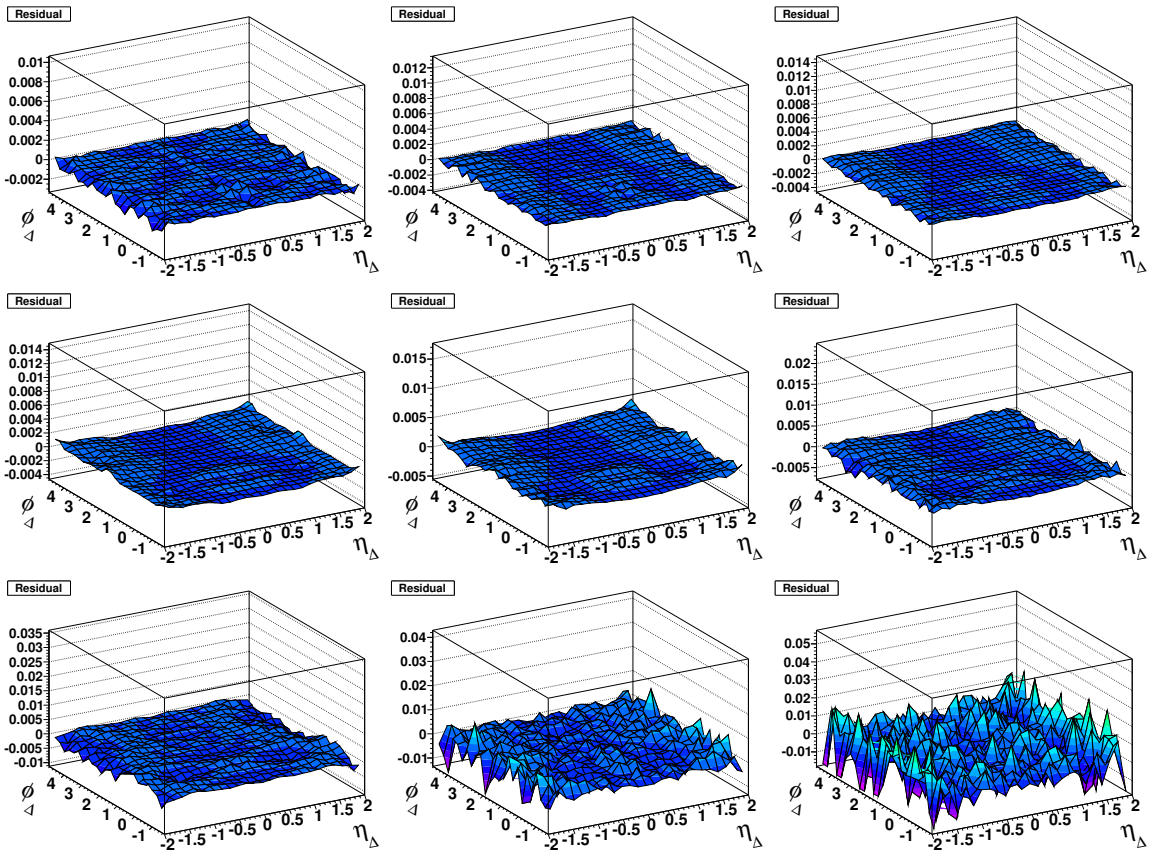

Figure A.27: Residuals for the fits to the histograms for 200 GeV 10-20% central collisions. Starting from the upper left the y_t bins are $y_t < 1.4$, $1.4 < y_t < 1.8$, $1.8 < y_t < 2.2$, $2.2 < y_t < 2.6$, $2.6 < y_t < 3.0$, $3.0 < y_t < 3.4$, $3.4 < y_t < 3.8$, $3.8 < y_t < 4.2$, and $y_t > 4.2$.

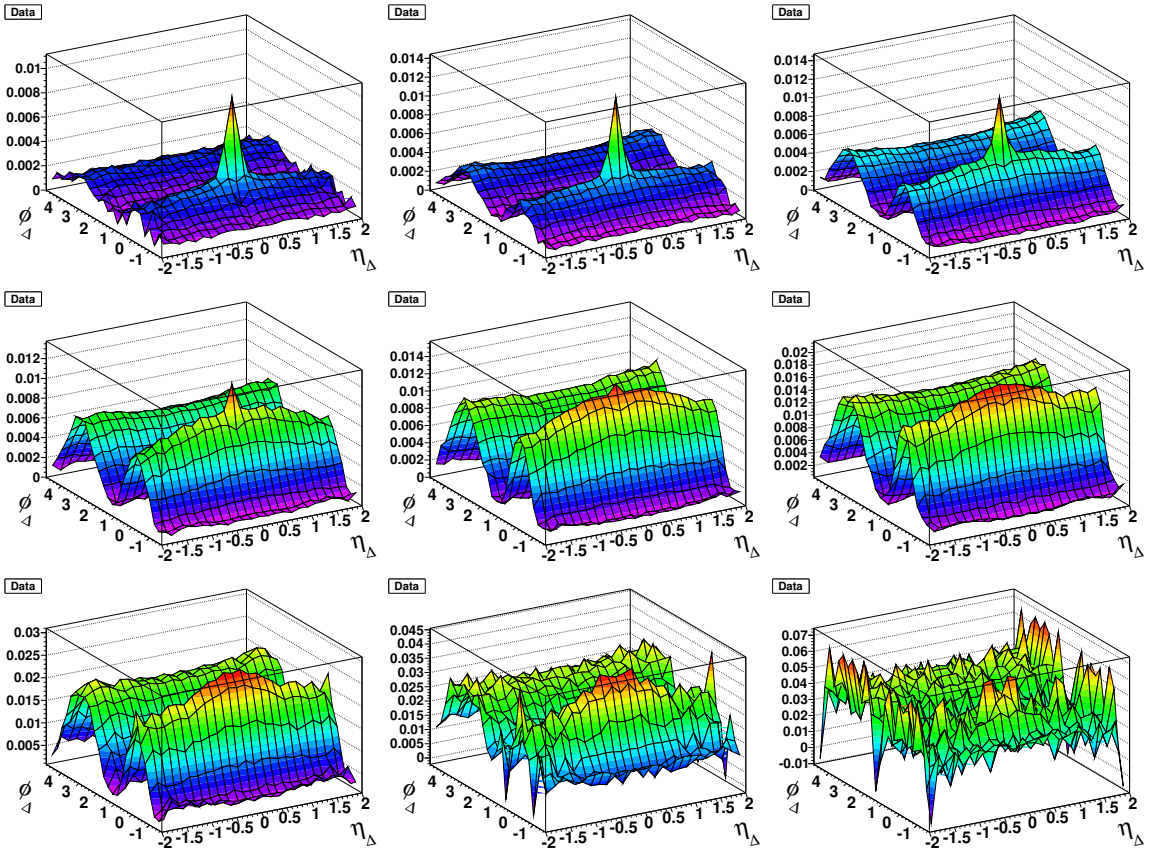

Figure A.28: Data histograms for 200 GeV 5-10% central collisions. Starting from the upper left the y_t bins are $y_t < 1.4$, $1.4 < y_t < 1.8$, $1.8 < y_t < 2.2$, $2.2 < y_t < 2.6$, $2.6 < y_t < 3.0$, $3.0 < y_t < 3.4$, $3.4 < y_t < 3.8$, $3.8 < y_t < 4.2$, and $y_t > 4.2$.

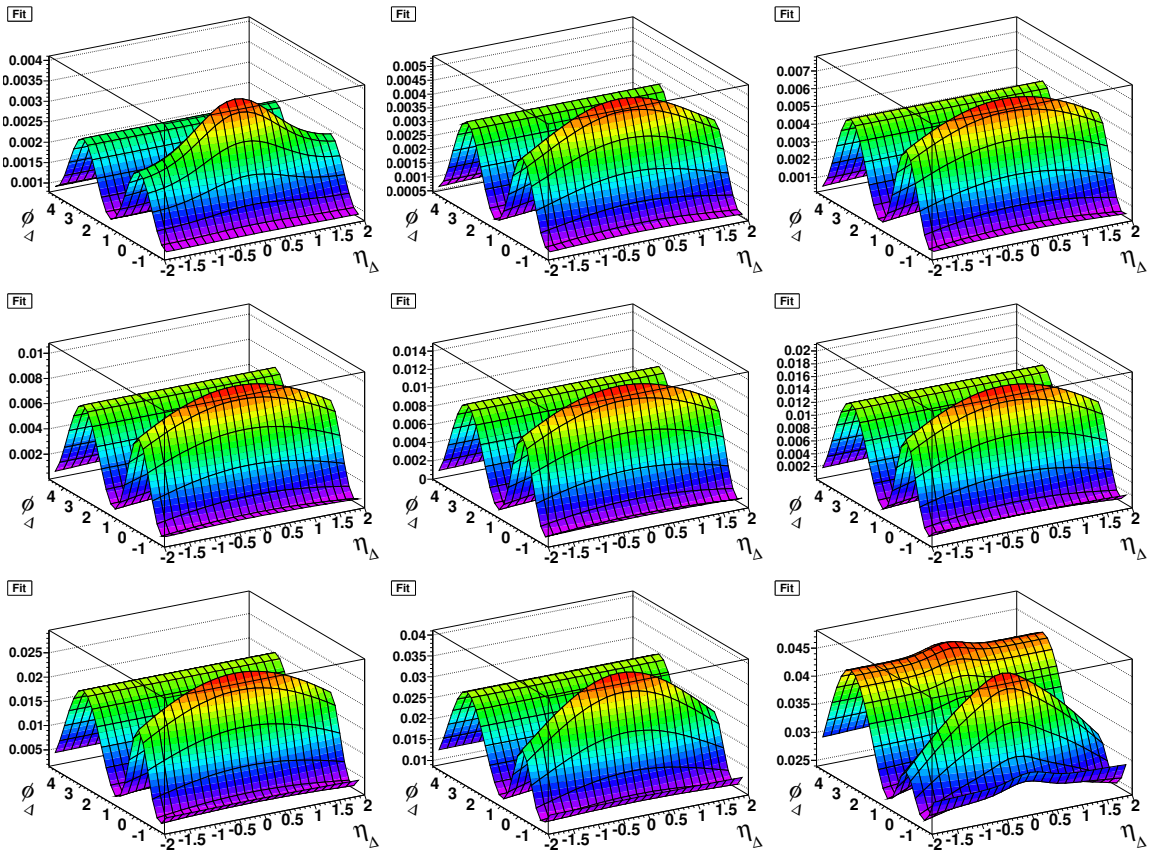

Figure A.29: Fits to the histograms for 200 GeV 5-10% central collisions. Starting from the upper left the y_t bins are $y_t < 1.4$, $1.4 < y_t < 1.8$, $1.8 < y_t < 2.2$, $2.2 < y_t < 2.6$, $2.6 < y_t < 3.0$, $3.0 < y_t < 3.4$, $3.4 < y_t < 3.8$, $3.8 < y_t < 4.2$, and $y_t > 4.2$.

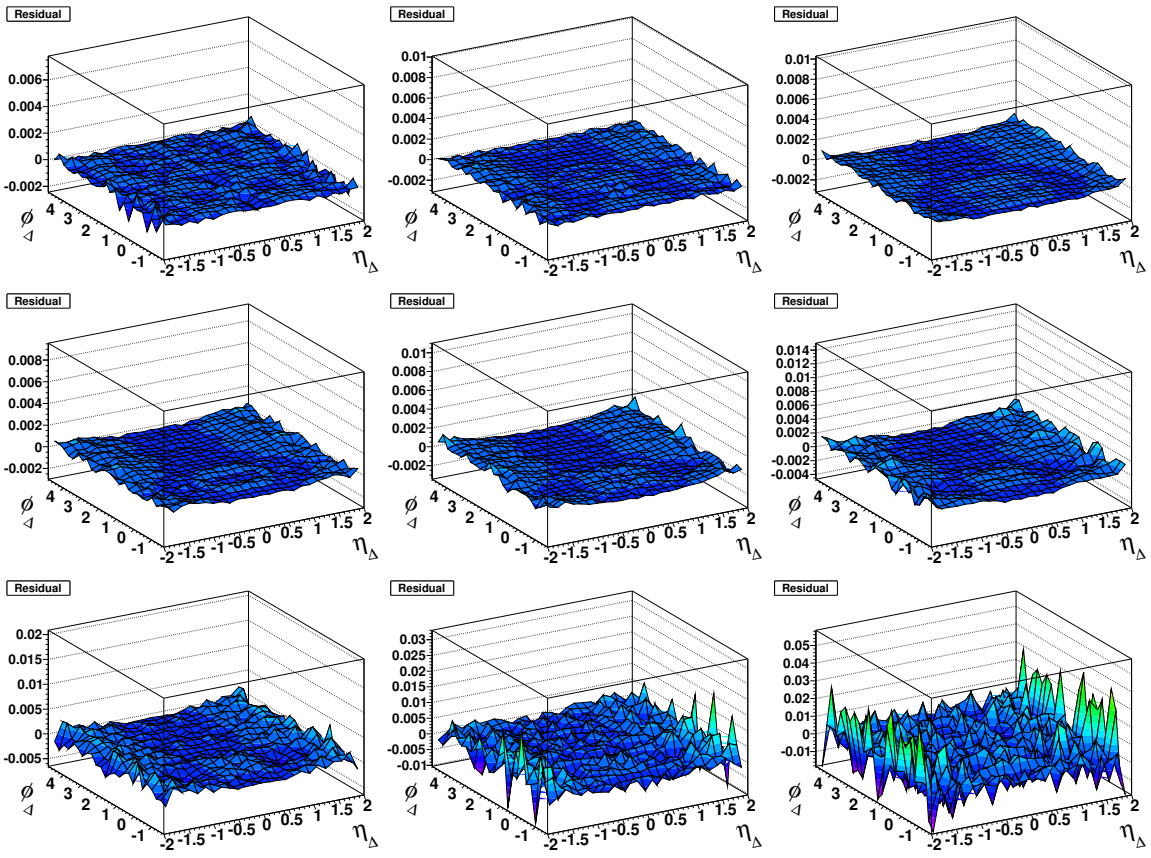

Figure A.30: Residuals for the fits to the histograms for 200 GeV 5-10% central collisions. Starting from the upper left the y_t bins are $y_t < 1.4$, $1.4 < y_t < 1.8$, $1.8 < y_t < 2.2$, $2.2 < y_t < 2.6$, $2.6 < y_t < 3.0$, $3.0 < y_t < 3.4$, $3.4 < y_t < 3.8$, $3.8 < y_t < 4.2$, and $y_t > 4.2$.

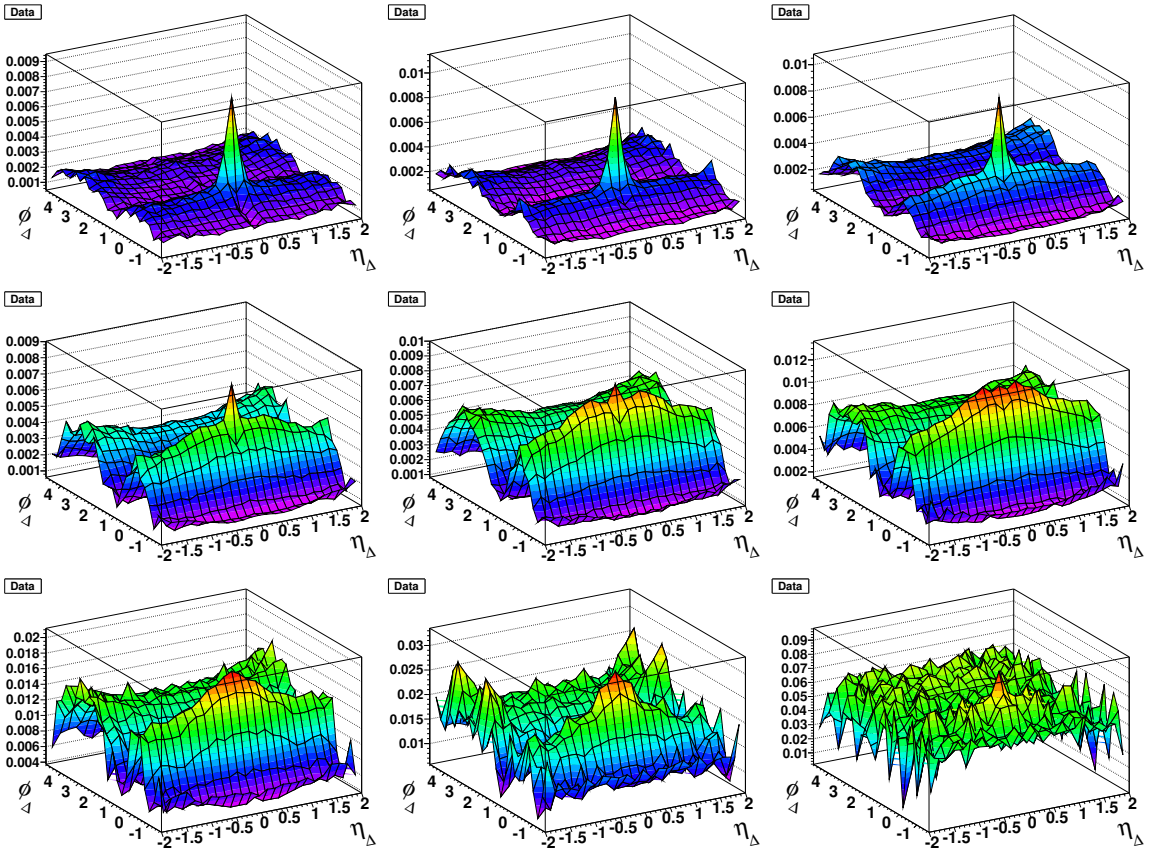

Figure A.31: Data histograms for 200 GeV 0-5% central collisions. Starting from the upper left the y_t bins are $y_t < 1.4$, $1.4 < y_t < 1.8$, $1.8 < y_t < 2.2$, $2.2 < y_t < 2.6$, $2.6 < y_t < 3.0$, $3.0 < y_t < 3.4$, $3.4 < y_t < 3.8$, $3.8 < y_t < 4.2$, and $y_t > 4.2$.

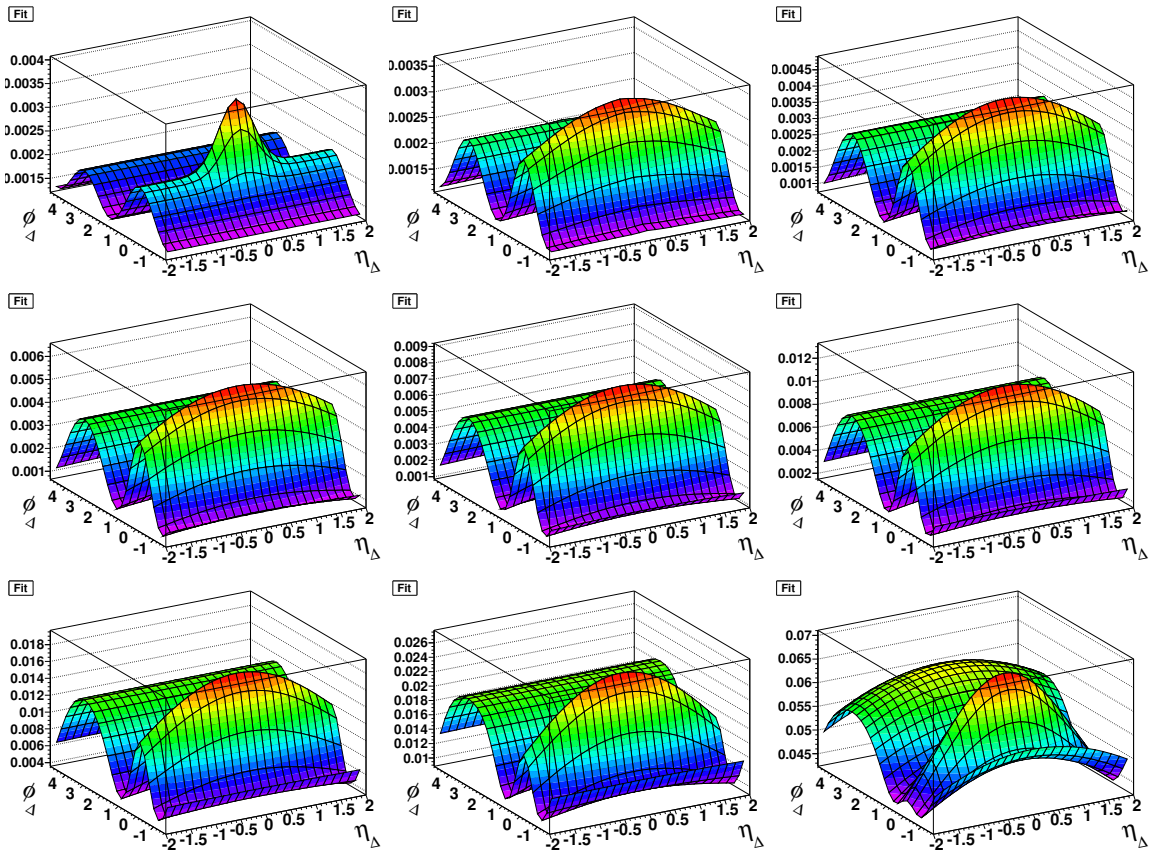

Figure A.32: Fits to the histograms for 200 GeV 0-5% central collisions. Starting from the upper left the y_t bins are $y_t < 1.4$, $1.4 < y_t < 1.8$, $1.8 < y_t < 2.2$, $2.2 < y_t < 2.6$, $2.6 < y_t < 3.0$, $3.0 < y_t < 3.4$, $3.4 < y_t < 3.8$, $3.8 < y_t < 4.2$, and $y_t > 4.2$.

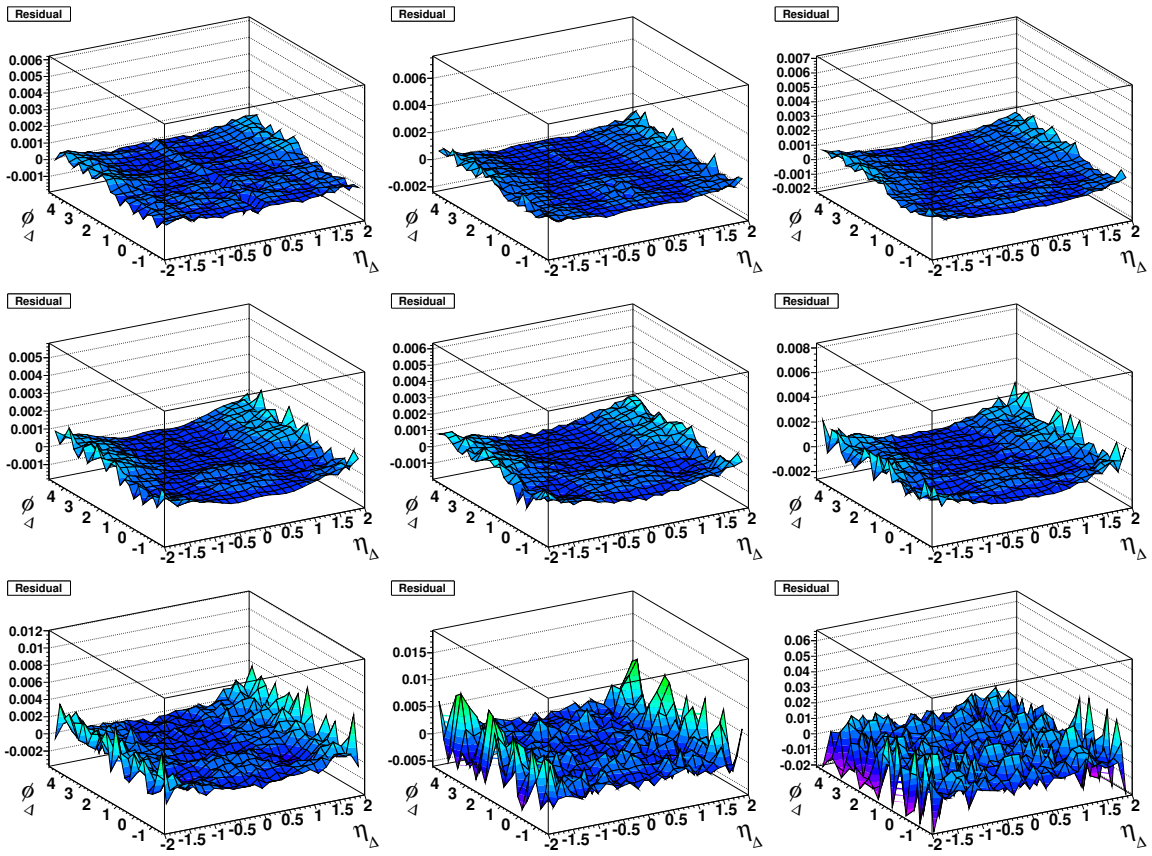

Figure A.33: Residuals for the fits to the histograms for 200 GeV 0-5% central collisions. Starting from the upper left the y_t bins are $y_t < 1.4$, $1.4 < y_t < 1.8$, $1.8 < y_t < 2.2$, $2.2 < y_t < 2.6$, $2.6 < y_t < 3.0$, $3.0 < y_t < 3.4$, $3.4 < y_t < 3.8$, $3.8 < y_t < 4.2$, and $y_t > 4.2$.

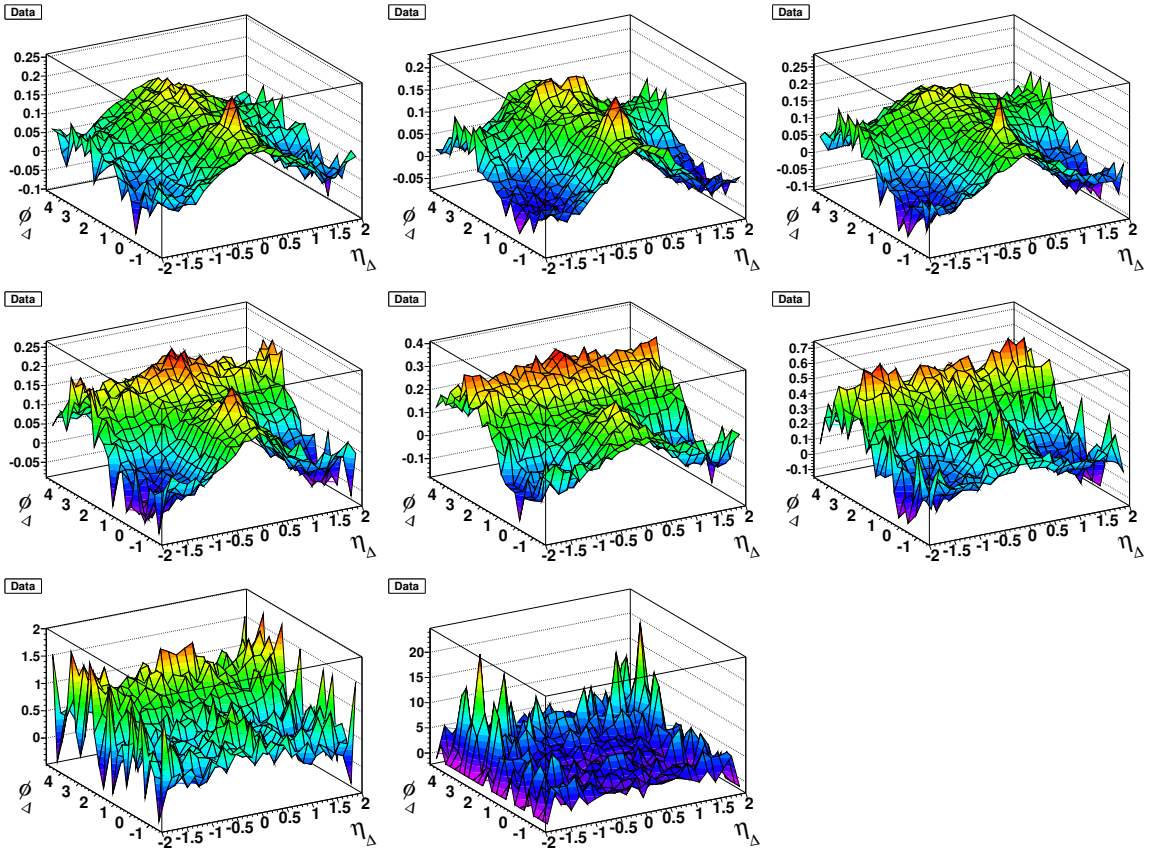

Figure A.34: Data histograms for 62 GeV 90-100% central collisions. Starting from the upper left the y_t bins are $y_t < 1.4$, $1.4 < y_t < 1.8$, $1.8 < y_t < 2.2$, $2.2 < y_t < 2.6$, $2.6 < y_t < 3.0$, $3.0 < y_t < 3.4$, $3.4 < y_t < 3.8$, and $3.8 < y_t < 4.2$.

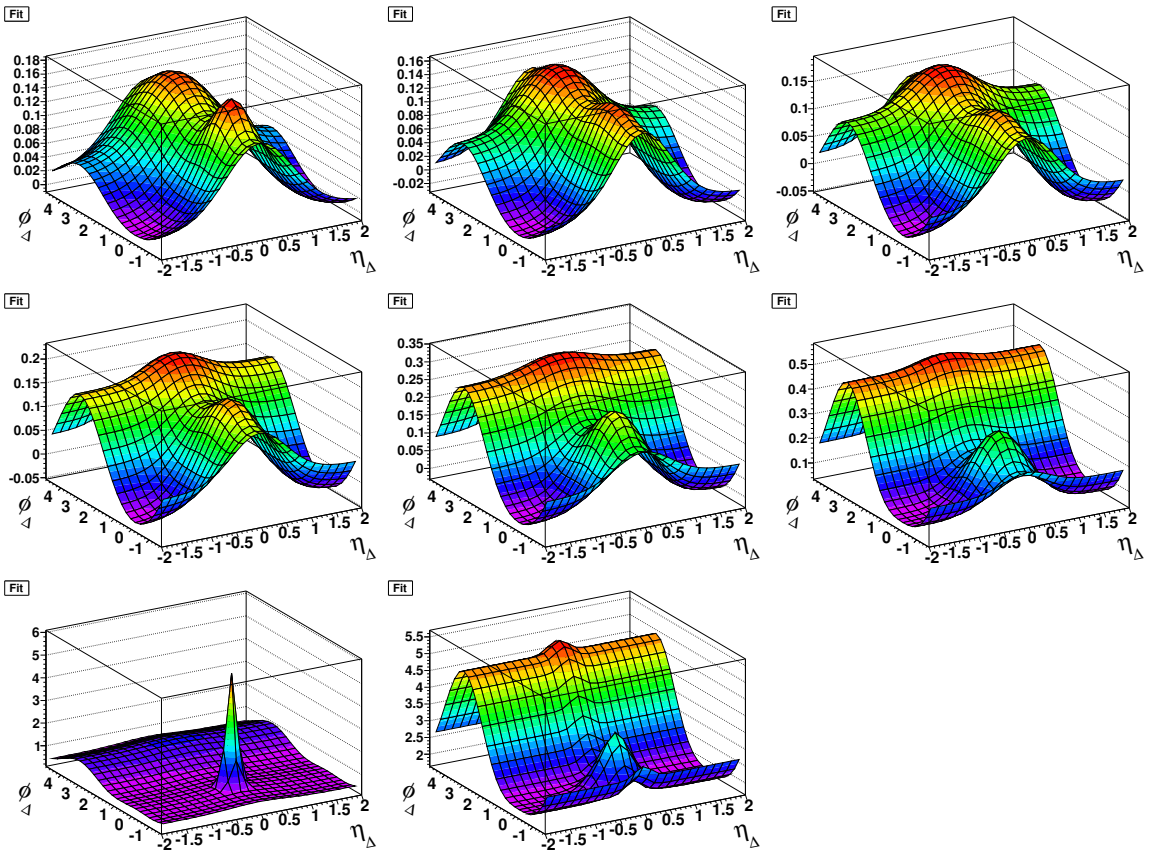

Figure A.35: Fits to the histograms for 62 GeV 90-100% central collisions. Starting from the upper left the y_t bins are $y_t < 1.4$, $1.4 < y_t < 1.8$, $1.8 < y_t < 2.2$, $2.2 < y_t < 2.6$, $2.6 < y_t < 3.0$, $3.0 < y_t < 3.4$, $3.4 < y_t < 3.8$ and $3.8 < y_t < 4.2$.

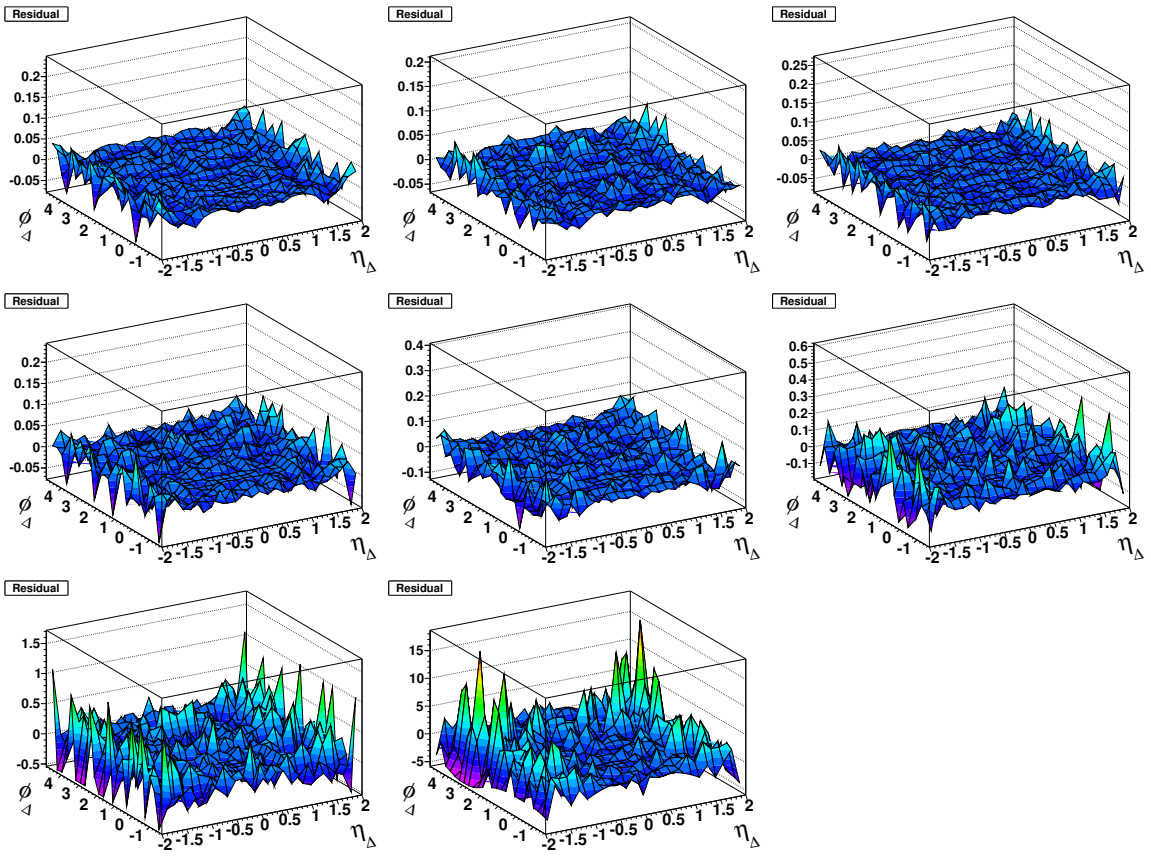

Figure A.36: Residuals for the fits to the histograms for 62 GeV 90-100% central collisions. Starting from the upper left the y_t bins are $y_t < 1.4$, $1.4 < y_t < 1.8$, $1.8 < y_t < 2.2$, $2.2 < y_t < 2.6$, $2.6 < y_t < 3.0$, $3.0 < y_t < 3.4$, $3.4 < y_t < 3.8$ and $3.8 < y_t < 4.2$.

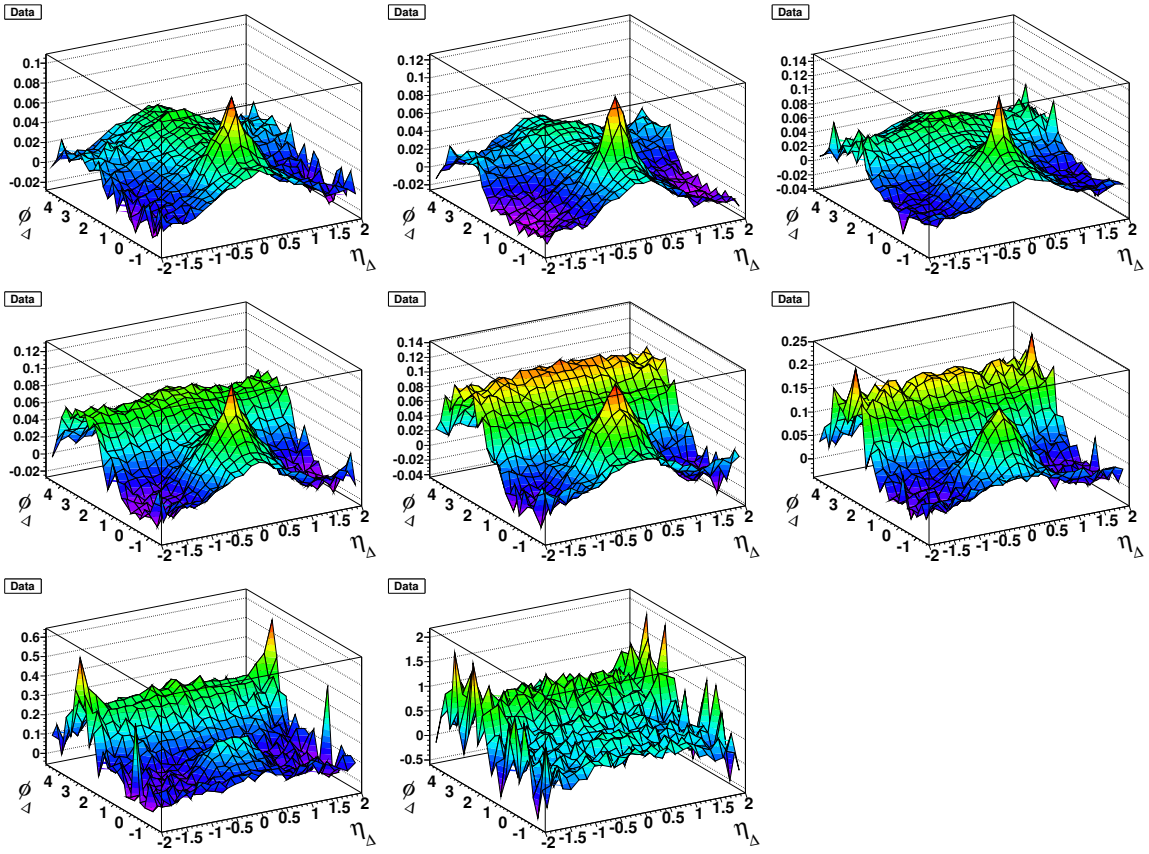

Figure A.37: Data histograms for 62 GeV 80-90% central collisions. Starting from the upper left the y_t bins are $y_t < 1.4$, $1.4 < y_t < 1.8$, $1.8 < y_t < 2.2$, $2.2 < y_t < 2.6$, $2.6 < y_t < 3.0$, $3.0 < y_t < 3.4$, $3.4 < y_t < 3.8$, and $3.8 < y_t < 4.2$.

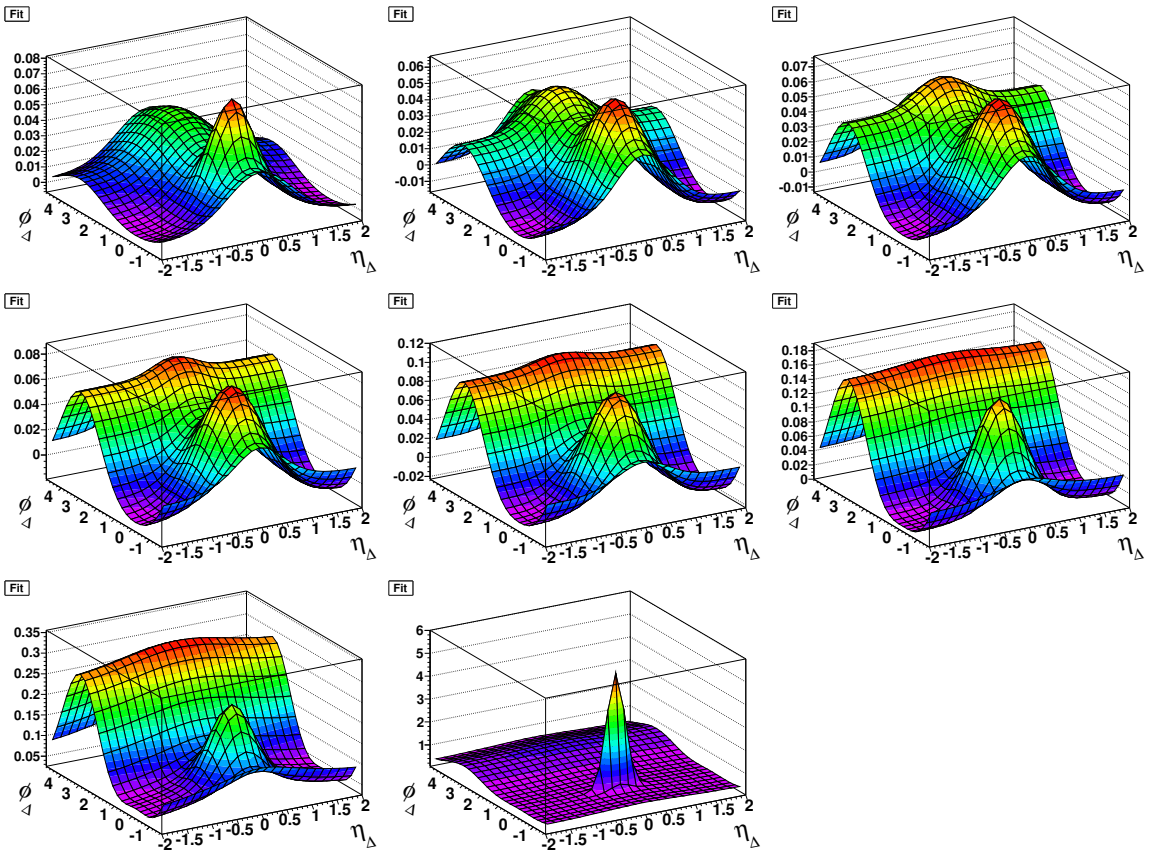

Figure A.38: Fits to the histograms for 62 GeV 80-90% central collisions. Starting from the upper left the y_t bins are $y_t < 1.4$, $1.4 < y_t < 1.8$, $1.8 < y_t < 2.2$, $2.2 < y_t < 2.6$, $2.6 < y_t < 3.0$, $3.0 < y_t < 3.4$, $3.4 < y_t < 3.8$ and $3.8 < y_t < 4.2$.

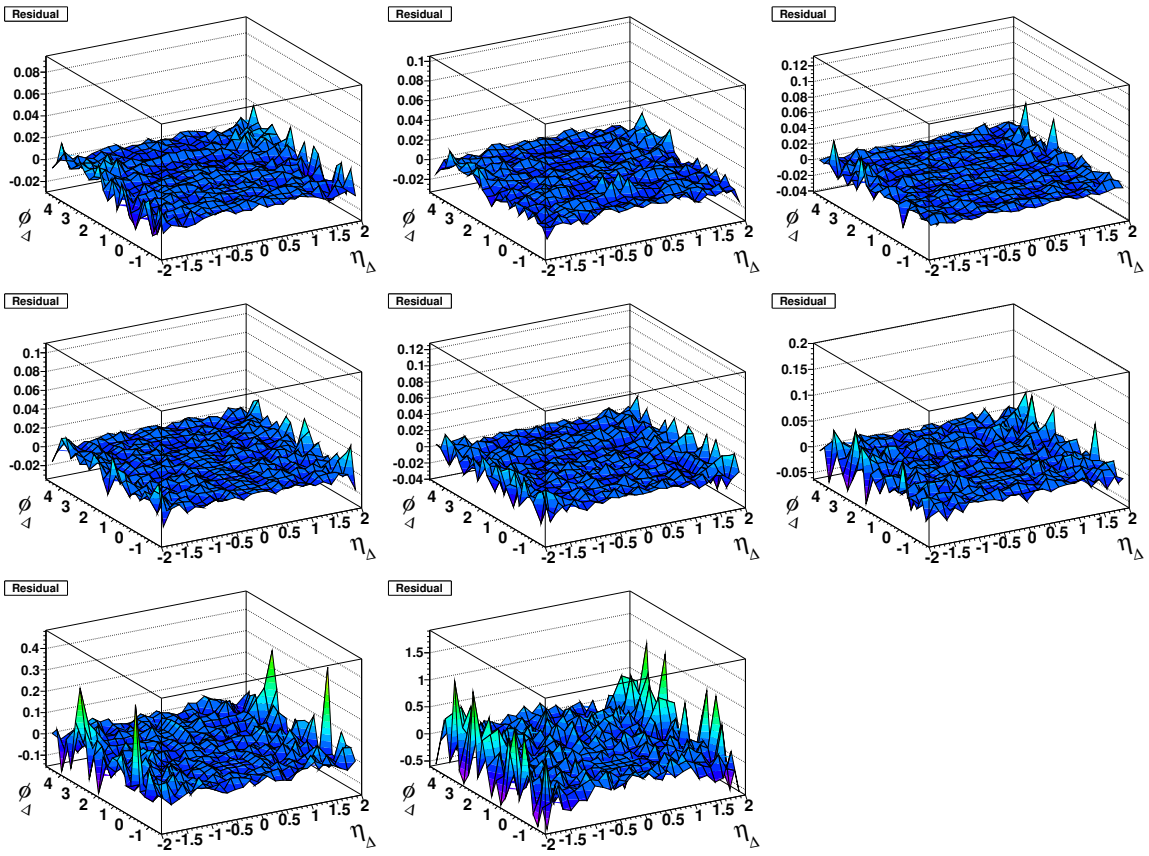

Figure A.39: Residuals for the fits to the histograms for 62 GeV 80-90% central collisions. Starting from the upper left the y_t bins are $y_t < 1.4$, $1.4 < y_t < 1.8$, $1.8 < y_t < 2.2$, $2.2 < y_t < 2.6$, $2.6 < y_t < 3.0$, $3.0 < y_t < 3.4$, $3.4 < y_t < 3.8$ and $3.8 < y_t < 4.2$.

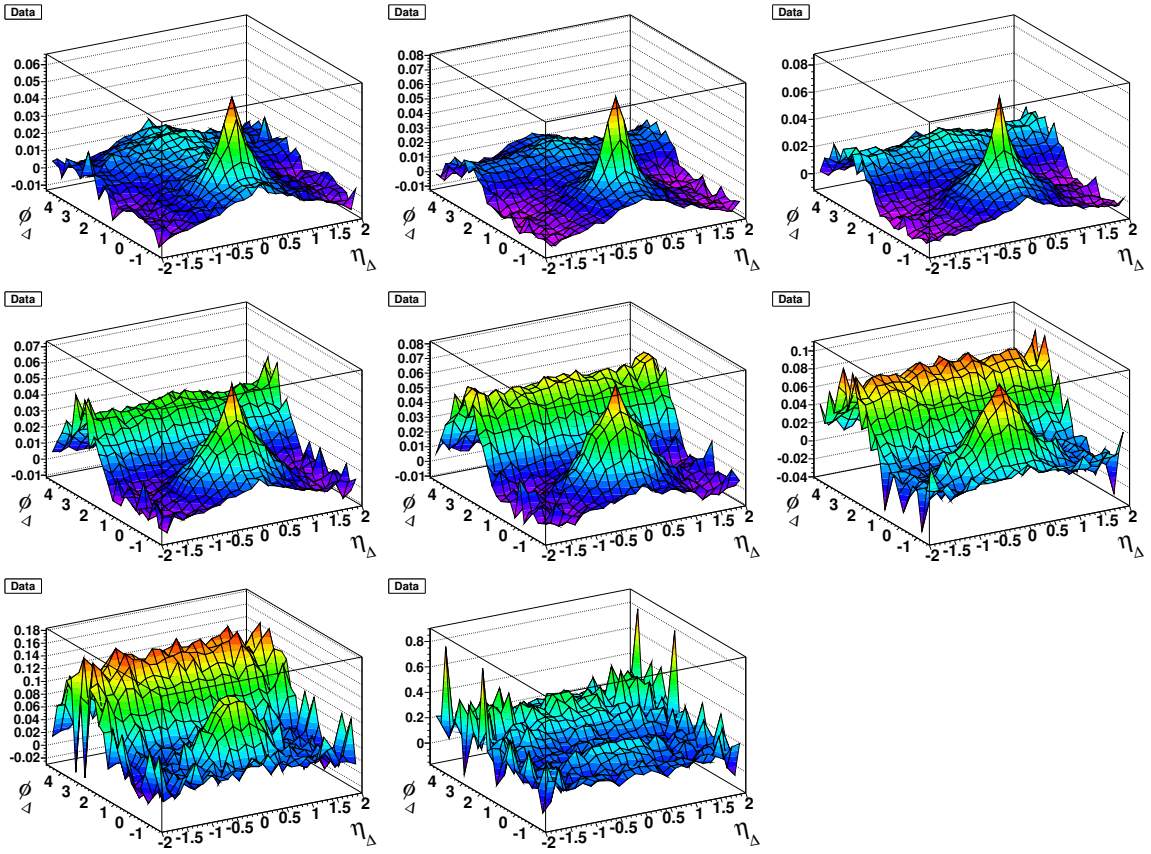

Figure A.40: Data histograms for 62 GeV 70-80% central collisions. Starting from the upper left the y_t bins are $y_t < 1.4$, $1.4 < y_t < 1.8$, $1.8 < y_t < 2.2$, $2.2 < y_t < 2.6$, $2.6 < y_t < 3.0$, $3.0 < y_t < 3.4$, $3.4 < y_t < 3.8$, and $3.8 < y_t < 4.2$.

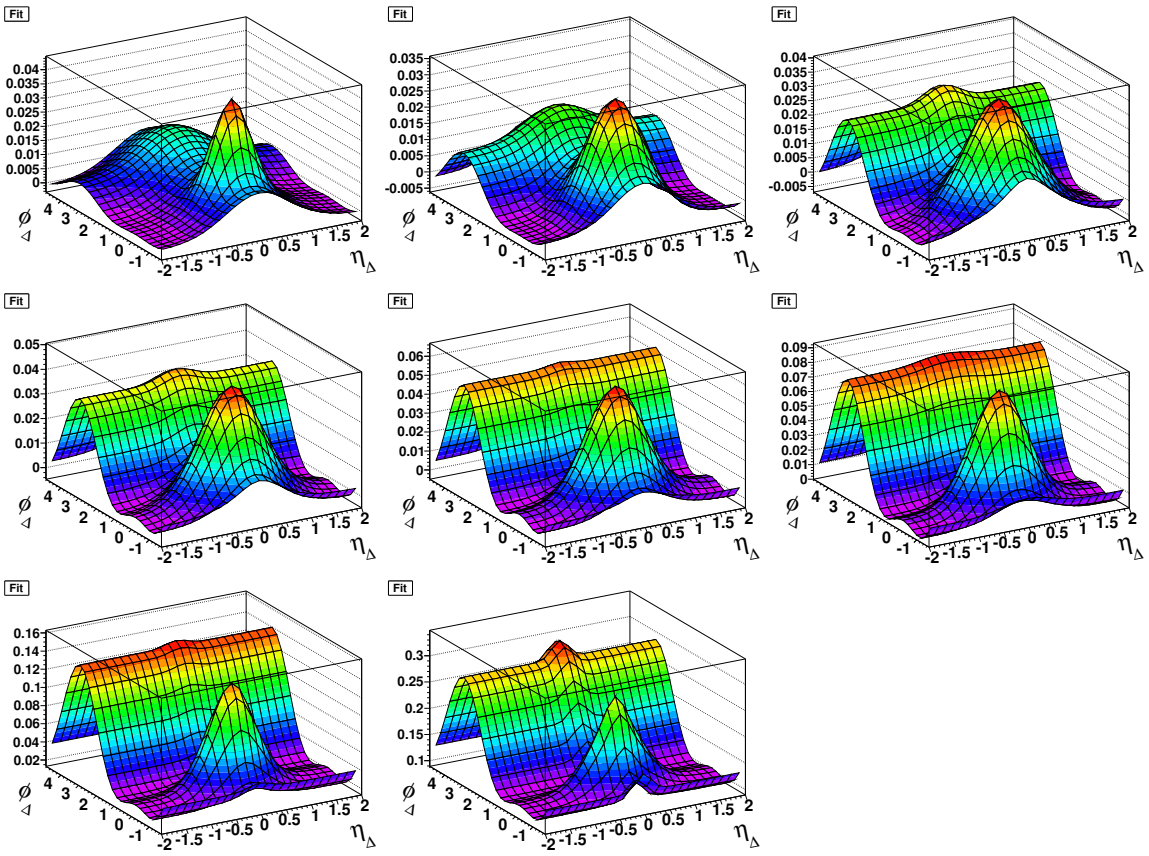

Figure A.41: Fits to the histograms for 62 GeV 70-80% central collisions. Starting from the upper left the y_t bins are $y_t < 1.4$, $1.4 < y_t < 1.8$, $1.8 < y_t < 2.2$, $2.2 < y_t < 2.6$, $2.6 < y_t < 3.0$, $3.0 < y_t < 3.4$, $3.4 < y_t < 3.8$ and $3.8 < y_t < 4.2$.

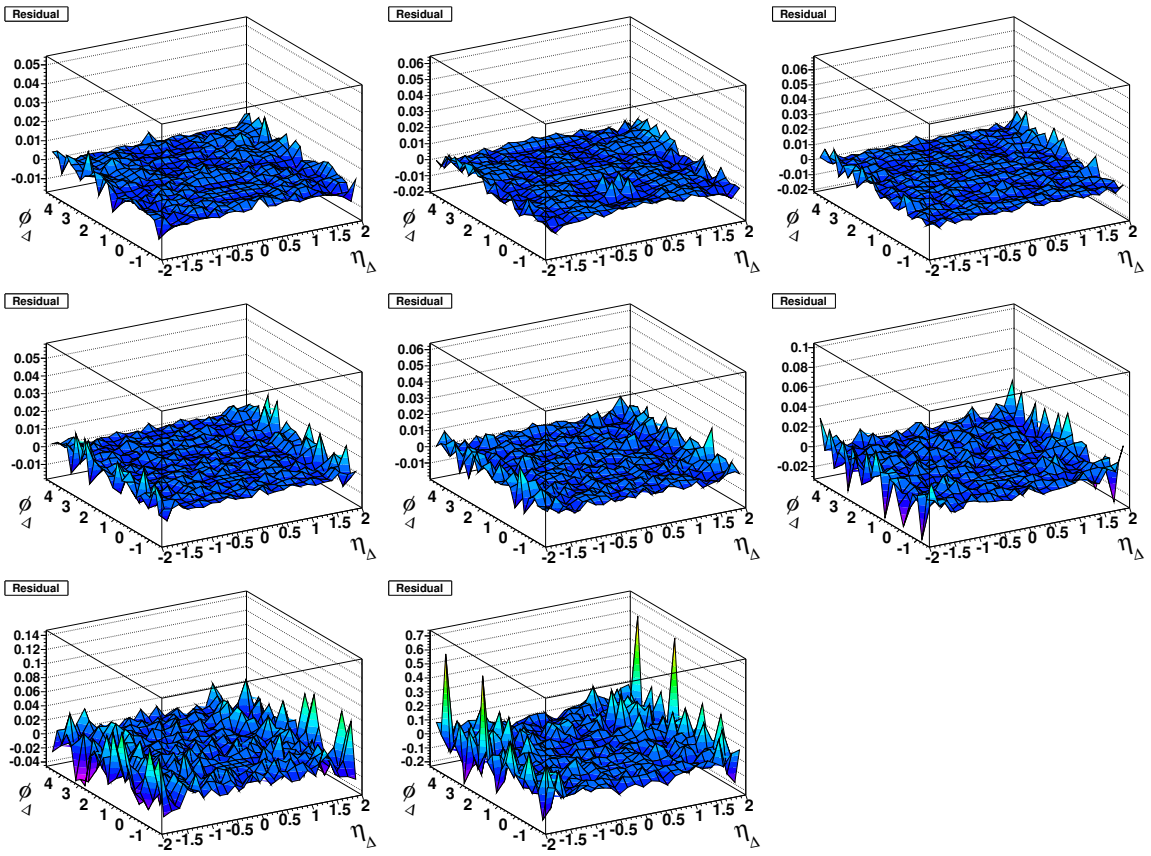

Figure A.42: Residuals for the fits to the histograms for 62 GeV 70-80% central collisions. Starting from the upper left the y_t bins are $y_t < 1.4$, $1.4 < y_t < 1.8$, $1.8 < y_t < 2.2$, $2.2 < y_t < 2.6$, $2.6 < y_t < 3.0$, $3.0 < y_t < 3.4$, $3.4 < y_t < 3.8$ and $3.8 < y_t < 4.2$.

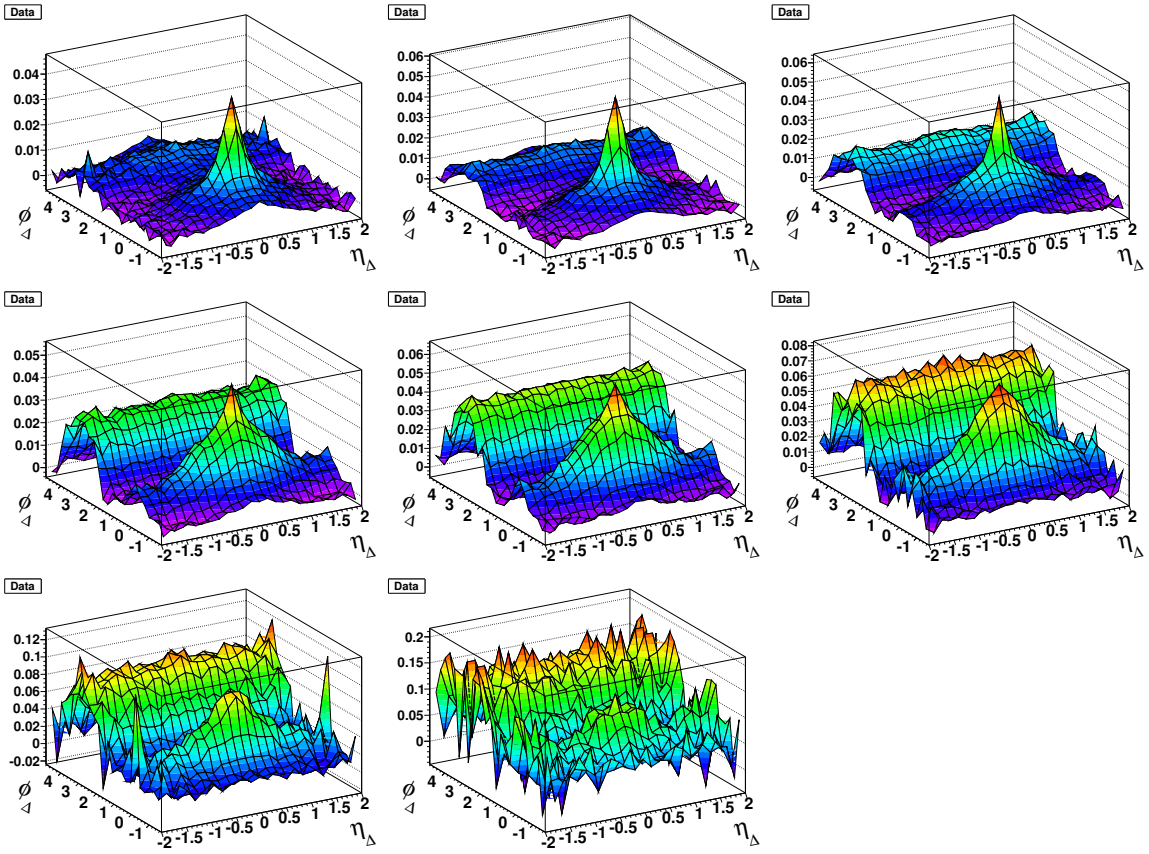

Figure A.43: Data histograms for 62 GeV 60-70% central collisions. Starting from the upper left the y_t bins are $y_t < 1.4$, $1.4 < y_t < 1.8$, $1.8 < y_t < 2.2$, $2.2 < y_t < 2.6$, $2.6 < y_t < 3.0$, $3.0 < y_t < 3.4$, $3.4 < y_t < 3.8$, and $3.8 < y_t < 4.2$.

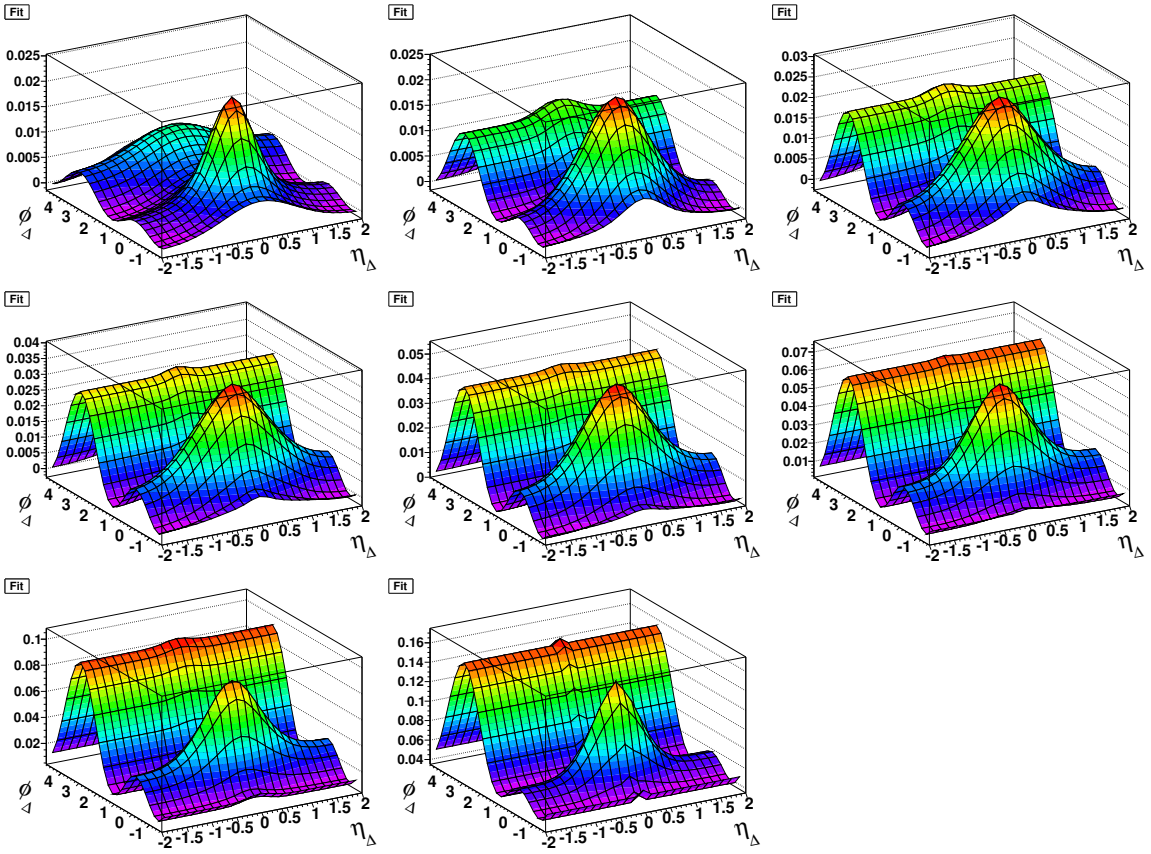

Figure A.44: Fits to the histograms for 62 GeV 60-70% central collisions. Starting from the upper left the y_t bins are $y_t < 1.4$, $1.4 < y_t < 1.8$, $1.8 < y_t < 2.2$, $2.2 < y_t < 2.6$, $2.6 < y_t < 3.0$, $3.0 < y_t < 3.4$, $3.4 < y_t < 3.8$ and $3.8 < y_t < 4.2$.

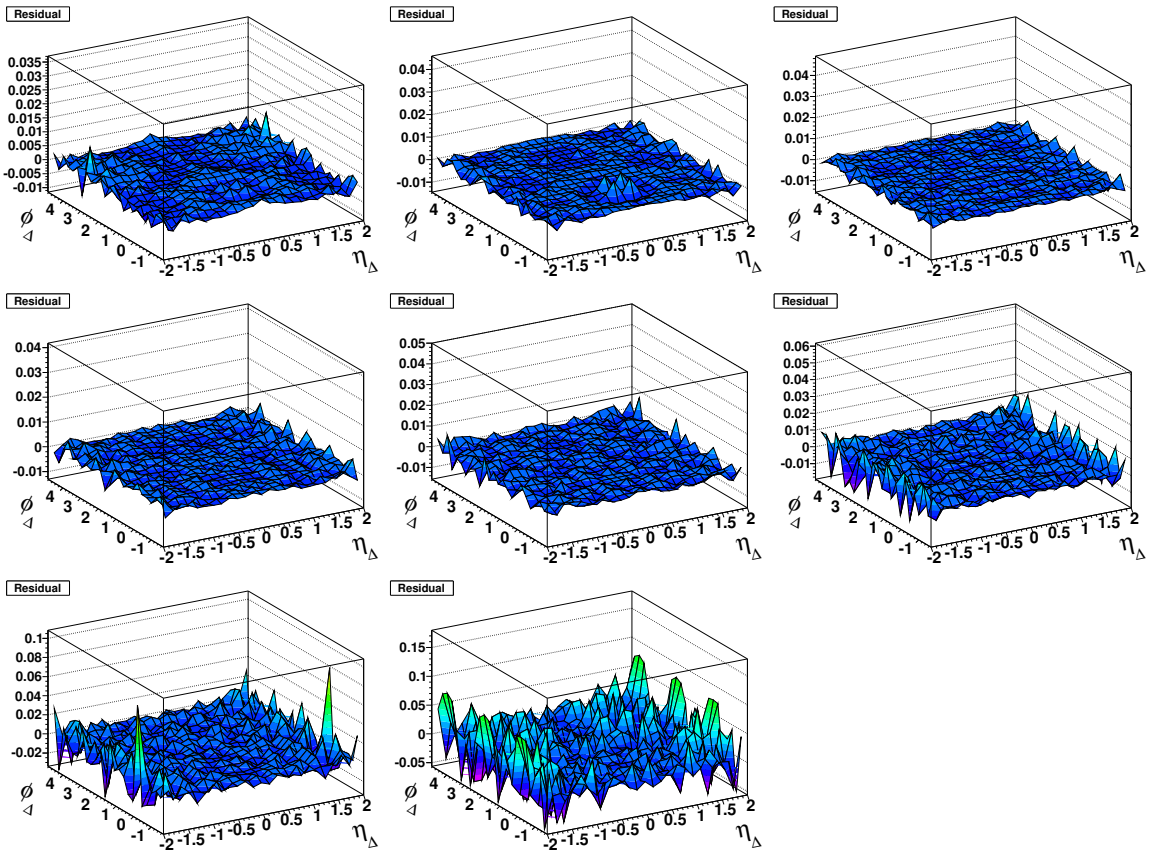

Figure A.45: Residuals for the fits to the histograms for 62 GeV 60-70% central collisions. Starting from the upper left the y_t bins are $y_t < 1.4$, $1.4 < y_t < 1.8$, $1.8 < y_t < 2.2$, $2.2 < y_t < 2.6$, $2.6 < y_t < 3.0$, $3.0 < y_t < 3.4$, $3.4 < y_t < 3.8$ and $3.8 < y_t < 4.2$.

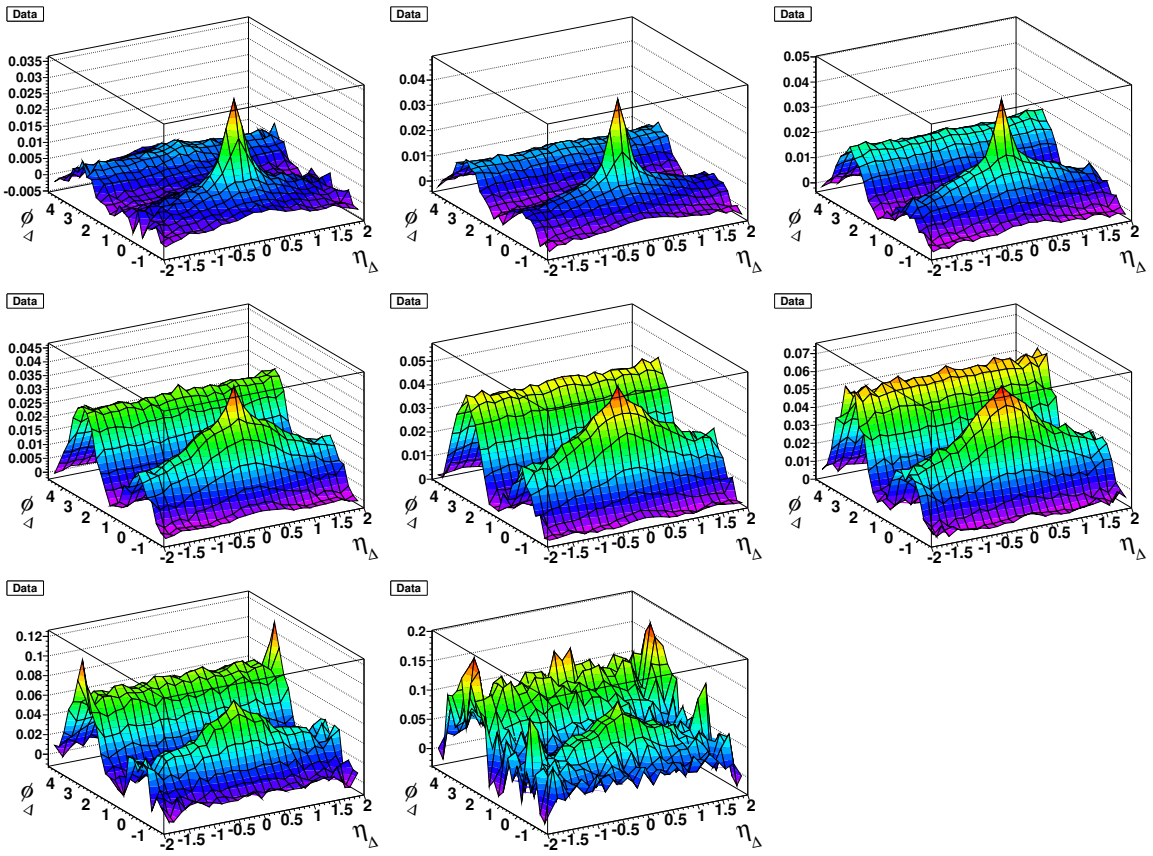

Figure A.46: Data histograms for 62 GeV 50-60% central collisions. Starting from the upper left the y_t bins are $y_t < 1.4$, $1.4 < y_t < 1.8$, $1.8 < y_t < 2.2$, $2.2 < y_t < 2.6$, $2.6 < y_t < 3.0$, $3.0 < y_t < 3.4$, $3.4 < y_t < 3.8$, and $3.8 < y_t < 4.2$.

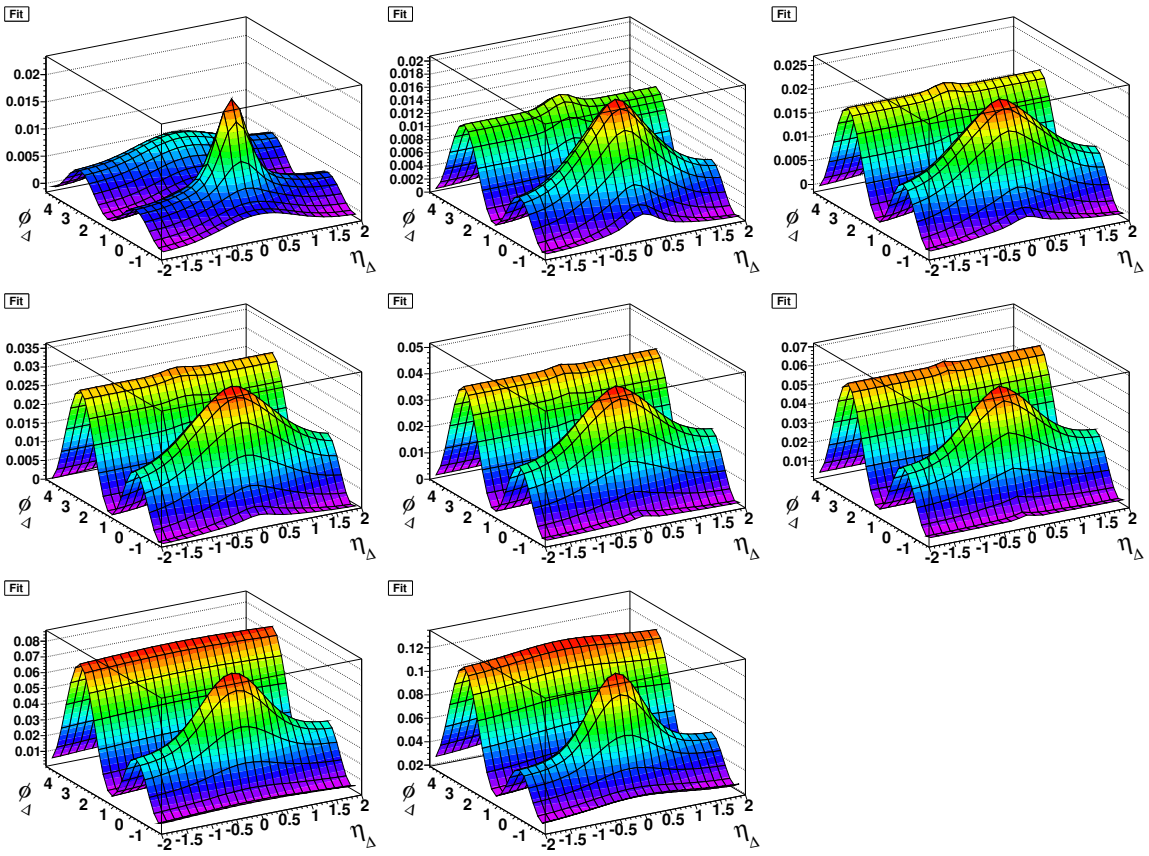

Figure A.47: Fits to the histograms for 62 GeV 50-60% central collisions. Starting from the upper left the y_t bins are $y_t < 1.4$, $1.4 < y_t < 1.8$, $1.8 < y_t < 2.2$, $2.2 < y_t < 2.6$, $2.6 < y_t < 3.0$, $3.0 < y_t < 3.4$, $3.4 < y_t < 3.8$ and $3.8 < y_t < 4.2$.

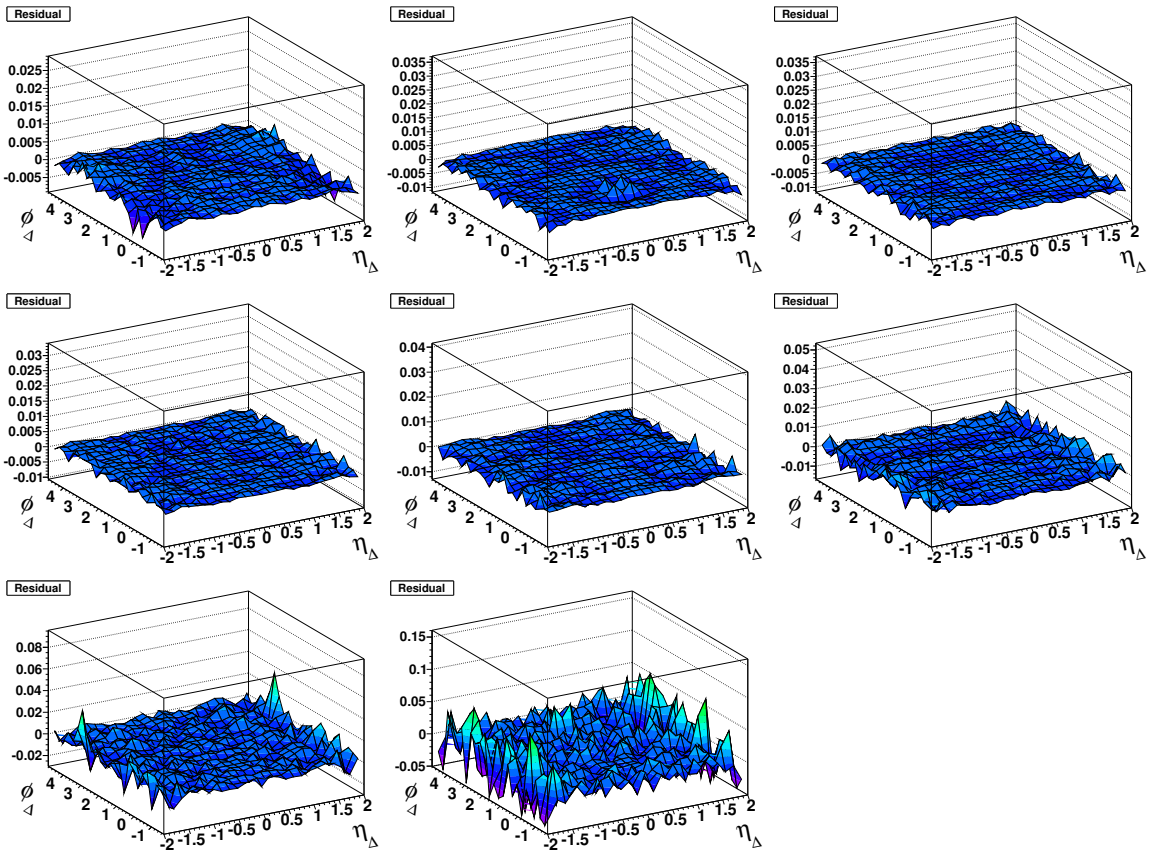

Figure A.48: Residuals for the fits to the histograms for 62 GeV 50-60% central collisions. Starting from the upper left the y_t bins are $y_t < 1.4$, $1.4 < y_t < 1.8$, $1.8 < y_t < 2.2$, $2.2 < y_t < 2.6$, $2.6 < y_t < 3.0$, $3.0 < y_t < 3.4$, $3.4 < y_t < 3.8$ and $3.8 < y_t < 4.2$.

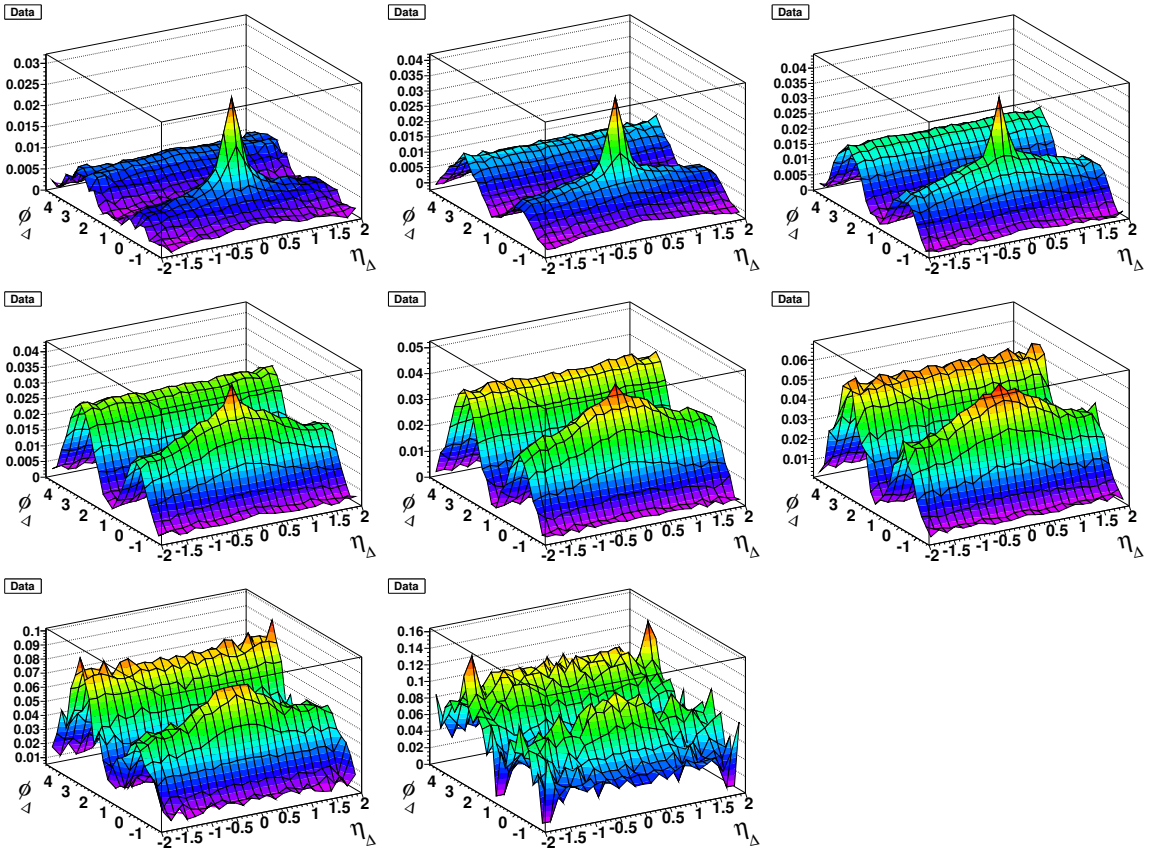

Figure A.49: Data histograms for 62 GeV 40-50% central collisions. Starting from the upper left the y_t bins are $y_t < 1.4$, $1.4 < y_t < 1.8$, $1.8 < y_t < 2.2$, $2.2 < y_t < 2.6$, $2.6 < y_t < 3.0$, $3.0 < y_t < 3.4$, $3.4 < y_t < 3.8$, and $3.8 < y_t < 4.2$.

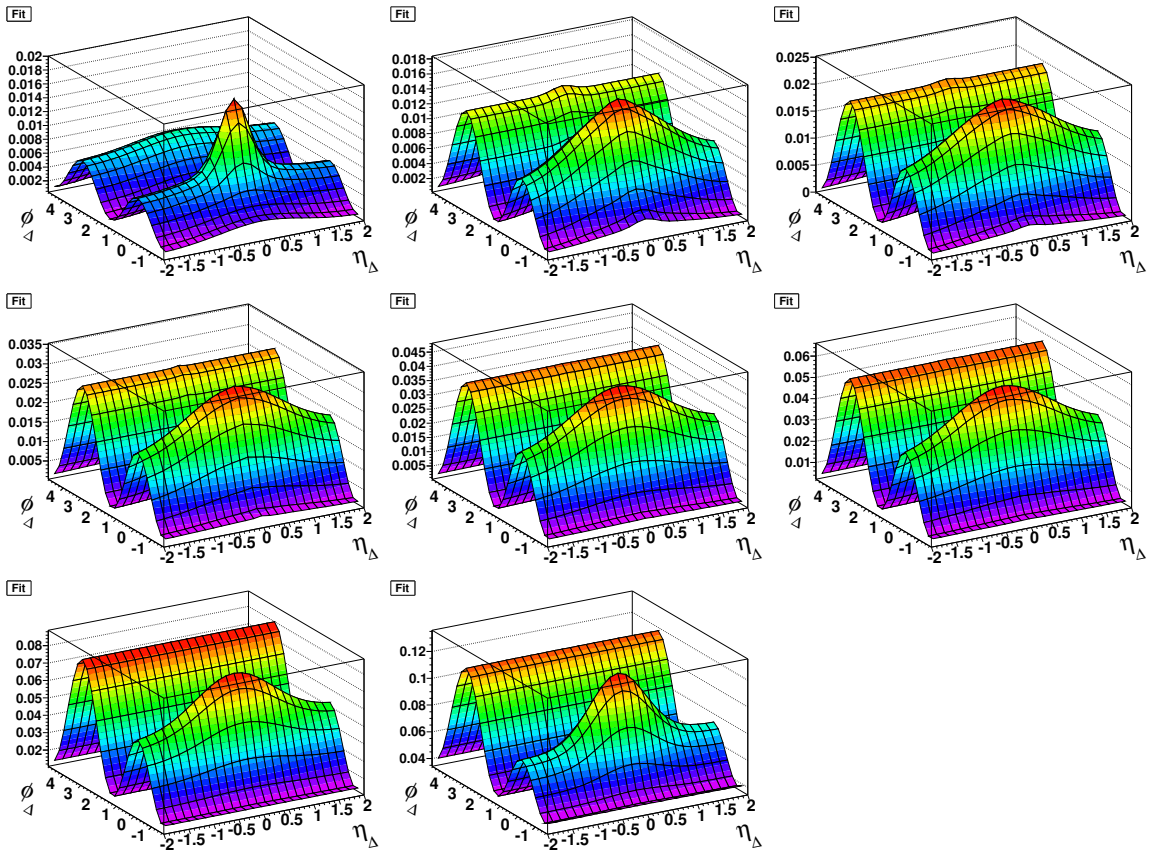

Figure A.50: Fits to the histograms for 62 GeV 40-50% central collisions. Starting from the upper left the y_t bins are $y_t < 1.4$, $1.4 < y_t < 1.8$, $1.8 < y_t < 2.2$, $2.2 < y_t < 2.6$, $2.6 < y_t < 3.0$, $3.0 < y_t < 3.4$, $3.4 < y_t < 3.8$ and $3.8 < y_t < 4.2$.

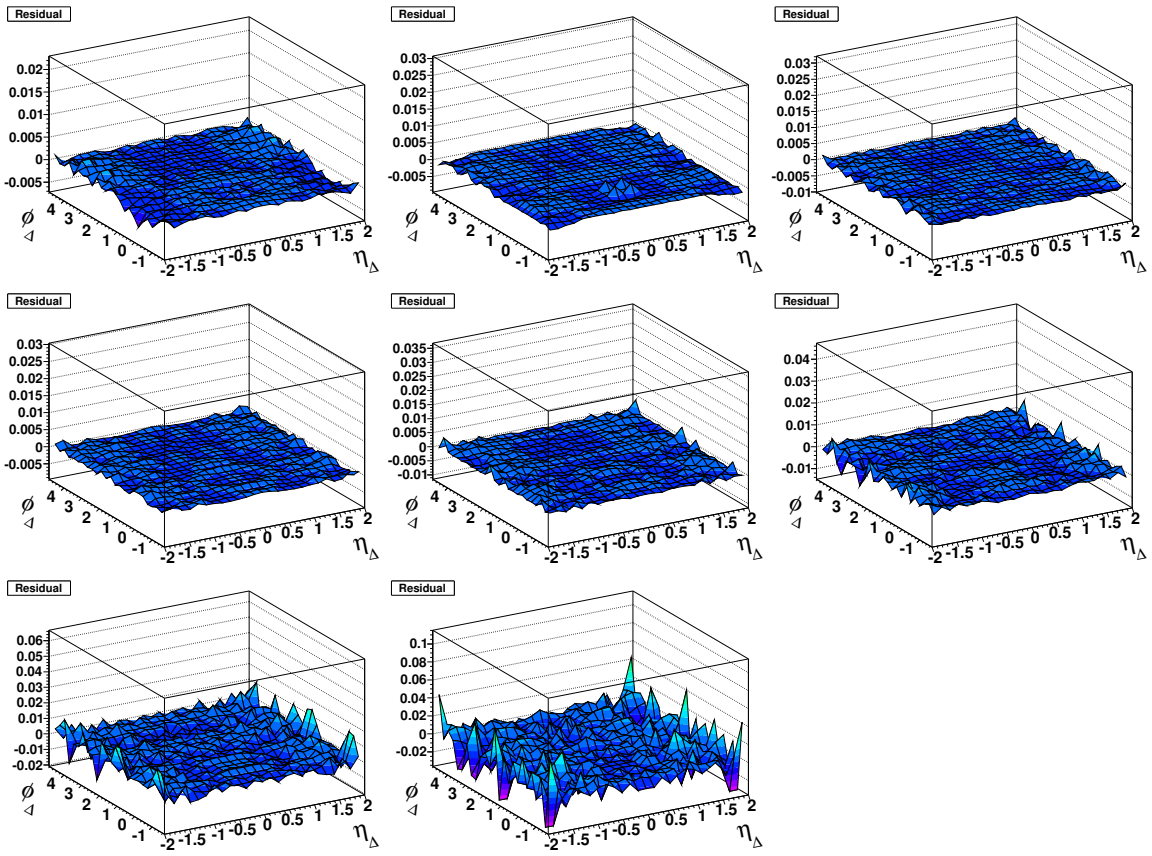

Figure A.51: Residuals for the fits to the histograms for 62 GeV 40-50% central collisions. Starting from the upper left the y_t bins are $y_t < 1.4$, $1.4 < y_t < 1.8$, $1.8 < y_t < 2.2$, $2.2 < y_t < 2.6$, $2.6 < y_t < 3.0$, $3.0 < y_t < 3.4$, $3.4 < y_t < 3.8$ and $3.8 < y_t < 4.2$.

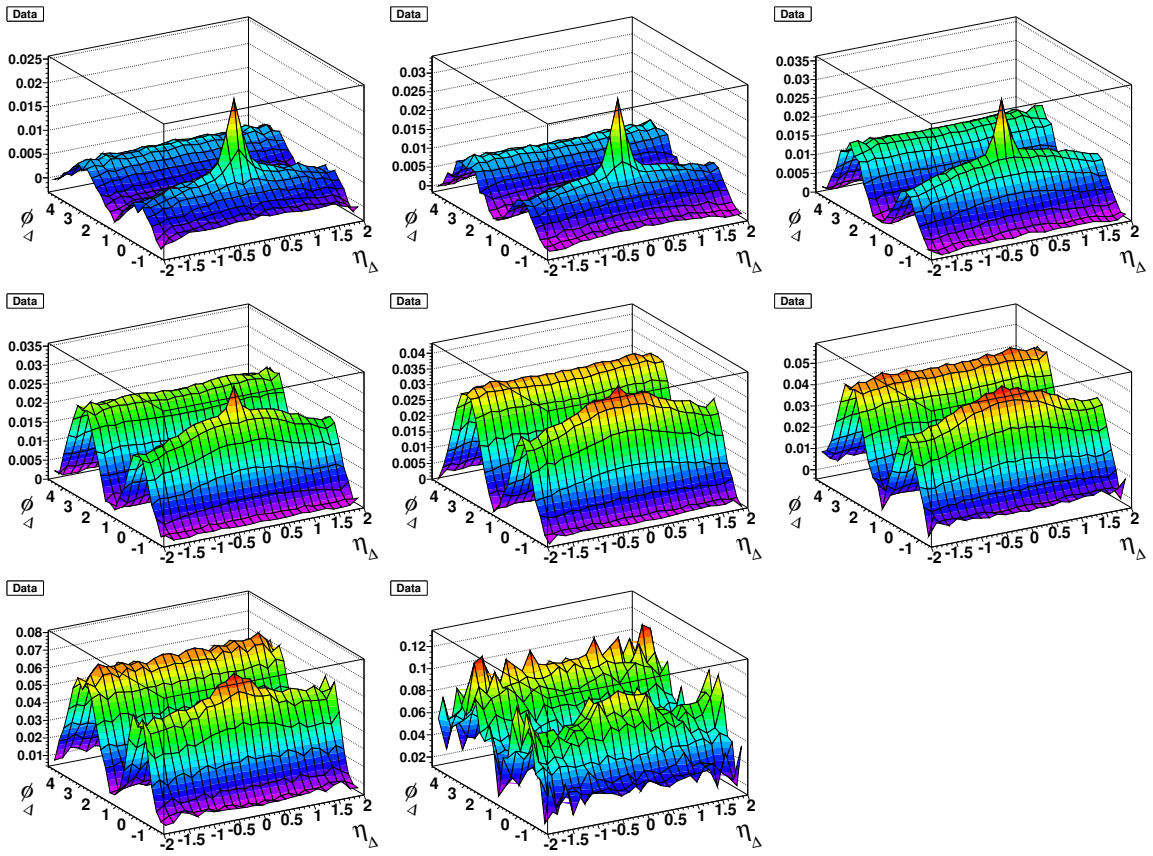

Figure A.52: Data histograms for 62 GeV 30-40% central collisions. Starting from the upper left the y_t bins are $y_t < 1.4$, $1.4 < y_t < 1.8$, $1.8 < y_t < 2.2$, $2.2 < y_t < 2.6$, $2.6 < y_t < 3.0$, $3.0 < y_t < 3.4$, $3.4 < y_t < 3.8$, and $3.8 < y_t < 4.2$.

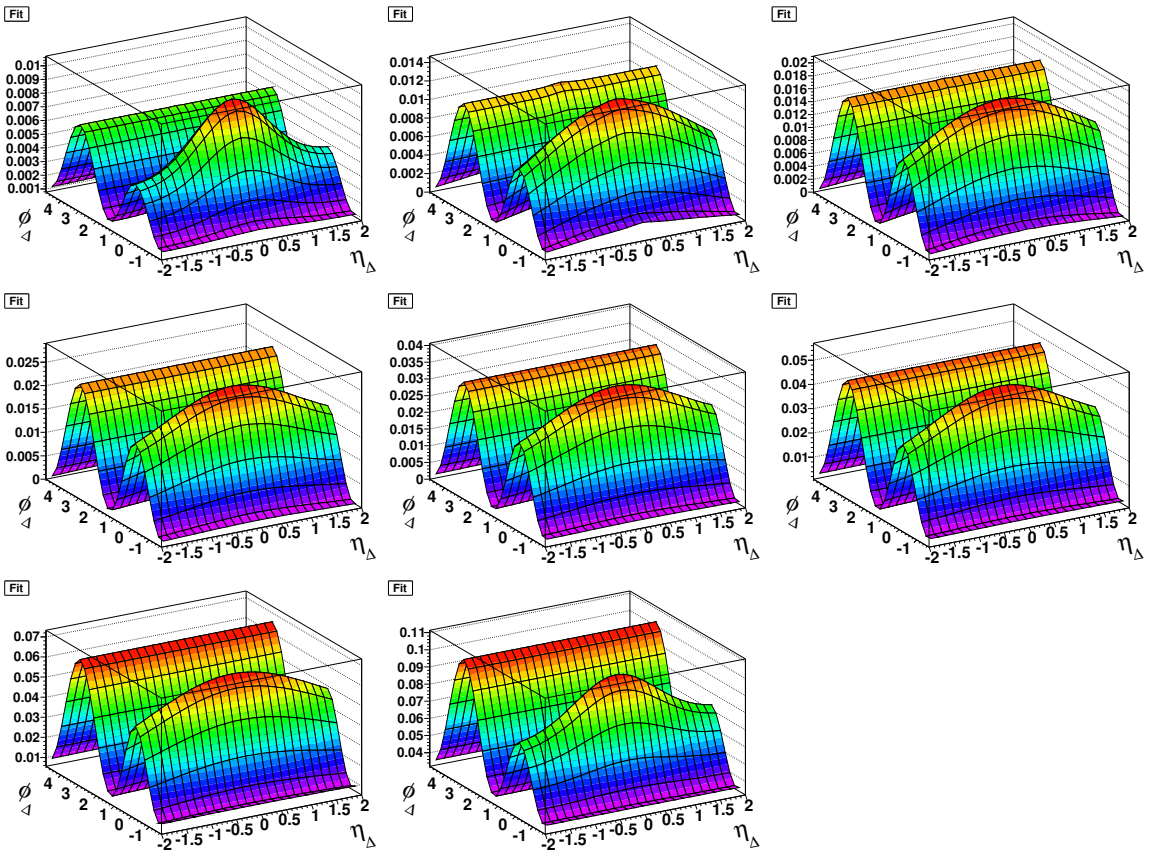

Figure A.53: Fits to the histograms for 62 GeV 30-40% central collisions. Starting from the upper left the y_t bins are $y_t < 1.4$, $1.4 < y_t < 1.8$, $1.8 < y_t < 2.2$, $2.2 < y_t < 2.6$, $2.6 < y_t < 3.0$, $3.0 < y_t < 3.4$, $3.4 < y_t < 3.8$ and $3.8 < y_t < 4.2$.

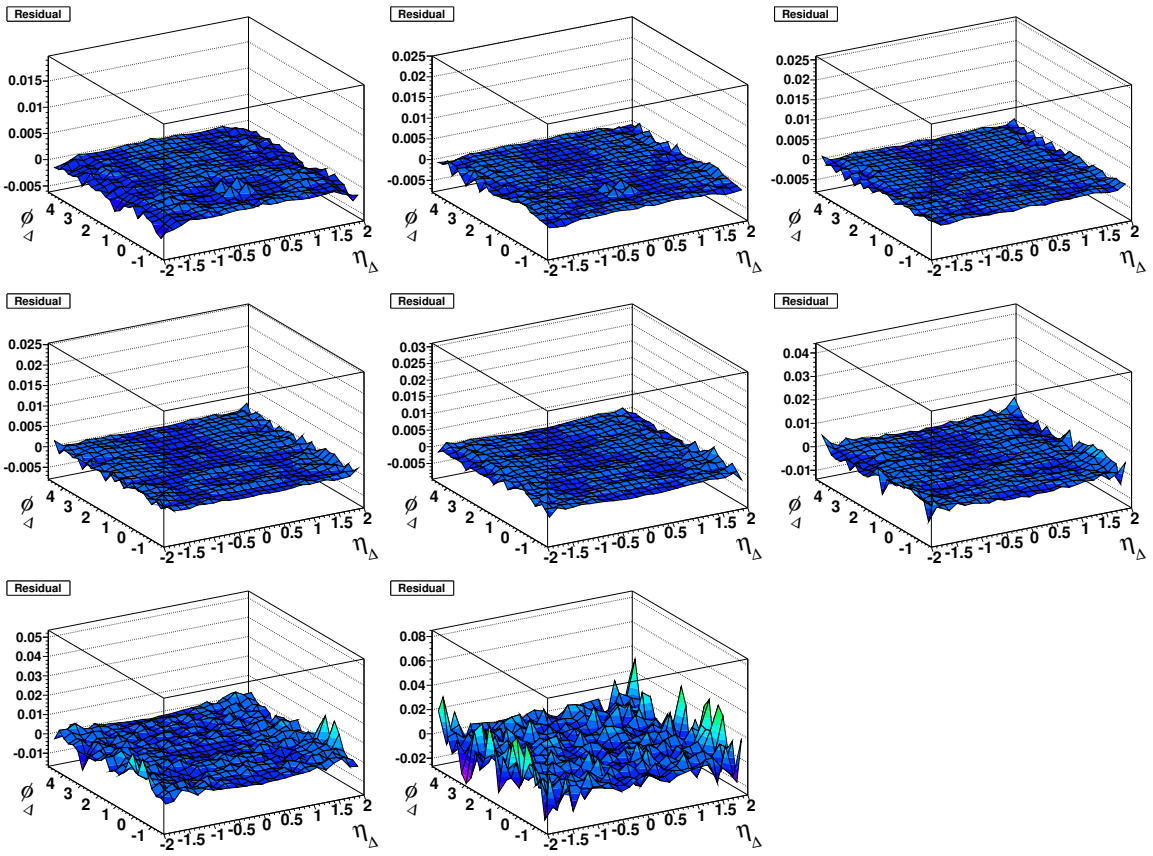

Figure A.54: Residuals for the fits to the histograms for 62 GeV 30-40% central collisions. Starting from the upper left the y_t bins are $y_t < 1.4$, $1.4 < y_t < 1.8$, $1.8 < y_t < 2.2$, $2.2 < y_t < 2.6$, $2.6 < y_t < 3.0$, $3.0 < y_t < 3.4$, $3.4 < y_t < 3.8$ and $3.8 < y_t < 4.2$.

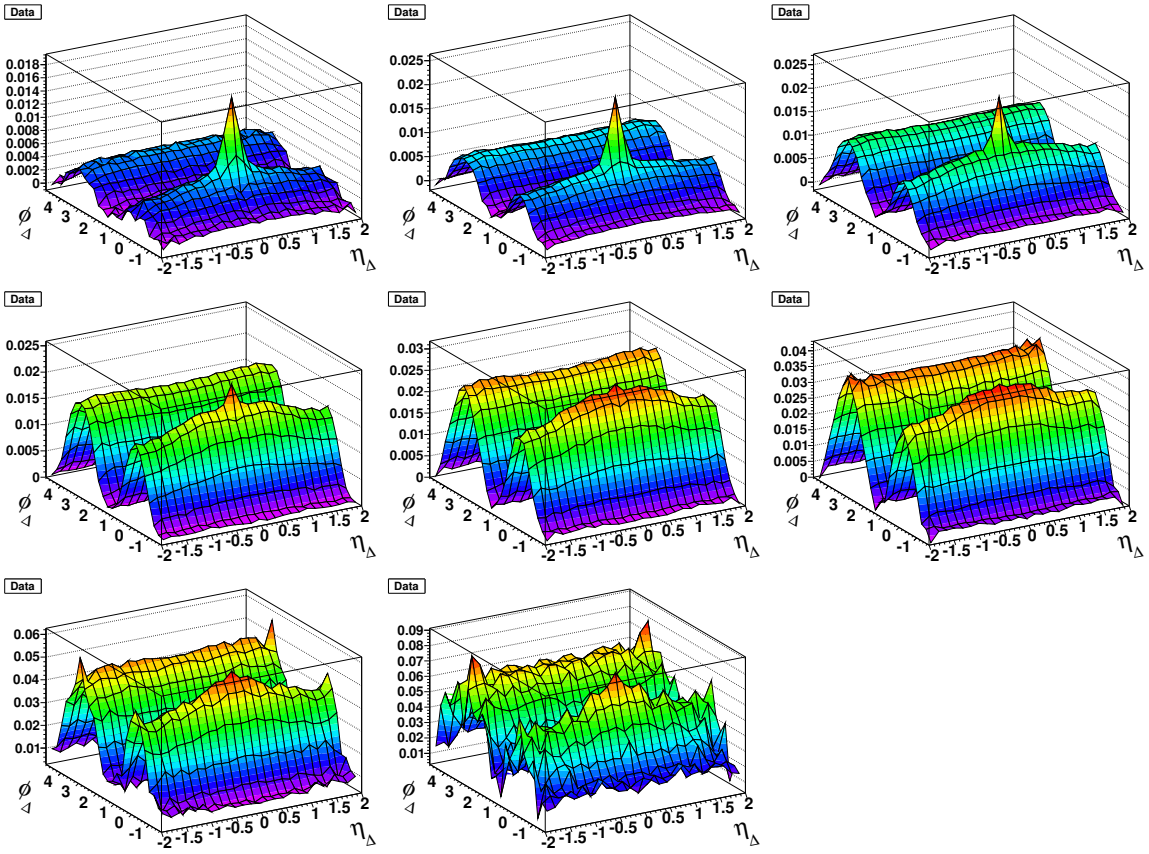

Figure A.55: Data histograms for 62 GeV 20-30% central collisions. Starting from the upper left the y_t bins are $y_t < 1.4$, $1.4 < y_t < 1.8$, $1.8 < y_t < 2.2$, $2.2 < y_t < 2.6$, $2.6 < y_t < 3.0$, $3.0 < y_t < 3.4$, $3.4 < y_t < 3.8$, and $3.8 < y_t < 4.2$.

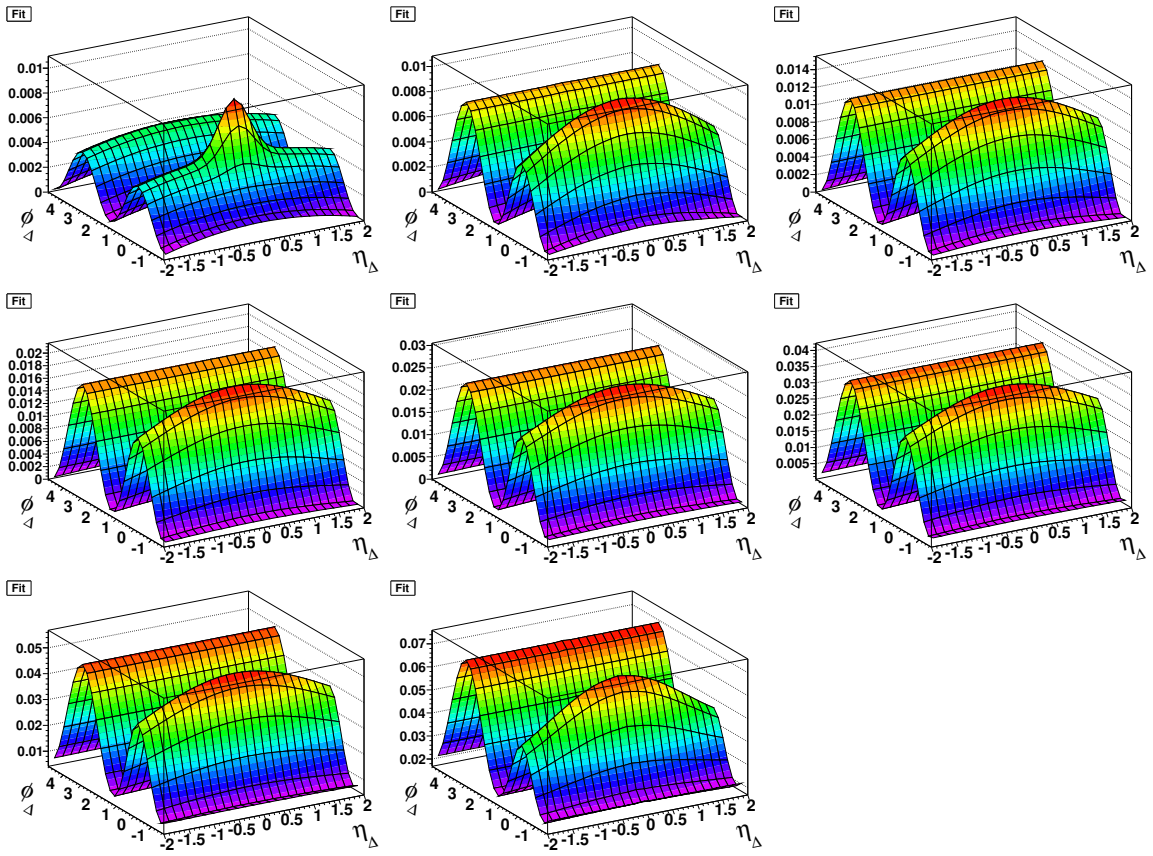

Figure A.56: Fits to the histograms for 62 GeV 20-30% central collisions. Starting from the upper left the y_t bins are $y_t < 1.4$, $1.4 < y_t < 1.8$, $1.8 < y_t < 2.2$, $2.2 < y_t < 2.6$, $2.6 < y_t < 3.0$, $3.0 < y_t < 3.4$, $3.4 < y_t < 3.8$ and $3.8 < y_t < 4.2$.

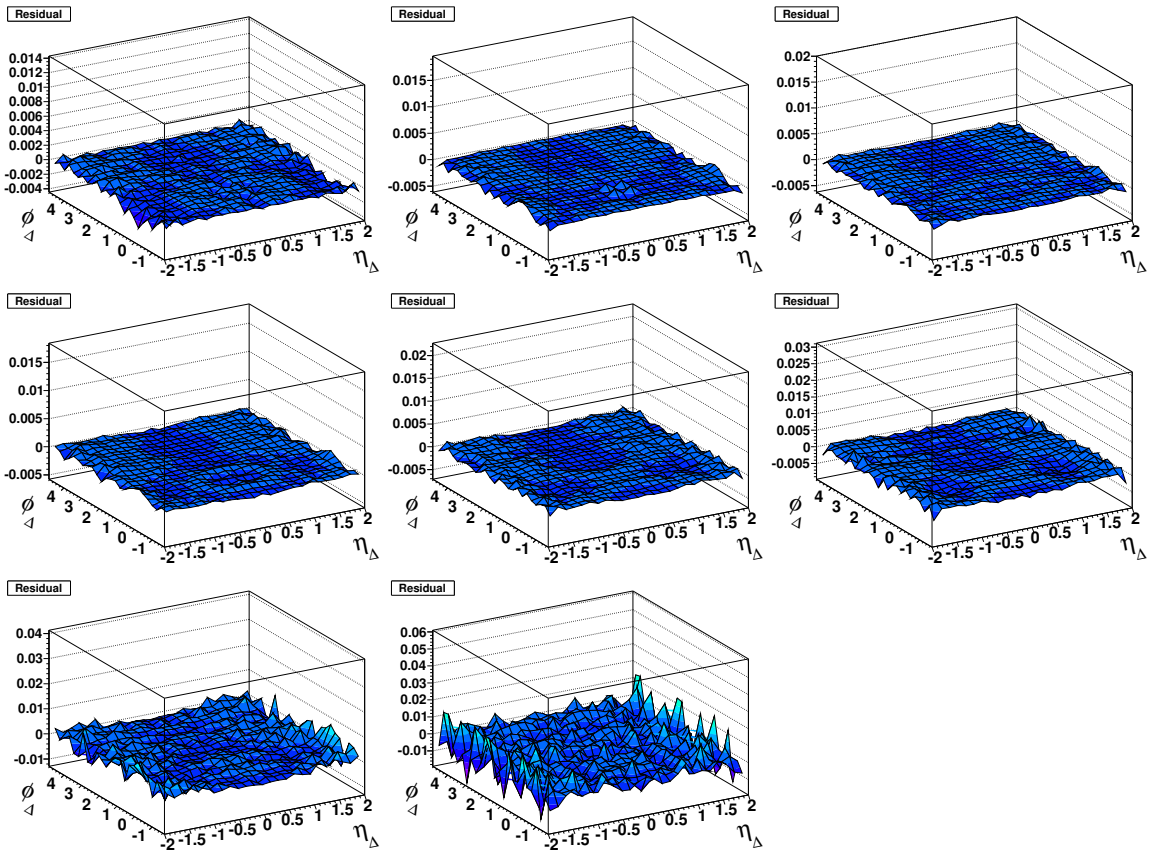

Figure A.57: Residuals for the fits to the histograms for 62 GeV 20-30% central collisions. Starting from the upper left the y_t bins are $y_t < 1.4$, $1.4 < y_t < 1.8$, $1.8 < y_t < 2.2$, $2.2 < y_t < 2.6$, $2.6 < y_t < 3.0$, $3.0 < y_t < 3.4$, $3.4 < y_t < 3.8$ and $3.8 < y_t < 4.2$.

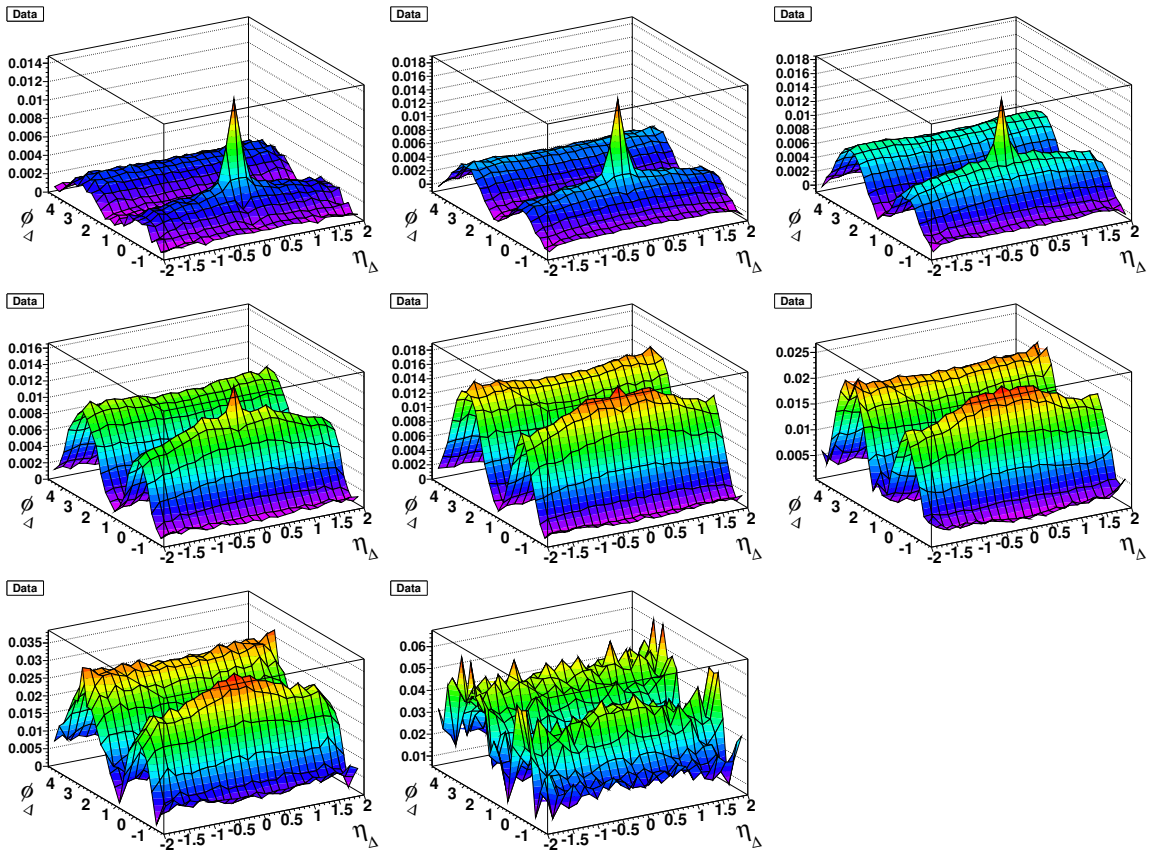

Figure A.58: Data histograms for 62 GeV 10-20% central collisions. Starting from the upper left the y_t bins are $y_t < 1.4$, $1.4 < y_t < 1.8$, $1.8 < y_t < 2.2$, $2.2 < y_t < 2.6$, $2.6 < y_t < 3.0$, $3.0 < y_t < 3.4$, $3.4 < y_t < 3.8$, and $3.8 < y_t < 4.2$.

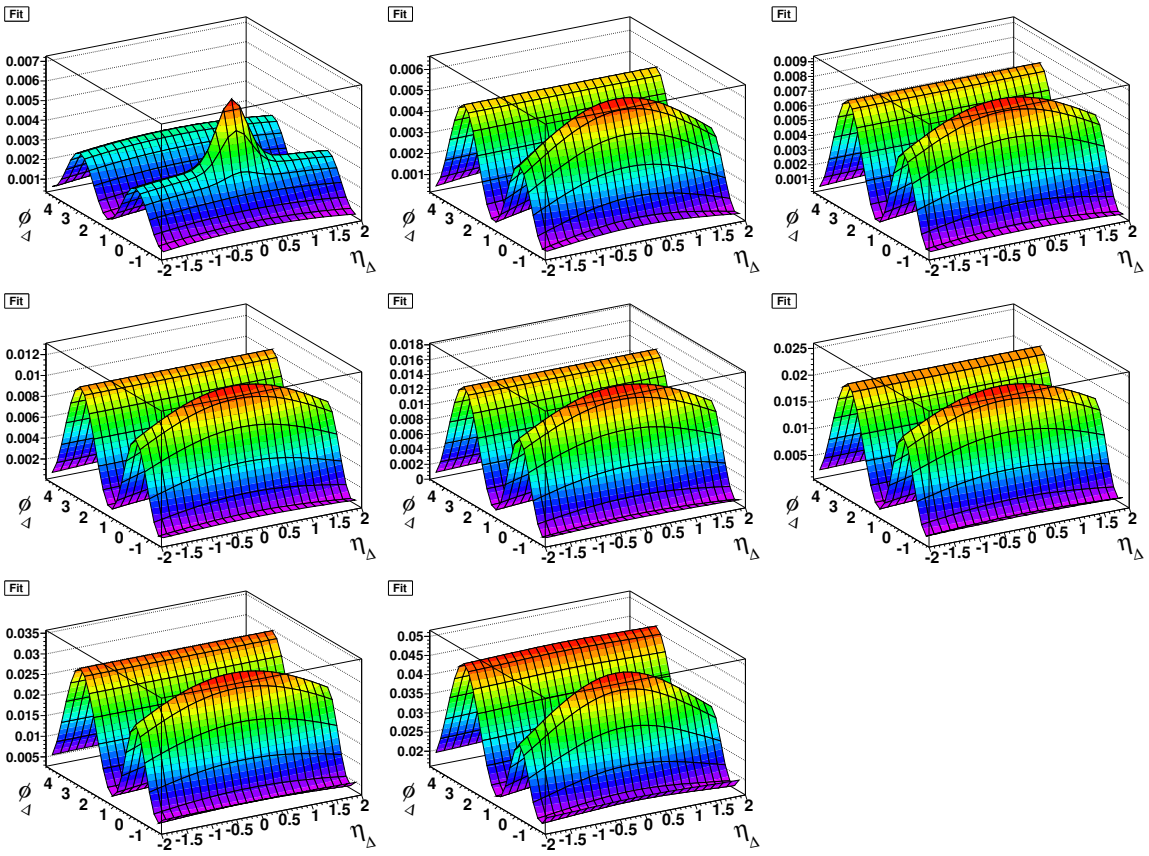

Figure A.59: Fits to the histograms for 62 GeV 10-20% central collisions. Starting from the upper left the y_t bins are $y_t < 1.4$, $1.4 < y_t < 1.8$, $1.8 < y_t < 2.2$, $2.2 < y_t < 2.6$, $2.6 < y_t < 3.0$, $3.0 < y_t < 3.4$, $3.4 < y_t < 3.8$ and $3.8 < y_t < 4.2$.

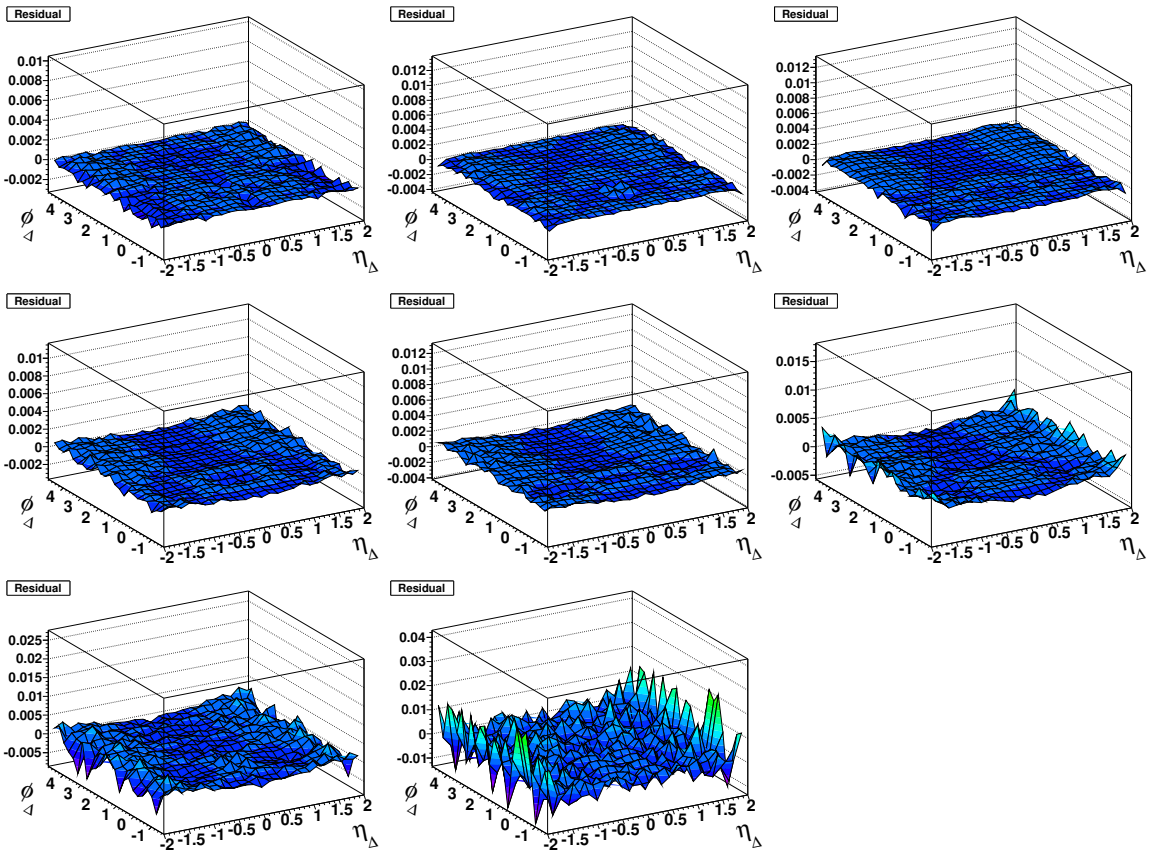

Figure A.60: Residuals for the fits to the histograms for 62 GeV 10-20% central collisions. Starting from the upper left the y_t bins are $y_t < 1.4$, $1.4 < y_t < 1.8$, $1.8 < y_t < 2.2$, $2.2 < y_t < 2.6$, $2.6 < y_t < 3.0$, $3.0 < y_t < 3.4$, $3.4 < y_t < 3.8$ and $3.8 < y_t < 4.2$.

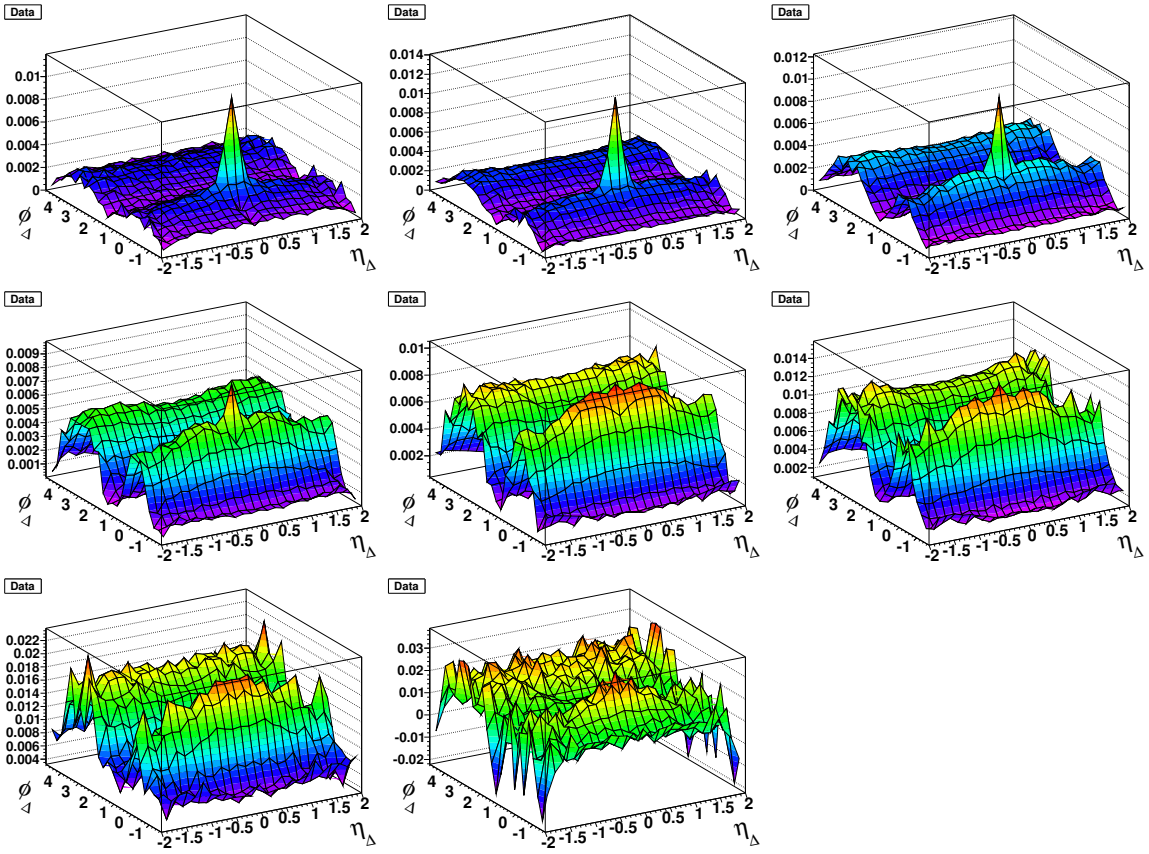

Figure A.61: Data histograms for 62 GeV 5-10% central collisions. Starting from the upper left the y_t bins are $y_t < 1.4$, $1.4 < y_t < 1.8$, $1.8 < y_t < 2.2$, $2.2 < y_t < 2.6$, $2.6 < y_t < 3.0$, $3.0 < y_t < 3.4$, $3.4 < y_t < 3.8$, and $3.8 < y_t < 4.2$.

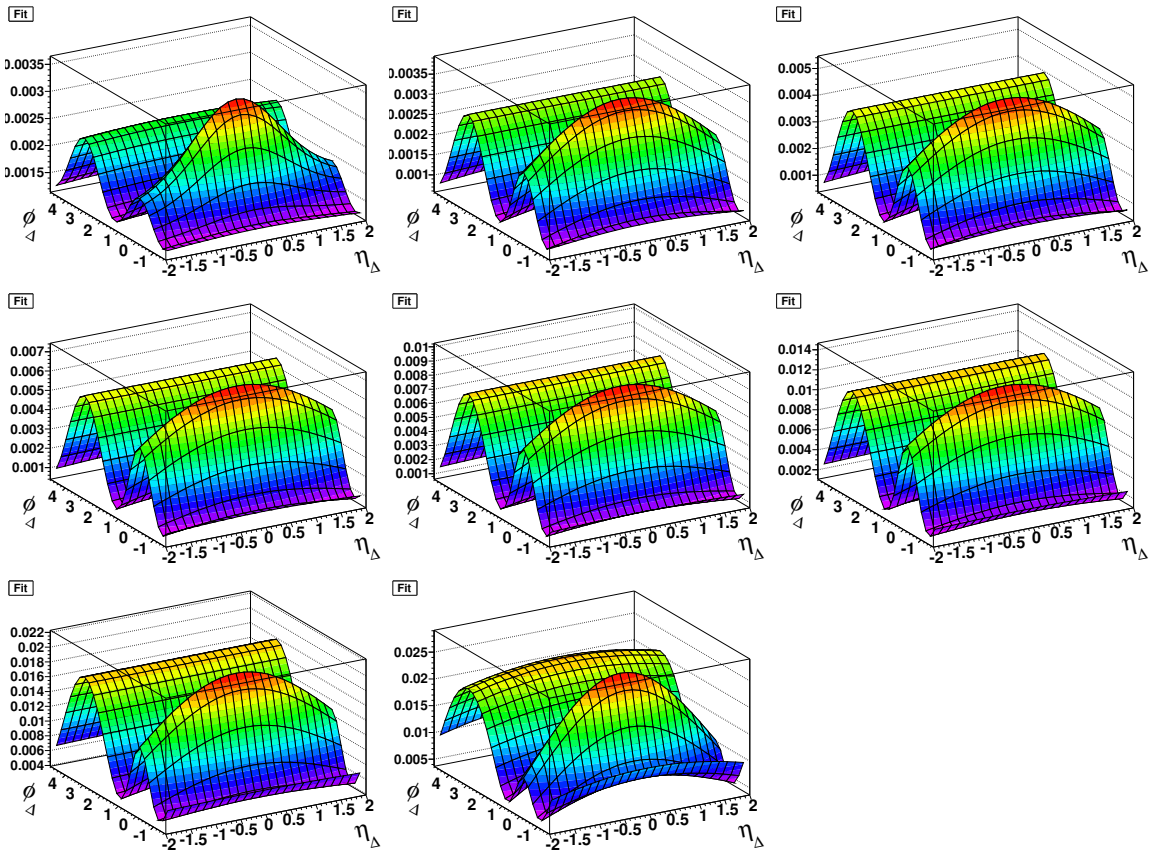

Figure A.62: Fits to the histograms for 62 GeV 5-10% central collisions. Starting from the upper left the y_t bins are $y_t < 1.4$, $1.4 < y_t < 1.8$, $1.8 < y_t < 2.2$, $2.2 < y_t < 2.6$, $2.6 < y_t < 3.0$, $3.0 < y_t < 3.4$, $3.4 < y_t < 3.8$ and $3.8 < y_t < 4.2$.

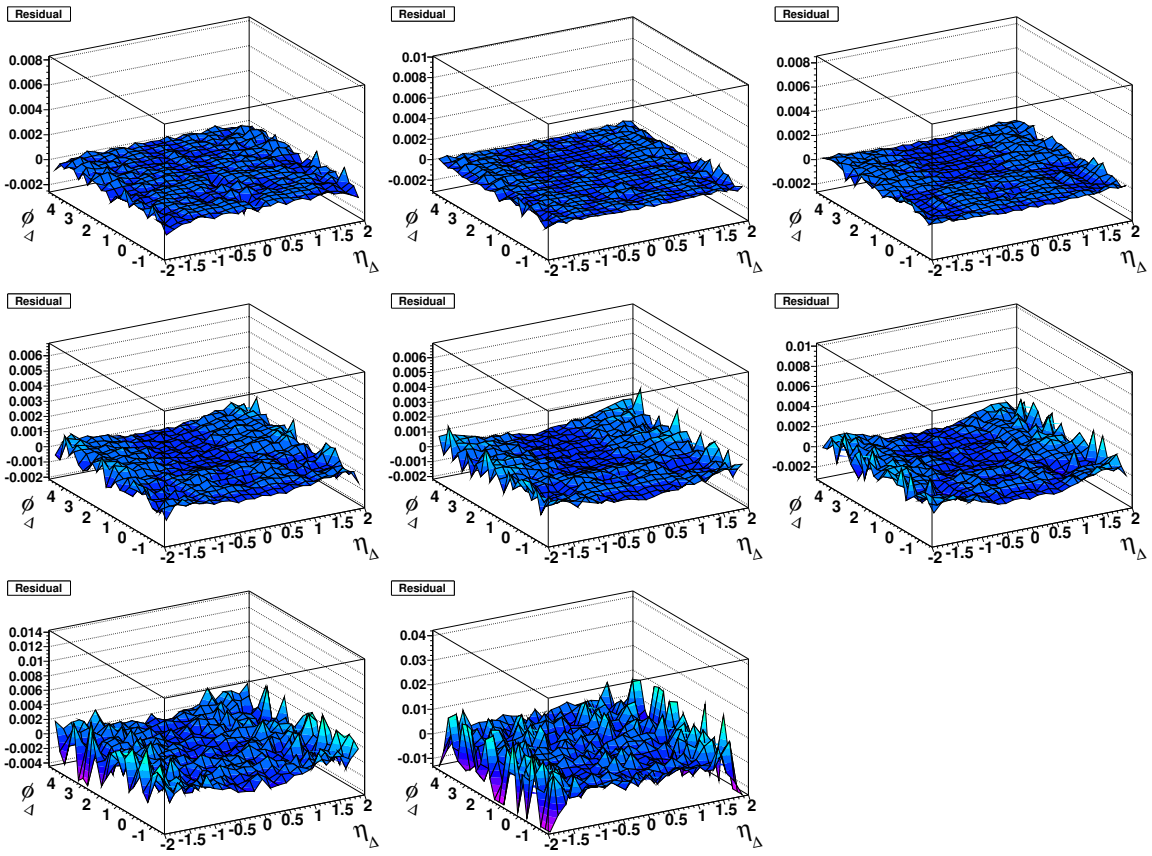

Figure A.63: Residuals for the fits to the histograms for 62 GeV 5-10% central collisions. Starting from the upper left the y_t bins are $y_t < 1.4$, $1.4 < y_t < 1.8$, $1.8 < y_t < 2.2$, $2.2 < y_t < 2.6$, $2.6 < y_t < 3.0$, $3.0 < y_t < 3.4$, $3.4 < y_t < 3.8$ and $3.8 < y_t < 4.2$.

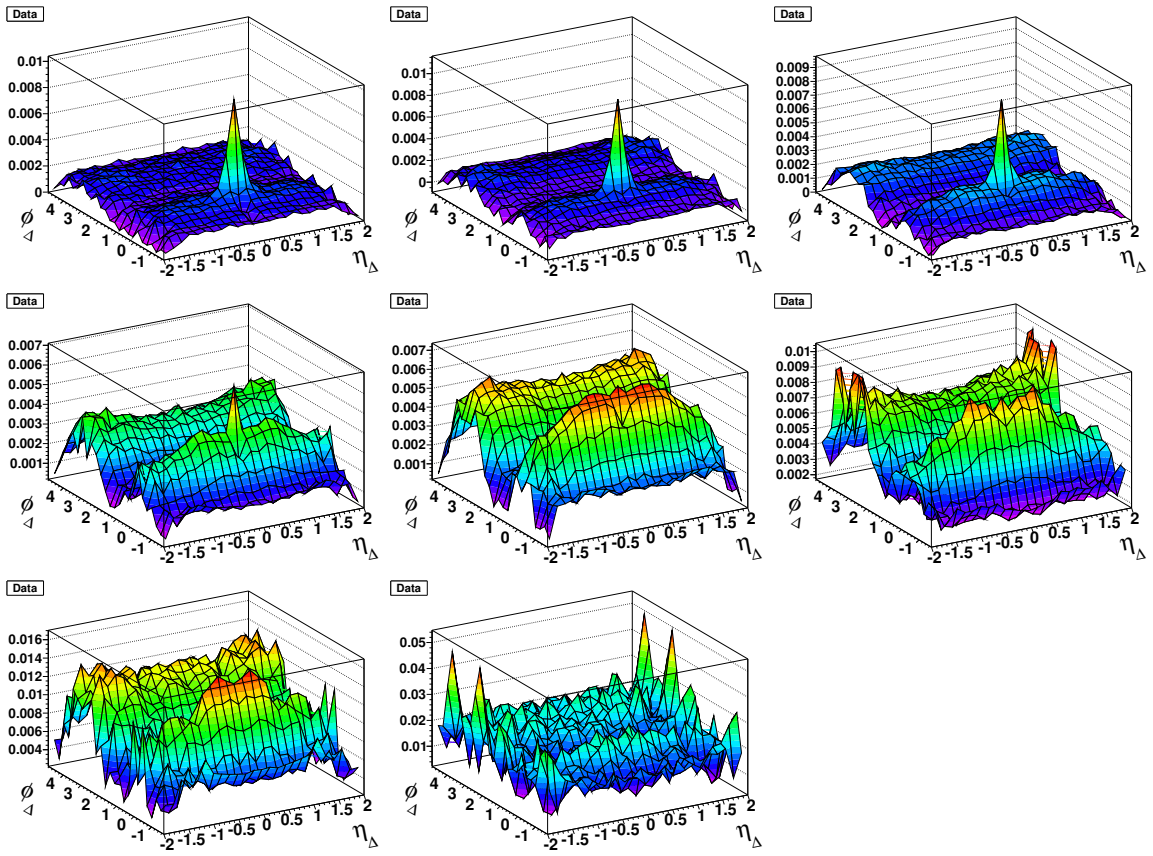

Figure A.64: Data histograms for 62 GeV 0-5% central collisions. Starting from the upper left the y_t bins are $y_t < 1.4$, $1.4 < y_t < 1.8$, $1.8 < y_t < 2.2$, $2.2 < y_t < 2.6$, $2.6 < y_t < 3.0$, $3.0 < y_t < 3.4$, $3.4 < y_t < 3.8$, and $3.8 < y_t < 4.2$.

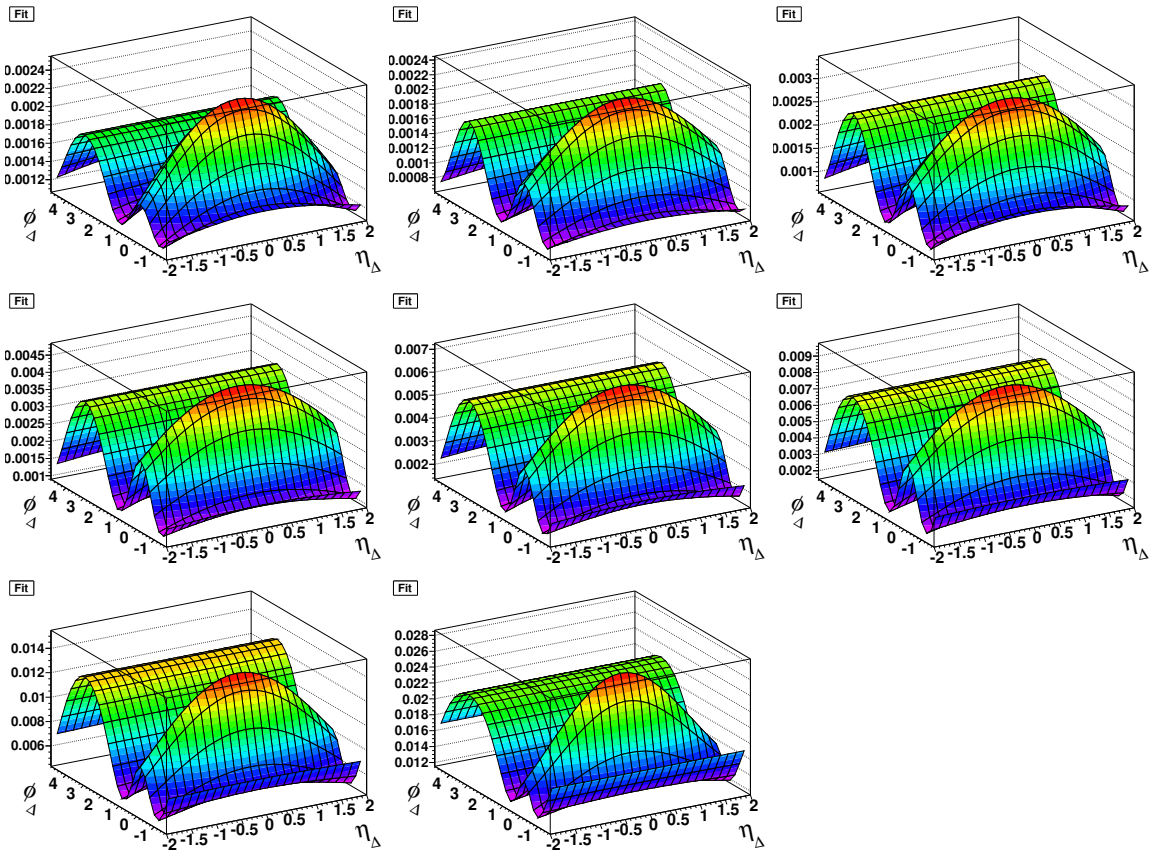

Figure A.65: Fits to the histograms for 62 GeV 0-5% central collisions. Starting from the upper left the y_t bins are $y_t < 1.4$, $1.4 < y_t < 1.8$, $1.8 < y_t < 2.2$, $2.2 < y_t < 2.6$, $2.6 < y_t < 3.0$, $3.0 < y_t < 3.4$, $3.4 < y_t < 3.8$ and $3.8 < y_t < 4.2$.

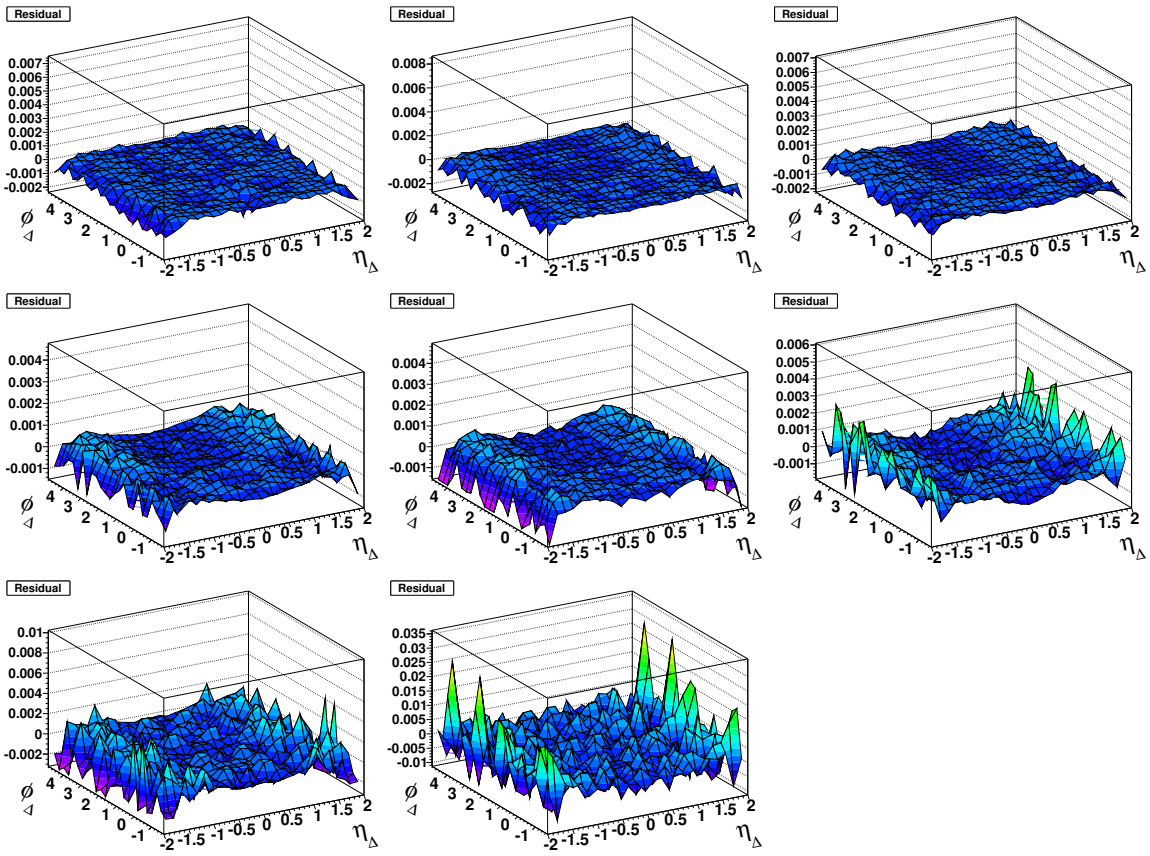

Figure A.66: Residuals for the fits to the histograms for 62 GeV 0-5% central collisions. Starting from the upper left the y_t bins are $y_t < 1.4$, $1.4 < y_t < 1.8$, $1.8 < y_t < 2.2$, $2.2 < y_t < 2.6$, $2.6 < y_t < 3.0$, $3.0 < y_t < 3.4$, $3.4 < y_t < 3.8$ and $3.8 < y_t < 4.2$.